Design, Construction, and Operation of Xenoscope and Photosensor Characterisation for the DARWIN Observatory

---

Dissertation

zur

Erlangung der naturwissenschaftlichen Doktorwürde
(Dr. sc. nat.)

vorgelegt der

Mathematisch-naturwissenschaftlichen Fakultät

der

Universität Zürich

von

Frédéric Girard

aus

Kanada

Promotionskommission

Prof. Dr. Laura Baudis (Vorsitz)
Prof. Dr. Ben Kilminster
Dr. Patricia Sanchez-Lucas

Zürich, 2023

Abstract

The existence of dark matter has been demonstrated with high certainty by cosmological and astrophysical observations. Its nature is, however, still a mystery, and its uncovering constitutes one of the greatest challenges of modern physics. Numerous beyond-the-Standard-Model theories predict the existence of at least one type of particle with properties compatible with those of dark matter. The favourite candidate particle is the weakly interacting massive particle (WIMP). The field of direct WIMP dark matter detection is currently dominated by experiments deploying liquefied noble elements in dual-phase time projection chambers (TPCs), which are continuously becoming larger and more sensitive.

The next-generation observatory, DARWIN, will deploy about 40 tonnes of instrumented liquid xenon (LXe) in a 2.6 m $\times$ 2.6 m cylindrical dual-phase TPC. The experiment will explore the full parameter space for spin-independent (SI) WIMP-nucleus elastic scattering, down to the neutrino fog, where neutrinos will become a dominant source of background for dark matter searches. DARWIN will also aim to measure other rare-event signatures, such as the neutrinoless double-beta decay ($0\nu\beta\beta$) of ^{136}Xe, and solar and atmospheric neutrino interactions in xenon.

The increased detector size and sensitivity requirements of DARWIN raise new technological challenges for dual-phase xenon TPCs. The detection of charge-proportional scintillation light at the top of the TPC, essential for three-dimensional event position reconstruction, and particle discrimination, requires the drift of generated ionisation electrons at their interaction site up to the top of the detector. This is ensured by a homogeneous, vertical electric field. Along their drift, electrons can be absorbed by electronegative impurities dissolved in the xenon, which can hinder the correct energy reconstruction of particle interactions. The xenon must therefore be continuously purified to the sub-parts-per-billion (ppb) level to ensure the survival of the drifting electrons.

In this thesis, we report on the design, construction, and operation of Xenoscope, a DARWIN-sized facility in the vertical dimension, built to demonstrate the drift of electrons over 2.6 m in LXe. A detailed description of facility infrastructure and key detector sub-systems is given, including the support structure, the gas handling and xenon purification systems, and the cryogenic and thermal insulation systems. Through rigorous global coordination of the project, we have successfully commissioned the facility during a 5-week long test run with 80.66 kg of LXe, demonstrating the operational readiness of Xenoscope. We subsequently operated a 53 cm tall LXe purity monitor with 343 kg of xenon to quantify the achievable purity level. The 89-day long run ended with an electron lifetime of (681 ± 17) ms. We also developed a data-driven model to characterise the performance of the purification system and predict the time evolution of the electron lifetime in Xenoscope.

We also report on the characterisation of vacuum ultra-violet (VUV)-sensitive silicon photomultipliers (SiPMs) from Fondazione Bruno Kessler and on the operation of Hamamatsu SiPMs in Xurich II, a small-scale TPC operated locally at the University of Zurich. This photosensor type is viewed as a potential candidate to replace the photomultiplier tubes (PMTs) used in numerous

current low-background particle detection experiments and considered for the baseline design of DARWIN. Our testing shows that the current generation of VUV-sensitive SiPM has improved in performance over the last generations, particularly in terms of their lower dark count rates, which is relevant to prevent accidental coincidence events. At LXe temperatures, SiPMs are however still outperformed by PMTs in terms of correlated and uncorrelated noise, and are hence not yet suitable for use in large-scale detectors.

Acknowledgements

There are a lot of people to whom I owe a lot for my success, as it would have been impossible to achieve so much without them. I would first like to thank Prof. Dr. Laura Baudis for her support throughout the years. The trust she put in me was instrumental in giving me the freedom I needed to accomplish everything I set out to achieve with Xenoscope. The goals we set out for ourselves were never easy, but Laura always seemed to facilitate things. I would like to thank her for the years of scientific discussions, for the many opportunities she offered us, for the career advise, and for her dedication to our success. Her open door policy is one of the best I have experienced, and she will always find time in her busy schedule to hear our concerns, and share thoughts and solutions. I am grateful to have had her as a mentor for all these years, and look forward to our continued collaboration for years to come.

I would also like to thank Dr. Patricia Sanchez-Lucas, my direct supervisor, for all her encouragement, for her attentive ear, for being a good friend. Her natural scientific talent, her work ethic, and her passion for research were a great source of inspiration throughout the years. I surely hope that our paths will cross again, be it for science, or the pleasure to meet an old friend again.

I thank Prof. Dr. Ben Kilminster, who followed my work as part of my thesis committee from the beginning. His kind words, open door and open discussions helped create the safe and focused work climate in which I evolved.

I would like to give special thanks to Dr. Diego Ramirez and Dr. Jose Cuenca Garcia for all our discussions, and for the revision and correction of this thesis. Your help and feedback will forever be remembered, and I trust that you will ensure the success of Xenoscope for years to come.

Next, I would like to thank my friend Dr. Kevin Thieme. I remember the first time Kevin and I saw each other. He didn't have to say anything, his face said "Who the &?@! is that guy? He's twice my size...". We quickly developed a chemistry based on our love of detector physics, of mechanical apparatuses, of beer, and of liquid nitrogen. I enjoyed his meticulous attention to detail, his inventive genius, and his overall understanding of physics. We worked as one in a lab. I will miss working with someone like him, who makes things work every time, no matter what. I however know I have made a friend for life, so it really could be worse. See you at the $b\bar{b}$.

I would like to thank people I worked with over the years, who I have come to love as well. When people talk about the work-life balance, they seem to forget sometimes that the work environment is also a part of life. Therefore, I am grateful to all that made my life even more enjoyable, with a beer at the Irchel Bar, with a meal at the restaurant, or with a ski-day in the swiss alps. Special thanks to Dr. Adam Brown, Dr. Patricia Sanchez-Lucas, Ricardo Peres, Giovanni Volta, Gabriela Araujo, Dr. Alessandro Manfredini, Dr. Diego Ramirez, Dr. Jose Cuenca Garcia, Paloma Cimental, Alexander Bismark, Yannick Mueller, and Dr. Yanina Biondi.

As an experimental physicist, I have come to heavily rely on the technical knowledge and

knowhow of many. Without them to facilitate the realisation of our experiments, our lab work would surely be more laborious. I would therefore like to thank the whole team of the mechanical workshop: Reto Maier, Silvio Scherr, Chris Albrecht, Bruno Lussi, Marcel Schaffner, Brandon Markwalder, Noah Regensburger, Manuel Klokow, Thomas Schär, Stevan Vujmilovic, and Max Spoerry. Besides learning to be a particle physicist, I developed with your help many personal skills from a unique learning environment, from parts designing to precision machining. I think it is easy to overlook, or forget, how important your profession is to my field, and I would like to underline how big of an impact all of you have had on our success in the lab.

I would also like to equally thank the team of the electronics workshop: Dr. Achim Vollhardt, David Wolf, Daniel Florin, and Antonio Tejada. I was once told by Prof. Dr. Jacques Farine that "all experimental physicists do is try to convert some physical process to electrons that can then be detected as an electric signal", and that electronics experts are therefore essential to our success. He was definitely right. Thank you for all the support and knowledge you give us on a daily basis.

Je veux remercier toute ma famille au Canada : maman, papa, Catherine, Pierre-Luc, Émilie, Sean. Je sais qu'il est difficile de voir partir un proche aussi loin, pour aussi longtemps. Je suis reconnaissant de votre soutien continu et de vos encouragements. Revenir à la maison est toujours un bon moment, et j'ai toujours hâte de vous revoir. Merci aussi à Linda, Cynthia, et David, qui nous supportent toujours malgré la distance qui nous sépare. Je remercie aussi tous mes amis québécois, particulièrement : Shayne, Stéphanie, Luc-Olivier, Benoit, Bianka, Axel, Caroline, Francis, Marie-Ève, Vincent, et Judith. Je suis toujours heureux de vous revoir à chacun de nos passages à Montréal, et je vous remercie pour votre amitié inconditionnelle, on s'ennuie de vous.

Finalement, merci Jen. Merci de m'avoir donné tout le support dont j'avais besoin, de m'écouter, de me conseiller. Me suivre à Zürich était beaucoup te demander, mais tu l'as fait sans hésiter. Je suis fier de ce que nous avons accompli, professionellement, individuellement, et aussi de ce que nous avons accompli ensemble. Notre mariage a définitivement été un des plus beaux moments de notre vie, et j'attends avec impatience notre prochaine aventure. Je t'aime!

À la mémoire de

Rolande Froment (1936 - 2021)

Claudette Poudrier (1943 - 2022)

Preface

It should be obvious that any doctoral student has, and will, need the help of many people during the long voyage that are doctoral studies. No matter how easy or complex the task, we rely, more often than not, on the support of advisors, supervisors, technicians, fellow students, and postdocs.

The work presented in this thesis was therefore accomplished with the help and support of numerous people within our astroparticle research group. Often, our work is collaborative in nature. Therefore, not all the work discussed in this thesis is solely mine. I provide here a summary of my own contributions to each project and the contributions of others.

- **Chapters 3 and 4:** I took part in the conceptual and technical design phases of the Xenoscope facility from the beginning, quickly taking the lead on the initial hardware design work. I have dedicated myself to ensuring the harmonious fit of all the subsystems of the facility, and to making the whole facility perform flawlessly. I designed and assembled several major components of the facility, such as the support structure and infrastructure, the cryostat and top flange assemblies, the cooling tower, and the vacuum and thermal insulation systems. I jointly designed and assembled the gas handling system with Kevin Thieme. Kevin and I always worked together: we brainstormed, machined parts, experimented, and constantly perfected our design ideas. We assembled most of the facility hardware together, with major contributions from Patricia Sanchez-Lucas, Ricardo Peres, Yanina Biondi and Alessandro Manfredini. This continuous cooperative work led us to the facility-wide commissioning in under 2.5 years.

  I oversaw and performed the commissioning phase jointly with Kevin Thieme. We developed and adjusted the operational procedures, benchmarked the different systems of the facility, while Alessandro Manfredini ensured the overall safety of the installations through the implementation of a reliable slow control and alarming system. Following the commissioning, I trained, taught, and supervised my colleagues on the operation of Xenoscope. I participated to the measurement campaign, lead by Yanina Biondi, of the electron lifetime in Xenoscope with a liquid xenon purity monitor, where my role was to ensure the continuous operation of the facility, as well as overseeing the filling and the recuperation of the xenon. Finally, my last contribution to the project was the development and testing of a new 50 kV high-voltage distribution system with Andrea Paloma Cimental Chávez, for use in the second phase of Xenoscope, the 2.6 m TPC.

  The design and results of the commissioning phase were published in Ref.:

  [1] – L. Baudis *et al.*, *Design and construction of Xenoscope — a full-scale vertical demonstrator for the DARWIN observatory*, *Journal of Instrumentation* **16** (2021) P08052 [2105.13829].

for which I am one of three corresponding authors. At the moment of writing, an article presenting the results of the measurement campaign with the liquid xenon purity monitor is in preparation.

In this thesis, I aim to give a complete description of Xenoscope, in all its complexity. In this context, I describe several systems whose design and realisation were the responsibility of other people. I want to list here the contributions of those responsible for the design, development, and/or construction and assembly of major subsystems:

Kevin Thieme:	Heat exchanger system x-y levelling system Ball of Xenon Gas cylinder storage array Finite Element Analysis of the support structure Top flange and cryostat simulations supervisor
Yanina Biondi:	LXe Purity monitor TPC Electric field simulations
Alessandro Manfredini:	Slow control system
Ricardo Peres:	SiPM array
Alexander Bismark:	LXe level control and monitoring (TPC)
Andrea Paloma Cimental Chávez:	High-voltage system (TPC)

Finally, I would like to acknowledge the contribution of all other members of the Xenoscope team, past and present, who have contributed with discussions, who have helped with the assembly, disassembly, detector operations, or in any other way, to this very large project.

I would like also recognise the incredible help and support we have received throughout this project from the mechanical workshop of the physics department at UZH, and from the electronics workshop.

The concept of the x-y levelling system of Xenoscope was conceived by K. Thieme (90 %) and myself (10 %) [2]. This invention, whose novelty was confirmed by both the Swiss Federal Institute of Intellectual Property and the German Patent and Trade Mark Office, was registered as a German Utility Model in 2022 [3]. At the time of writing, a Swiss patent (CH718439A2 [4]) has been *Applied For*.

- **Chapter 5:** The silicon photomultiplier analyses presented in this chapter, namely the measurement of the dynamic range of the Hamamatsu VUV3 multi-pixel photon counters, and the characterisation of the two FBK silicon photomultipliers, are my own. We are grateful to the *Fondazione Bruno Kessler* for providing the test samples of their SiPMs. I would like to thanks Başak Çiğdem Özcan with whom I acquired part of the FBK VUV-HD $10\times10\,\mathrm{mm}^2$ (2018) data.

  I was part of the team that made upgrade of the Xurich II TPC with silicon photomultipliers happen. Our success, however, relied heavily on the work of past members of our group, who designed and constructed the cryostat, gas system, TPC, and other relevant systems, and whose work was published in ref. [5]. In particular, Julien Wulf was instrumental with his

studies of Hamamatsu silicon photomultipliers, the preparation of the silicon photomultiplier array, and the development of the DAQ and processing software. I was involved in the preparation of the Xurich II hardware during the upgrade, and I also upgraded the DAQ hardware and software to enable multi-ADC operation with zero length encoding.

The operation and the analyses of the upgraded Xurich II detector were performed by Kevin Thieme, helped by Patricia Sanchez-Lucas. The results of the first xenon TPC with silicon photomultipliers were published in:

[6] – L. Baudis *et al.*, *The first dual-phase xenon TPC equipped with silicon photomultipliers and characterisation with* ^{37}Ar, *The European Physical Journal C* **80** (2020) 477 [2003.01731].

Finally, I believe there are times when science meets art. Throughout my doctoral studies, I have often documented the progress of our research through photography. We have always placed some effort and design considerations into both functionality, and aesthetics. The result was, in my opinion, the ideal blend of beauty, functionality, and precision. In this spirit, I have included, at the end of each chapter, photographs that depict the intrinsic beauty of science.

Contents

List of Figures

List of Tables

Introduction

The nature of dark matter is one of the big mysteries of modern physics [7]. Its existence is well motivated by cosmological and gravitational observations at galactic and extragalactic scales, which our gravitational models fail to explain. A leading theory is the presence of invisible, weakly interacting matter not described by the Standard Model (SM) of particles [8].

For decades, increasingly sensitive experiments were designed to try to detect, or produce, dark matter. To date, the lack of a dark matter detection has only allowed experiments to set upper limits on the mass-dependent cross section of candidate particles. DARk matter WImp search with liquid xenoN (DARWIN), a next-generation experiment for dark matter search and neutrino physics, will use one of the most sensitive technologies for particle detection, the time projection chamber (TPC).

The topics of this doctoral dissertation are hardware research and development (R&D) projects for DARWIN. In particular, we tried to address some of the many conceptual and engineering challenges that DARWIN will have to face. We therefore designed, constructed, and operated Xenoscope, a DARWIN-scale demonstrator facility, with the goal of demonstrating the feasibility of drifting electrons in LXe over a distance of 2.6 m. We also investigated novel photodetectors for potential use in DARWIN.

The outline of this thesis is as follows:

The concept of particle dark matter is first introduced in chapter 1. We start with the presentation of some of the main evidence of the existence of dark matter, followed by the description of some well-motivated candidate particles. We then describe the different methods used for their detection, with a focus on direct detection experiments.

Chapter 2 then focuses on xenon as a target material for dark matter searches, and specifically in dual-phase xenon TPCs. We then give an overview of the DARWIN experiment, its baseline design, and its physics reach as a multi-physics observatory.

Chapter 3 details the design and construction of Xenoscope. We present all its subsystems, including the support infrastructures, the xenon gas handling, purification , and storage systems, the cryogenic and thermal insulation systems, and finally the slow control system. This chapter ends with a presentation of two of the major operational procedures established with successive

operations of the facility, namely the filling, and the recuperation of xenon to and from the cryostat.

Chapter 4 describes the operation of Xenoscope, first in its commissioning run, followed by the operation of a 0.53-m tall LXe purity monitor (PM) used to measure the achievable purity of the LXe in Xenoscope. We present a predictive electron lifetime model, which is then modified into a data-driven model. This chapter ends with the description of the 2.6 m TPC planned for Xenoscope, with a focus on the production of a novel, in-house made high-voltage (HV) feedthrough. We conclude with a brief overview of the potential future applications of Xenoscope.

Finally, we present in chapter 5 an investigation of silicon photomultipliers (SiPMs) as potential replacements for the traditional photomultiplier tubes (PMTs) used in low-background, low-energy searches. We start with a general description of light detection in silicon. We present a measurement of the dynamic range of a Hamamatsu VUV-3 Multi-Pixel Photon Counter (MPPC), and the characterisation of two SiPMs from Fondazione Bruno Kessler (FBK). We conclude with the presentation of some contributions to the upgrade of Xurich II, a local, small-scale xenon TPC, the first to be operated with SiPMs.

1

Particle Dark Matter

The world that surrounds us is simple. It is governed by a few universal Laws of Physics. And yet, when we look at its every detail, our world can appear infinitely complex. Thousands of philosophers and scientists have devoted their lives to uncovering the true nature of our Universe, and describing it with physical and mathematical representations of everything surrounding us.

Over the last two centuries, major discoveries have exponentially improved our understanding of the Universe, from the infinitely small to the infinitely large. The identification of the electron by J. J. Thomson in 1897 [9] opened the door to the world of particles.

Since then, a whole zoo of particles has been discovered. The Standard Model of particle physics contains seventeen elementary particles, that are the fundamental building blocks of matter [11]. A graphical representation of the Standard Model is shown in figure 1.1. Twelve elementary particles are fermions, with spin $1/2$: six quarks, the constituents of hadrons, and six leptons. These two categories are further classified into four groups, where the particles differ only by their mass. The two groups of quarks are referred to after their lightest particle: the *up*-like, with charge $2/3$, and the *down*-like, with charge $-1/3$. The two groups of leptons are the charged leptons, with charge -1, and their associated neutral, massless (according to the Standard Model) neutrinos. The observation of neutrino oscillations in Super-Kamiokande and the SNO experiment in the late 1990s proved, however, that the neutrinos are indeed massive [12].

The Standard Model is based on several decades of theoretical formalism and experimental observations [13]. The theory is immensely successful, correctly predicting the existence of the top quark (1995 [14]), of the tau neutrino (2000 [15]), and more recently of the Higgs Boson (2012 [16, 17]).

Despite its resounding success, the Standard Model fails to paint the full picture of particle physics. The *strong CP problem*, the *gauge hierarchy problem*, and the *neutrino mass problem* are some of the strongest shortcomings of the theory. These are all well described in ref. [18]. Additionally, and as we will discuss in this chapter, there is strong evidence for the existence of physics beyond the Standard Model due to the existence of dark matter.

In this chapter, we will thus paint a revealing portrait of dark matter. We will first expose some of the most compelling astrophysical evidence for its existence in section 1.1. We will elaborate

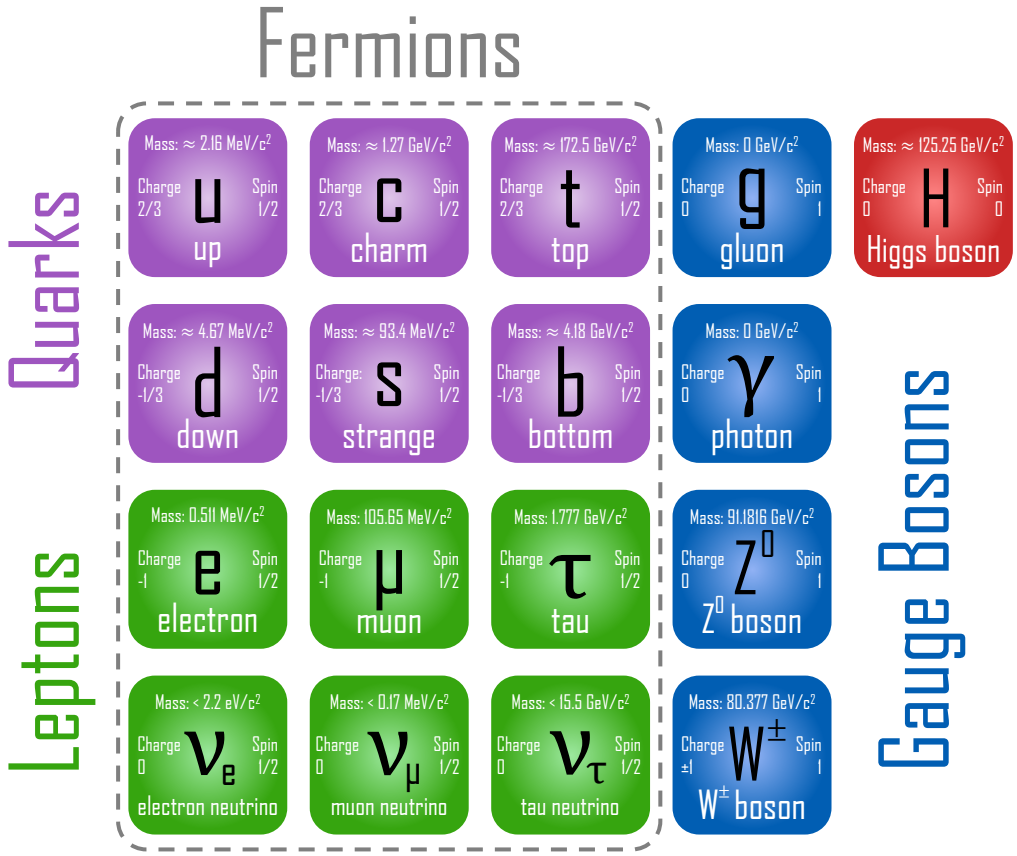

Figure 1.1: The Standard Model of particles. Seventeen elementary particles constitute the building blocks of all known particles: six quarks, six leptons, and five bosons. Particle properties taken from ref. [10].

on potential candidate particles in section 1.2, and we will give an overview, in section 1.3, of the different methods exploited to detect – or produce – and possibly identify dark matter.

1.1 Astrophysical Evidence for the Existence of Dark Matter

The scientific community has now broadly recognised the existence of dark matter. Although it has yet to be detected, we have observed a plethora of astrophysical and cosmological consequences that indicate the existence of invisible matter across different scales in the Universe. We have compiled below a list of some of the most compelling arguments supporting the existence of dark matter.

1.1.1 Velocity Dispersion and Galactic Rotation Curves

Swiss astronomer Fritz Zwicky observed, already in 1933, galactic anomalies in Abell 1656, also known as the *Coma cluster*, a cluster of galaxies of which he was studying the velocity dispersion [19]. He highlighted a discrepancy between the mass of the cluster inferred from its observed

luminosity and that obtained with the virial theorem, which states:

$$2\langle K\rangle = -\langle V\rangle \,, \tag{1.1}$$

where $\langle K\rangle$ is the average over time of the kinetic energy of the system and $\langle V\rangle$ is its average over time of the potential energy. Zwicky suggested the presence of non-luminous, obscure matter inside the cluster, "*dunkle Materie*", to reconcile the disagreement between the two conflicting observations. Although Zwicky is often credited with being the first to correctly interpret non-luminous matter as explaining rotational effects at extra-galactic scales, many others, including Öpik [20], Kapteyn [21], Jeans [22], and Oort[23], observed similar effects and coined the term "dark matter" before Zwicky.

A defining observation was thereafter made by astronomy pioneers Vera C. Rubin and Kent W. Ford, this time at the galactic scale [24]. In 1970, they witnessed a discrepancy between the theoretical and the observed radially-dependent orbital velocities of stars in the Andromeda galaxy (M31) derived from the observation of Hα emission in H II regions. Whereas the classical theory of gravitation predicts the velocity to be inversely proportional to the radial distance:

$$v(r) = \sqrt{\frac{GM(r)}{r}}\,, \tag{1.2}$$

where G is the gravitational constant, $M(r)$ is the enclosed mass of the galaxy at the radius r, they observed a flatter velocity distribution with increasing distance from the galactic center. This measurement is shown in figure 1.2a. A simple explanation is the presence of a spherical dark matter halo several times the luminous mass, with a density profile of $\rho(r) \propto 1/r^2$ at large radii [25, 26]. During the following decades, hundreds of thousands of observations in as many other systems, such as the case of NGC 6503 shown in figure 1.2b, permitted us to deepen our understanding of galactic mechanics. [27, 28].

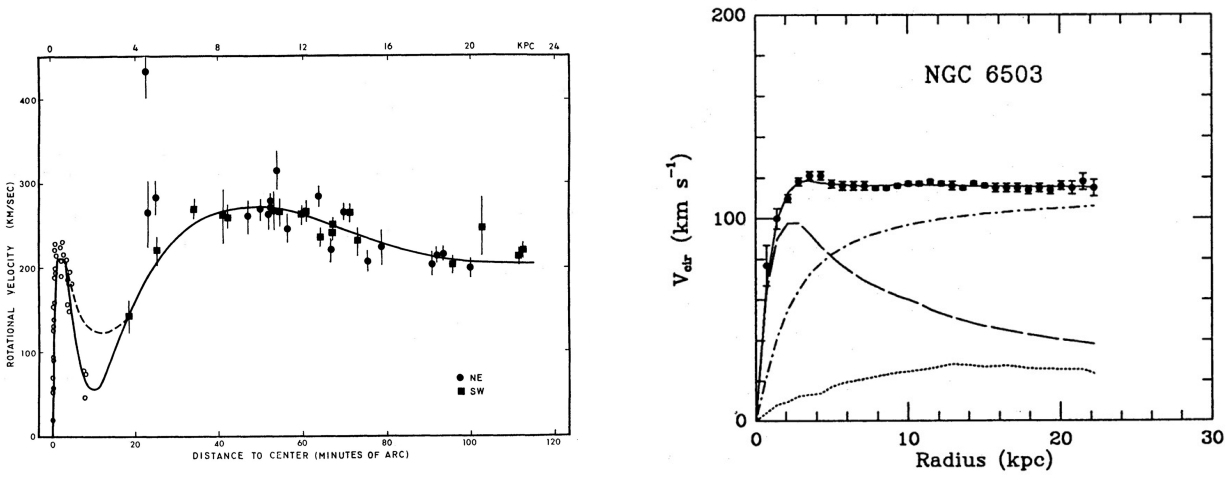

(a) (b)

Figure 1.2: Examples of galactic rotation curves. **(a)** "Rotational velocities of OB association in M31, as a function of distance from center". This graph from the original publication of V. Rubin and K. Ford (1970) shows the flat trend, with distance from the center, in M31. Figure from ref. [24]. **(b)** This three parameter dark halo fit of the NGC 6503 galaxy is a prime example of the discrepancy of classical orbital mechanics and models including a dark matter component to the mass of galaxies. Legend: visible components (dashed); gas (dotted); dark halo (dash-dot). Figure from ref. [27].

1.1.2 Merger of Galaxy Clusters

The observation of unexplained gravitational effects at large scales strongly suggests the existence of some invisible form of matter. The merger of galaxy clusters can further inform us on some other important properties of dark matter.

The observation technique relies on the concept of gravitational lensing, schematically shown in figure 1.3. The concept was theorised by Albert Einstein as early as 1912, before publishing his theory of general relativity [30]. As the gravitational field of a massive object warps space-time, as derived from the theory of general relativity, it can deflect light passing in its vicinity. Such an object located between an observer and a luminous, distant object, acts as a magnifying glass. Einstein was encouraged to publish a small note on the topic by Rudi W. Mandl, which he did in 1936 [31]. Others, such as Oliver Lodge [32] and Arthur Stanley Eddington [33], have also independently contributed to the development of the theory of gravitational lensing. All the aforementioned physicists initially thought the phenomenon was too weak to be observed. This observation technique is not light-based, but instead relies on gravitational effects on the light produced by more distant objects. It is therefore a powerful tool used to infer and quantify the presence of non-luminous matter.

Astronomers use weak gravitational lensing to determine the mass distribution of astronomical objects. Large mass distributions located in between an observer and a distant luminous source can bend the light coming from distant objects, distorting the observed image. Weak gravitational lensing relies on statistical analyses, measuring the shear of the lensing field, which allows for the determination of the distribution of mass.

Although gravitational effects on the velocity distribution of luminous matter in galaxy clusters inform on the significant amounts of dark matter therein, gravitational lensing techniques can reveal the mass distribution of non-luminous matter in galactic superstructures. Additionally, observations

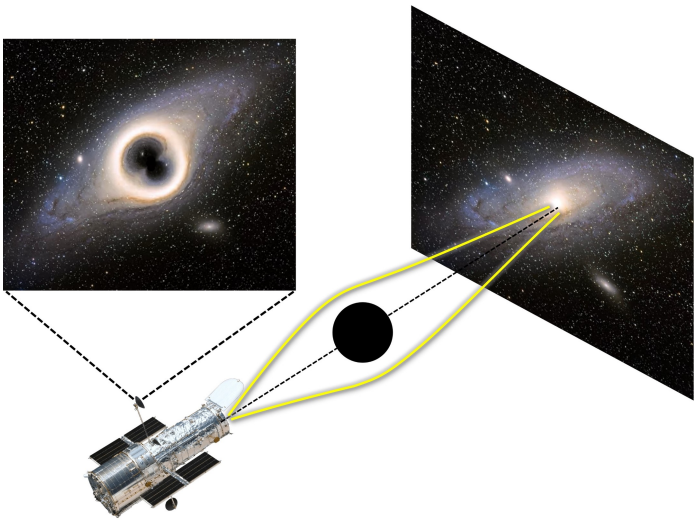

(a)

(b)

Figure 1.3: Gravitational lensing. **(a)** Schematic of gravitational lensing. In this simulated image, the gravitational field of a massive object located in between an observer and a distant object deflects the light, distorting the observed image. Photo credit: [29]. **(b)** Photograph of Abell 370 galaxy cluster. The gravity of the cluster magnifies fainter galaxies in the background, producing rings of light. Photo credit: NASA, ESA, and J. Lotz and the HFF Team (STScI).

of extra-galactic mergers reveal the collisionless nature of dark matter.

Perhaps the most famous example is the *Bullet Cluster* (cluster 1E 0657-56). Figure 1.4a shows a composite image of the cluster. The pink X-ray data from the Chandra X-ray Observatory [34] are superimposed over an optical photograph (Photo credit: NASA/STScI; Magellan/U.Arizona/D.Clowe et al. [37]). The mass inferred from both visible and weak gravitational lensing data, is overlaid in blue [35, 36]. Interstellar gases from both clusters are thought to have interacted and been affected by ram pressure during the merger. They warmed up and finally cooled down by emitting X-ray radiation. Meanwhile, the stars were separated from the interstellar gas as they continued unaffected on their journey. The weak gravitational lensing studies show that the total mass outside the interaction site is much larger than the mass accounted for by the luminous matter, indicating the presence of a large amount of non-luminous dark matter. This therefore implies that this matter is non- or weakly-interacting with normal matter and itself, and in the absence of Coulomb interactions that dark matter is chargeless.

Although famous, the Bullet cluster is not unique. Figure 1.4b shows Abell 2744, nicknamed the Pandora Cluster, a complex collision of at least four galaxy clusters. The X-ray data obtained from the Chandra X-ray Observatory is overlaid in red, and the mass distribution from optical and weak gravitational lensing data in blue [38]. When the visible and X-ray emitting mass are compared to the total mass inferred from gravitational lensing, it is estimated that stars account for only 5 % of the total mass, while hot, X-ray emitting gas accounts for 20 %. The rest of the mass, around 75 %, is thought to be dark matter.

Astronomers have now identified hundreds of extra-galactic objects where the gravitational effects of invisible mass can be observed. This direct proof of non-interacting, non-luminous, uncharged dark matter reinforced in the mid-2000s the already-accepted existence of this yet-to-be identified type of matter.

(a) (b)

Figure 1.4: Examples of mergers of galaxy clusters. **(a)** Cluster 1E 0657-56, also known as the *Bullet Cluster*. Photo credit: X-ray [34], lensing maps [35, 36], optical: NASA/STScI [37]; Magellan/U.Arizona/D.Clowe et al. **(b)** Abell 2744, also know as the *Pandora Cluster*. Photo credit: X-ray: NASA/CXC/ITA/INAF/J.Merten et al, Lensing: NASA/STScI; NAOJ/Subaru; ESO/VLT, Optical: NASA/STScI/R.Dupke [38].

1.1.3 Cosmic Microwave Background

In 1965, Arno Penzias and Robert Wilson, two radio-astronomers working on a Holmdel radiometer, a horn radio-antenna intended for radio-astronomical observations, discovered by chance a radio-frequency signal that seemed to emanate from everywhere in the sky, homogeneously. This signal, named the Cosmic Microwave Background (CMB), is thought to be a relic of the past, from a time when photons first decoupled from the hot hydrogen plasma, approximately 370 000 years after the Big Bang [40]. From then on, photons were free to propagate through the Universe. As the Universe expanded, the wavelength of the photons lengthened, lowering their energy. Today, the CMB is well described with a black body function with a mean temperature of $T = (2.725\,5 \pm 0.000\,6)\,\mathrm{K}$ [41]. The two astronomers studied the signal, which eventually warranted them the 1978 Nobel Prize in Physics [42, 43].

Temperature intensity variations were carefully mapped by the Cosmic Background Explorer (COBE, 1989-1993 [44]), the Wilkinson Microwave Anisotropy Probe (WMAP, 2001-2010 [45]) and the Planck space observatory (2009-2013 [39]). The latter two experiments also studied the polarisation of the CMB. Figure 1.5a shows the temperature anisotropies of the CMB as measured by Planck. The tiny temperature variations ($\pm 300\,\mu\mathrm{K}$) are the consequence of small density variations in the primordial soup of matter at the time of the recombination. The grey outline is the outline of a mask applied where residuals from foreground emission are expected to be substantial, mostly due to our galactic disk. The data shown inside the mask are inpainted [46].

The temperature anisotropies of the CMB can be expressed as a spherical harmonic expansion:

$$T(\theta, \phi) = \sum_{lm} a_{lm} Y_{lm}(\theta, \phi), \tag{1.3}$$

where a_{lm} is the amplitude of each mode, and Y_{lm} are the spherical harmonics. The analysis of the power spectrum of the temperature anisotropies, shown in figure 1.5b, informs on key parameters of the ΛCDM (*Lambda-Cold-Dark-Matter)* model, considered the Standard Model of cosmology [48]. Indeed, the fit of the spectral analysis constrains, amongst others, the baryon density parameter

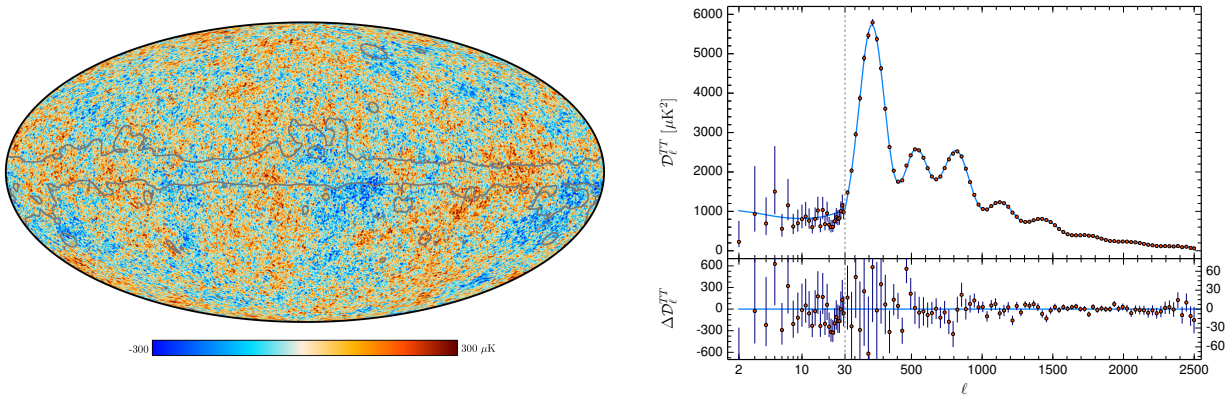

(a) (b)

Figure 1.5: The Cosmic Microwave Background. **(a)** This image shows the CMB anisotropies, with a mean temperature of 2.725 5 K, measured by the Planck space observatory. The grey outline is the outline of a mask applied where residuals from foreground emission are expected to be substantial. **(b)** Power spectrum of the CMB temperature map. The model of the anisotropies allows for the quantification of the energy-mass components of the Universe to a high significance level. Figures from ref. [39].

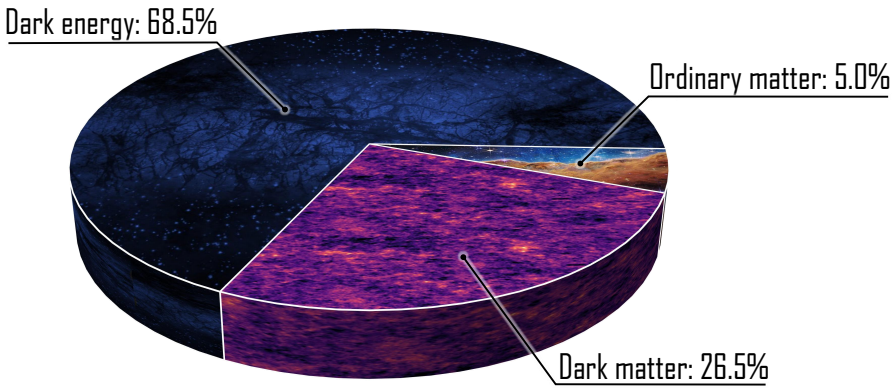

Figure 1.6: Energy-matter content of the Universe, calculated from CMB anisotropy models. Only 5 % of the mass-energy budget of the Universe is composed of normal matter. There is over five times more dark matter than ordinary matter, while the rest is dark energy, responsible for the accelerated expansion of the Universe. Numbers inferred from ref. [47].

$\Omega_b h^2 = (0.0224 \pm 0.0001)$, where h is the reduced Hubble constant. Comparatively, the dark matter density parameter, $\Omega_c h^2 = (0.120 \pm 0.001)$, is hence $5.3\times$ higher. Finally, the cosmological constant $\Omega_\Lambda = (0.685 \pm 0.007)$ provides information on the dark energy density, which is responsible for the accelerated expansion of the Universe [47]. The energy-matter content of the Universe can therefore be calculated from these three parameters, and is shown as a pie-chart in figure 1.6.

1.2 Candidate Particles

The resounding success of the Standard Model of particles reinforces the belief that dark matter may be composed of one – or many – particles, forming a dark sector sometimes decoupled from the Standard Model. As a result, multiple theories were developed, proposing candidate particles, spanning from 10^{-22} eV to 10^{10} eV, over 32 orders of magnitude in mass [50]. The landscape of suggested candidates for dark matter is well presented in the Venn diagram from Tim Tait [49], shown in figure 1.7. We will further discuss here only a few of the most strongly motivated candidates.

1.2.1 Weakly Interacting Massive Particles

Weakly Interacting Massive Particles (WIMPs), a type of particle that arises in many beyond-the-Standard Model theories, are the most sought-after and studied candidates. WIMP candidates are non-baryonic particles, as required from CMB data, with masses between $\mathcal{O}\left(2\,\mathrm{GeV/c^2}\right)$ and $\mathcal{O}\left(100\,\mathrm{TeV/c^2}\right)$. As their name implies, WIMPs should interact at the weak-scale or lower [51]. Simulations of large-scale structure formation agree well with the hypothesis of cold dark matter (CDM), which is preferred over warm or hot dark matter theories [52]. To fit the constraints of CDM models and empirical observations, candidate particles are generally required to be non-relativistic at the time of decoupling, and electrically neutral. Constraints on large-scale structure formation and observations of galactic mergers set the self-interaction of WIMPs to $\sigma/m < 0.7\,\mathrm{cm^2/g}$ [53].

It is interesting to wonder how WIMP dark matter came to be, especially at such a high density. If stable WIMPs were produced as a thermal relic of the Big Bang and interacted at or below the weak-scale, they would naturally exist today with the correct relic density to explain dark matter, a

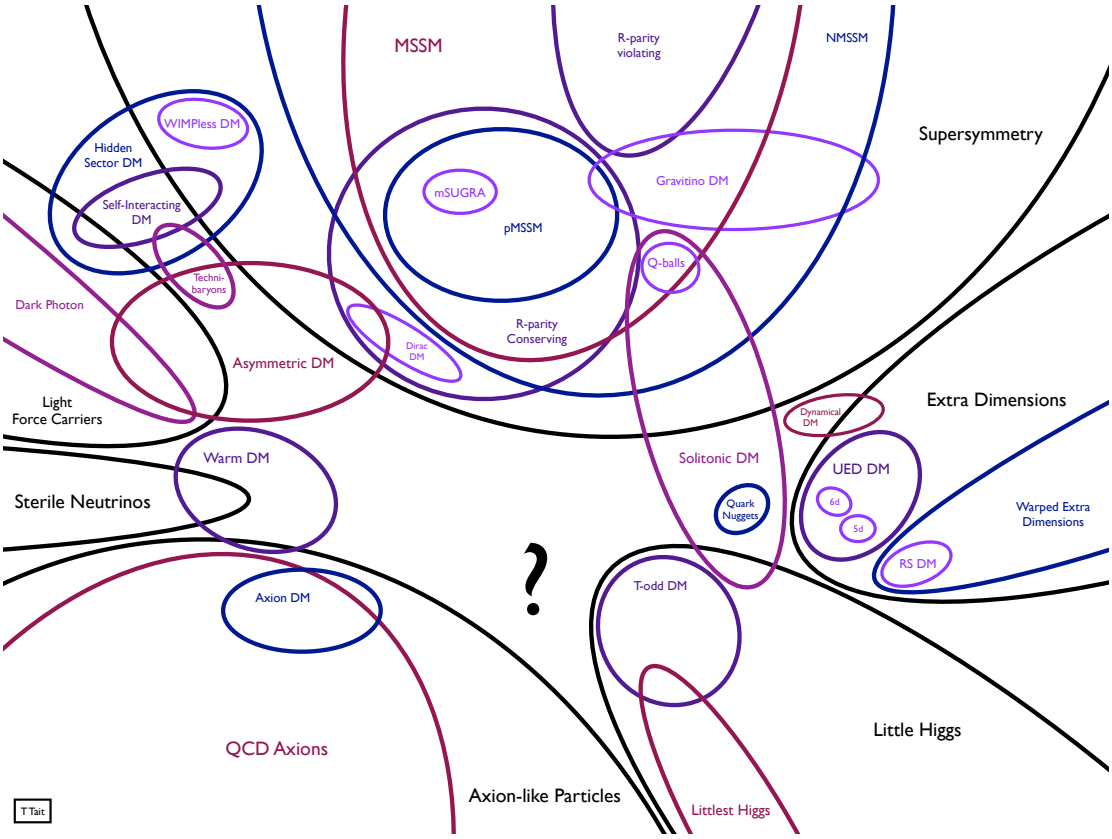

Figure 1.7: The landscape of dark matter candidates particles and theories. Figure from Tim Tait [49].

principle known as the *WIMP miracle*. A freeze-out process could explain such a phenomenon, as shown in figure 1.8 [18]. According to this robust theory, at the Big Bang, the Universe was hot and dense. WIMPs were produced and they annihilated in thermal equilibrium. As the Universe cooled-down, and its temperature fell below that of the masses of WIMPs, dark matter production could no longer be sustained, and the number of dark matter particles became Boltzmann suppressed and fell exponentially $\left(\propto e^{-\frac{m_\chi}{T}}\right)$. Concurrently, the rapid expansion of the Universe increased the mean distance between WIMPs, such that they could no longer freely annihilate. Hence, the density of dark matter became frozen out. The relic abundance is inversely proportional to the self-interaction cross section, and can be expressed as $\Omega_\chi h^2 = 3 \cdot 10^{-27}\,\mathrm{cm}^3\,\mathrm{s}^{-1}/\langle \sigma_A \mathrm{v} \rangle$ [54].

Some WIMP candidates are predicted by supersymmetric theories (SUSY), developed as extensions of the Standard Model [54, 56, 57]. An example is the minimal supersymmetric extension to the Standard Model (MSSM), in which every particle in the Standard Model is attributed a supersymmetric partner. The lightest supersymmetric particle (LSP), one of four neutralinos that are a combination of the superpartners of the neutral gauge bosons and Higgs particles, was for a long time a favourite candidate. It is stable under R-parity, which ensures that supersymmetric particles are formed and destroyed in pairs. The LSP cannot decay to supersymmetric particles as its mass is too low, and it cannot decay to Standard Model particles because of R-parity [58].

Other theories that postulate the existence of WIMPs include models with compactified universal extra dimensions (UEDs). These have the same gauge symmetries and particle content as the Standard Model, embedded in five or six flat space-time dimensions. An example of such theories is the Kaluza–Klein (KK) theory, where the Lightest Kaluza–Klein (LKK) particle is a promising

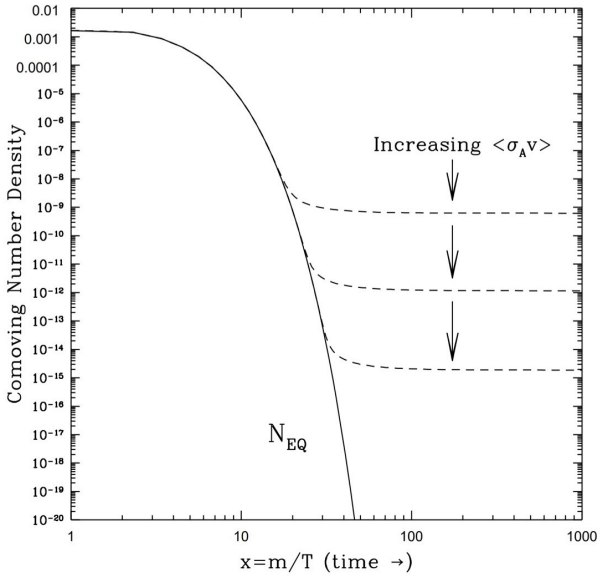

Figure 1.8: Schematic of the WIMP freeze-out mechanism, from thermal equilibrium to the expended Universe. As the hot and dense Universe after the Big-Bang started to cool, WIMP production could not be sustained and the dark matter density fell exponentially. As the Universe expended, the annihilation of dark matter particle was stopped, freezing-out the dark matter density. The final density is inversely proportional to the self-interaction cross section. Figure from ref. [55].

dark matter candidate, often a heavy copy of the hypercharge gauge boson with properties of a WIMP [59–61]. However, collider searches at the Large Hadron Collider (LHC) have ruled out many of the UED theories [62].

1.2.2 Other Dark Matter Candidates

Many other theories have been proposed to explain the observed abundance of dark matter in the Universe. Baryonic matter in the form of massive compact halo objects (MACHOs) [63] – which include brown dwarfs, Jupiter-sized planets, stellar black-hole remnants, white dwarfs, and neutron stars – was suggested to potentially make up all of the missing mass in the Milky Way. The combined limits of the EROS and MACHO collaborations set an upper limit on the mass of the dark matter halo made up of MACHOs at 10 %, therefore ruling out MACHOs as the full explanation for the missing mass [64]. Furthermore, CMB models require dark matter to be non-baryonic, therefore excluding baryonic MACHOs as full dark matter constituents. Neutrinos were once considered reasonable candidates, but constraints on the neutrino density from CMB anisotropy analysis combined with large-scale structure data suggest $\Omega_\nu h^2 \lesssim 0.0067$ [65]. Neutrinos are therefore too light to account for all of the dark matter. Finally, modified Newtonian dynamics (MOND) theories have tried to explain astrophysical anomalies without resorting to the postulation of beyond-the-Standard Model particles by modifying the classical laws of gravitation [66, 67]. These modified theories can be very successful at explaining galactic rotation curves, but they generally cannot explain every effects associated with dark matter. In particular, MOND theories cannot solve the mysteries of galaxy cluster collisions, the formation of large scale structures, or the CMB anisotropies.

Axions are another promising type of dark matter candidate particle. These theoretical particles originate from the theory formulated by Roberto Peccei and Helen Quinn, known as the Peccei-

Quinnn mechanism, introduced as a solution to the *strong CP problem* in quantum chromodynamics [68]. Steven Weinberg and Frank Wilczek showed that a spontaneous symmetry-breaking of the Peccei-Quinn symmetry leads to the existence of a light, massive spin 0 boson with a decay constant proportional to the weak scale [69, 70]. The density of the theorised particle, with its mass constrained to the 10^{-6} to $10^{-5}\,\mathrm{eV/c^2}$ range, could naturally be consistent with that of dark matter assuming the correct non-thermal production and decay rates [71, 72]. Dedicated experiments searching for axions include the Axion Dark Matter Experiment (ADMX) [73, 74] and the CERN Axion Solar Telescope (CAST) [75]. Both are exploiting the conversion of axions to X-ray photons in a magnetic field.

1.3 Detection of Dark Matter

The evidence is compelling, and numerous hypotheses have been proposed in an attempt to explain empirical observations while also steering the focus of the many experimental dark matter searches. These are categorised into three types, as illustrated schematically in figure 1.9.

Indirect detection searches look for dark matter particle annihilation that produces detectable Standard Model particles – in particular, γ-rays, neutrinos and antimatter [76]. As the annihilation rate depends on the local density of dark matter, indirect searches are often focused on high-gravity regions, such as galactic centers, or nearby celestial bodies such as the Sun.

Ground-based experiments such as HESS [77], VERITAS [78], MAGIC [79], and HAWC [80], as well as the spaceborne experiment Fermi-LAT [81, 82], conduct indirect dark matter searches using γ-spectroscopy, looking for dark matter decays from a few GeV to a few TeV.

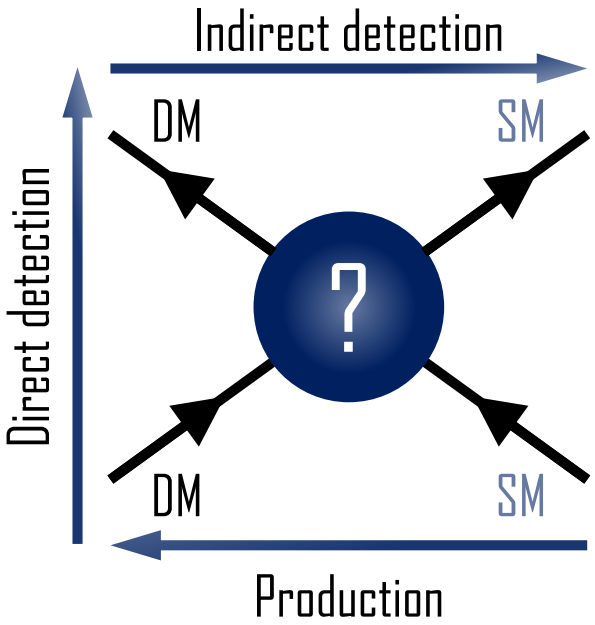

Figure 1.9: Schematic Feynman diagram of dark matter detection methods. Indirect searches aim to detect Standard Model (SM) decay products of dark matter (DM) annihilation. Production searches aim to produce dark matter particles for high-energy collisions of Standard Model particles, with missing energy as the signature of the production. Finally, the direct detection of dark matter aims to detect the scattering of dark matter particles with Standard Model particles.

Notable indirect searches focused on the emission of neutrinos from the Sun and from the galactic centre include IceCube [83, 84] and ANTARES [85, 86], and the lower threshold experiments PINGU [87, 88] and DeepCore [89]. Finally, cosmic-ray antimatter searches, focused on the detection of relatively rare particle species, such as positrons, antiprotons, and antinuclei, are led by experiments such as AMS-02 aboard the International Space Station [90] and PAMELA [91].

Given the elusive nature of dark matter, its production in particle colliders would have the signature of missing energy and transverse momentum, as the particles would escape the detector while avoiding detection. Many production searches have been carried out by experiments such as ATLAS and CMS at the LHC, focused on dark matter interactions via the Higgs or Z boson [92–94], and at fixed-target experiments that focus on sub-GeV dark matter searches. The latter subset of experiments includes NA64 at CERN [95], MiniBooNE at Fermilab [96], APEX [97] and HPS [98] at JLab, and TREK [99] at J-PARC. A dark matter production experiment, by its nature, could not claim the detection of a particle due to the lack of direct observations. It can, however, inform and be informed by direct and indirect dark matter searches.

The last detection method, which is of greater interest for this work, is the direct detection of dark matter, which we will discuss in more detail.

1.3.1 Direct Detection

The direct detection of dark matter refers to the detection of the elastic [100] or inelastic [101] scattering of a dark matter particle with baryonic matter. The interaction can be with the nucleus of an atom, referred to as a *nuclear recoil*, or with atomic electrons, known as an *electronic recoil*. Electrically neutral dark matter should preferably interact via elastic nuclear scattering, although this is only true for fairly heavy WIMPs. Contrary to neutrons, which are known to multiply scatter [102–104], WIMPs, due to their weakly interacting nature, should have a single scatter signature. However, distinguishing single neutron recoils from WIMPs would be difficult.

The interaction rate of WIMPs with a target volume can be generally written as:

$$R = Nn\langle\sigma\mathbf{v}\rangle\,, \tag{1.4}$$

where N is the number of target nuclei, n is the local number density of WIMPs, and $\langle\sigma\mathbf{v}\rangle$ the averaged product of the interaction cross section and relative velocity of WIMPs to the target.

Direct detection experiments can generally measure the energy imparted to the target material, so it is typical to express the energy-dependent interaction rate. First, from kinematics, we can write the recoil energy E as:

$$E = \frac{\mu_{\chi,A}^2\mathbf{v}^2}{m_A}\left(1-\cos\theta\right)\,, \tag{1.5}$$

where $\mu_{\chi,A} = \frac{m_\chi m_A}{m_\chi+m_A}$ is the reduced WIMP-nucleus mass, with m_χ and m_A the masses of the WIMP and the target nucleus respectively, and v is the dark matter velocity. An end-to-end collision results in the maximum energy transfer, at $\theta = 180^\circ$, and is therefore $E_{\max(v)} = \frac{2\mu^2\mathbf{v}^2}{m_A}$.

The differential interaction rate can then be expressed as:

$$\frac{\mathrm{dR}}{\mathrm{d}E} = \frac{\rho_\chi}{m_\chi m_A}\int v\,\frac{\mathrm{d}\sigma}{\mathrm{d}E}\,f(\mathbf{v},t)\;\;d^3\mathbf{v}\,, \tag{1.6}$$

where ρ_χ is the local WIMP density (in our solar system according to the standard halo model, $\rho_\chi \approx 0.3\,\mathrm{GeV}/(\mathrm{c}^2\cdot\mathrm{cm}^3)$ [105]), and $\frac{\mathrm{d}\sigma}{\mathrm{d}E}$ is the WIMP-nucleus scattering cross section. The time-dependence on the velocity distribution accounts for local circular speed, the motion of the Sun relative to the local standard of rest (LSR), and the seasonal variations due to the revolution of the Earth around the Sun. The velocity component in equation 1.6 shows that it should be possible to observe an annual modulation of the dark matter detection rate, with a maximum around the month of June [106]. From an idealised, isothermal halo model, WIMPs are assumed to have a Maxwell-Boltzmann velocity distribution with a most probable velocity of $v_0 = 220\,\mathrm{km/s}$, and a cutoff at the escape velocity $v_{esc} = 550\,\mathrm{km/s}$ [26, 107].

The differential interaction cross section is often expressed as the sum of the spin-dependent (SD) and the spin-independent (SI) cross sections σ_{SD} and σ_{SI}:

$$\frac{\mathrm{d}\sigma}{\mathrm{d}E} = \frac{m_A}{2v^2\mu_{\chi,A}^2}\left[\sigma_{\mathrm{SD}}F_{\mathrm{SD}}^2(E) + \sigma_{\mathrm{SI}}F_{\mathrm{SI}}^2(E)\right], \tag{1.7}$$

where $F_i(E)$ are the nuclear form factors for each process, which contain the WIMP-nucleus dependence on the energy transfer [110]. We can treat the cross sections of SD and SI interactions separately.

Only target nuclei with at least one unpaired nucleon contribute significantly to the SD channel. Table 1.1 lists some isotopes potentially capable of producing SD interactions. The SD interaction cross section is commonly written with the separate contributions of proton and neutron:

$$\sigma_{\mathrm{SD}} = \frac{32}{\pi}\mu_{\chi,A}^2 \cdot G_{\mathrm{F}}^2 \cdot \left[a_p\cdot\langle S_p\rangle + a_n\cdot\langle S_n\rangle\right]^2 \cdot \frac{J+1}{J}, \tag{1.8}$$

where G_{F} is the Fermi coupling constant, a are the effective couplings of the nucleons, $\langle S\rangle$ are the expected values of the nucleon nuclear spin contents, and J is the total nuclear spin [111].

SI interactions, on the other hand, are interactions with all the nucleons (Z protons, and $A-Z$

Nucleus	Z	Odd nucleon	J	$\langle S_{\mathrm{p}}\rangle$	$\langle S_{\mathrm{n}}\rangle$	Ref.
^{1}H	1	p	1/2	0.5	0	
^{7}Li	3	p	1/2	0.497	0.004	[108]
^{19}F	9	p	1/2	0.441	-0.109	[108]
^{23}Na	11	p	3/2	0.248	0.020	[109]
^{27}Al	13	p	5/2	-0.343	0.030	[54]
^{29}Si	14	n	1/2	-0.002	0.130	[54]
^{35}Cl	17	p	3/2	-0.083	0.004	[54]
^{39}K	19	p	3/2	-0.180	0.050	[54]
^{73}Ge	32	n	9/2	0.030	0.378	[54]
^{93}Nb	41	p	9/2	0.460	0.080	[54]
^{125}Te	52	n	1/2	0.001	0.287	[109]
^{127}I	53	p	5/2	0.309	0.075	[109]
^{129}Xe	54	n	1/2	0.028	0.359	[109]
^{131}Xe	54	n	3/2	-0.009	-0.227	[109]

Table 1.1: Table of nuclear properties for the calculation of spin-dependent cross sections.

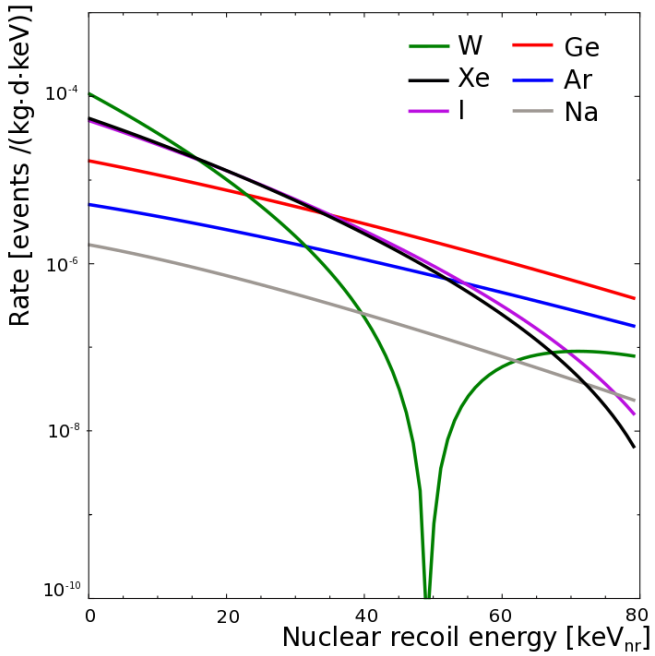

Figure 1.10: Differential event rate vs. nuclear recoil energy, assuming a WIMP mass of 100 GeV/c^2 and a cross section of 10^{-45} cm^2. The effect of the mass of the target on the cross section ($\propto A^2$) is clearly demonstrated. Figure from ref. [111].

neutrons). Assuming zero momentum transfer, the total SI cross section is therefore the sum of the coupling to the protons and the neutrons [26]:

$$\sigma_{\mathrm{SI}} = \frac{4\hbar^2 c^2}{\pi}\mu^2 \left(Z f_{\mathrm{p}} + (A - Z) f_{\mathrm{n}}\right)^2 , \tag{1.9}$$

where the f_{p} and f_{n} are respectively the coupling between WIMPs, and the protons and neutrons. The SI cross section for the interaction with a single nucleon is:

$$\sigma_{\mathrm{SI},N} = \frac{4}{\pi}\mu_{\chi,N}^2 f_N^2 , \tag{1.10}$$

where $\mu_{\chi,N}^2$ is the WIMP-nucleon reduced mass. With the assumption that $f_p = f_n = f_N$, and combining equations 1.9 and 1.10, the total SI cross can then be written as:

$$\sigma_{\mathrm{SI}} = \left(\frac{\mu_{\chi,A}}{\mu_{\chi,N}}\right)^2 A^2 \, \sigma_{\mathrm{SI},N} . \tag{1.11}$$

The SI cross section is therefore proportional to the square of the number of nucleons in the nucleus, as demonstrated in figure 1.10 for a WIMP mass of 100 GeV/c^2 and a cross section of 10^{-45} cm^2 [111]. This provides a clear advantage to experiments using targets made of heavy atoms. At high WIMP masses, the reduced mass is approximately equal to the number of nucleons, which then makes the SI cross section proportional to A^4.

These cross section calculations are a simplified approximation, and the formalism of the complete field theory describing WIMP-nucleus interactions can be found in refs. [100, 112, 113].

1.4 Direct Detection Experiments

There are a multitude of direct detection experiments, past, present, and future. A broad range of target materials and detection techniques are used. One common characteristic of these searches is the requirement for low backgrounds and low energy thresholds in order to detect rare and low-energy recoils. The common practice is to shield experiments with high-density, low-radioactivity materials, and/or water shields. Furthermore, the background from cosmic radiation is reduced to a minimum by installing the detectors in deep underground laboratories, where the rock overburden blocks the majority of cosmic-ray radiation.

We can generally identify three detection channels. The first is scintillation, which refers to the property of a target material to emit photons following the imparting of energy from an impinging particle. The transfer of energy can also be done mechanically, whether in the form of heat, or, in the case of crystalline matter, in the form of phonons. Finally, ionisation refers to the release of electrons from the target. Typically, experiments exploit one or two of the three detection methods. Multi-channel readout allows for discriminating nuclear recoils (NRs) and electronic recoils (ERs), providing a powerful background rejection tool for experiments. The three detection channels are illustrated schematically in figure 1.11, along with the classification of some of the leading direct detection experiments. Experiments using all three detection channels have been proposed, such as EURECA [114], and noble-liquid bubble chambers [115–117].

Experiments exploiting the mechanical channel include bubble chambers, calorimeters, and cryogenic bolometers. First, in bubble chambers, the target medium is superheated and kept in a

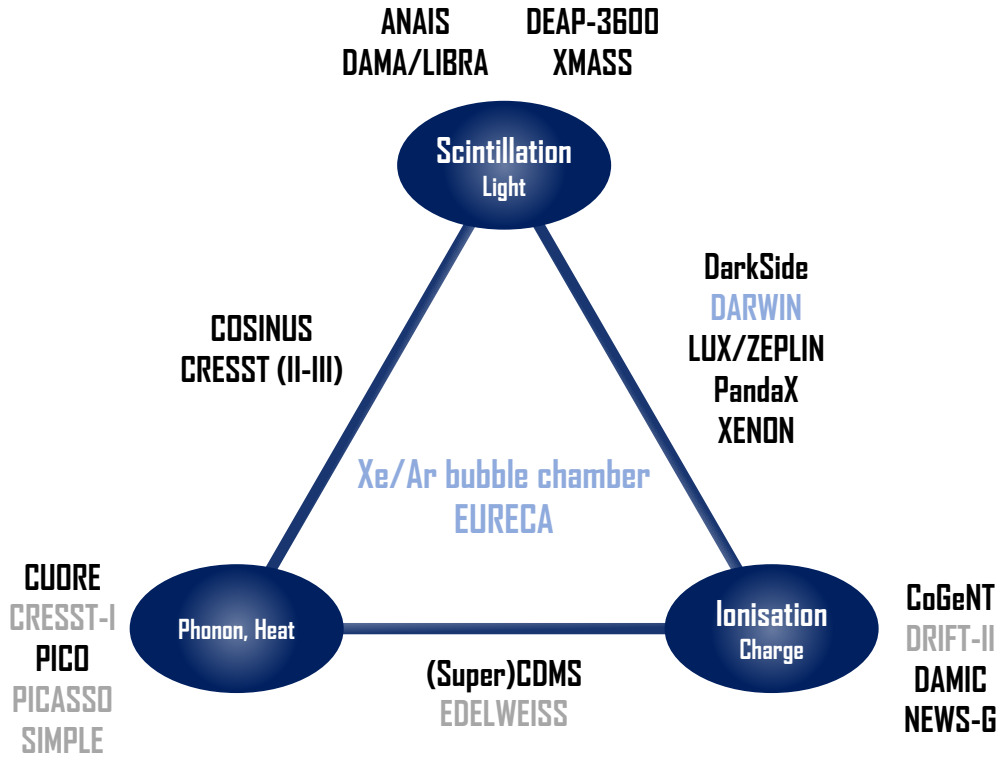

Figure 1.11: Schematic of the three main particle detection methods. Experiments typically exploit one or two detection channels. Multi-channel detection usually offers a way to distinguish between the different types of interacting particle, improving the background rejection significantly. Past experiments are labeled in gray, current in black, and future in blue.

metastable state, such that a small energy deposit triggers a local phase-transition. Acoustic signals and/or stereoscopic images of events can be recorded, with the former used to perform highly sensitive frequency analyses to efficiently discriminate particles, while the latter allows for volume fiducialisation. The SIMPLE [118] and the PICASSO [119] experiments pioneered the use of superheated liquids for dark matter searches using freons, which are rich in ^{19}F, and make for sensitive SD experiments. PICASSO deployed an array of 32 droplet detectors at SNOLAB [120], for a total active mass of 3 kg of C_4F_{10} suspended in a polymerised gel matrix. The PICASSO experiment later joined forces with the COUPP experiment [121] to form the PICO collaboration [122]. The experiment, with tunable detector energy thresholds of $\mathcal{O}(1\,\text{keV})$, has been leading the SD searches with PICO-2L (2.91 kg C_3F_8) [123] and PICO-60 (36.8 kg CF_3I, 52.2 kg C_3F_8) [124, 125]. They have also shown the insensitivity of their bubble chambers to electronic recoils at thresholds above a few keV [126]. Future detectors include PICO-40L, a right-side-up – buffer-free version of the PICO bubble chamber [127], and PICO-500 [128].

Cryogenic bolometers, on the other hand, detect the energy imparted from WIMP-nucleon interactions in the form of heat. An example is the neutrinoless double beta ($0\nu\beta\beta$) experiment CUORE (471 kg TeO_2) [129]. The EDELWEISS experiment conducted a three-phase search (EDELWEISS I-II and III), using high-purity germanium (HPGe) crystals at millikelvin temperatures and simultaneously reading-out phonon and ionisation signals. The number and masses of the detectors deployed at each of the three phases are: EDELWEISS I: 3× 320 g [130]; EDELWEISS II: 10× 400 g [131]; EDELWEISS III 24× 820-890 g [132]. In a similar experiment, CDMS [133] exploited the bolometer technology with photolithographically patterned sensors to also detect both ionisation and phonon signatures of energy deposits in HPGe (230 g) and silicon (100 g) crystals cooled to millikelvin temperatures. The dual-channel detection method allows for particle discrimination and high energy resolution measurements [134]. CDMSlite [135] deployed low-mass detectors to improve their sensitivity to low-mass WIMPs, while SuperCDMS is an expansion of the initial experiment with 600 g of germanium equipped with transition edge sensors, operated at the Soudan Underground Laboratory [136], with a planned upgrade of the experiment to be operated at SNOLAB [137]. The bolometric experiments typically have a good sensitivity to lower mass WIMPs due to their $10-100\,\text{eV}$ thresholds.

A different combination of detection methods was used in the CRESST cryogenic calorimeters. After the completion of the first experimental phase using only the detection of heat in a total of 262 g sapphire crystals (Al_2O_3) with tungsten transition edge thermometers, photosensitive silicon-on-sapphire wafers were added in phases II and III to $CaWO_4$ crystals to detect scintillation light to perform particle discrimination [138–140]. The COSINUS experiment exploits a similar technique with NaI crystals [141].

In the case of experiments exploiting solely the scintillation channel, we can cite two noble liquid scintillator experiments, the argon-based experiment DEAP-3600 [142], and the xenon-based experiment XMASS [143, 144]. A second type of experiment, based on NaI(Tl) crystals, include COSINE-100 [145], ANAIS [146], and DAMA/NaI (DAMA/LIBRA) [147]. The latter, which started its operation in 1995 and employs 250 kg of highly radio-pure NaI(Tl) in its final phase, has reported the detection of an annual modulation of single recoil events, consistent with that expected from a WIMP signal, with a statistical significance of 9.5σ (12.9σ) in the 1-6 keV (2-6 keV) region in 2019 [148]. This claim, however, contradicts the lack of modulation signal observed in many other dark matter searches [149].

Some experiments using only the detection of charge signals include gas proportional counters such as the negative-ion TPC used in the DRIFT experiment [150], and the NEWS-G experiment [151], which uses a neon-methane filled sphere. Solid-state ionisation experiments, very sensitive to WIMP-masses $< 10\,\text{GeV/c}^2$ due to their energy threshold of $\mathcal{O}(10\,\text{eV})$, include DAMIC [152]

using seven 6 g silicon charge-coupled devices (CCDs), and CoGeNT [153] with a 443 g HPGe detector.

Finally, some of the most sensitive dark matter experiments combine the readout of both scintillation and charge. These operate cryogenic liquefied noble gases, such as argon and xenon, in single or dual-phase TPCs [155]. The argon experiment DarkSide operated DarkSide-50, a 46.4 kg dual-phase argon TPC [156], and the collaboration is currently building DarkSide-20k, a multi-tonne argon TPC to be deployed at Laboratori Nazionali del Gran Sasso (LNGS) [157]. The 128 nm wavelength photons are shifted to higher wavelength spectrum centered around 420 nm with tetraphenyl butadiene (TPB) evaporated coatings to allow their detection with conventional photosensors [158]. The background rejection in scintillating argon experiments can be aided by pulse shape discrimination (PSD) techniques [159]. As will be discussed in the next chapter, PSD is not possible in xenon experiments, but these benefit from the self-shielding effect and the increased sensitivity to SI WIMP-nucleus elastic scattering due to the heavy atomic mass number of the target. Notable xenon TPC experiments include LUX [160] and ZEPLIN [161, 162]. The two joined forces to form the LUX-ZEPLIN collaboration, which is operating a 7 tonne dual-phase xenon TPC [163, 164]. The XENON collaboration operated four detector: XENON10 (14 kg [1] [165]), XENON100 (62 kg [1] [166]),

[1] Active mass.

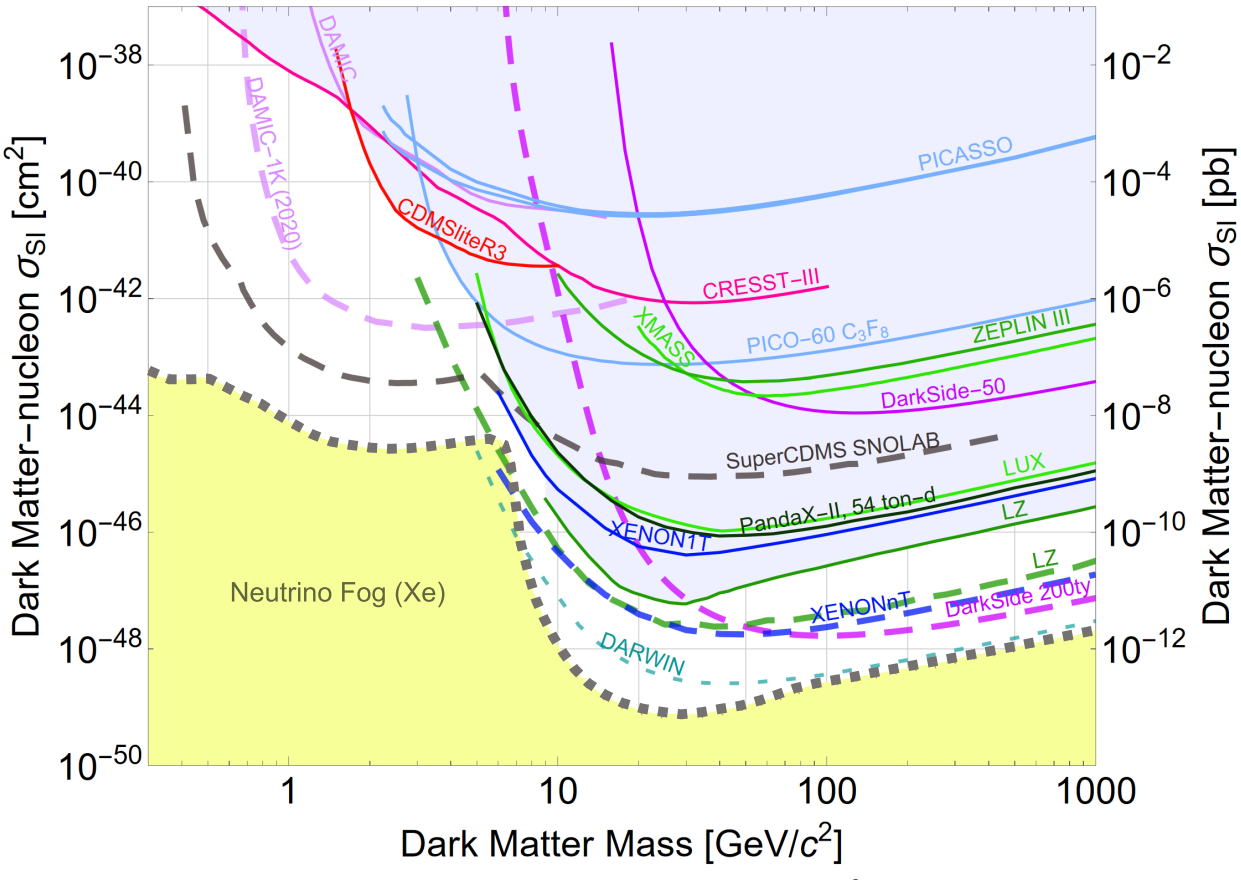

Figure 1.12: Excluded regions and sensitivity projections for spin-independent WIMP cross-section measurements. The parameter space is dominated by noble liquid experiments, which are projected to reach the neutrino fog with the next-generation detectors. Past this point, coherent elastic neutrino-nucleus scattering (CEνNS) will become an irreducible background for dark matter experiments, but will enable the study of neutrino interactions. Figure generated with [154].

XENON1T (1.3 t [1] [167]), and their current experiment XENONnT (5.9 t [1] [168]). Other notable xenon-based experiments include PandaX [169–171] and the next-generation experiment DARWIN for dark matter search and neutrino physics [172], which will be the focus for the remainder of this thesis.

This review of the current status of the field of dark matter direct detection can be further summarised with figure 1.12 for SI searches. Experiments typically report their results in the absence of a signal as upper limits on the dark matter-nucleon cross-section as a function of the mass of the dark matter particle. Higher exposures (mass$\times$time) lower the curves, while lower energy thresholds contribute to pushing the curves both to lower cross-sections and lower WIMP masses. Finally, the choice of a target influences the probable WIMP-mass range, as the momentum transfer to the nucleus is maximum when the masses of both the WIMP and the target are matched [111]. As can be seen in the figure, the field is dominated by noble gas TPC experiments. During the next decade, experiments will become sensitive enough to detect CEνNS [173–175]. Past this barrier known as the *neutrino fog* [2] [176], neutrinos will become a source of irreducible background for dark matter searches, which in turn will open the door to new neutrino studies [177].

1.4.1 Summary

The search for dark matter is more active than ever. Observational proofs of the existence of exotic matter in the universe that is not explained by the theory of the Standard Model of particle physics are undeniable at this point. The most considered explanation is the existence of at least one type of non-baryonic particle, massive, chargeless, and weakly interacting, which constitutes 84.1 % of all the matter in the Universe.

Many experimental ventures, using particle colliders, astrophysical observations, or cutting-edge particle detectors, now aim to detect this enigmatic particle. Direct detection experiments aim to detect the energy deposits of elastic WIMP-nucleus scatterings on the order of a few keV. The field is dominated by experiments using a state-of-the-art detection method, the noble-liquid, dual-phase time projection chamber. In the next chapter, we will present and discuss this technology, and its implication for DARWIN, the next-generation observatory.

[1] Active mass.

[2] Until recently, the term *neutrino floor* was preferred.

"In the End, everything dies...
Me... You... Even the brightest
star in the night's sky..."

Ricardo Mota Peres, 2022

Ricardo Mota Peres is a young Portuguese physicist whom I enjoyed working with during my doctoral studies. These words were spoken during the 2022 *Three Minute Thesis* contest in Zurich, Switzerland, where Ricardo described his work on the detection of neutrinos produced by Supernovae using XENONnT. Supernovea are the explosion of dying stars. When such a cosmic event happens in our galaxy, it can appear very bright in the sky and can potentially be visible during the day to the naked eye.

XENON1T

LNGS, 2019

2

Dual-Phase Xenon TPCs and The DARWIN Observatory

Xenon is an element widely used in our daily lives. It is employed in specialised, high-luminosity lighting products [178]. It is also found profusely in the field of medicine, as a radioisotope [179], in magnetic resonance imaging (MRI) machines [180, 181], and as an anaesthetic agent [182]. Xenon is also a propellant in spacecraft and satellites as its high atomic mass grants ion drives very high specific impulses, making for very efficient, compact, and lightweight propulsion systems [183, 184]. In recent years, xenon has been used in high aspect ratio (HAR) plasma etch processes employed in the production of electronic components, such as flash memory chips, and other semiconductors [185]. Finally, xenon is employed in the field of photonics, often mixed with halogens of other noble gases to produce excimer lasers [186, 187].

The noble element was discovered in 1898 by two chemists, William Ramsay and Morris William Travers, in a liquefied air sample. They named the newly found element after the Greek word *xenos* – meaning *stranger*. The pair is also credited with the discovery of neon and krypton, as well as the study of the properties of other noble gases. Ramsey, who was awarded the 1904 Nobel Prize in Chemistry "in recognition of his services in the discovery of the inert gaseous elements in air and his determination of their place in the periodic system" [188], estimated in 1903 the relative volume amount of xenon in the atmosphere at 5.8 parts per billion (ppb) [189]. The modern accepted value is (0.087 ± 0.001) parts per million (ppm) per volume.

Xenon is obtained commercially as a by-product of air liquefaction. Most of the xenon production in the world is therefore assured by industries requiring large amounts of liquefied gases, such as the smelting industry. During the separation of liquid oxygen (LO_2) and liquid nitrogen (LN_2), xenon is extracted from xenon and krypton-enriched oxygen in silica gel or adsorption columns. The recovered gas mixture is finally separated by distillation. The purity of distilled xenon can reach values as high as 99.995 % [190, 191].

As discussed in the previous chapter, the high atomic number of xenon makes it very sensitive to spin-independent WIMP-nucleon interactions due to the A^2 dependence of the SI cross section. Two of its isotopes, ^{129}Xe and ^{131}Xe, also have an unpaired neutron, making them sensitive to SD interactions. With a liquid density of 2 854.7 kg/m^3 at 177 K, 2.0 bar, xenon is an appealing particle

detection medium as experiments can rapidly accumulate exposure, i.e. mass $\times$ time.

In this chapter, we describe the concept of particle detection using xenon. We first present the properties of xenon as a target for particle detection in section 2.1. We then discuss the concept of the dual-phase TPC in section 2.2. In section 2.3, we describe the DARWIN observatory, a proposed next-generation multi-tonne LXe experiment, along with a summary of the sensitivity projections for multiple physics channels.

2.1 Liquid Xenon as a Target

With an atomic number of 54, xenon is the fifth noble gas element. It is the heaviest noble element with non-radioactive isotopes, having an average atomic mass of 131.293 u [192]. Some important atomic, thermodynamical, and optical properties of xenon are listed in table 2.1, as well as its natural isotopic abundances. The element is odorless, colorless, tasteless, and non-toxic [196]. It is a simple asphyxiant, heavier than air, and generally accumulates at floor level. Thought for a long time to be completely chemically inert due to its full valence electron shell, xenon can form a few unstable chemical compounds by combining with, for example, fluoride (XeF_2, XeF_4, XeF_6), oxygen (XeO_4) and platinum ($XePtF_6$).

Because of its high density and atomic number, LXe effectively stops photons penetrating the volume from the outside, quickly attenuating them at the outer edges of the detector. Likewise, photons and other products of nuclear decays, such as electrons, protons, and α particles, are stopped near their decay sites [200]. Figure 2.1 shows the energy-dependent mean attenuation length of particles in xenon at 177 K and 2.0 bar. Self-shielding is also observed in liquid argon, albeit less effectively than in LXe, resulting in a more stringent fiducialisation of the active volume.

Compared to other liquid inert gases, xenon liquefies at the relatively high temperature of 177.88 K at 2 bar. LXe handling thus only requires the use of relatively simple cryogenic systems. Figure 2.2 shows the phase diagram of xenon. The region highlighted in blue indicates the typical operational parameter space of xenon dual-phase TPCs, with the blue point denoting the

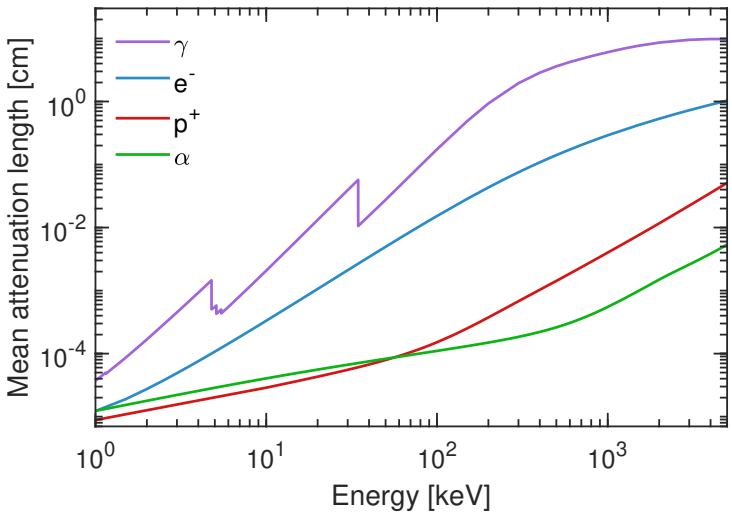

Figure 2.1: Energy-dependent mean particle attenuation length in LXe at 177 K and 2 bar. The high stopping power creates a low-background region in the middle of large LXe volumes. Data retrieved from: (γ) [201], (e^-, p^+, α) [202].

Property	Value	Note	Ref.
Atomic			
Atomic number:	54		
Mean atomic mass:	131.293 u		[192]
Electronic configuration:	$1s^2\ 2s^2\ 2p^6\ 3s^2\ 3p^6\ 4s^2\ 3d^{10}\ 4p^6\ 5s^2\ 4d^{10}\ 5p^6$		[192]
Thermodynamic:			
Density:	$2\,854.7\,kg/m^3$	liquid, at boiling point [3]	[193]
	$18.694\,kg/m^3$	gaseous, at boiling point [3]	[193]
Melting point:	161.41 K	at 2 bar	[192]
Boiling point:	177.88 K	at 2 bar	[192]
Triple point:	(161.38 ± 0.02) K $(0.816\,0 \pm 0.000\,1)$ bar		[194, 195]
Critical point:	289.733 K 58.42 bar		[192]
Enthalpy of vaporisation:	95 587 kJ/kg		[196]
Latent heat of fusion:	17.48 kJ/kg		[196]
Heat capacity C_p:	$0.160\,67\,kJ/kg \cdot K$ [3]		[196]
Heat capacity C_v:	$0.095\,651\,kJ/kg \cdot K$ [3]		[196]
Optical			
Refractive index:	(1.69 ± 0.02)	at 589 nm	[192]
Scintillation wavelength:	(174.8 ± 0.2) nm	at 168 – 169 K, 1.10 – 1.17 bar	[197]
	178 nm	at 160 K	[198]
LXe attenuation length:	(364 ± 18) mm	at 168 – 169 K	[192]
Isotopic abundance:			
^{124}Xe:	(0.095 ± 0.005) %	ECEC, $(1.8 \pm 0.6)\,10^{22}$ y	[199]
^{126}Xe:	(0.089 ± 0.003) %	Stable	[199]
^{128}Xe:	(1.910 ± 0.013) %	Stable	[199]
^{129}Xe:	(26.401 ± 0.138) %	Stable	[199]
^{130}Xe:	(4.071 ± 0.022) %	Stable	[199]
^{131}Xe:	(21.232 ± 0.051) %	Stable	[199]
^{132}Xe:	(26.909 ± 0.055) %	Stable	[199]
^{134}Xe:	(10.436 ± 0.035) %	2β-, $> 5.8 \cdot 10^{22}$ y	[199]
^{136}Xe:	(8.857 ± 0.072) %	2β-, $(2.165 \pm 0.061) \cdot 10^{21}$ y	[199]

Table 2.1: Properties of xenon.

target operational parameters in Xenoscope, which will be later discussed in chapters 3 and 4. In dual-phase mode, TPCs operate at saturation. Xenon features a triple point at (161.38 ± 0.02) K and $(0.816\,0 \pm 0.000\,1)$ bar. The critical point is located at 289.733 K and 58.42 bar. Above these values, xenon is supercritical and does not behave like a noble gas. This property allows for its storage in much larger quantities for relatively small pressure increases.

Xenon has six stable isotopes, listed in table 2.1. Three radioactive isotopes show non-null abundances due to their long half-lives. The first, ^{124}Xe, decays via double electron capture, with a half-life of $(1.8 \pm 0.6) \cdot 10^{22}$ y. The rare process was recently measured by the XENON1T and XENONnT experiments [203, 204]. ^{134}Xe and ^{136}Xe are two isotopes that decay via double-beta decay, with half-lives $> 5.8 \cdot 10^{22}$ y and $(2.165 \pm 0.061) \cdot 10^{21}$ y respectively. Moreover, ^{136}Xe is one of the few isotopes for which $0\nu\beta\beta$ decay is theoretically permitted, with a decay energy of

[3] At 2.0 bar, 177.88 K.

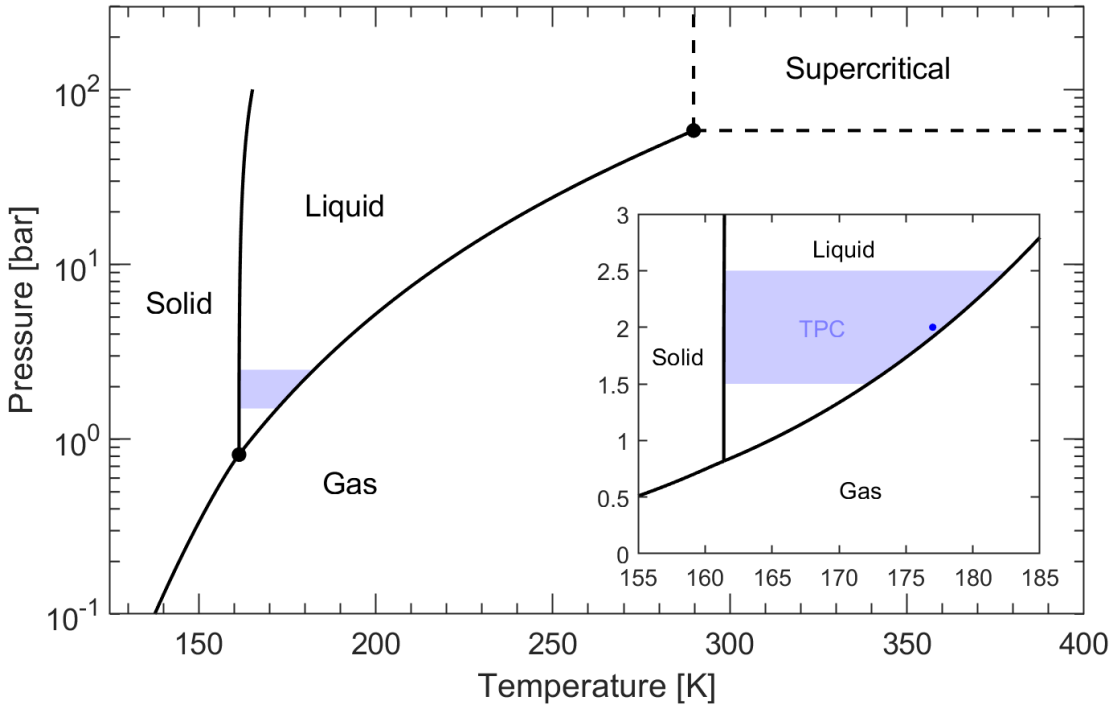

Figure 2.2: Phase diagram of xenon. The highlighted region identifies the typical operating parameter space of xenon TPCs, while the blue point identifies the target operational setpoint for Xenoscope. Data retrieved from ref. [196].

$(2\,457.83 \pm 0.37)$ keV [205, 206]. With a natural abundance of (8.857 ± 0.072) %, it could be possible to detect this yet unobserved decay-mode in multi-tonne scale xenon facilities, although dedicated $0\nu\beta\beta$ decay experiments typically deploy xenon enriched at up to 90 % of ^{136}Xe [207].

Perhaps the most useful property of xenon in the context of particle detection is the production of scintillation photons following the imparting of energy from a particle. Xenon scintillates in the vacuum ultraviolet (VUV) range, with reported values of 174.8 and 178 nm [197, 198]. It has, at zero electric field and recoil energy 122 keV, a light yield of 63 photons/keV, granting it a very good energy resolution [208]. Xenon is transparent to its own scintillation, with a mean photon attenuation length of (364 ± 18) mm at (170 ± 1) K [209]. The imparted energy in the target from an interaction with a particle is shared between the production of scintillation, ionisation, and heat, of which only the first two are detected in dual-phase TPCs.

Scintillation radiation can be released in two separate processes [210]. In the first case, an excited xenon atom Xe^* – or exciton – can form an excited dimer Xe_2^* – or excimer – with a neighbouring atom. The excimer decays to its ground state with the emission of a scintillation photon:

$$Xe^* + Xe \rightarrow Xe_2^* \rightarrow 2Xe + \gamma. \tag{2.1}$$

In the second process, the recombination of ionised xenon atoms (Xe^+) with surrounding electrons

yields:

$$Xe^+ + Xe \rightarrow Xe_2^+ \tag{2.2}$$

$$Xe_2^+ + e^- \rightarrow Xe^{**} + Xe \tag{2.3}$$

$$Xe^{**} \rightarrow Xe^* + \text{heat}\,. \tag{2.4}$$

As in equation 2.1, the excited xenon atom in equation 2.4 then de-excites with the emission of a photon. These scintillation processes are characterised by two decay components due to the de-excitation of singlet $({}^1\Sigma_u^+)$ and triplet $({}^3\Sigma_u^+)$ spin states. Table 2.2 summarises the de-excitation times for different types of particle interactions.

At no electric field, relativistic electrons produce scintillation with only one component, which disappears with the application of an electric field. This is possibly due to the slow recombination of electrons with ions [210]. Different types of particle interactions produce different ratios of singlet and triplet states excimers, resulting in different, characteristic pulse shapes. However, due to the small time separation between the two decay components of LXe scintillation, the discrimination of the interacting particle type via PSD is extremely hard. PSD is however possible in other noble liquefied gases, such as liquid argon (LAr), where time differences are of the order of a few milliseconds [214]. The recombination probability is also influenced by the type of interaction, NR interactions typically featuring a higher linear energy transfer (LET) than ER interactions. At high LET, electron-hole pairs are created in close proximity, enhancing the recombination probability, and hence the scintillation yield [210]. Another process that can enhance the scintillation yield is the Migdal effect [215, 216]. At low recoil energies ($\mathcal{O}(1-10\,\text{keV})$), a nucleus and its electrons should recoil as a whole. Some electrons could however be left behind following a NR, in which case their recombination would produce extra scintillation light, and unrecombined electrons could amplify the ionisation signal.

Some processes have the opposite effect, reducing, or quenching, the scintillation yield. In the case of higher energy recoils where the LET is high, a high exciton density can produce biexcitonic quenching:

$$Xe^* + Xe^* \rightarrow Xe_2^{**} \rightarrow Xe + Xe^+ + e^-\,, \tag{2.5}$$

where two excited isomers combine before decaying to one neutral and one ionised xenon atom. The ionised electron rapidly loses its energy before recombination. The net effect of this process is the reduction of the number of scintillating excited isomers, which in turn reduces the scintillation output.

The light and charge yields can also be quenched if some of the initial recoiling nucleon transfers some energy to neighbouring atoms. When the transferred energy becomes lower than the minimum electronic excitation energy, the energy effectively becomes heat. This effect is energy-dependent and can be described by the energy-dependent Lindhard factor $\mathcal{L}$ [217]. It is minimal for ER events,

Particle	Singlet [ns]		Triplet [ns]		Ref.
	0 kV	4 kV	0 kV	4 kV	
α	4.2	22	4.2	22	[211, 212]
Fission fragments	4.1	21	4.1	21	[211, 212]
Relativistic electron	45*	(2.2 ± 0.3)		(27 ± 1)	[211–213]

Table 2.2: Decay times of LXe scintillation for α particles, fission fragments and relativistic electrons. *Note that the scintillation from relativistic electrons, at no electric field, has only one component.

as the heat produced is negligible, but it is significant for NR events [218].

2.2 The Dual-Phase Xenon Time Projection Chamber

As mentioned before, xenon is an excellent choice as a medium for particle detection due to its scintillation characteristics, its transparency to its own scintillation light, its chemical inertness, and its heavy atomic mass. All these characteristics are well exploited in xenon dual-phase TPCs. These particle detectors exploit the scintillation and ionisation properties of the liquefied noble gas when interacting with particles to determine the three-dimensional position and deposited energy of the interaction in the active volume. Their instrumentation with single-photon, VUV-sensitive photosensors grants them energy thresholds of $\mathcal{O}(1\,\mathrm{keV})$, making them very well suited for the detection of low-energy events, such as those of WIMP interactions.

The working principle of the typical noble-element dual-phase TPC is shown in figure 2.3. The instrumented volume (depicted here as a cylinder) is delimited on its perimeter by light reflector

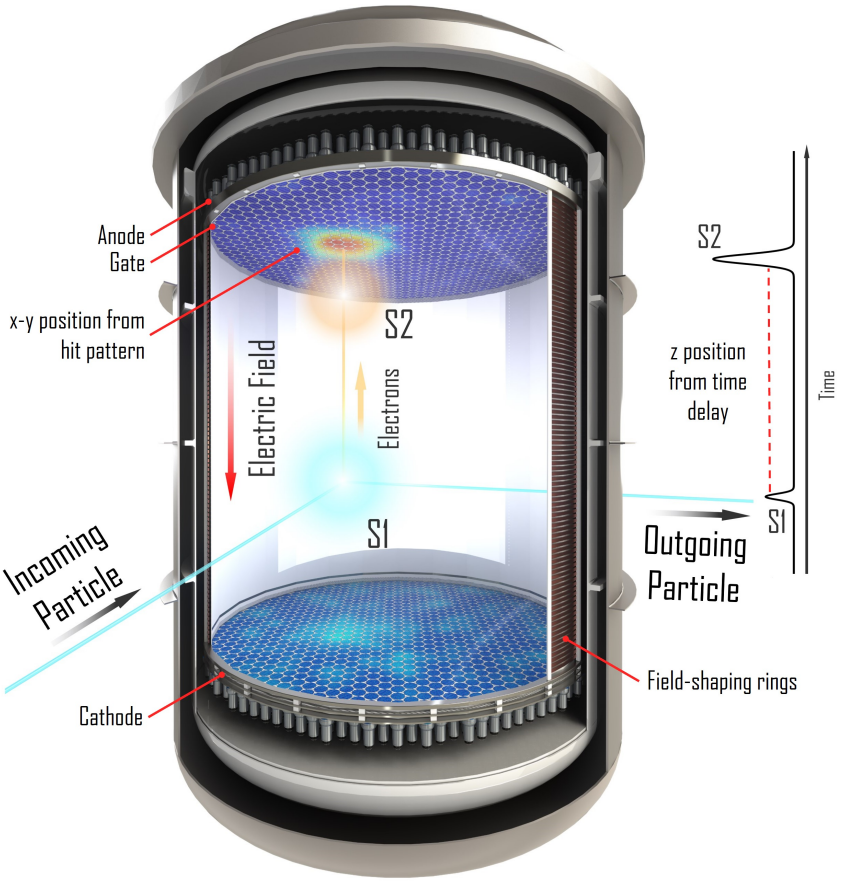

Figure 2.3: Schematic of a TPC. When an incoming particle interacts with the xenon target, the latter produces scintillation photons and free electrons through the recombination of excimers. The prompt scintillation photons are detected in the photosensor arrays as the S1 signal. The free electrons are drifted upwards by a vertical electric field and are extracted in the gas region by a high-strength electric field. The electrons interact with the xenon gas which produces a second scintillation signal (S2). The time elapsed between the S1 and the S2 informs on the depth (z) of the interaction, while the high-pattern of the S2 reveals the x-y position of the initial interaction site.

panels that maximise the light collection in two photosensor arrays located at the top and bottom of the cylinder. Three electrically-biassed electrodes with high optical transparency ensure the production of a permanent – two-stage – vertical electric field, used in a first step to drift electrons towards the top of the detector and in a second step to extract them to the gas phase. The negatively biassed cathode at the bottom powers a chain of field-shaping rings surrounding the cylindrical active volume, connected to one another via a resistor chain. Each subsequent ring is therefore held at a lower voltage than the preceding one in the chain. This produces a gradient of equipotential planes, which directs the electric field vertically throughout the active volume. The non-continuous nature of the field shaping rings can produce regions of closed field lines in their close proximity, limiting the usable LXe volume for the drift of electrons towards the top of the detector. Extra screening meshes can be deployed between the biassed electrodes and the photosensors to protect them from the high electric fields produced in close proximity to the anode and cathode [168].

The resistor chain is terminated at the gate, located just under the liquid-gas interface, which is finely adjusted with a weir or bell system [163, 219]. The third electrode, the anode, sits $\mathcal{O}(10\,\mathrm{mm})$ above the gate. The close proximity of the two top electrodes produces of a high-electric field region, which is used to extract electrons to the gas phase with virtually 100 % efficiency [220].

Upon the interaction of a particle with the xenon, the photosensor arrays detect the prompt scintillation light produced at the interaction site. The detection of the prompt signal (S1) marks the initial time of the interaction. Concurrently, the ionised electrons which do not recombine with the xenon atoms are drifted along the vertical electric field $\mathcal{O}(100\,\mathrm{V/cm})$, towards the top of the detector. The drift velocity $\mathcal{O}(1\,\mathrm{m/ms})$ is field-dependent and saturates at high-field values [223]. As they pass the gate, they enter the high field region of $\mathcal{O}(10\,\mathrm{kV})$ and are extracted from the LXe. The electrons are quickly accelerated in the gas phase, where they undergo a photo-luminescence process from their interaction with the gas atoms, producing a second scintillation signal – the S2 – proportional to the number of extracted electrons. As the electric field is homogeneously directed upwards, the shape of the S2 signal provides detailed information about the x-y coordinates of the interaction site, generally with a transverse resolution of $\mathcal{O}(1\,\mathrm{cm})$ [224, 225]. As demonstrated in a small-scale TPC with a resolution of $\mathcal{O}(1\,\mathrm{mm})$ [6], this position resolution is dependent on the geometry and granularity of the photosensor array, and on its distance to the liquid-gas interface. Furthermore, as the strength of the electric field is *a priori* known, the measured time delay between the detection of the S1 and S2 light signals can be used to calculate the depth (the z-coordinate) of the interaction site. Taken together, these allow for three-dimensional position reconstruction of particle interactions in the detection medium. The total light collection in the TPC is typically maximised by upholstering the walls of the field cage with low-radioactivity, high-reflectivity reflector panels. A typical choice is the use of polytetrafluoroethylene (PTFE).

With its two-signal topology, the dual-phase TPC allows for position-based volume fiducialisation, as well as background discrimination based on the ratio of the strengths of the two scintillation signals (S2/S1). ER events generally tend to yield more electrons than NR events. An excellent example of this is shown in figure 2.4. Internal and external calibration sources were deployed during a calibration campaign in the XENON100 TPC to produce ER events (CH_3T, red), and NR events (^{241}AmBe, black), demonstrating the discrimination power of the detector [221].

For ERs, where scintillation quenching is negligible, the total energy E released by an interaction is equal to the energy used to produce n_γ scintillation photons and n_{e^-} ionised electrons:

$$E = W\left(n_\gamma + n_{e^-}\right) , \tag{2.6}$$

where W is the average energy needed to produce an exciton or an electron-ion pair. This, however,

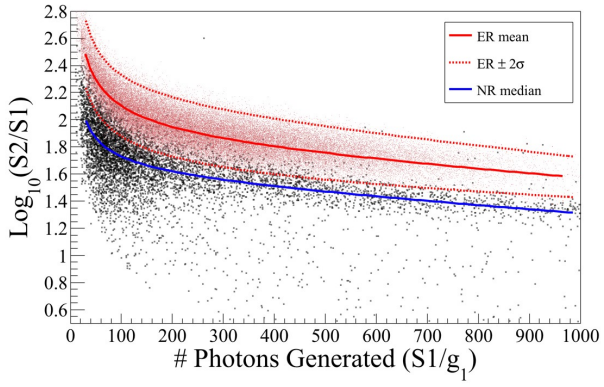

Figure 2.4: Example of electronic (red) and nuclear (black) recoil discrimination in XENON100. ER were produced with CH_3T and NR with ^{241}AmBe sources, at an electric field of 366 V/cm. The red and blue curves are respectively the mean values of the ER and NR data. Figure from ref. [221].

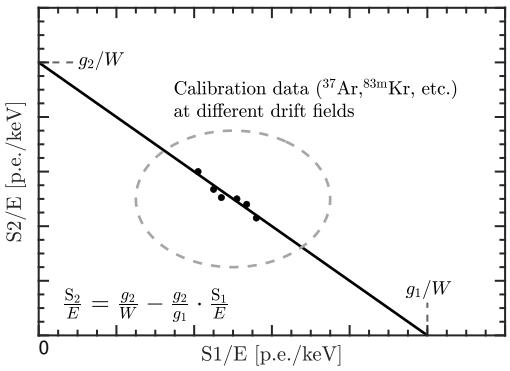

Figure 2.5: Schematic of a TPC calibration. At different drift fields, the light yield (S1) and the charge yield (S2) are anti-correlated. The detector-dependent gains g_1 and g_2 can be determined from the x and y-intercepts, while the slope is the ratio $-\frac{g_2}{g_1}$ [222].

assumes that all energy quanta W produce one free quantum. For NR events, the scintillation and ionisation signals are quenched:

$$E = W\left(n_\gamma + n_{e^-}\right)\mathcal{L}^{-1}, \tag{2.7}$$

inversely proportional to the energy-dependent Lindhard factor $\mathcal{L}$ ($\approx$ 0.1 - 0.2 [217]). Since the ratio $S2/S1$ is smaller for NR events than for ER events, the W-value must be smaller for NR interactions, as the energy required to produce an exciton is smaller than that required to produce an electron-hole pair. However, the Lindhard factor effectively compensates for this effect, and the W-value is hence generally assumed to be the same for both types of interactions. For LXe, the accepted value is $W = (13.7 \pm 0.2)$ eV [226], though recent measurements by nEXO [227] and our group at the University of Zurich [2, 228] have reported values of $(11.5 \pm 0.1$ (stat) ± 0.5 (syst)) eV and $11.5^{+0.2}_{-0.3}$ (syst) eV respectively. The number of quanta can be further expressed with detector-dependent gains as the linear combination of the S1 and S2 signals:

$$E = W\left(\frac{\mathrm{S1}}{g_1} + \frac{\mathrm{S2}}{g_2}\right), \tag{2.8}$$

where $g_1 := \mathrm{S1}/n_\gamma$ and $g_2 := \mathrm{S1}/n_{e^-}$ are respectively the detector-dependent scintillation and ionisation gains. Figure 2.5 depicts a typical calibration plot [4], with anti-correlated energy-corrected S1 and S2 signals due to the conservation of energy. The gains g_1 and g_2 can be empirically determined by calibrating the detector with radioactive sources with known decay energies, and by varying the value of the drift field. Examples of sources injected directly into the LXe are ^{83m}Kr ^{37}Ar, CH_3T and ^{220}Rn. External sources, for example the neutron-emitting ^{241}AmBe, and γ-sources such as ^{228}Th, ^{137}Cs, ^{60}Co, ^{22}Na, are also used to calibrate dual-phase xenon TPC [221, 229, 230].

[4] Also known as the *Doke* plot.

2.3 The DARWIN Observatory

In spite of their success, noble element dual-phase TPCs did not lead to a quick detection of dark matter particles. In an attempt to significantly increase the sensitivity of their detectors, field-leading experiments rapidly undertook the next phases of their scientific agendas, which led to succesive increases in the size of dark matter detectors. As a general example, the XENON collaboration constructed and operated XENON10 [165], XENON100 [166], XENON1T [167], and XENONnT [168] over a span of $\sim$ 15 years. Building upon the lessons learned and the experience acquired by the LXe community through research and development, DARWIN will push the limits of LXe technology.

With a 50 t xenon mass (40 t instrumented), the sensitivity of the experiment will improve on that achieved by its predecessors, such as XENONnT [168] and LZ [164]. The LNGS in Italy is the primary location option with its 3 600 water meter equivalent of overburden. The DARWIN collaboration submitted a letter of intent to the underground laboratory in 2019. The siting of the experiment is however still undecided, with multiple site being considered, such as SNOLAB in Canada [120], the Laboratoire Sous-terrain de Modane in France [231], and the Sanford Underground Research Facility in the United-States of America [232]. In this section, we discuss the conceptual design of DARWIN, and its physics reach.

2.3.1 Baseline Design

Figure 2.6a shows a rendering of the baseline design used in simulations to calculate the sensitivity of DARWIN to several physics channels [172]. The DARWIN TPC will be 2.6 m both in diameter and height. Titanium is preferred over stainless steel for the double-walled cryostat to reduce the radioactive budget of the experiment. To minimise the amount of material used while preserving their structural integrity, the two cryostat vessels feature torispherical domes, flanges, and stiffening rings. A pressurised flat floor in the inner vessel reduces the amount of "dead" xenon space at the bottom, where otherwise a large amount of LXe would not be instrumented.

The field cage ensuring the homogeneity of the electric field is composed of 92 oxygen-free high thermal conductivity (OFHC) copper field shaping rings, covered on the inside by PTFE reflector panels. This structure is supported by 24 PTFE pillars, though stronger materials suffering less linear thermal contraction, such as polyamide-imide (PAI), are also considered. The three stretched-wire electrodes and the two screening meshes will be mounted on low-radioactivity titanium frames at the top and bottom of the TPC. The electrodes will produce a vertical electric drift field of $\mathcal{O}(100\,\mathrm{V/cm})$ between the bottom cathode and the gate, and an extraction field at the liquid-gas interface between the gate and the anode of $\mathcal{O}(10\,\mathrm{kV/cm})$. Two photosensor arrays will be used to detect the VUV scintillation light of xenon. The DARWIN baseline design calls for the deployment of $\sim$ 1 800 R11410 3" PMTs from Hamamatsu Photonics K.K [233]. As will be discussed in chapter 5, the type of photosensor to be used in DARWIN is still undecided. Manufacturers constantly improve the designs and the functionality of their photosensors. The DARWIN collaboration is actively testing and developing new photosensing devices and schemes, with the goal of improving the sensitivity to low-light events while further reducing the radioactive budget and the costs of photosensors [234–236].

As seen in figure 2.6b, the cryostat will be installed inside a multi-layer concentric radiation shield. The inner shield is composed of a gadolinium-doped water neutron veto, instrumented with PMTs. The assembly is installed in a $\mathcal{O}(12\,\mathrm{m})$-diameter water-Cherenkov shield, also instrumented

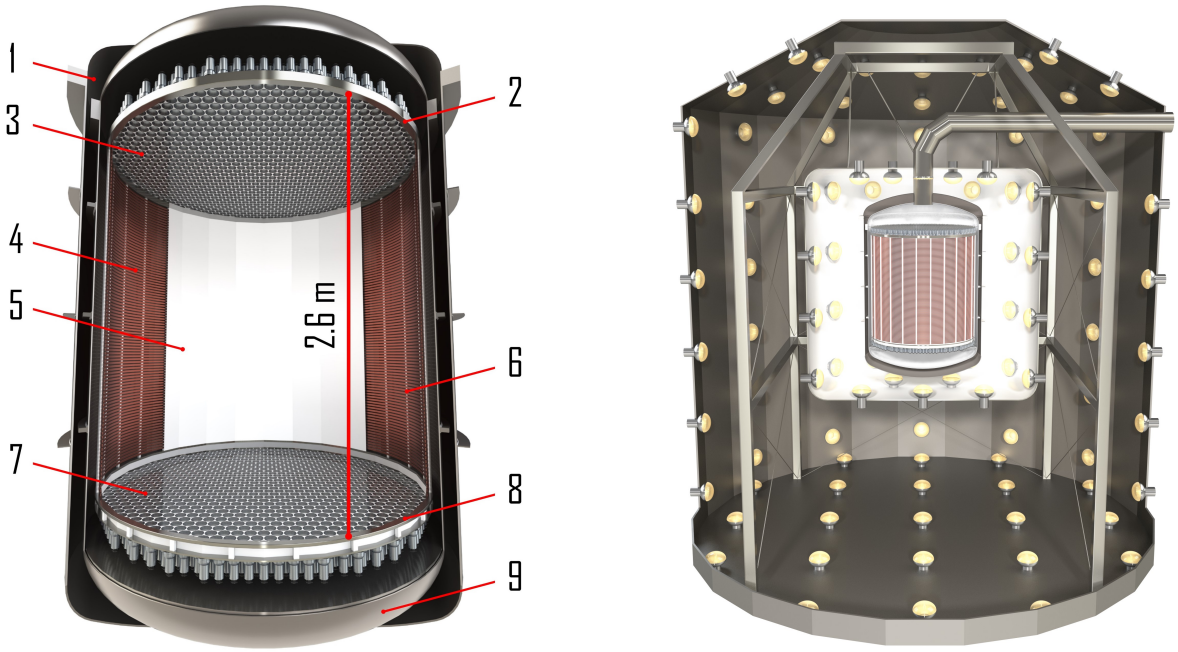

(a) (b)

Figure 2.6: Baseline design of DARWIN. The geometry is simplified to be used in sensitivity simulations. **(a)** Legend: (1) Outer vessel; (2) Top electrodes; (3) Top PMT array; (4) Field cage; (5) PTFE reflector panels; (6) PTFE pillars; (7) Bottom PMT array; (8) Bottom electrodes; (9) Inner vessel. **(b)** Conceptual design of the concentric radiation shield. The TPC is surrounded by an inner neutron veto filled with gadolinium-doped water. The whole assembly is submerged in a larger Cherenkov veto water tank. Both vetoes are instrumented with PMT. Figure inspired by ref. [172].

with PMTs, to detect the Cherenkov radiation from passing muons. The water also thermalises fast neutrons and attenuates γ-radiation emitted from nuclear decays in the cavern walls [237].

2.3.2 WIMP interactions

The direct detection of dark matter is the primary objective of DARWIN. As seen in figure 1.12, the aim is to cover all of the accessible SI parameter space, down to the neutrino fog, reaching a WIMP sensitivity of $10^{-49}\,\mathrm{cm}^2$ at a WIMP mass $m_\chi = 40\,\mathrm{GeV/c^2}$, assuming an exposure of $200\,\mathrm{t}\cdot\mathrm{y}$. Furthermore, the projected upper limit on the WIMP-neutron SD cross-section from ^{129}Xe and ^{131}Xe, as seen in figure 2.7, will also cover most of the accessible parameter space. Complementary searches covering a common region will be conducted at the high-luminosity LHC [238].

These estimates are based on some assumptions about the background of the experiment. Figure 2.8 shows the calculated differential energy spectra in DARWIN. Neutrinos from the solar pp-chain and ^{7}Be production will be the dominant backgrounds for ER, while for NR, the dominant background stems from the photosensors and other detector materials. Most contaminants dissolved in the target material can be removed by purification, either before its deployment or online.

Radioactive noble gases are, however, chemically inert. Therefore, they cannot be chemically purified and form the main intrinsic radioactive background. A problematic isotope is ^{85}Kr, a β-emitter with a half-life of 10.76 y. Natural krypton can be found at the ~ 5 ppm level in research-

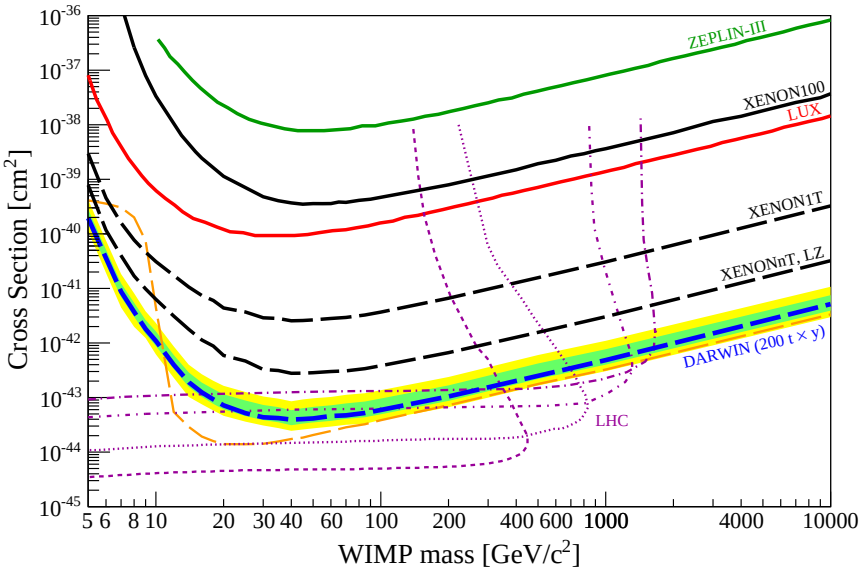

Figure 2.7: WIMP-neutron SD upper limits and projections. Limits are displayed in solid lines, while projections are dashed. The high-luminosity LHC will cover a common region [238]. Figure from ref. [172].

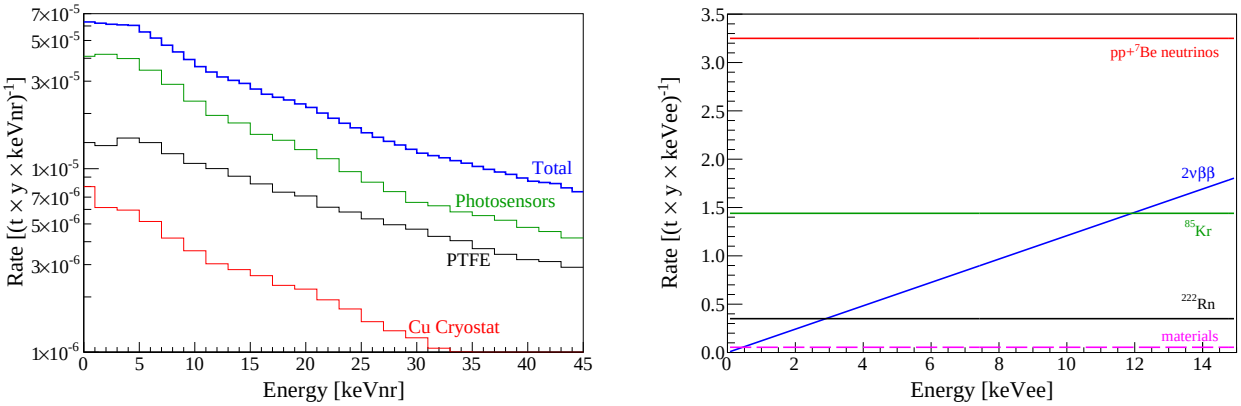

Figure 2.8: Differential energy spectra in DARWIN, assuming an infinite energy resolution and 100 % NR acceptance. **(a)** NR backgrounds. PMTs are the dominant source of background due to their relatively high radioactivity and close proximity to the active volume. **(b)** ER backgrounds. The dominating background will be the pp and ^{7}Be neutrinos. Both figures from ref. [104].

grade xenon [239]. Its concentration can be reduced to less than parts per trillion (ppt) via cryogenic distillation due to its high vapour pressure [240]. While the target concentration for DARWIN is 0.1 ppt, a much lower values were already achieved in XENON1T, with a concentration ^{nat}Kr/Xe of 0.048 ppt at the outlet of the distillation system [241]. The ratio ^{85}Kr/^{nat}Kr was measured at $(1.7 \pm 0.3) \cdot 10^{-11}$ mol/mol in XENON1T [242]. ^{222}Rn, an isotope part of the ^{238}U chain, is emanated from the surface of materials from the decays of ^{226}Ra. Materials contacting the xenon should therefore be selected to have a low radon emanation level. The target for DARWIN is 0.1 µBq/kg of xenon, while a concentration of <1 µBq/kg was achieved in XENONnT [204]. Some other important ER backgrounds are the $2\nu\beta\beta$ decays of ^{134}Xe and ^{136}Xe, and the γ-radiation of decays in the detector materials. Finally, cosmogenic and radiogenic neutrons, as well as CEνNS mainly from ^{8}B, are a source of NR background that can mimic a WIMP signal. The estimated sensitivity for

WIMP-nucleon interactions assumes an ER-rejection level of 99.98 % at an NR-acceptance of 30 %, a level already achieved in dual-phase xenon TPCs [243].

While energy thresholds of $\mathcal{O}(1\,\text{keV})$ can be achieved in xenon TPCs, the sensitivity to CEνNS will negatively impact the searches at low WIMP masses, and in this region of the parameter space, only limited gains in sensitivity would be made for thresholds below 5 keV. More detailed discussions on the sensitivity of DARWIN to WIMP interactions can be found in refs. [104, 172].

2.3.3 Neutrinoless Double Beta Decay

In its baseline design, DARWIN will have, in the instrumented volume, 3.6 t of ^{136}Xe. Therefore, it is a prime candidate to investigate $0\nu\beta\beta$ decay, even without enrichment in ^{136}Xe. The predicted sensitivity limit to its $0\nu\beta\beta$ decay is $T^{0\nu}_{1/2} = 2.9 \cdot 10^{27}$ y, and the discovery sensitivity at 3σ of $T^{0\nu}_{1/2} = 1.2 \cdot 10^{27}$ y [205] [5]. Figure 2.9 shows the sensitivity to the $0\nu\beta\beta$ decay half-life at the 90 % confidence level as a function of the fiducial volume and the exposure time. These estimations again assume certain background contributions and detector properties. The signal topology is a single-site event from the thermalisation of two electrons over $\mathcal{O}(\text{mm})$, with a Q-value of $(2\,457.83 \pm 0.37)$ keV. Bremsstrahlung photons can be emitted during the electron thermalisation. Lower energy photons will be rapidly absorbed, though higher energy ones (> 300 keV) could interact further than the assumed resolvable distance in DARWIN of 15 mm, leading to potential multi-site misidentification. This assumption on the spatial resolution results in a 90.4 % acceptance as single-site events. It is also assumed that the most-probable decay energy distribution is that of back-to-back electron emission, where they both share an energy of $Q_{\beta\beta}/2$.

The background components used to calculate the $0\nu\beta\beta$ sensitivity are shown in figure 2.10a. Intrinsic backgrounds in the region-of interest for this measurement are dominated by the decay of ^{137}Xe from cosmic activation by muon-induced neutrons [244], with a production rate of $(7.85 \pm 0.26) \cdot 10^{-1}$ atom/(t · y) [5]. Other sub-dominant backgrounds include neutrino-electron scattering of ^{8}B neutrinos with a flux of $(5.46 \pm 0.66) \cdot 10^{6}\,\text{cm}^{-2}\,\text{s}^{-1}$ [245], and the $2\nu\beta\beta$ of ^{136}Xe with

[5] From an erratum to be published in 2023.

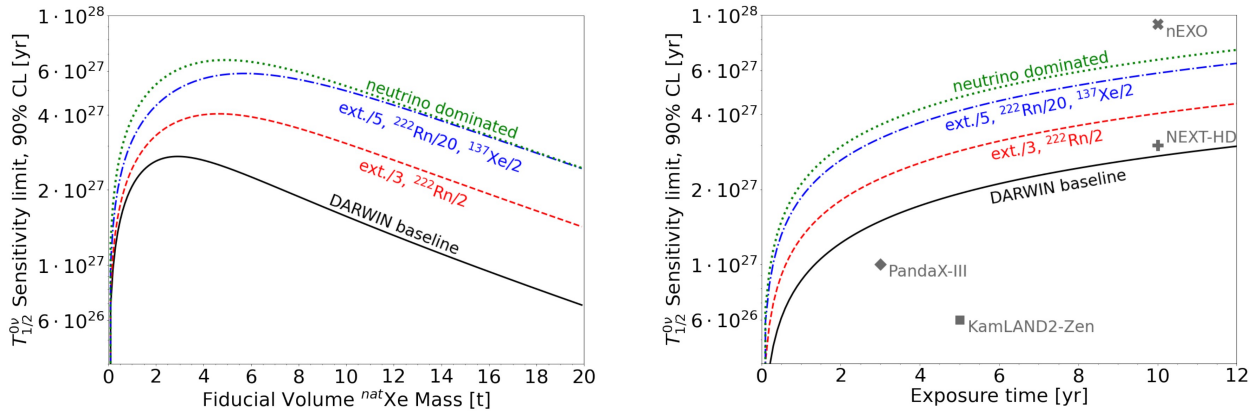

(a) (b)

Figure 2.9: Sensitivity to $T^{0\nu}_{1/2}$ at the 90% confidence level for the baseline design, and with optimistic backgrounds considerations: **(a)** as a function of the fiducial volume, assuming an exposure time of 10 y. **(b)** as a function of the exposure time for the optimal fiducial volume. DARWIN will be competitive with near-future experiments without enrichment. Figures from ref. [205] [5].

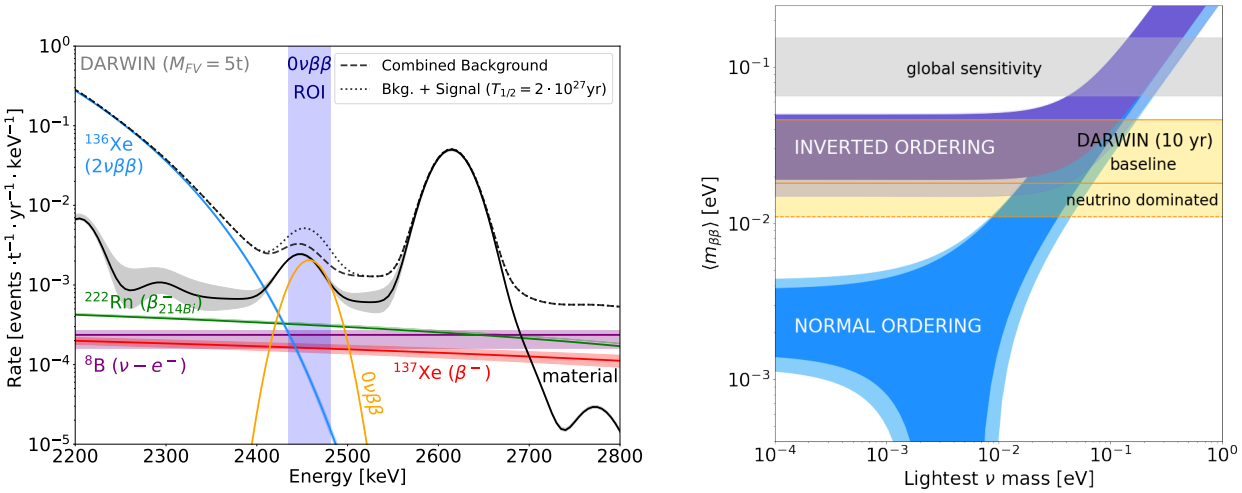

(a) (b)

Figure 2.10: Background components for $0\nu\beta\beta$ in DARWIN and neutrino mass hierarchy. **(a)** Predicted background spectrum around the $0\nu\beta\beta$ decay region-of-interest for the 5 t fiducial volume. The $0\nu\beta\beta$ curve is a hypothetical signal of 0.5 count/y, corresponding to $T^{0\nu}_{1/2} = 2 \cdot 10^{27}$ y. **(b)** Effective Majorana neutrino mass vs. lightest neutrino mass. With a 50 t · y exposure, DARWIN can reach a Majorana neutrino mass limit of 18 – 46 meV, enough to exclude the inverted mass-hierarchy. Figure from ref. [205] [6].

a half-life $T^{2\nu}_{1/2} = (2.165 \pm 0.061) \cdot 10^{21}$ y [246]. As discussed in the case of WIMP sensitivity, ^{222}Rn can be removed by online cryo-distillation, while ^{214}Bi, the dominant intrinsic background contribution for $0\nu\beta\beta$ decay, can be suppressed with more than 99.8 % efficiency with BiPo tagging, the decay-daughter ^{214}Po decaying with a half-life $T_{1/2} = 164.3\,\mu$s [247].

Finally, backgrounds from radioactive decays in detector materials, from the uranium-thorium chain, ^{60}Co β-decay, cosmogenically activated ^{44}Ti, and ^{222}Rn decay, are the principal sources of background. Overall projections for DARWIN assume background levels comparable with those reported by other experiments [248, 249].

With its sensitivity to $0\nu\beta\beta$ decay, DARWIN can also address the open question of neutrino mass hierarchy. Assuming a 50 t · y exposure, the half-life lower limit translates to a Majorana neutrino mass upper limit of 18 – 46 meV. As seen in figure 2.10b, this is sufficient, in the event of no $0\nu\beta\beta$ detection, to completely exclude the inverted hierarchy scenario for Majorana neutrinos, where the third neutrino mass eigenstate is the lightest, followed by the first and the second.

The complete sensitivity study to $0\nu\beta\beta$ decay, including the background simulations and comparison to other $0\nu\beta\beta$ experiments, can be found in ref. [205].

2.4 Solar Neutrinos

While neutrinos are regarded as an irreducible background for dark matter searches at the sensitivity of DARWIN, their interactions with the xenon target can also be studied [247]. In particular, solar neutrinos can inform on stellar properties, such as the metallicity of the Sun [251–253]. Current and next-generation LXe-based observatories will be sensitive to neutrino-electron

[6] From an erratum to be published in 2023.

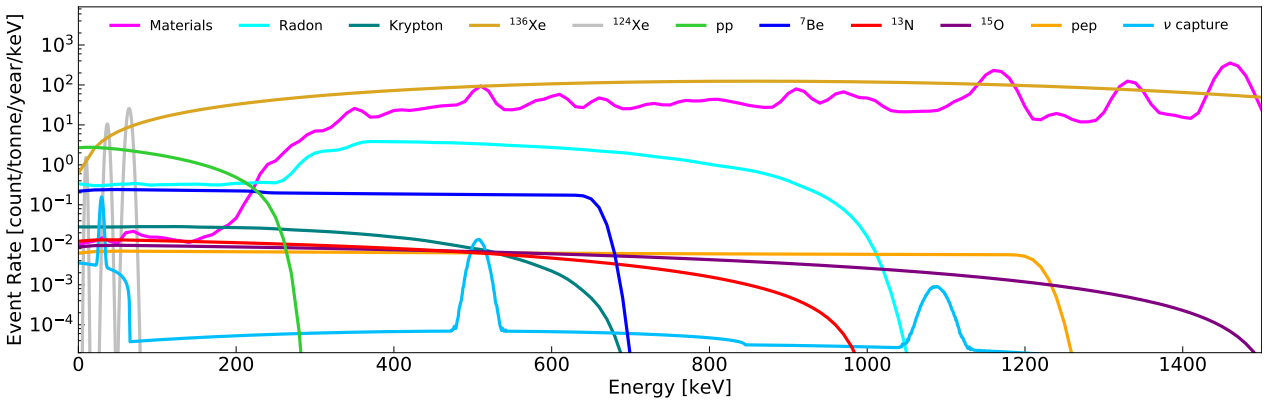

Figure 2.11: Relevant electron recoil spectra for solar neutrino studies. Shown are five solar neutrino components following from the high-metallicity standard solar model, neutrino capture on ^{131}Xe, and five backgrounds up to 1.5 MeV. The materials component is based on a 30 t fiducial volume. Figure from ref. [250].

elastic scattering and to CEνNS, at the $\sim$ MeV scale [164, 168, 172]. DARWIN aims to measure the solar neutrino flux with a 1 % precision. This will then lead to the reconstruction, in the energy range 1 – 200 keV, of the electroweak mixing angle $\sin^2\theta_w$ [254], and of the electron neutrino (ν_e) survival probability P_{ee} (i.e. the probability to detect on Earth an ν_e as a ν_e).

Similar geometric and background assumptions as discussed in the last two sections were considered in the sensitivity study presented in ref. [250], though the concentration in ^{nat}Kr and ^{222}Rn is assumed to be one order of magnitude lower than what is currently achieved in other experiments [255]. Figure 2.11 shows the relevant electron recoil spectra for the detection of solar neutrinos in DARWIN. The dominant background contribution of the $2\nu\beta\beta$ decay of ^{136}Xe could be suppressed with the depletion of the natural xenon, which would however hinder the search for $0\nu\beta\beta$ decay. Apart from the radioactive decays from the uranium-thorium chain in the materials, the biggest background contribution comes from ^{222}Rn.

The sensitivity to each neutrino and background component was assessed with multivariate spectral fits [250]. Figure 2.12 shows the exposure dependence of the measured relative uncertainty of the solar neutrino components and for neutrino capture, assuming a high metallicity model. The solid and dashed curves are calculated for natural and depleted targets, respectively. DARWIN

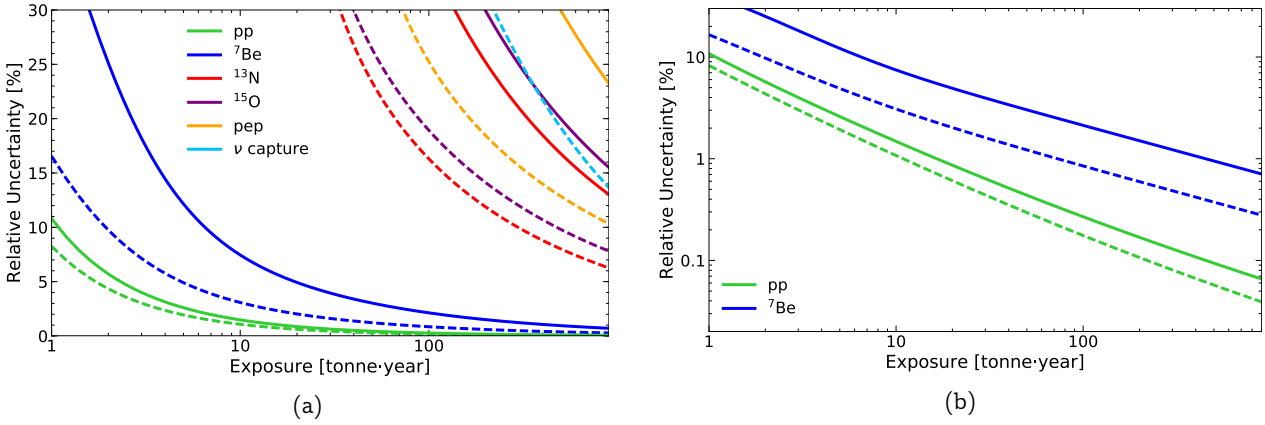

Figure 2.12: Measured relative uncertainty vs. exposure. The solid (dashed) curves are calculated for natural (depleted) targets. **(a)** Global view. **(b)** Close-up on the *pp* and ^{7}Be neutrino components for clarity. Figures from ref. [250].

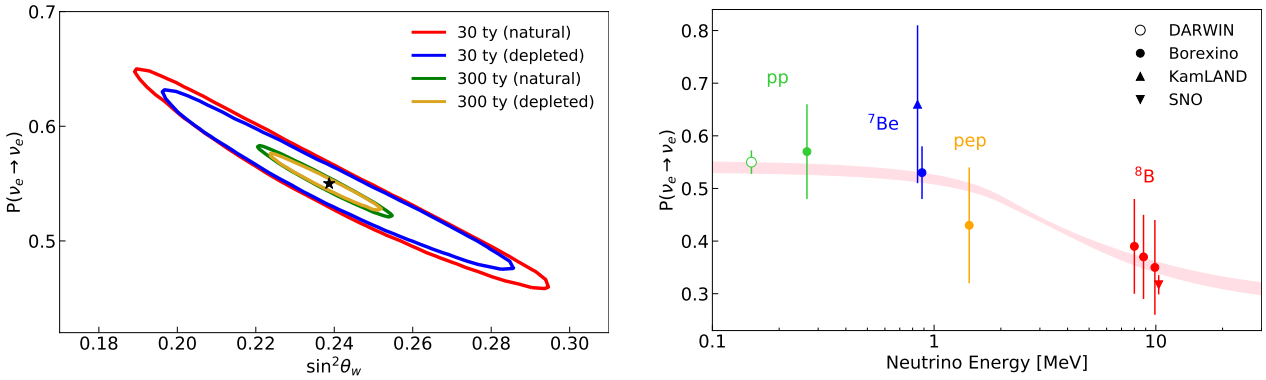

(a) (b)

Figure 2.13: (a) 68% confidence regions of $\sin^2\theta_w$ and P_{ee}. (b) ν_e survival probability vs. neutrino energy assuming the high-metallicity standard solar model. Figures from ref. [250].

would match the current precision of the *pp* and the ^{7}Be fluxes set by Borexino (10 %, 2.7 %) with 1 t · y and 60 t · y exposures respectively. It would also allow for the detection of ^{13}N and ^{15}O, and *pep* neutrinos, the latter requiring the use of a depleted target.

Finally, figure 2.13a shows the maximum likelihood estimators of $\sin^2\theta_w$ and P_{ee} resulting from toy experiments. The 2D distribution describes the 68 % confidence regions for two exposures, in the natural and depleted xenon cases. Figure 2.13b shows a comparison with other experiments of the P_{ee}. DARWIN would perform the first measurement of these two parameters at energies lower than 200 keV, with a respective precision of 5.1 % and 4.0 % with a natural xenon target, and 4.2 % and 3.1 % with depleted xenon.

In addition to the study summarised above, it was shown that in the depleted case, DARWIN will also be capable of measuring the neutrino mixing angle $\sin^2\theta_{13}$, with the potential to exclude $\sin^2\theta_{13} = 0$ [256].

2.5 Outlook

DARWIN will be a unique research observatory for multiple physics channels. It will be sensitive to many types of dark matter interactions, as well as many other rare and/or low-energy interactions, such as $0\nu\beta\beta$, and neutrino interactions. In addition to those discussed in this chapter, DARWIN will be able to observe the CEνNS of solar ^{8}B neutrinos and of neutrinos from galactic supernovae [257]. It will also be able to probe diffuse supernova neutrinos via CEνNS [258], while searches for light dark matter candidates such as solar axions, galactic axion-like particles, and dark photons will also be carried out [172, 259].

Limitations in the sensitivity to WIMP interactions from current experiments will necessarily be addressed, amongst other changes, by scaling up the detection volume, and by lowering the background levels through improved shielding of the active region, material selection, and purification of the xenon [260]. In the rest of this thesis, we will discuss our investigations to address two of the main challenges that DARWIN will face during its conception, namely the engineering and conceptual challenges related to the geometrical scaling up of the detector, and the choice of the photodetector detector type.

"How often do you find time
to gaze into the stars?"

Laura Baudis, 2016

Laura Baudis is a world-renowned astroparticle physicist, working on the experimental detection of dark matter and neutrinoless double beta decay. She is a member of the GERDA, LEGEND and XENON collaborations, and she is a founding member and spokesperson of the DARWIN collaboration. She spoke these words at the beginning of her talk at the TEDxCERN event in Meyrin, Switzerland. I am proud to have had her as a mentor for over 5 years.

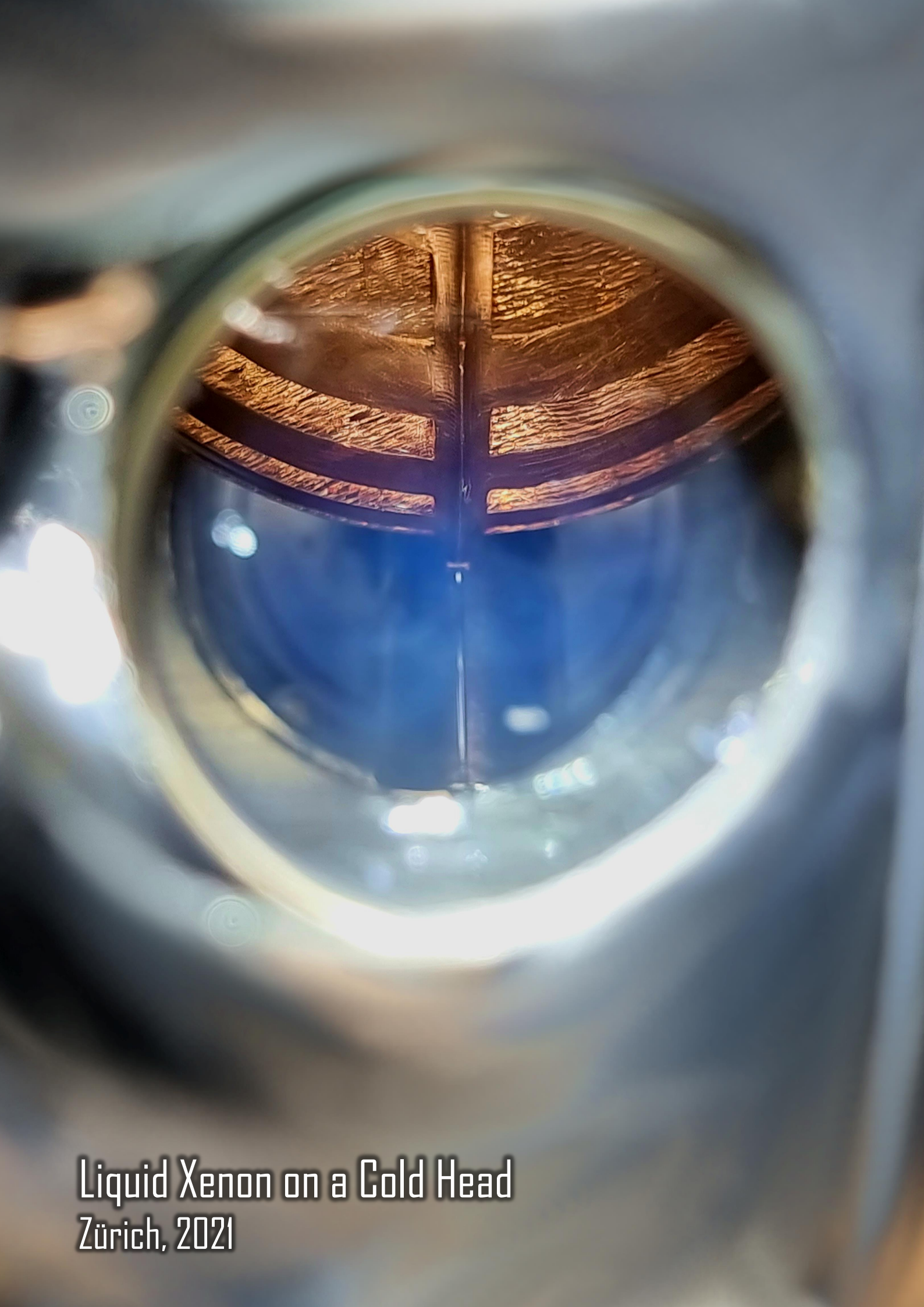

Liquid Xenon on a Cold Head

Zürich, 2021

3

Design and Construction of Xenoscope

With its 50 tonnes of LXe, the DARWIN observatory will be of unprecedented scale for a dual-phase xenon TPC. This increase in size over existing dark matter experiments, such as XENONnT [168] and LZ [164], introduces a number of new challenges that necessitate the use of new or improved technologies. In an effort to investigate the liquid xenon technology at these new scales, two member groups of the DARWIN collaboration built full-scale facilities. Our collaborators at the Albert-Ludwig-Universität-Freiburg, Germany, built Pancake [261], a full- DARWIN-diameter sized vessel used to test electrodes for electric field homogeneity and to perform sagging studies of the electrode material in LXe. At the University of Zurich, we designed and built Xenoscope, a DARWIN-scale demonstrator in the vertical direction, to address the challenges that naturally arise in a detector as tall as DARWIN, namely the survival time and drift of electrons in LXe. The Xenoscope facility takes inspiration from other scaled-down demonstrator facilities of the current generation of dark matter experiments using LXe [262–264]. The primary objective of Xenoscope is to demonstrate, for the first time, the drift of electrons in LXe over a distance of 2.6 m. This requires the mastery of high voltage and purification systems to, respectively, apply a strong and homogeneous electric field in the drift region and ensure electron survival during their drift, as discussed in chapter 2. Secondary objectives are the study of electron cloud diffusion, and of the optical properties of LXe.

In this chapter, we describe the technical design and construction of Xenoscope. We start with a general presentation of the design process in section 3.1 and of the facility in section 3.2. Follows a technical description of the gas handling system (section 3.3), of the cryogenic system (section 3.4) and an overview of the slow control (SC) system (section 3.5). Finally, we discuss the operational procedures in section 3.6. This chapter incorporates and expands on the hardware of Xenoscope reported in ref. [1].

3.1 Design Process

The construction of the Xenoscope facility was a large scale undertaking. As such, a comprehensive design process, shown schematically in figure 3.1, was employed to facilitate the construction effort, from the conceptual stage to the long-term operation. We can identify seven steps:

- **Proposal - Planning**
  The main objectives of the project were exposed and discussed. Important features of the facility were identified and served as a guide throughout the design phase. Boundary conditions, such as budget, physical space, and other constraints, were taken into account to begin shaping the project.

- **Design - Development**
  The project was broken down into subsystems. The design phase iteratively brought the project from the conceptual stage to production; three-dimensional technical drawings were produced with the Dassault Systemes SolidWorks® software [265], using the computer-aided design (CAD) technology [266]. Rapid identification of key components of a subsystem was beneficial at this stage, as they might have imposed some limitations on the final design. Simulations and engineering studies informed on the projected performance and safety of sub-assemblies. Finalised designs were reviewed with experts (engineers, technicians, machinists, etc.) to improve them with the prospect of machining, construction, and assembly of parts. Prototypes were produced to quickly identify shortcomings and correct them before part production began.

- **Construction - Acquisition**
  Approved technical drawings were passed on to the construction and acquisition stages. Parts were machined, and commercially available parts were acquired. Rigorous tracking of parts was vital to avoid unnecessary delays.

- **Assembly Installation**
  Parts were gradually assembled, and sub-assemblies were mounted in the facility. Preliminary tests were performed to confirm that the sub-assemblies were in operational condition. Subsystems were integrated with one another, and the full facility was prepared for operations.

- **Commissioning**
  The commissioning phase refers to the review of the facility as a whole. Operators verified that every subsystem was planned, designed, and installed properly. The initial operation of the facility established the final operational procedures. Periodical maintenance requirements

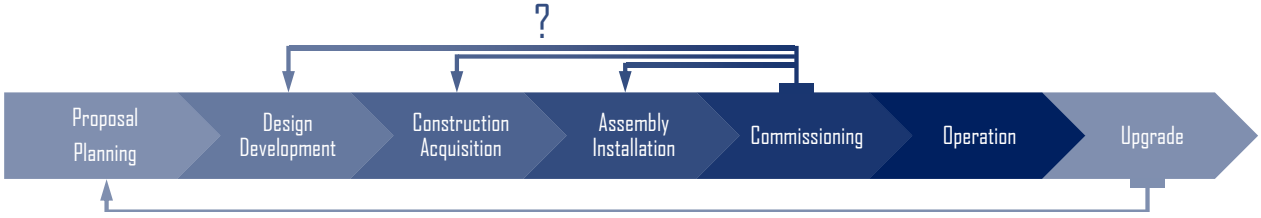

Figure 3.1: Design process scheme. A methodological approach streamlines the design process. Each step ensures the successful realisation of the project, leading to the commissioning of the hardware. Corrections are applied until the implementation is deemed satisfactory and ready for normal operation. The design can then be improved with upgrades.

were also listed and revised. Following the commissioning of the facility, unforeseen issues were identified; these can lead to a re-design, to the production of replacement parts, or to the reassembly of an affected subsystem.

- **Operation**
  Following the successful commissioning phase, the qualified facility was ready to be operated continuously under normal conditions. Operational procedures are continuously optimised and adapted to the evolving R&D needs.

- **Upgrade**
  Concurrent with normal operations, upgrades to the facility can be planned, designed, and constructed. Between operational runs, upgrades are assembled and integrated into the facility. The resuming of normal operations is usually preceded by a partial commissioning of the upgraded subsystems.

The design phase of Xenoscope started in late 2018, guided by a few restricting parameters: the cryostat had to host a TPC with a vertical drift length of 2.6 m, and contain up to a maximum of 400 kg of LXe. Finally, the full facility was to be installed in the assembly hall of the physics department of the University of Zurich, with dimensions of 8.2 m $\times$ 6.8 m $\times$ 8.2 m.

3.2 Support Infrastructure

The Xenoscope facility, shown schematically in figure 3.2, was designed and constructed at the University of Zurich and assembled in the high-bay area of the assembly hall of the Department of Physics. It is designed to a small-diameter LXe cryostat capable of housing a detector of full DARWIN-height in $\sim$ 400 kg of LXe. The facility comprises a cryogenic and a gas handling system, as well as two xenon storage systems. The assembly hall is equipped with a 4-tonne bridge crane, a closed-loop water-cooling system, a compressed air system, oxygen level sensors, and emergency air exhausts at floor level to rapidly evacuate heavier-than-air xenon gas in case of a major leak. An uninterruptible power supply (UPS) provides emergency supply in electricity of up to one hour in case of mains power loss.

In this section, we present the two main components of the support infrastructure: the support structure (section 3.2.1) and the cryostat levelling system (section 3.2.2).

3.2.1 Support Structure

The support structure is constructed with 50 mm $\times$ 50 mm Bosch Rexroth extruded aluminium profiles [268]. These are ideal for R&D projects such as Xenoscope, as they provide flexibility in mounting new components anywhere on the facility and are well adapted to continuously evolving ventures. Three structural sections can be identified: the inner frame, the outer frame, and the staircase assembly.

The $\sim$ 1.5 tonnes xenon-filled cryostat is supported by the inner frame. Finite Element Analysis (FEA) simulations, seen in figure 3.3a, were produced during the design phase to inform on the structural properties of the support structure design. It is composed of four stacked segments, each with three vertical weight-bearing profiles. The cubic outer frame, with a volume of $4 \times 4 \times 4\,\mathrm{m}^3$, provides lateral support to the inner frame and support for the floor of the upper level. The lower

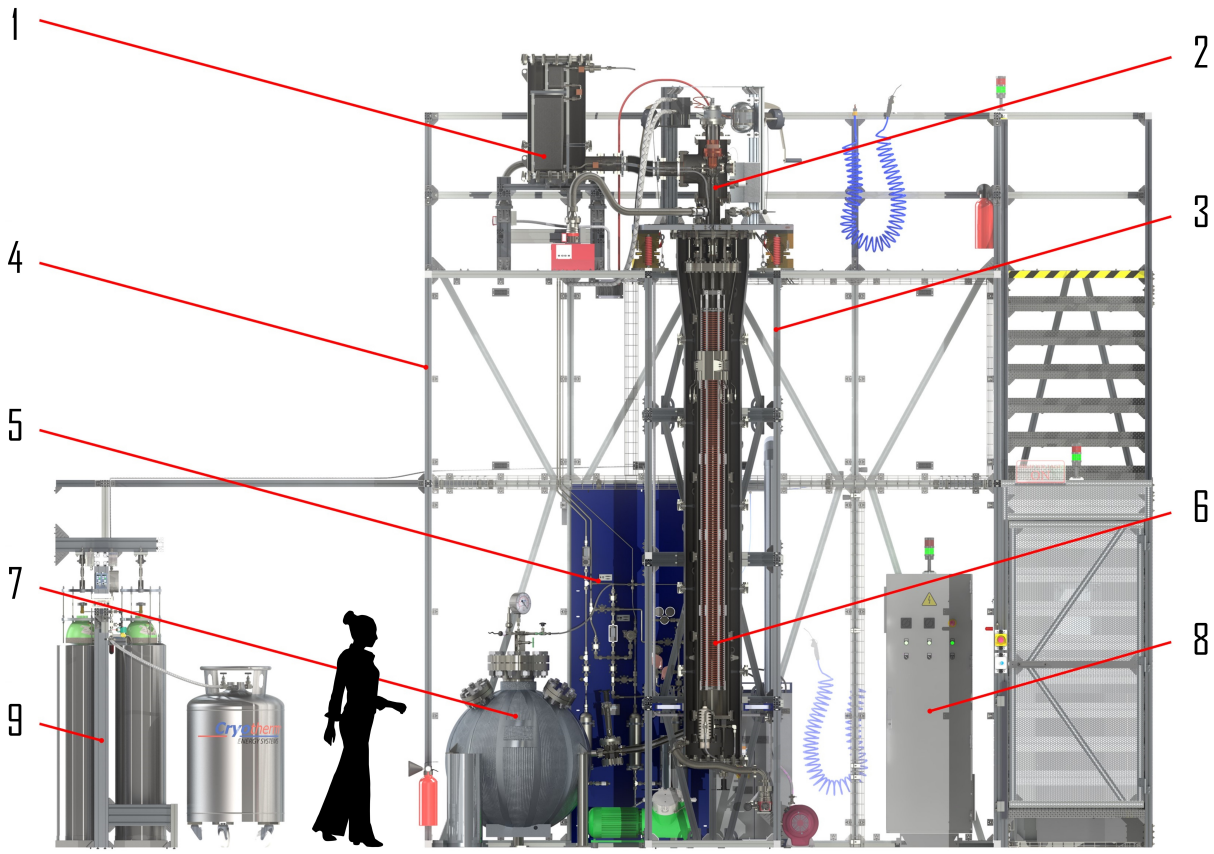

Figure 3.2: Schematic view of the Xenoscope facility with the 2.6 m TPC installed in the 24.8 cm diameter and 312 cm height cryostat. Legend: (1) Heat exchanger assembly; (2) Cooling tower; (3) Inner frame; (4) Outer frame; (5) Purification gas panel; (6) TPC in the cryostat; (7) High-pressure xenon storage vessel of liquid recovery system; (8) Power distribution cabinet; (9) Gas Cylinder Storage Array. Figure adapted from ref. [1].

section is enclosed by acrylic panels to help minimise dust accumulation during the assembly of the inner systems. Two double doors grant access to the inside for the cryostat assembly.

The outer and inner structures are securely attached to the floor to prevent undesired structural movements. For both assembly and normal operation, the upper level can be accessed by a staircase, fully enclosed by a safety perimeter with interlocks. During operations with high voltages, the interlock secures access to the upper level by locking the access door. The interlock system also prevents the tempering of the back section of the instrumentation rack, under the stairs, by interrupting the mains electrical power delivered to HV delivery modules.

Following the completion of the design phase, an engineering study of the support structure was performed by Roffler Ingenieure GmbH [267] to ensure that the structure, in particular the inner frame, could support the estimated 1.5 tonnes of the detector and cryostat assembly. Figure 3.3b shows the FEA study of the entire structure. In addition, the simulation revealed that the top platform can withstand an additional load of 200 kg/m^2.

The support structure was constructed and installed in the assembly hall of the Department of Physics at the University of Zurich in August 2019 by FMS Technik AG [269].

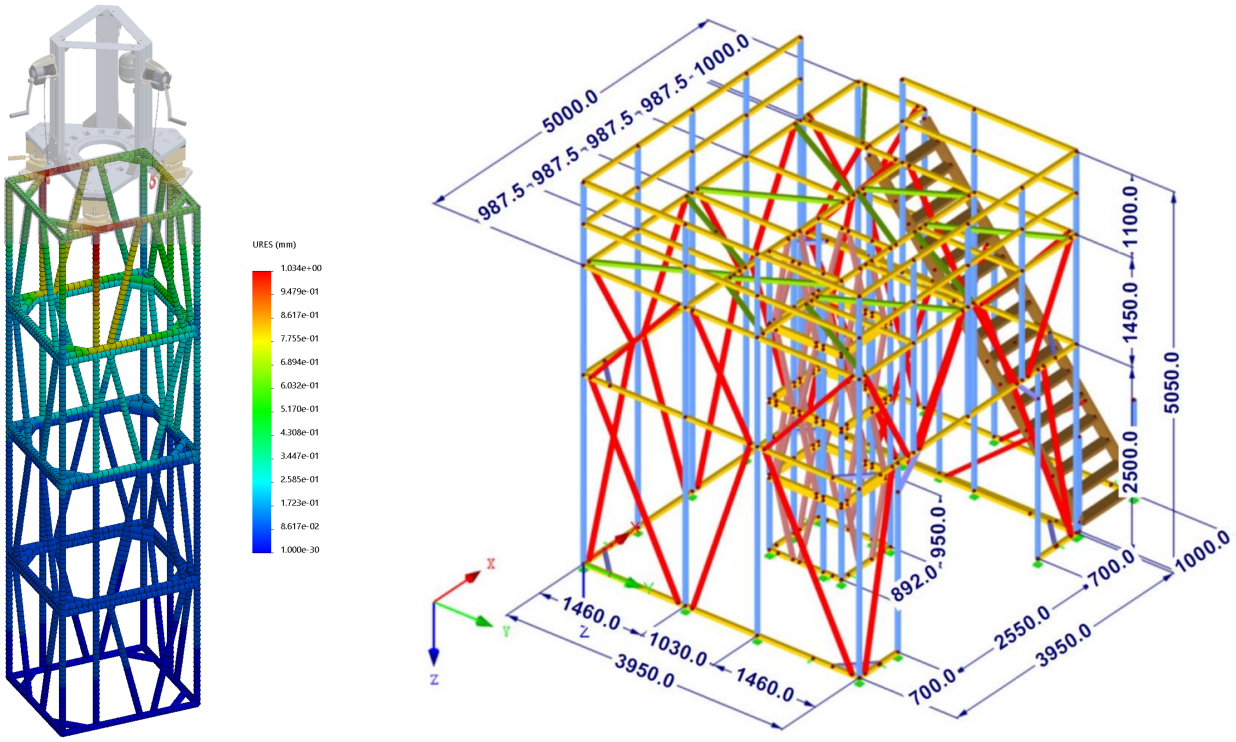

(a) (b)

Figure 3.3: Simulations of the support structure. **(a)** Mechanical design Finite Element Analysis (FEA) simulation of the inner frame produced during the design phase. The image displays the displacement of the assembly under load (self gravity and 666.6 kN per levelling leg). The levelling assembly, described in section 3.2.2, is overlaid at the top of the inner frame to indicate the load placement. **(b)** Mechanical design FEA model of the frame produced by Roffler Ingenieure GmbH [267]. All dimensions are in mm.

3.2.2 Levelling System

The parallelism of the gas-liquid interface to the electrodes is critical for ensuring homogeneous electron extraction to the gas phase and ionisation signal amplification [6].

In Xenoscope, the top flange assembly of the cryostat is permanently mounted under a high-rigidity, magnesium-aluminium alloy (EN AW-5083) triangular suspension plate (below, referred to as *top plate*), coupled to three levelling legs [1, 2]. A rendering of the levelling assembly can be seen in figure 3.4a. In this configuration, the cryostat hangs like a pendulum (see figure 3.2), so rigid centering arms are installed at the bottom to prevent undesired motions during operation. The inner vessel is also constrained by three spacers installed on the outside of its lowest section to prevent its motion inside the outer vessel.

The majority of the mass of the cryostat assembly is resting on coil springs located inside the three levelling legs, shown in figure 3.4b, while the three screw/counter-screws can lift up to 80 kg each. Atop the screw is a hemispherical dome, nested in a corresponding hemispherical cavity in the top block. A pin installed on the side of the dome prevents its rotation relative to the top block during the actuation of the screw mechanism.

The equilateral shape of the top plate favours a more even load distribution on the three levelling legs, each supporting a maximum load of $\sim$ 700 kg. Polyurethane vibration damper plates, 25 mm-thick, are installed between the levelling legs and the top plate to reduce low-frequency vibrations,

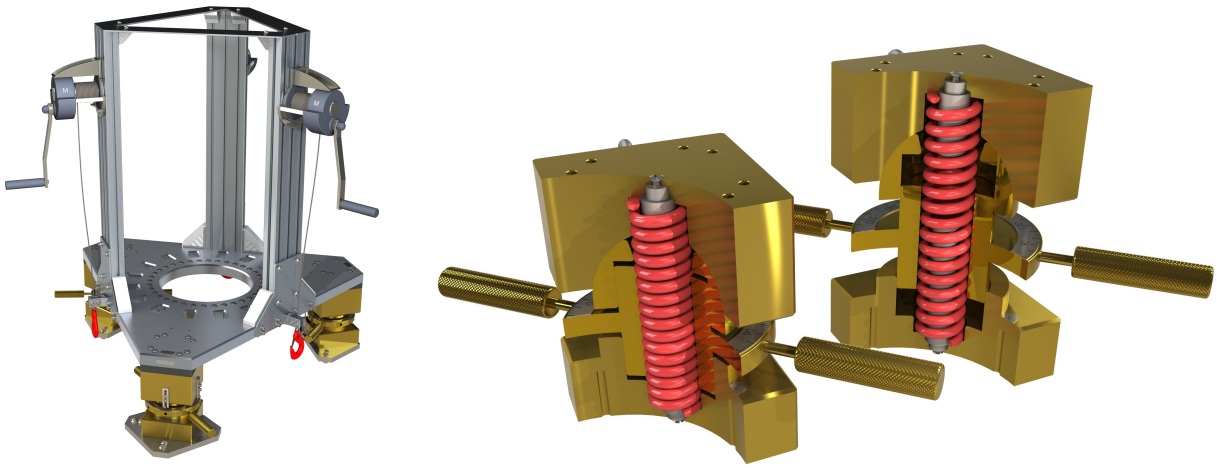

(a) (b)

Figure 3.4: Levelling system of Xenoscope. **(a)** Levelling assembly composed of a magnesium-aluminium equilateral triangular plate mounted on three levelling legs. The levelling assembly is installed on the upper level of the facility, where the cryostat is hung (see figure 3.3a). **(b)** Levelling legs rendered in maximum (left) and minimum (right) compression. Each levelling leg can withstand a load of up to 700 kg.

below 50 Hz, which could be transmitted to the cryostat by instruments mounted to the support structure. The top and bottom blocks are attached to each other with a chain to prevent unwanted lifting of the leg assembly. The concept of the levelling legs is currently registered by a Utility Model at the German Patent and Trade Mark Office, and an application for a Swiss Patent has been deposed.

The levelling assembly is completed by a three-sided hoist system, used to assemble the detectors and the cryostat vessels underneath it. The hoist system is designed to be operated in unison by three operators, with a fourth one guiding the lifted parts from underneath.

3.3 Xenon Gas Handling, Purification and Storage Systems

The gas handling system is used to transfer xenon between the different sections of the experimental setup. It is physically separated into two sections: the purification gas panel (section 3.3.1) is located on the lower level, while a second gas panel, the heat exchanger gas panel (section 3.3.2), is located on the frame of the heat exchanger assembly (later described in section 3.4.4) on the upper level of the facility. These two sections are connected to the cryostat and to two gas storage solutions: a gas cylinder storage array (GCSA) used to perform gas-phase xenon recuperation, and Ball of Xenon (BoX), used for gravity-assisted LXe recuperation. The storage solutions will be described in more detail in sections 3.3.3 and 3.3.4 respectively.

The P&ID of the Xenoscope facility, a schematic representation of the gas system, is shown in figure 3.5. Two xenon gas lines (high-pressure and low-pressure) can be identified. The high-pressure line handles the high pressures achieved when transferring xenon from the GCSA and BoX. It is composed of Swagelok® [270] seamless 1/4" stainless steel tubing and high-pressure components, is designed to accommodate xenon pressures of up to 200 bar. The low pressure side, designed to handle the gas recirculation in the purification loop, is built with 1/2" stainless steel components to reduce the pressure drop resulting from friction and turbulence in the conduits, maximising the

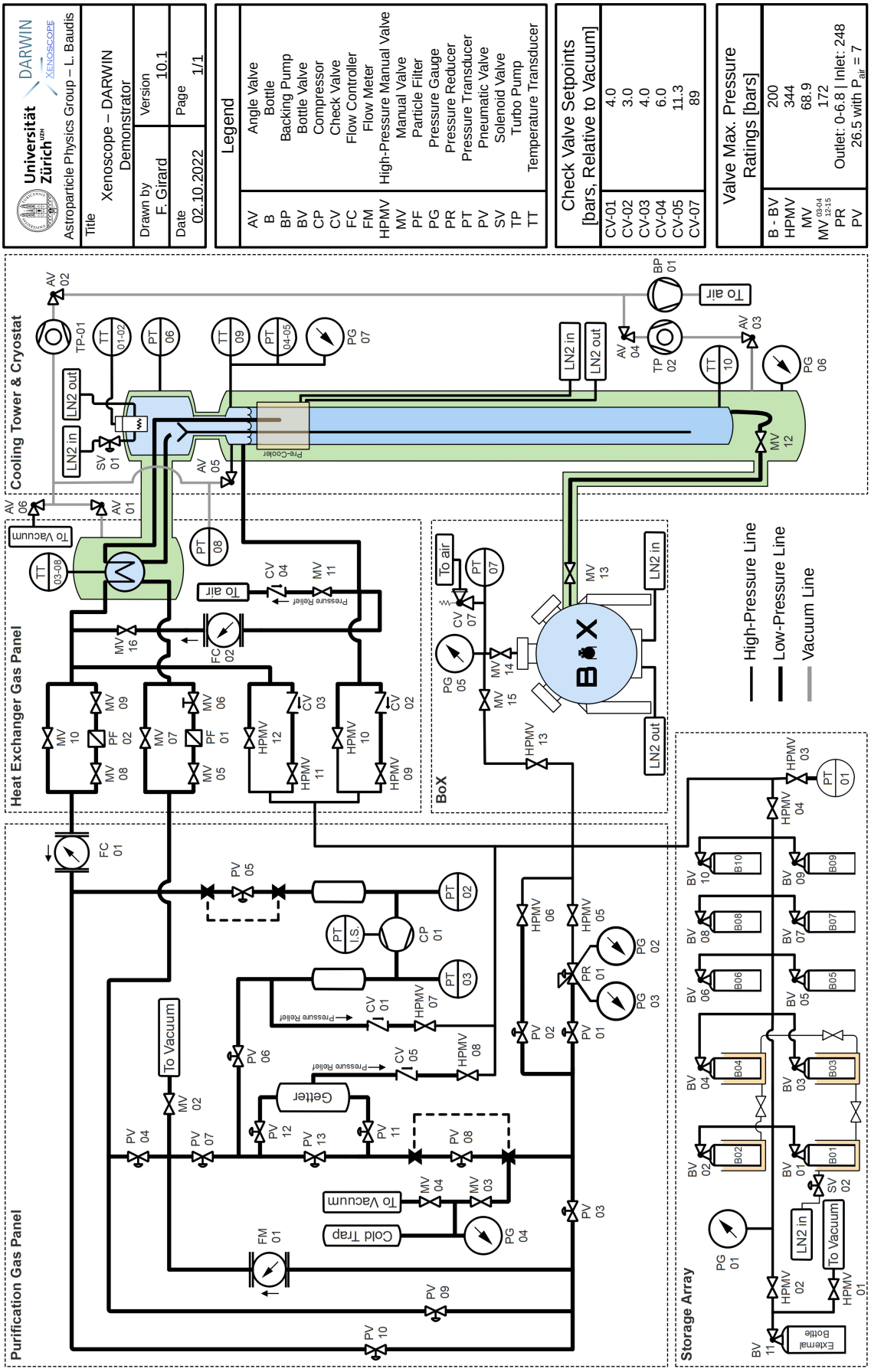

Figure 3.5: Detailed Piping and Instrumentation Diagram (P&ID) of the Xenoscope facility. The facility can be schematically separated into four zones, indicated by dashed lines. Three line types (high-pressure, low-pressure, and vacuum) are identified by their line thickness and color. Manual valve MV-01 has been removed from the system and is deliberately missing from the P&ID. The naming scheme of the components can be found in the table on the right side.

xenon flow. High-pressure manual valves (HPMVs) are used as shutoff valves and separate the high and low pressure regions when filling the detector, while a pressure regulator lowers the gas pressure when it is transferred from the high to the low pressure side. Table 3.1 lists the different valve types used in the facility, along with some of their attributes. Whenever possible, Swagelok® VCR connectors were preferred for their excellent cleanliness and repeatable use. Only non-silver coated VCR gaskets (SS-*XX*-VCR-2-VS, where *XX* specifies the gasket size) were used to prevent the introduction of fine silver particulates in the xenon.

3.3.1 Purification Gas Panel

The purification gas panel is located on the ground floor of the facility. It mounts most of the hardware necessary for the recirculation of xenon and its purification. Gaseous xenon (GXe) is recirculated by a dual-diaphragm KNF Neuberger [271] GXe compressor, model PM32352-N1400.1.2.12E. This model can produce a maximum of 3.0 bar pressure difference to atmosphere, achieving a theoretical maximum flow of up to 250 standard litres per minute (slpm) of gas nitrogen (GN_2) at 0 bar pressure drop. The double diaphragm configuration prevents the loss of xenon in the event of a diaphragm failure. The inner space (i.e. the space between the two diaphragms) of both compressor heads are connected together, filled with 1 bar of GXe. They are instrumented by a SMC ISE1-01-55CL pressure switch [272] (later upgraded to a Swagelok S model pressure transducer, see section 4.2.3). The flow of xenon is controlled by a Teledyne Hastings HFC-203 mass flow controller [273] installed upstream of the GXe compressor, calibrated up to 100 slpm. A Teledyne Hastings HFC-201 mass flow meter is installed downstream of the GXe compressor to ensure consistent flow between the inlet and the outlet of the GXe compressor, as well as to monitor xenon flow during recuperation, which cannot be done with the flow controller.

The purification gas panel, seen in figure 3.6 hosts the main components of the purification loop. The purity of the LXe is instrumental in the efficient drift of electrons over long distances. Xenoscope uses a xenon purifier similar to those used in XENON1T to remove impurities for the xenon [219]. The MonoTorr PS4-MT50-R-535 hot metal getter manufactured by SAES Pure Gas [274] is factory certified for recirculation flows of up to 70 slpm of xenon, delivering sub-ppb levels of H_2O, O_2, CO, CO_2, N_2, H_2, and CH_4. Room temperature GXe is flushed through the active material of the

Valve Type	Model	Max. Pressure @ 25°C [bar]	Instances
Pneumatic Bellows Sealed	SS-8BK-V47-1D	26.5 with $P_{air} = 7.0$	PV-*XX*
Bellows Sealed	SS-8BK-V47 SS-4BK-V51	68.9	MV-02 MV-05 to MV-11
Low-Temperature Bellows Sealed	SS-8URW-V47-TF-26598	172	MV-03 - MV-04 MV-12 to MV-15
Integral-Bonnet Needle	SS-1RF4	344	HPMV-*XX*
Pressure Reducing Regulator	KPR1FRF412A20020	Inlet: 248 Outlet: 0 - 6.8	PR-01
Check valve	SS-4CA-VCR-*XX*	206 Cracking: See figure 3.5	CV-*XX*

Table 3.1: List of valves used in Xenoscope. Model numbers marked with *XX* can be of varying configuration.

getter, zirconium-alloy pellets (Zr-V-Fe) heated to 420 °C, which absorb impurities present in the xenon. An integrated heat exchange radiator cools the GXe after its passage in the getter cartridge to bring it back to room temperature. A $3 \cdot 10^{-3}$ µm fine particulate filter is installed immediately after the getter cartridge to prevent the transmission of getter materials into the rest of the system.

The purification gas panel features dual-acting pneumatic valves to provide an additional level of safety by enabling remote actions from operators. The valves are actuated by a valve controller, supplied with air from the air-supply system of the building at 7 barg. A dry-nitrogen bottle regulated at 6 barg serves as a backup in case of the unlikely failure of the main air supply system. A check valve with a cracking pressure of 0.3 bar (i.e. pressure difference at which gas flow is detected) prevents back flow from the nitrogen bottle to the main air supply line. The nitrogen bottle is therefore only used when the pressure of the line drops below 6 bar. This system ensures an uninterrupted supply of air to the valves at all times.

Two buffer volumes are installed inline with the GXe compressor to limit the rate of pressure drops at the inlet in case of GXe deprivation, and to protect it from sudden pressure spikes at the outlet in case of flow constriction downstream. The purification gas panel also features a cold trap, equipped with a pressure gauge and an evacuation port for pumping, which can be used to achieve an ultra-high vacuum in the whole system prior to the initial filling. The cold trap can also be used to cryo-pump and freeze the GXe present in the gas lines in order to safely perform maintenance without the need for a full recuperation. For this reason, both MV-03 and MV-04 are bellows-sealed valves rated for temperatures down to 73 K. Finally, the cold trap, serves as a parallel buffer volume during gas recirculation, which helps prevent unwanted pressure oscillation caused by the GXe compressor.

3.3.2 Heat Exchanger Gas Panel

The heat exchanger gas panel, seen in figure 3.7, is located on the top level of Xenoscope, on the frame of the heat exchanger assembly. Two bypassable particulate filters are located at the supply and return lines. GXe coming from the cryostat can be passed through a 40 micron coarse particulate filter before being directed to the purification panel. Xenon coming back to the cryostat can be circulated through a 0.003 micron particulate filter, mainly used before filling the cryostat with LXe to prevent dust, rust, or any undesirable particulates present in the pipes of the gas system from entering the inner vessel. This filter cannot be used for high flow recirculation of the xenon, as the high pressure drop of this filter increases the pressure downstream of the GXe compressor. The coarse filter, on the other hand, produces little pressure drop and is almost always used.

Three check valves are located on this panel. The first is the emergency relief to air, CV-04, connected directly to the cryostat, with a cracking pressure of 8.0 bar. This valve is meant as a last resort to prevent failure of the cryostat due to overpressure. A self-sealing valve was chosen over a burst disc to reduce the amount of xenon vented to air in the event of an emergency. The other two connect the cryostat and the return line to the GCSA (see section 3.3.3) to allow for automatic recuperation in case of pressure increase in the cryostat or after the heat exchanger for example, in the case of xenon freezing in the heat exchanger.

The filtration gas panel also hosts digital panel meters used for temperature and pressure readings of the cryostat and the heat exchanger assembly. The panel meter reading the pressure from the cryostat features a programmable threshold relay used to actuate the solenoid valve of the LN_2 emergency cooling system (see section 3.4.3) when the pressure in the inner vessel is above 2.3 bar.

Figure 3.6: Purification gas panel. The gas handling system is seen attached to the back of the panel. The hot metal getter inside its cabinet can be seen on the right. The green pump in front of the panel is the GXe compressor. BoX (section 3.3.4) can be seen on the left.

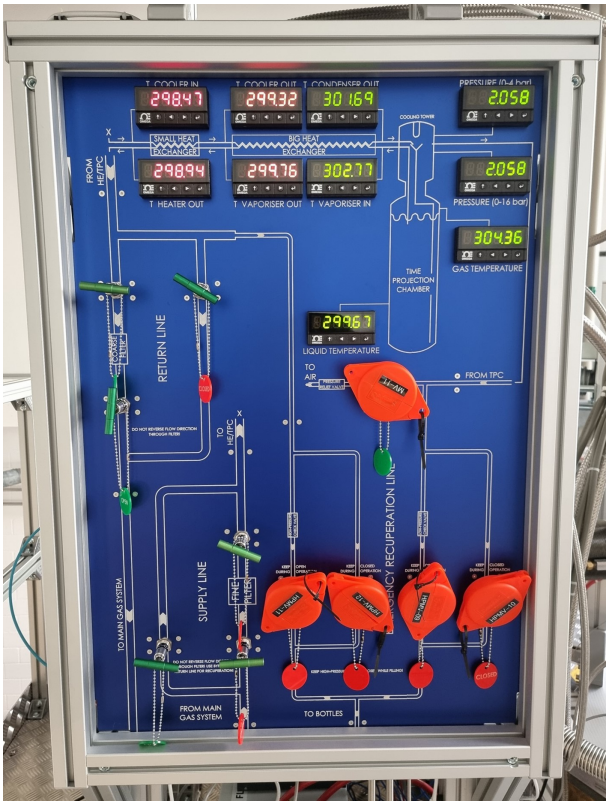

Figure 3.7: Heat exchanger gas panel attached to the frame of the heat exchanger. Panel meters display the temperatures and pressures measured at different places on the detector and retransmit the data to the SC (see section 3.5).

3.3.3 Gas Cylinder Storage Array

When not in use, the xenon can be stored in the GCSA seen in figure 3.8a. Up to ten 40 l aluminium gas cylinders are hung from load cells from Mettler-Toledo Schweiz GmbH [275]. Four cylinders hang inside 122 cm deep Dewar flasks to allow cryopumping of the xenon, a process that consists of transferring GXe by freezing it inside the gas cylinders cooled down to 77 K with LN_2. The Dewars are inter-connected in series at their bottoms by vacuum insulated lines isolated with vacuum-jacketed cryogenic valves, allowing the transfer of LN_2 to subsequent Dewars in the chain. Cane-shaped drains prevent accumulated moisture from entering the cryogenic line. These four gas cylinders can freeze the full amount of xenon used in Xenoscope. All four cryopumping cylinders are fitted with 1 400 W band heaters to prevent freezing of the cylinder valves, which could result in xenon leaks. The heaters are controlled by Proportional–Integral–Derivative (PID) controllers, with the temperature taken on the side of the cylinders. As the xenon warms up and evaporates following recuperation, it is redistributed to the rest of the bottles in the array. In total, up to 470 kg of xenon can be stored in the array at room temperature. The recuperation scheme is explained in section 3.6.2.

The GCSA is also used as an automatic xenon recuperation solution. When Xenoscope is normally operated, the first gas cylinder in the array is kept cold with LN_2 at all times. A liquid level control system from KGW-Isotherm [276] actively controls the LN_2 level. In the event of a pressure

(a) (b)

Figure 3.8: Xenon storage solution. **(a)** gas cylinder storage array (GCSA). Seen here are nine gas cylinders used in Xenoscope, with a tenth space reserved for future expansion of the xenon inventory. **(b)** Ball of Xenon (BoX). The pressure vessel can hold gases with a pressure of up to 90 bar ($\sim$ 450 kg of xenon at room temperature).

rise above pre-determined thresholds in the gas handling system or in the cryostat, strategically located check valves release GXe to the high-pressure line, which is also continuously monitored. The gas is ultimately frozen into the B-01 gas cylinder (refer to figure 3.5). This solution was preferred to the typical use of a burst disc to prevent the venting of xenon to atmosphere. Since intermittent venting generally cools down the LXe in the cryostat, this scheme gives operators ample time to react to undesired situations and bring the facility back to a safe state.

3.3.4 Ball of Xenon

Ball of Xenon (BoX) is a spherical pressure vessel that can store up to 450 kg of xenon at room temperature. Unlike the GCSA, BoX can be used to recover the xenon from the cryostat directly in liquid form, circumventing the slow evaporation process for cryopumping. A P-trap trapping a bubble of GXe is connected to a low-temperature cryogenic valve (MV-12) located under the bottom flange of the inner vessel of the cryostat. This valve can be actuated through a magnetically-coupled rotatory feedthrough installed on the bottom flange of the outer vessel. A vacuum-insulated cryogenic line connected to a second cryogenic valve (MV-13) completes the connection to BoX. The connection to the side of the pressure vessel being lower than the bottom of the inner vessel ensures a complete transfer of the LXe during gravity-assisted recuperation.

The spherical pressure vessel was produced by KASAG Swiss AG [277] following the conceptual design study presented in ref. [2]. Shown in figure 3.8b, BoX is instrumented with both an analogue and a digital pressure gauge with continuous pressure reading through the SC. The assembly is

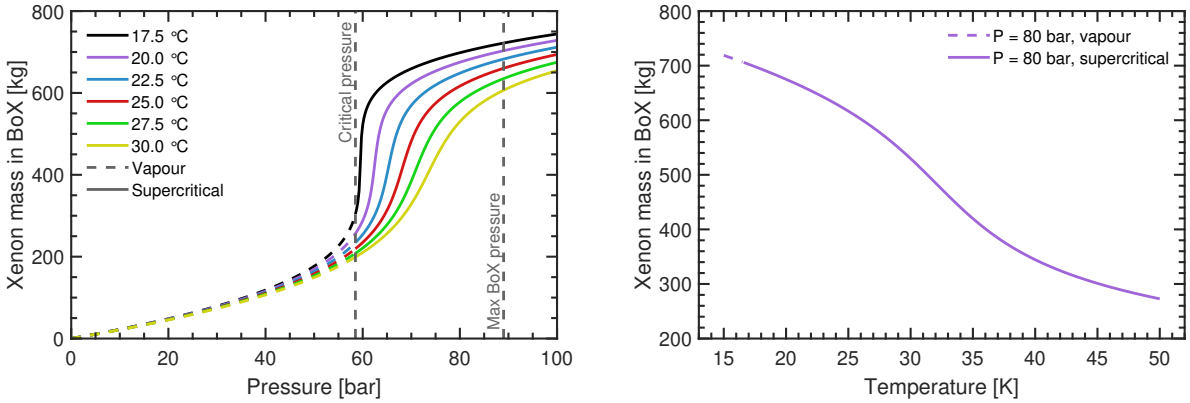

Figure 3.9: Mass of xenon in BoX. **(a)** Xenon mass in BoX vs. pressure, at temperatures ranging from 17.5 to 30.0 °C. The xenon is stored in vapour form below the critical pressure ($P = 58.420$ bar) and becomes supercritical above [193]. **(b)** Xenon mass in Box at 80 bar vs. temperature. The nominal mass of 450 kg is reached at a temperature of 33.55 °C.

factory-rated up to 90 bars. A pressure relief valve, with a factory-certified cracking pressure of 89 bar, serves as the ultimate fail-safe, venting GXe to air in case excessive pressure build-up. Figure 3.9a shows the mass of xenon stored in BoX as a function of pressure, assuming a pressure vessel volume of 0.390 m^3. Xenon becomes supercritical above its critical pressure ($P = 58.420$ bar), at which point the pressure only marginally increases with the addition of more xenon gas. Hence, this behaviour allows the storage, at fixed volume, of substantially more xenon than in the case of a perfectly noble gas. We can see, however, in figure 3.9b that the maximum allowable xenon mass stored in BoX is highly dependent on the temperature. At the nominal mass of 450 kg, we would read a pressure of 80 bar at a temperature of 33.55 °C. The temperature of the assembly is normally controlled with an air recirculation system. However, failure of this system, coupled with direct sun exposure during the summer months, could increase the room temperature significantly. Therefore, the temperature inside the inner frame is kept between 19 and 23 °C with the use of a 900 W air conditioning unit, which also ensures air exchange with the rest of the room. Pressure alarms must be set on the pressure of BoX at ($P_{\text{alarm}} = P_{\text{BoX}} + 5$ bar), and 80 bar, to alert operators well in advance in case of pressure rise. As a good practice, BoX should not be left overfilled, ($M_{\text{BoX}} < 350$ kg), with excess xenon transferred to the GCSA.

BoX connects to the high-pressure line of the gas handling system, allowing for the filling of the xenon in a similar way to the GCSA. BoX is thermally insulated with several layers of double-sided aluminised bubble wrap. A copper cooling block is bolted under the spherical pressure vessel. Before performing the gravity assisted recuperation of xenon, BoX is pre-cooled with LN_2. Thermal contact between the cooling block and the sphere is improved with the application of Apiezon® N Grease mixed with pure powdered silver. The gravity-assisted recuperation to BoX is explained in section 3.6.2. Further details about the design and construction of BoX can be found in ref. [2].

3.4 Cryogenics

The cryogenic system of Xenoscope is designed to provide the necessary cooling power to liquefy the xenon stored as gas and control the temperature and pressure in the main vessel. In this section, we present six different subsystems contributing to the cryogenic aspect of Xenoscope: the

cryostat (section 3.4.1) and thermal insulation (section 3.4.2), the cooling tower (section 3.4.3), the heat exchanger assembly (section 3.4.4), the umbilical section (section 3.4.5), and the pre-cooler (section 3.4.6).

3.4.1 Cryostat

The detectors of Xenoscope are housed inside a cylindrical, double-walled stainless steel cryostat. The design of the cryostat is modular for ease of production and assembly. Figure 3.10 shows the cryostat with the two planned phases of the Xenoscope experiment: a 0.53 m tall PM and a 2.6 m tall TPC. The outer vessel is a vacuum chamber composed of six ISO-K-400 sections, while the inner vessel is a pressure vessel composed of six electropolished DN250CF sections, capable of containing 400 kg of LXe. Both vessels feature a conical section at their top to increase the volume hosting a large amount of cables and instruments. The sections of the inner (outer) vessel weigh $\sim$ 19.5 kg ($\sim$ 29.2 kg) each.

An engineering study by Helbling Technik AG [278] ensured that the structural integrity of the TPC housing could be maintained both in normal operations and in potential emergency situations, where the boiling of LXe could increase the pressure in the inner vessel significantly in a short period of time. A simulation of the CF flanges of the cryostat, a connector type normally designed for and used on vacuum vessels, was performed to confirm their suitability for containment of LXe up to 8 bar, at 170 K.

The top flange assembly of the cryostat, shown in figure 3.11a, is composed of an outer ISO-K-500 flange and an inner DN350CF flange. Six DN40CF feedthroughs, which host the cooling tower, cabling and instrumentation, are joined by six axial displacement bellows. A 13 mm-thick stainless steel ring was welded on top of the ISO-K-500 flange to ensure enough material was available for the 36 tapped mounting holes. The engineering study showed that our initial rigid, fully welded design would have been susceptible to welding ruptures caused by the uneven thermal contraction of the two flanges. The inner half of the top flange assembly, cooled almost to LXe temperature, will contract concentrically on the order of 1 mm while the top half remains at room temperature. In the production design, the two flanges are therefore joined by six concentrically-oriented stress-relieving stainless steel swivel arms of 20 mm diameter, suspended by 10 mm stainless steel dowel pins.

Figure 3.11b shows a mechanical design slpm of a single swivel arm. The top hinge is fixed in space. Two loads are applied: self gravity is applied to the whole assembly, and a 1 500 N downward force is applied to the underside of the lower hinge (indicated by the pink arrows in figure 3.11b, simulating 150 % of the weight of a filled inner vessel). The image on the left shows the factor of safety (FOS). In this case study, the minimum FOS is 19.8, well above our self-imposed FOS of 3. The image on the right shows the simulated elongation of the swivel arm assembly, magnified by $3.1{\cdot}10^3$. The total expected elongation of the arms is less than 7 µm, hence negligible.

3.4.2 Thermal Insulation

The vacuum between the two vessels of the cryostat is the main thermal insulator of the detector. It is composed of two HiPace® 80 turbomolecular pumps [279] from Pfeiffer Vacuum GmbH [280], located at the bottom of the outer vessel of the cryostat and at the vacuum chamber of the heat exchanger system. Angle valves at their inlet and outlet of the pumps allow for their replacement during operation in case of malfunction. Both pumps are evacuating the same volume and are

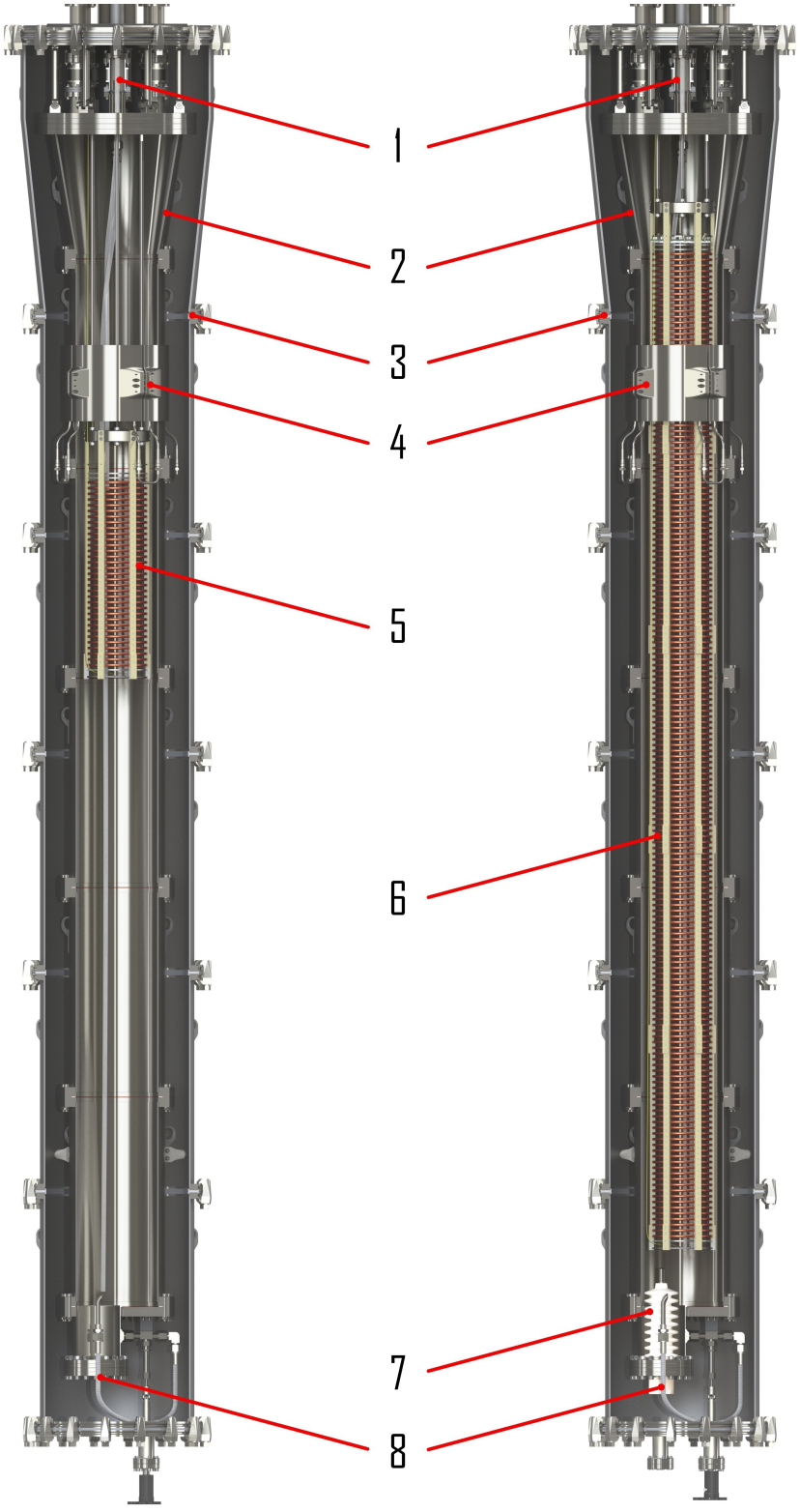

Figure 3.10: The two phases of Xenoscope. On the left, the 0.53 m PM, and on the right, 2.6 m TPC. The cryostat in composed of two nested cylindrical stainless steel vessels suspended from their top flanges. Legend: (1) Top flange; (2) Inner vessel; (3) Outer vessel; (4) Pre-cooler; (5) Purity monitor; (6) Time projection chamber; (7) High-voltage feedthrough; (8) BoX recuperation line.

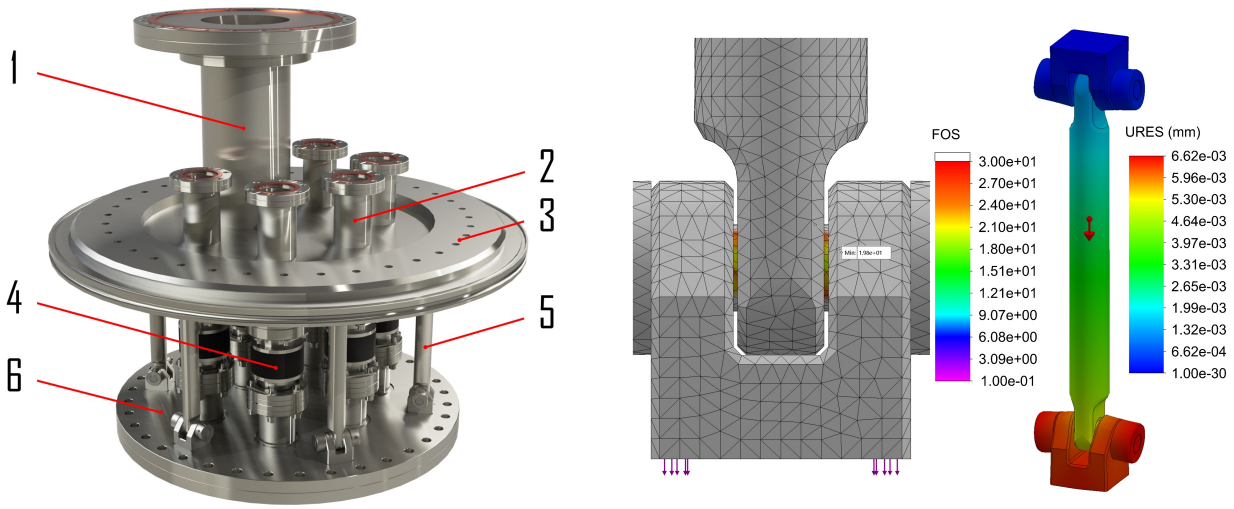

(a) (b)

Figure 3.11: Top flange assembly of the cryostat. **(a)** Legend: (1) Cooling tower feedthrough; (2) Instrumentation feedthroughs; (3) ISO-K-500 flange and welded ring; (4) Axial displacement bellows; (5) Swivel rods; (6) DN350CF flange. **(b)** Mechanical design FEA of the swivel arm. The top is fixed in space and a load of 1 500 N is applied to the base. The maximum expected elongation; on the order of 7 µm; is negligible. Figure 3.11a is adapted from ref. [1].

backed up by a common Pfeiffer Vacuum GmbH HiScroll® 12 roughing/backing pump [281], used to produce the pre-vacuum necessary to the start-up of the turbo pumps. The vacuum system can also be used to evacuate the inner vessel prior to xenon filling by using the roughing/backing pump with the top level HiPace® 80 turbomolecular pump. Pfeiffer Vacuum GmbH HiCube™ mobile pumping stations, each with a turbomolecular and a backing pump, can be installed at various locations around the experiment. In particular, the purification panel features two vacuum ports (purification path and cold trap, see section 3.3), and a second vacuum port is available near the heat exchanger enclosure. These extra ports can be used to speed up the initial pump down of the facility.

Superinsulation is required in order to minimise the heat load on the cold sections of the detector: the inner vessel of the cryostat (figure 3.12a), the cooling tower, the heat exchanger assembly, and tubing carrying LXe/GXe between these sections. Vacuum does not shield the inner vessel from thermal radiation, emitted from every surface with a temperature above absolute zero [282]. Therefore, every cryogenic component of the facility is insulated with a multi-layer insulation (MLI). The MLI, seen in figure 3.12b, was designed and produced by RUAG Space GmbH [283]. It is composed of three blankets of 10 layers of 12 µm-thick polyester sheets, aluminised at 400Å on both sides. The layers are perforated for use in vacuum with an open area of $0.05-0.1\,\%$. Each layer is separated by a layer of non-woven polyester spacer at $14-15\,\mathrm{g/m^2}$. With this configuration, the MLI allows for a maximum heat transfer of $0.6\,\mathrm{W/m^2}$. Tubing and hoses were insulated with 10 to 20 layers, depending on their location and their expected heat loads. Since the cryostat will be accessed multiple times during the lifetime of the facility, it was decided that the superinsulation of the cryostat would be assembled with stitched Velcro strips. The rest of the MLI is installed with low infrared emittance, low outgassing, COOLCAT B-R50 adhesive tape [284], indicated for use both in vacuum and in cryogenic assemblies.

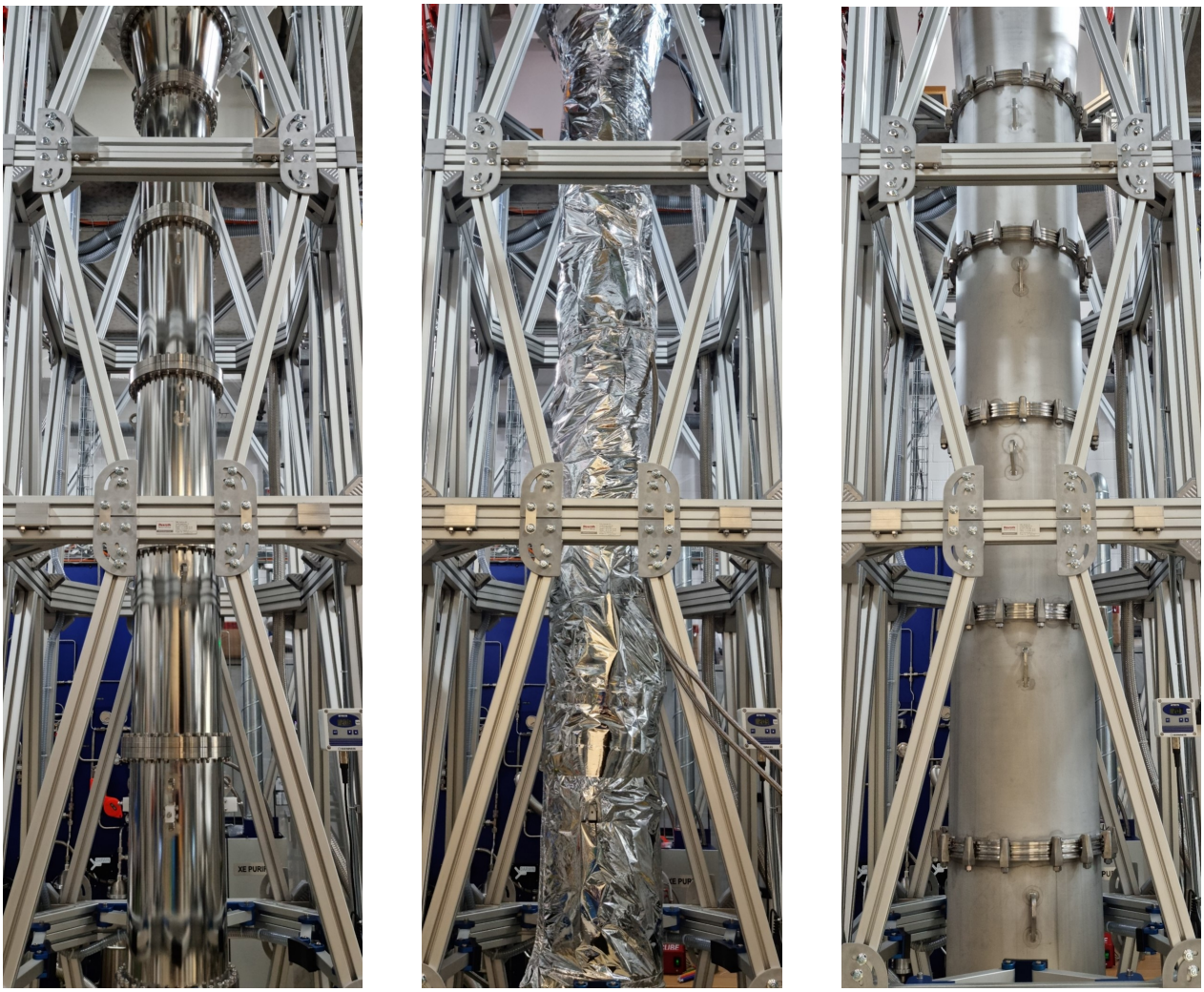

(a) (b) (c)

Figure 3.12: Cryostat of Xenoscope. **(a)** Inner vessel (DN250CF). **(b)** Multi-Layer Insulation (MLI). **(c)** Outer vessel (ISO-K-400).

3.4.3 Cooling Tower

The cooling tower subsystem, seen mounted on top of the top flange in figure 3.13a, provides the cooling power required for xenon condensation in the cryostat and its temperature regulation. An Iwatani [285] coaxial pulse tube refrigerator (PTR), model PC-150, provides a constant cooling power to the system. The geometry of this type of PTR puts the cold surface at the bottom plate, which is placed in a vacuum vessel for better thermal decoupling with its environment. The PTR is coupled to an OFHC copper cold head with a copper plate. A 44 Ω heater unit composed of two resistive strips mounted to a cylindrical copper cup attached between the PTR and the cold head allows for precise temperature control of the system with a maximum heating power of (209.7 ± 0.1) W. A total of four PT100 resistor temperature detectors (RTDs), each read out in 4-wire mode, are installed inside cavities in the cold head for temperature monitoring. The heater and the RTDs are connected to a DN40CF vacuum signal feedthrough installed on the vacuum enclosure. A Cryo-con Model 24C PID controller [286] keeps the temperature of the cold head stable by continuously biassing an external power supply, limited to 220 W, which powers the

heating strips. Only one RTD is used for temperature control, while the other three are installed for redundancy, as accessing the cooling tower for maintenance would be a major undertaking. Apiezon® N Grease [287], a thermal paste conceived for use in cryogenic vacuum systems, is applied between every part in the thermal conduction chain. The monolithic cold head was machined out of an OFHC copper cylinder. Slits are milled into the cold head to increase the contact area between the copper and GXe. The total contact area increase is $\sim$ 59, from 1 021 mm^2 with no slits, to 60 015 mm^2. The condensed xenon drips down from the hemispherical bottom in a single trickle of LXe, as seen in figure 3.14. The hemispherical shape of the cold head maximises the time condensed xenon spends in contact with the copper, increasing the cooling efficiency.

The cooling chamber has two opposing DN40CF ports. Seen in detail in figure 3.13b, the left port is connected to the heat exchanger system, while the right port is closed with a 24 mm sapphire viewport produced by Hositrad Vacuum Technology [288], rated to 11 bar overpressure. It is aligned with a DN63CF viewport on the vacuum vessel, allowing for the direct observation of the cold head. Figure 3.14 shows the cold head in three different conditions. Figure 3.14a shows the cold head during filling of GXe from the storage array (section 3.3.3) or from BoX (section 3.3.4). Xenon condenses on the cold head and drips from the knife-edge at its bottom tip into the funnel. In figure 3.14b, LXe is seen coming out of the supply line at the back, as it is liquefied in the heat exchanger system and in the umbilical. Finally, in figure 3.14c, solid xenon can be seen at the top

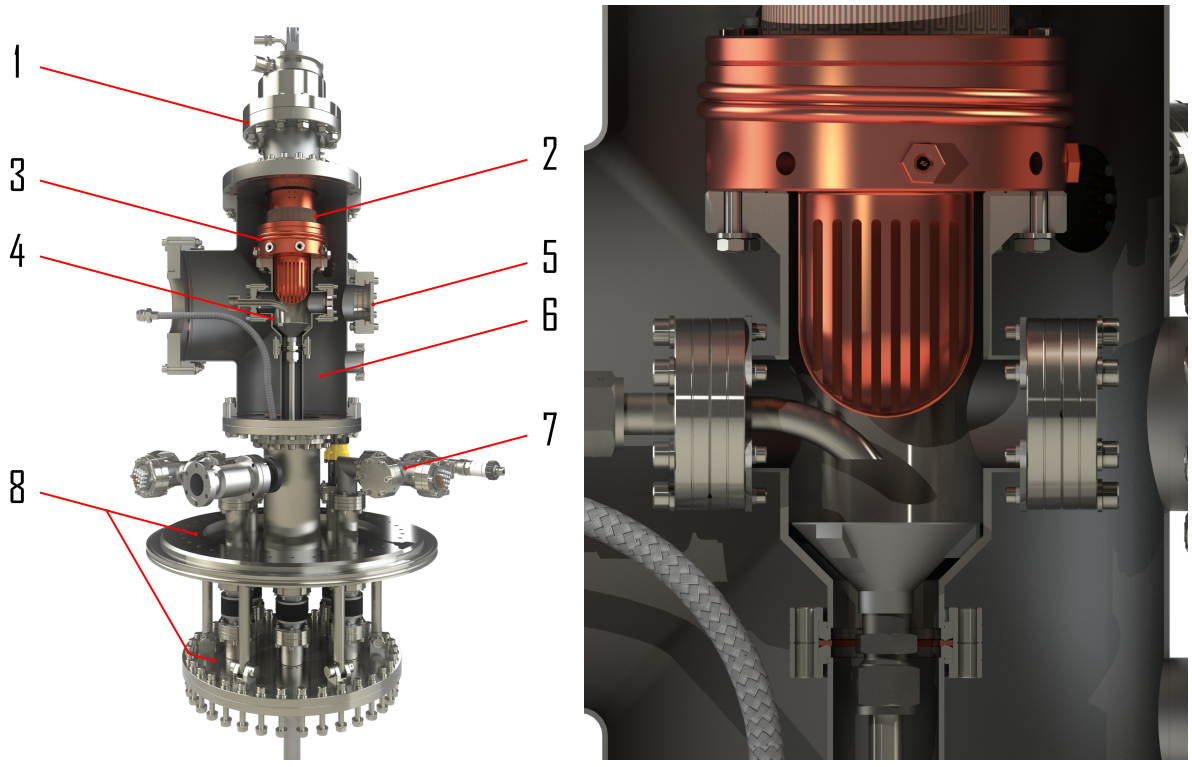

(a) (b)

Figure 3.13: Cross-sectional views of the cooling tower. **(a)** Cooling tower installed on the top flange. Legend: (1) PTR; (2) Heater; (3) Cold head; (4) Cooling chamber; (5) Viewport; (6) Vacuum chamber; (7) Feedthroughs (6×); (8) Top flange. **(b)** Close-up view of the cooling chamber. Xenon enters the chamber from the heat exchanger supply line (on the left). GXe introduced in the cooling chamber during filling is liquefied on the cold head and drops down in a funnel which carries the liquefied gas to the bottom of the cryostat in a 1/2" perfluoroalkoxy alkane (PFA) tube. During normal operations, xenon coming from the heat exchanger system exits the tube in a liquid state, and drops down directly in the funnel.

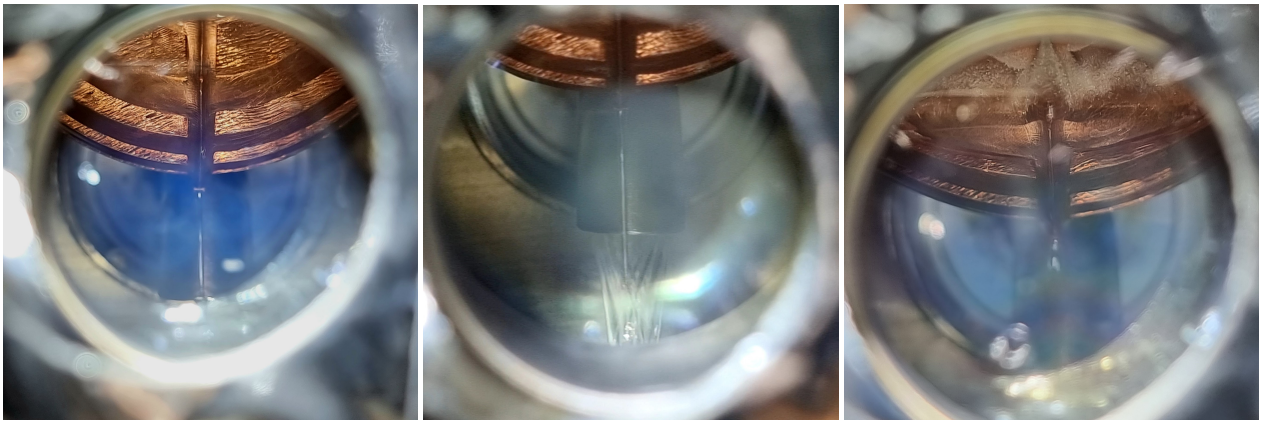

(a) (b) (c)

Figure 3.14: Cold head viewed through the viewport. **(a)** Cold head during the filling of xenon into the cryostat. GXe is introduced in the cooling chamber and is liquefied on the cold head. **(b)** Cold head while recirculating. LXe is seen at the back exiting the supply line coming from the heat exchanger system. **(c)** Cold head with a temperature set-point of 164 K. Frozen xenon, which drastically reduces the cooling power of the system, can be observed at the top of the cold head.

of the cold head held at a temperature of 164 K. The solid xenon acts as insulation on the cold head, drastically reducing the cooling power of the chamber. Over time, this results in an inability to keep the temperature of the LXe in the inner vessel stable, which slowly increases the pressure in the inner vessel. Increasing the temperature of the cold head melts the solid xenon and restores the cooling power of the chamber.

With the exception of the two viewports, which were simply wiped with ethanol absolute to avoid the weakening of their vacuum seals, all the components of the cooling tower were cleaned in an ultrasonic bath to best remove oils and metal dust that could have been left from the machining processes. The complete cleaning procedure differs for different part materials. Non-copper parts were ultrasonically cleaned with distilled water and Elma EC 10 acidic soap [289] for at least 10 minutes. They were then rinsed in distilled water, followed by 10 minutes in the ultrasonic bath in ethanol absolute. The parts were finally air dried and bagged until assembly, with special attention paid to blind screw holes to avoid corrosion. Copper parts were cleaned with the same protocol, followed by 10 minutes in the ultrasonic bath in a 2 wt/wt% citric acid solution to passivate their surfaces [290]. The parts were finally rinsed in a final ethanol absolute bath and bagged until assembly.

Since the cold head and the cooling chamber body are composed of different materials (OFHC copper and stainless steel respectively), the cooling chamber is sealed with a indium seal. Indium cold-welds to many different materials when compressed and is widely used in cryogenic applications. This material is also well suited for sealing parts that contract differently when cooled down. Indium seals are versatile, being used in a large temperature range, in regular and irregular geometries, where typical gasket material is impractical or unusable. The application method chosen for the cooling chamber is the "ring and groove method", explained in [291]. The seal of the cooling chamber is made with a 1.0 mm $\varnothing$ circular cross-section indium wire of 99.99 % purity (Sigma Aldrich 357073-5.6G [292]). The two flanges were thoroughly cleaned with acetone to remove any organic substance, which can degrade the bonding of indium to surfaces. As seen in figure 3.15, the wire is carefully pressed in a 1.0 mm wide $\times$ 0.62 mm deep groove machined in the stainless steel body of the cooling chamber. The ends of the wire are twisted together and cut to form a continuous seal. The cross-sectional area of the groove is 80% that of the wire. The cold head is

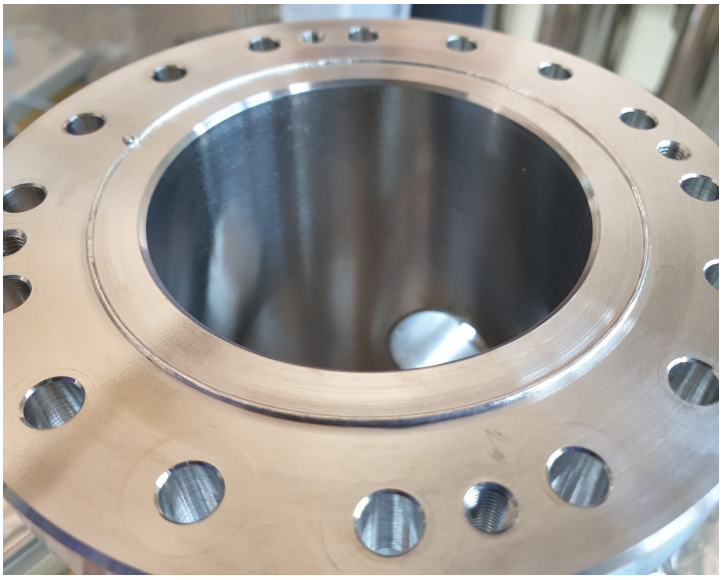

Figure 3.15: Indium seal of the cooling chamber. The indium wire is pressed into a square shaped groove. As seen in the top-left corner, the ends of the wire are twisted and cut to close the ring. The copper cold head sits directly on top of the cooling chamber.

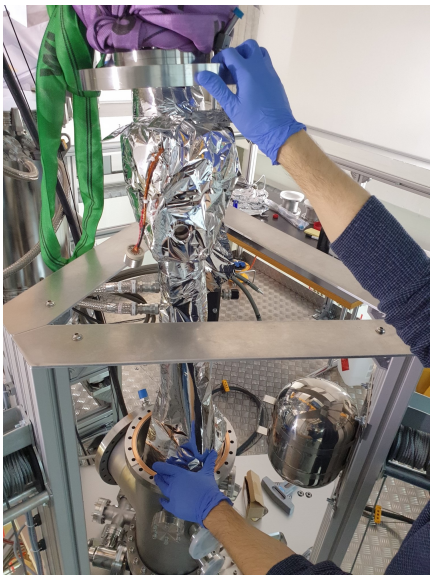

Figure 3.16: Installation of the cooling tower. The tower is lowered with a crane into the vacuum chamber on top of the facility. The whole assembly is covered with a MLI.

attached between the main body of the cooling chamber and the PTR adapter plate with sixteen M6 bolts. As even pressure is applied to the indium wire in a star pattern, it deforms and is extruded into the square shape of the groove. Once the volume of the groove is completely filled, the pressure applied to the indium wire increases dramatically, as indium is highly incompressible. The excess material deforms out of the groove and bonds to the two flanges. Once the seal is made, it can be difficult to separate the two bonded parts. To help with the separation of the chamber seal if ever needed, four extra tapped screw holes have been machined in the flange of the cooling chamber body. The pushing action from four screws can evenly undo the indium seal without damaging the flanges.

A stainless steel funnel sits at the bottom of the cooling chamber. A 1/2" PFA tube is attached with a tube fitting and carries the condensed xenon to the bottom of the cryostat. PFA is electrically non-conductive, and would not provoke an electrical breakdown if touching electrically biassed detector parts. The funnel sits on three raised feet, allowing GXe to flow from the inner vessel up to the cooling tower by convection.

The cooling tower is completed by a secondary LN_2 cooling system used in emergency situations, such as a loss of electrical power to the PTR, or insufficient cooling power because of an increased heat load. A vacuum insulated line connected to a Dewar on the ground floor is attached to a 1/4" tube on the outside of the vacuum chamber. A coiled copper tube coupled to the cold head is connected inside the vacuum vessel to two welded 1/4" Swagelok® VCR feedthroughs. Apiezon® N Grease is applied between the coil and the cold head to increase thermal conduction. A relay in the pressure readout electronics is automatically closed if the pressure exceeds 2.3 bar in the inner vessel. A cryogenic solenoid valve is then opened to flush LN_2. The enabling of the emergency cooling momentarily increases the temperature in the cold head instead of lowering it since the GN_2 in the line is warmer (room temperature) than the cold head. We refer to this counter-intuitive behaviour as the "Chernobyl Effect". As the LN_2 line cools down, the emergency cooling line rapidly lowers the temperature of the cold head, which in turn reduces the pressure inside the inner vessel. Once the

pressure falls back below 2.3 bar, the relay is opened, and emergency cooling stops. Assuming the cause of the temperature/pressure change is not yet resolved, this system allows for a modulation of the pressure in the inner vessel around 2.3 bar, preventing the automatic recuperation of GXe (see section 3.3) and giving sufficient time for operators to resolve the issue.

The inner cooling tower assembly was lifted with the bridge crane of the assembly hall. It was then separately vacuum-tested over the course of one week, down to a pressure of $1.0 \cdot 10^{-7}$ mbar. The chamber was dressed into its MLI jacket and was then lowered into its vacuum chamber, as shown in figure 3.16. The bottom of the inner assembly was then attached to the feedthrough connection at the inner vessel top flange, and the remaining vacuum connections were made.

3.4.4 Heat Exchanger Assembly

As LXe-based detectors grow in size, purity requirements of the detection medium become ever so greater. Low levels of impurities have been achieved by using low outgassing materials [293], and by increasing the purification efficiency. Due to the limited cooling power of commercial PTRs, cryogenic detectors have been using heat exchangers to achieve high recirculation flow with very low thermal losses [262, 294, 295].

In the heat exchanger system, LXe is extracted from the inner vessel and evaporated in a first heat exchanger. The second, smaller heat exchanger brings the vaporised gas to room temperature by exchanging the heat of room temperature gas coming back from the purification system. This incoming gas is therefore pre-cooled in the small heat exchanger and is liquefied in the larger one. The LXe is then brought back to the inner vessel.

The heat exchanger assembly of Xenoscope, shown schematically in figure 3.17a and installed

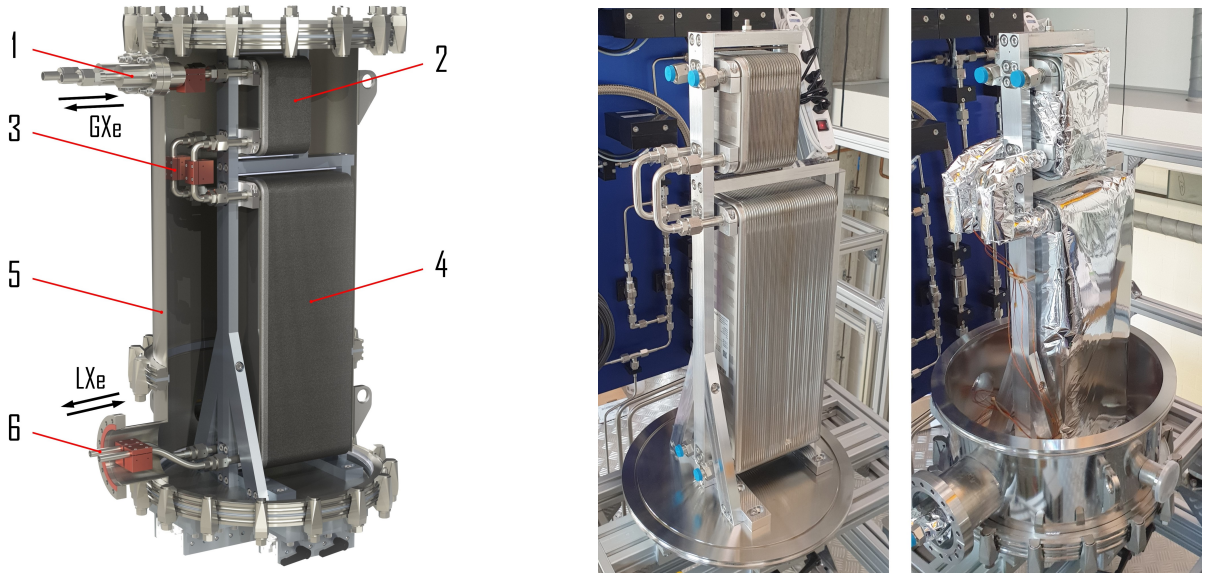

(a) (b)

Figure 3.17: Heat exchanger system of Xenoscope. **(a)** Schematic view of the heat exchanger system in its vacuum chamber. Legend: (1) Gas inlet/outlet; (2) Pre-cooler/post-heater; (3) Temperature sensors (6×); (4) Vaporiser/condenser; (5) Vacuum chamber; (6) Liquid inlet/outlet. **(b)** The heat exchanger is installed on an aluminium frame, inside the vacuum vessel. **(c)** Heat exchanger assembly covered by a MLI. Figure 3.17a is adapted from ref. [1].

on Xenoscope in figure 3.17b, is composed of two brazed stainless steel heat exchangers produced by Kelvion Holding GmbH [296], connected in series, and housed in a vacuum insulation vessel. The large heat exchanger has a total heat exchange area of 4.6 m^2 (Model GVH 500H-80) while the smaller heat exchanger is 0.66 m^2 (Model GVH 300H-40). In this configuration, the system has a calculated heat exchange power of 1.5 kW, enough to accommodate for recirculation flows above the targeted 100 slpm. Six PT100 RTDs used for monitoring the temperature of the xenon are mounted in copper blocks clamped at the inlets, outlets, and intermediate connections between the two heat exchangers. The heat exchanger system is described in more detail in ref. [2].

3.4.5 Umbilical Section

The umbilical section links the cooling tower and the heat exchanger assembly, and provides freedom of axial movement between the heat exchanger assembly and the cryostat assembly, required from the change in height of the cryostat as a function of its total weight. For example, the addition of 400 kg of LXe compresses the three springs of the levelling legs by up to 13 mm, as discussed in section 3.2.2. As seen in figure 3.18a, the umbilical section is composed of a flexible DN100CF vacuum conduit and two braided stainless steel flexible hoses, both wrapped in a MLI. The first is the return line, where LXe is sucked out of the inner vessel from the top of the liquid and directed to the heat exchanger, and the second is the supply line, where xenon coming back from the gas system and heat exchanger is directed to the cooling tower. A polyoxymethylene (POM) spacer is used to prevent the direct contact of the cold hoses with the walls of the vacuum vessel. The hoses are wrapped in superinsulation (see section 3.4.2).

The heat exchanger assembly is installed on sliding blocks and can freely move horizontally as needed during the filling or recuperation of xenon. A constraint on that freedom of movement is the constant length of the metal hose inside the assembly. Since the umbilical is a vacuum vessel, and neither the cryostat assembly nor the heat exchanger assembly are completely fixed, a force of about 800 N originating from the pressure difference between the inside vacuum and the atmospheric pressure compresses the bellows in the absence of a rigid structure. To prevent this compression, the cord length is kept constant by a set of two aluminium swivel arms whose length

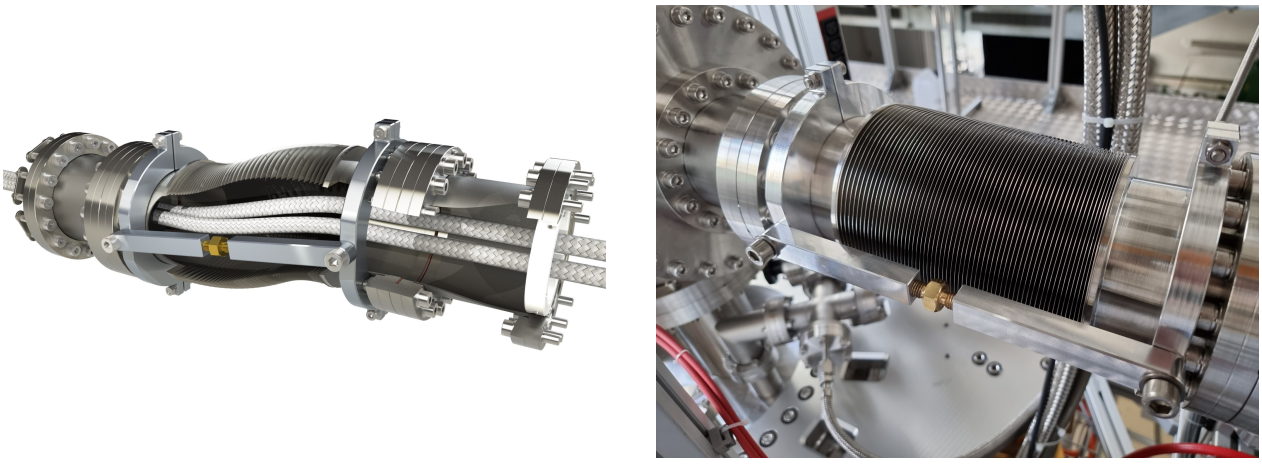

(a) (b)

Figure 3.18: Umbilical section. **(a)** Cross sectional view. Two stainless steel flexible hoses carry LXe to and from the cryostat. Swivel arms attached to the outside of the bellows prevent its contraction due to vacuum applied inside. **(b)** Umbilical section installed between the heat exchanger and the cooling tower.

can be adjusted with a double-ended left-right handed brass screw. The assembly is mounted to the rigid section of the bellows with two ring clamps. The umbilical section can be seen installed on the facility in figure 3.18b.

3.4.6 Pre-Cooler

The inner vessel requires an initial cooling period prior to the filling of LXe. Shown in figure 3.19a is a pre-cooling system made of four curved stainless steel coolers. This component was built to reduce the cool-down time and speed up the filling process by increasing the cooling power available to liquefy the xenon. The coolers are made of two machined stainless steel layers each, welded at their perimeter. Channels are machined on the plates to help distribute the LN_2 over the whole surface. Shown in figure 3.19b are four segments connected in series and attached to one another around the highest straight section of the inner vessel, making direct contact with the cryostat wall. The assembly is compressed on the outside of the inner vessel with four bolts per junction, permitting the concentric compression of the cooler to ensure good thermal contact.

Apiezon® N Grease is uniformly applied between the pre-cooler plates and the inner vessel of the cryostat to maximise the heat transfer, avoiding the trapping of air pockets that could produce virtual leaks [297]. Two 1/4 " braided stainless steel hoses connect the coolers to a DN40CF liquid feedthrough located at the bottom of the outer vessel, where they exit the vacuum. LN_2 is flushed into the coolers from a self-pressurising storage Dewar. The LN_2 boils-off in the cooling plates and exits in gas form by the outlet line, terminated by a brass phase separator.

The maximum cooling power was calculated from the maximum achievable fill speed during the operation of the PM (see section 4.2.3). As described in section 3.6.1, GXe is recirculated to and from the cryostat at $25-40$ slpm during filling. The filling speed is measured as:

$$\dot{m}_{\text{fill}} = \dot{m}_{\text{FM}} - \dot{m}_{\text{FC}}\,, \tag{3.1}$$

where $\dot{m}_{\text{FM}}$ and $\dot{m}_{\text{FC}}$ are the flows measured by the flow meter and the flow controller respectively. The uncertainty on the flows are taken as 1 % of the full scale of the flow meters (i.e. 1 slpm), in

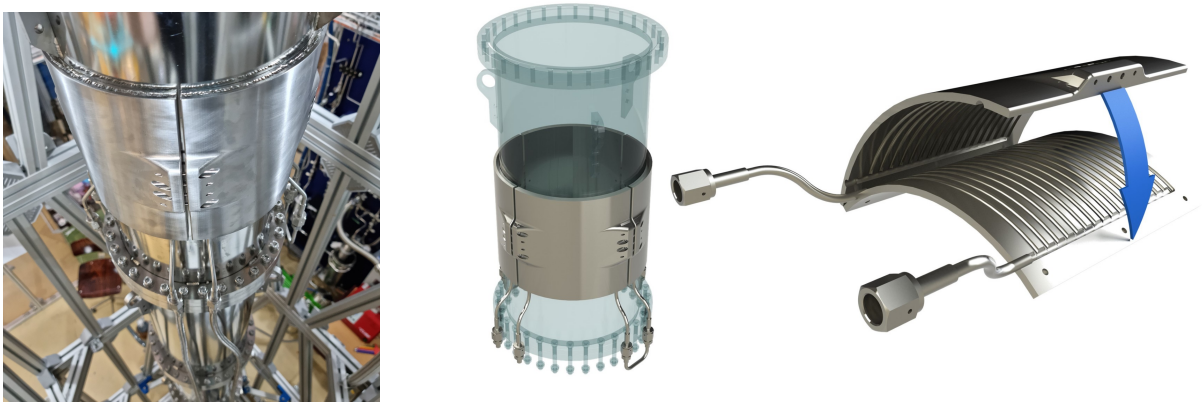

(a) (b)

Figure 3.19: Pre-cooler assembly. **(a)** Pre-cooler installed at the top of the inner vessel. **(b)** Four pre-cooler plates attached and pressed against the side of an inner vessel section (pale blue). Inside view of a pre-cooling plate. Channels are machined inside the stainless-steel plates to distribute the LN_2 homogeneously. Adapted from ref. [1].

accordance with the reported accuracy of the devices [273]. With only the cooling power of the PTR, using no heating, the filling speed measured at thermal equilibrium was:

$$\begin{aligned}\dot{m}_{\text{fill}_{\text{PTR}}} &= ((57.4 \pm 1.0) - (40.2 \pm 1.0))\,\text{slpm} \\ &= (17.2 \pm 1.5)\,\text{slpm}\,.\end{aligned} \tag{3.2}$$

With the pre-cooler enabled, the measured mass-flow was:

$$\begin{aligned}\dot{m}_{\text{fill}_{\text{PTR+PC}}} &= ((96.1 \pm 1.0) - (25.2 \pm 1.0))\,\text{slpm} \\ &= (70.9 \pm 1.5)\,\text{slpm}\,.\end{aligned} \tag{3.3}$$

We can therefore deduce the total filling speed of the pre-cooler:

$$\begin{aligned}\dot{m}_{\text{fill}_{\text{PC}}} &= \dot{m}_{\text{fill}_{\text{PTR+PC}}} - \dot{m}_{\text{fill}_{\text{PTR}}} \\ &= ((70.9 \pm 1.5) - (17.2 \pm 1.5))\,\text{slpm} \\ &= (53.7 \pm 2.2)\,\text{slpm}\,.\end{aligned} \tag{3.4}$$

Assuming Normal Temperature and Pressure (NTP) conditions, the cooling power of the pre-cooler at full LN_2 flow is:

$$\begin{aligned}P_{\text{PC}} &= \Delta\dot{m}_{\text{fill}_{\text{PC}}} \cdot \rho_{\text{GXe}} \cdot (C_{\text{p}} \cdot \Delta T + \Delta H_{\text{vap}}) \\ &= ((53.7 \pm 2.2))\,\frac{\text{l}}{\text{min}} \cdot 5.4885\ \frac{\text{g}}{\text{l}} \cdot \left(0.16067 \frac{\text{J}}{\text{g} \cdot \text{K}} \cdot 119\ \text{K} + 95.587\ \frac{\text{J}}{\text{g}}\right) \cdot \frac{1\ \text{min}}{60\ \text{s}} \\ &= (0.57 \pm 0.03)\,\text{kW}\,.\end{aligned} \tag{3.5}$$

ρ_{GXe} is the density of GXe at 1 bar, C_{p} is the heat capacity of GXe, ΔT is the temperature difference between room temperature and LXe temperature, and ΔH_{vap} is its latent heat of vaporisation of xenon [193, 196].

The pre-cooler is also used during the gravity-assisted recuperation, detailed in section 3.3.4. The pre-cooler helps to re-liquefy the xenon boiled-off in BoX during the transfer and lowers the temperature of the xenon in the cryostat, increasing the efficiency of the liquid transfer.

3.5 Slow Control System

The Xenoscope facility is monitored and controlled with a house-made SC system designed with a micro-service architecture [298]. It combines well-established automation software with orchestration, monitoring, and alarming tools usually used in the context of large-scale web services. Micro-controllers are responsible for collecting sensor data and controlling instruments. An industrial Programmable Logic Controller (PLC), a Simatic S7-1500 series from Siemens [299], and one Raspberry Pi [300] collect data and expose them to the rest of the system through open network protocols, namely Open Platform Communications (OPC) [301] and HTTP. Data collected from each sensor is ingested into Prometheus [302], a monitoring and alarming time-series database. Grafana [303], a visualisation platform, is used to visualise the acquired data on user-configurable dashboards. Well constructed dashboards can help quickly identify abnormal behaviours of the facility in real time. An example of an end-user graphical interface is shown in figure 3.20. Time series can also be used to easily create end-user customisable alarming rules. An alarming system, part of a set of tools offered by Prometheus, continuously processes the collected data, triggering

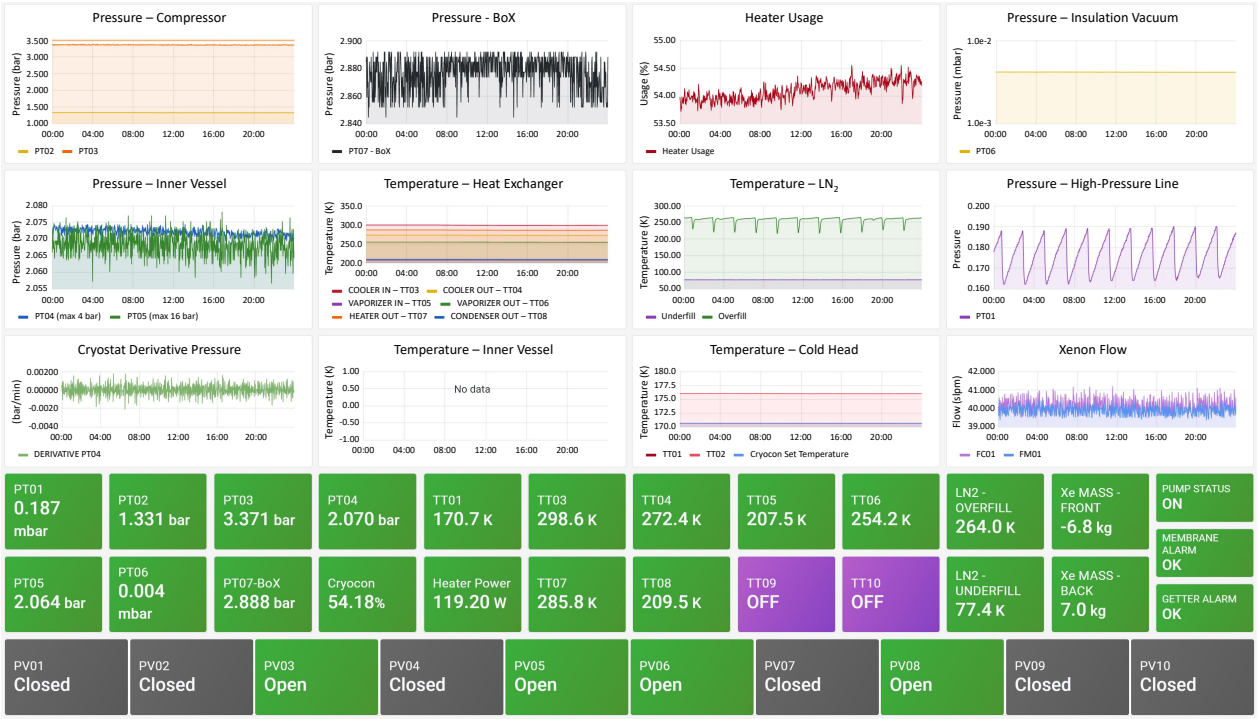

Figure 3.20: Example of a Slow Control dashboard. The highly customisable dashboards can graphically display the vitals of the whole facility, or a focused view of a given subsystem, rendering the visualisation of metrics very intuitive. Dashboards are also used to set and manage alarms.

alarms based on the configured rules. Grafana can be used to visually set the thresholds and rules with a graphical user interface, which are then used to trigger alarm notifications with Prometheus. Users are notified via e-mail and SMS by a third-party notification system.

All used software is open-source, apart from the proprietary PLC programming tools. For Xenoscope, the yearly availability target is 99.99 %, which corresponds to about 50 min downtime per year, including maintenance. The key to achieve such high availability is redundancy. The system is thus designed with redundant hardware and network connections, while the micro-service architecture guarantees that a failure of one service does not affect the others.

Kubernetes is used as the orchestration software for micro-services. It maintains the good health of the system by restarting services in case they become unresponsive. The SC follows a master-worker type of architecture with three machines: one master and two workers. The master node continuously checks the availability of each service and each worker node. In case one of the workers becomes unavailable, the load is automatically transferred to the remaining one. In case the master becomes unavailable, there is no effect on the provided service. The networking configuration of the system is shown in figure 3.21.

The dual-WAN fail-over router provides network redundancy. The default network service is provided by the University. In case of failure, the router automatically switches to a Long-Term Evolution (LTE) network service. In this last condition, the system is not directly reachable, but will continue to send alarm notifications. Furthermore, an external server continuously receives "heartbeats" from the system, alerting the users in the unlikely event of it being incapable of sending alert notifications.

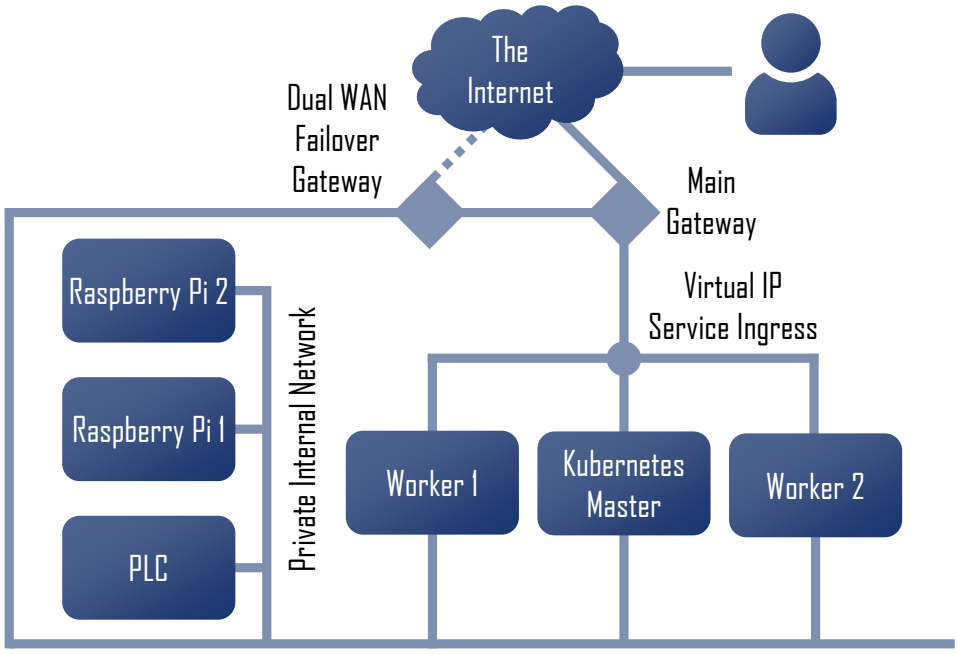

Figure 3.21: Networking configuration of the monitoring and control system. Three servers are operated in a Kubernetes master-worker configuration; they are connected to the internet via the main University gateway and a secondary dual Wide Area Network (WAN) fail-over router. The micro-controllers are instead connected only to an internal private network and not accessible from the internet. Figure adapted from ref. [1].

3.6 Operational Procedures

The gas handling procedures are multi-step processes that require caution. Xenon gas is a rare, non-renewable resource, and cautious handling procedures should be followed to minimise losses. Furthermore, with the improvement of the *free electron lifetime* in mind (see section 4.2.2), needed for multi-tonne scale xenon detectors, electronegative contaminants should be mixed as little as possible with the xenon. We detail below the two main operations performed on Xenoscope: the filling of the cryostat (section 3.6.1) and the recuperation of xenon (section 3.6.2).

3.6.1 Filling Procedure

The filling of the cryostat is an important milestone in the operation of any LXe experiment, following the installation of the instrumentation and the closing of the cryostat vessels. The facility must be prepared several days to several weeks in advance in prevision for the fill. Several important steps must therefore be identified.

First, the air in both cryostat vessels and in the gas handling system is evacuated with the roughing/backing pump. The systems are outgassed for several days by pumping them with the turbomolecular pumps, achieving vacuum levels of $< 10^{-4}$ mbar. Optional baking of the cryostat inner vessel can be performed using flexible heating strips, though care should be taken in doing so to not excessively heat plastic elements of the detector (such as PTFE, polyether ether ketone (PEEK), PAI) and electronic components, such as photosensors.

Following the outgassing phase, the outer vessel is isolated from the rest of the gas system, and will, from then on, act as the thermal vacuum insulation. GXe is added from BoX or from the GCSA up to 2 bar everywhere in the gas handling system and in the inner vessel. The gas is recirculated at room temperature and purified with the getter for a minimum of 24 hours to scrub electronegative contaminants from surfaces. Finally, the PTR is switched on and the temperature of the cold head is lowered to 174 K. The inner vessel cools down as liquefied xenon makes contact with the inner bottom flange. Without constant recirculation, the lack of natural convection in the inner vessel due to its large size creates a large temperature gradient along the cryostat. The whole inner vessel is then cooled down with the help of the convection produced by the recirculation of the GXe through the recirculation loop. The pre-cooler can also be used to speed up the initial cooldown. GXe is continuously recirculated from the beginning of the filling procedure to ensure sufficient convection is maintained, without which filling would become impossible after $\sim$ 20 kg, as witnessed during the commissioning run (section 4.1).

Figure 3.22 shows the P&ID describing the filling paths. The path used to fill GXe from the GCSA is traced in green, while the path used to fill from BoX is traced in blue. During filling, the HPMVs are shut to protect low pressure regions of the gas system, with the exception of HPMV-05

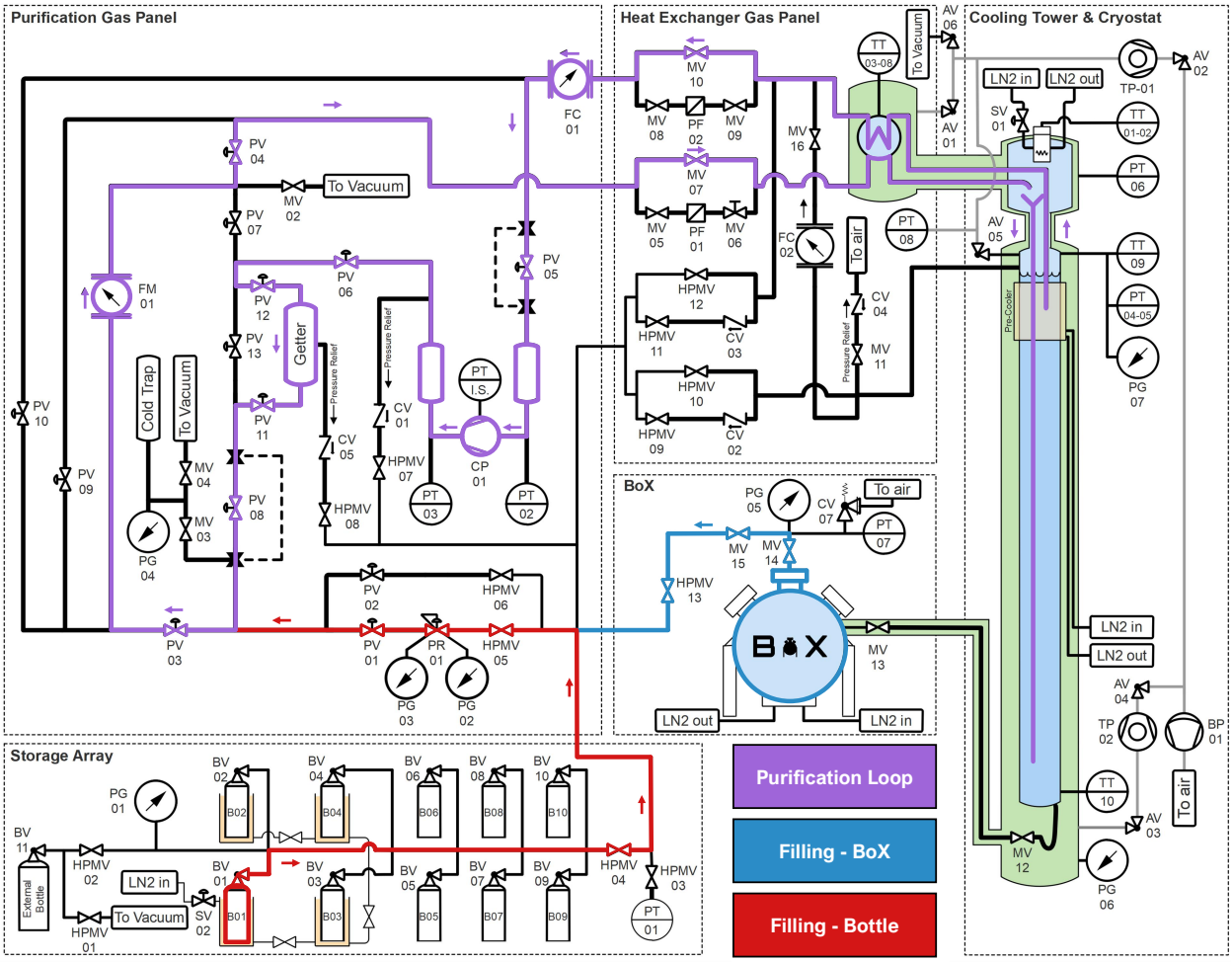

Figure 3.22: P&ID of the filling procedure. High-pressure GXe is taken from the GCSA (red path) or BoX (blue path). The pressure regulator (PR-01) is used to add GXe to the recirculation loop (red path). The difference in flow between the flow controller (FC-01) and the flow meter (FM-01) is used as a metric of the added xenon.

located immediately upstream of the pressure regulator (PR-01). The pressure regulator is used to add GXe to the recirculation loop. At high fill rates with large pressure differences, the pressure drop in the pressure regulator due to the expansion of the gas cools it down significantly and can lead to the freezing of the mechanism of the pressure regulator. To prevent this, a PID -controlled, 100 W heating cartridge is installed in a copper block coupled to the back of the pressure regulator. A PT100 RTD installed in the block is used to adjust the heat load and control the temperature of the heating block between 25 °C and 70 °C during filling. If the heat load from the heating block is not sufficient (e.g. at high filling flow), a heat gun can be used to prevent the freezing of the pressure regulator.

Since the GXe is added after the flow controller (FC-01), the difference in flow between the flow controller and the flow meter (FM-01) is a measure of the fill rate, normalised to atmospheric pressure and a temperature of 0 °C. During filling, the liquid level inside the inner vessel is monitored with PT100 RTDs located at various heights. When the liquid reaches a sensor, its temperature immediately drops in a step-like manner, allowing for the discrete estimation of the liquid level. Starting with the TPC phase, two coaxial capacitive level meters will be used to continuously monitor the liquid level.

At the end of filling, the connections to the gas cylinder and BoX are shut off, and the remaining high-pressure gas in the high-pressure line is added to the cryostat. Residual gas in that line is then cryopumped back to B-01, constantly cooled with LN_2, which serves as the emergency recuperation vessel. The HPMVs protecting check valves are finally opened to enable the automatic recuperation system.

3.6.2 Recuperation Procedure

The standard procedure for recuperating the xenon from a full cryostat was established from the experience acquired during the facility commissioning and during Phase 1. The first xenon recuperation was performed with the GCSA only, during the commissioning run, and is described in section 4.1. The subsequent runs (Runs 1, 2 and 3) saw both the use of BoX and of the GCSA. Lessons learned from these runs informed on a standard recuperation scheme, as described below. Figures 3.23 and 3.24 show the recuperation diagrams for the liquid phase recuperation and the gas phase recuperation, respectively.

The gravity-assisted recuperation to BoX, the first step in xenon recuperation, starts with the cooldown of BoX by flushing LN_2 in its cooling block. This initial cooldown lasts only a few hours, until the pressure inside BoX is ~ 0.5 bar. Although the cooldown period can however be extended up to 24 hours to further bring down the temperature in BoX to speed up the gravity-assisted recuperation. In the meantime, the cryogenic line connecting BoX and the cryostat is cooled down by opening MV-12, allowing LXe to fill the line.

The recirculation of GXe in the purification loop is stopped once the cooldown phase is completed. With the PTR cooling still enabled, LXe can be transferred from the cryostat to BoX by opening the cryogenic valve MV-13. Part of the LXe flowing into BoX vaporises upon contact with the wall of the pressure vessel, leading to a gradual pressure increase. The pressures in BoX and in the inner vessel are equalised by opening a path between the two vessels (blue path). The gas flow from BoX to the cryostat is read from the mass flow meter (FM-01). As the recuperation proceeds and BoX cools down further, the gas flow drops exponentially. An alternate path (red path in figure 3.23) can be used to bypass the heat exchanger. The two paths used conjointly increase the total gas flow, but prevent the readout of the total mass flow, as part of the gas then bypasses the mass flow

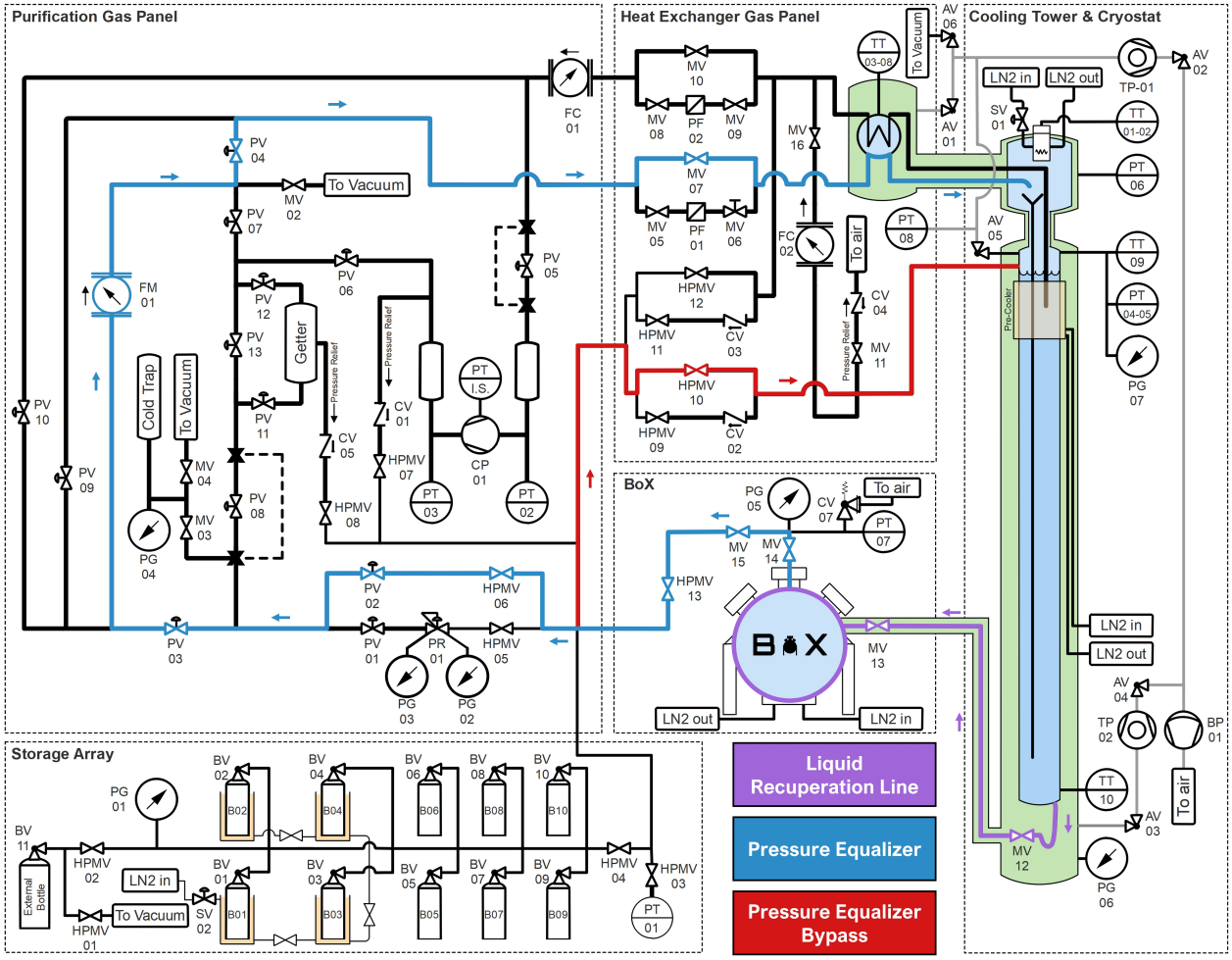

Figure 3.23: P&ID of the gravity-assisted recuperation to BoX. LXe is transferred from the cryostat to BoX (purple path). The gas pressures in the two vessels are equalised through the blue path. The gas flow is read on FM-01. The red path is an alternate route used to increase the overall gas flow, at the cost of not measuring the total gas flow.

meter.

Data from the SC suggest that the use of the pre-cooler during the gravity-assisted recuperation to BoX speeds up the process by reducing the pressure in the inner vessel, which in turn favours gas flow from BoX to the inner vessel, ultimately reducing the pressure in BoX. However, this correlation cannot be confirmed without a precise liquid level measurement. This behaviour will be investigated at a later time with the deployment of the long level meters alongside the 2.6 m TPC. At the end of Run 2, 175 kg of LXe were recuperated in BoX in 9h23m, for an average recuperation speed of 18.65 kg/h. It is of interest to note that the liquid recuperation to BoX is arbitrarily stopped when the gas flow from BoX to the cryostat seems to reach a constant value. The inclusion of a liquid level monitoring system (see section 4.3) will provide valuable data regarding the recuperation speed and efficiency.

The second part of the recuperation is performed by cryopumping gas in the GCSA. The PTR is shut down, and the cold head temperature is raised to $\sim$ 315 K. With BoX isolated and at least one cylinder cooled down with LN_2, the path highlighted in purple in figure 3.24 is opened, and GXe starts flowing from the inner vessel to the GCSA. The recuperation speed is highly dependent on the heat load on the inner vessel, as the evaporation of LXe requires 95.587 kJ/kg [196]. The

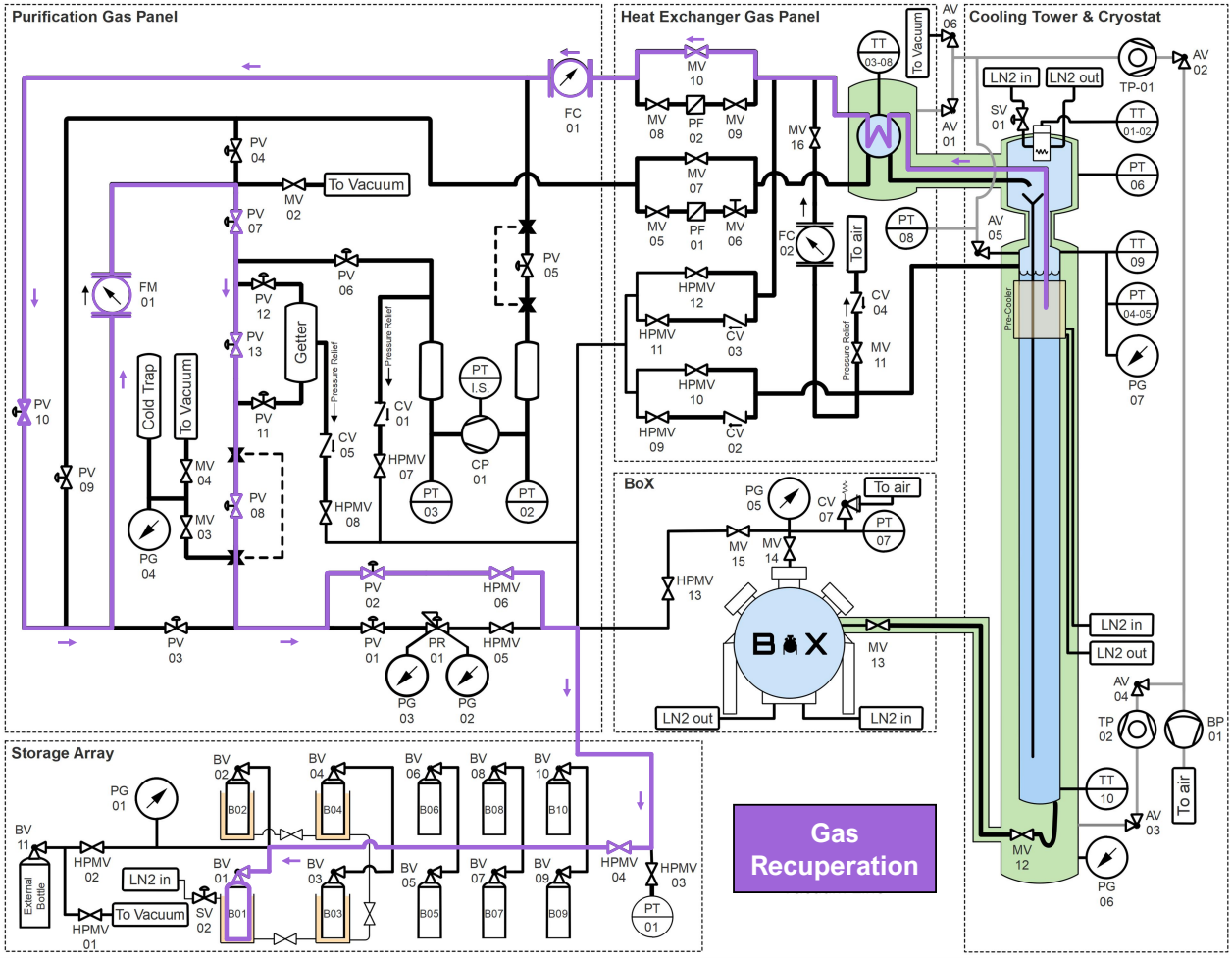

Figure 3.24: P&ID of the recuperation to the GCSA. GXe is cryopumped into one of four gas cylinders installed in Dewars of LN_2. The flow meter FM-01 is used to monitor the recuperation speed.

quick evaporation of LXe can therefore produce a net cooling effect on the inner vessel, lowering the gas pressure, and hence the temperature of the LXe must be continuously monitored and kept above its freezing point (e.g. 161.4 K at 1.5 bar). The recuperation can be sped up by breaking the insulation vacuum with dry nitrogen to enable the convective heat exchange from the outer to the inner vessel, while preventing the introduction of moisture inside the vacuum vessel, which would condense on the outside of the inner vessel and in between the layers of the MLI. Moisture that might have entered the outer vessel can be evacuated within a few days using the backing pump with its ballast valve open after the vessels have fully warmed up.

The recuperation is deemed complete when the pressure in the inner vessel reaches less than 10 mbar. The residual gas can be further recuperated by using a completely empty gas cylinder, or the cold trap located on the purification gas panel. When reaching a residual pressure at the mbar level, one can expect a global xenon loss of only a few grams, a quantity well below the accuracy of the mass scale reading of the GCSA. Every valve in the gas system should then be closed, bringing the system to a neutral state, and xenon in the GCSA should be redistributed equally between all the bottles. This step is optional, but reduces the chances of inadvertently leaving a gas cylinder in an overfilled state.

3.7 Summary

The design and construction of the Xenoscope facility at the University of Zurich has been an endeavour of over three years. In this chapter, we have described the design, testing, production, and assembly of the main systems. The installation of some initial systems, namely the support structure, the cryostat and vacuum systems, the cryogenic systems, the gas handling system, the GCSA and the SC, naturally led to the first GXe and LXe fills and the facility-wide commissioning in early 2021. Followed the operation of various detectors, which are discussed in the next chapter. The first upgrades to the facility, BoX and the cryostat pre-cooler, complemented the initial design of Xenoscope later that same year, significantly increasing the LXe filling and recuperation speeds.

Special attention to every detail in the design, combined with the use of modern CAD software and simulation tools, ensured the harmonious integration of the numerous interlaced systems, the safety of the installations, with an emphasis on the global cleanliness of the facility, and in particular on the xenon-touching surfaces. In the next chapter, we will discuss the operational aspects of Xenoscope.

"Keep your Eyes on the stars, and your feet on the ground"

Theodore Roosevelt, *circa* 1900

These inspirational words were spoken, in many variation, by Theodore Roosevelt. At its core, this quote invites us to keep reaching for higher, aspire for more, while at the same time, to be continuously mindful of the effort and dedication needed to achieve our goals. As we, astroparticle physicists, seek to uncover the nature of dark matter with ultra-low background, underground detectors, we might rephase this saying by "Keep your Eyes on the stars, and your feet underground".

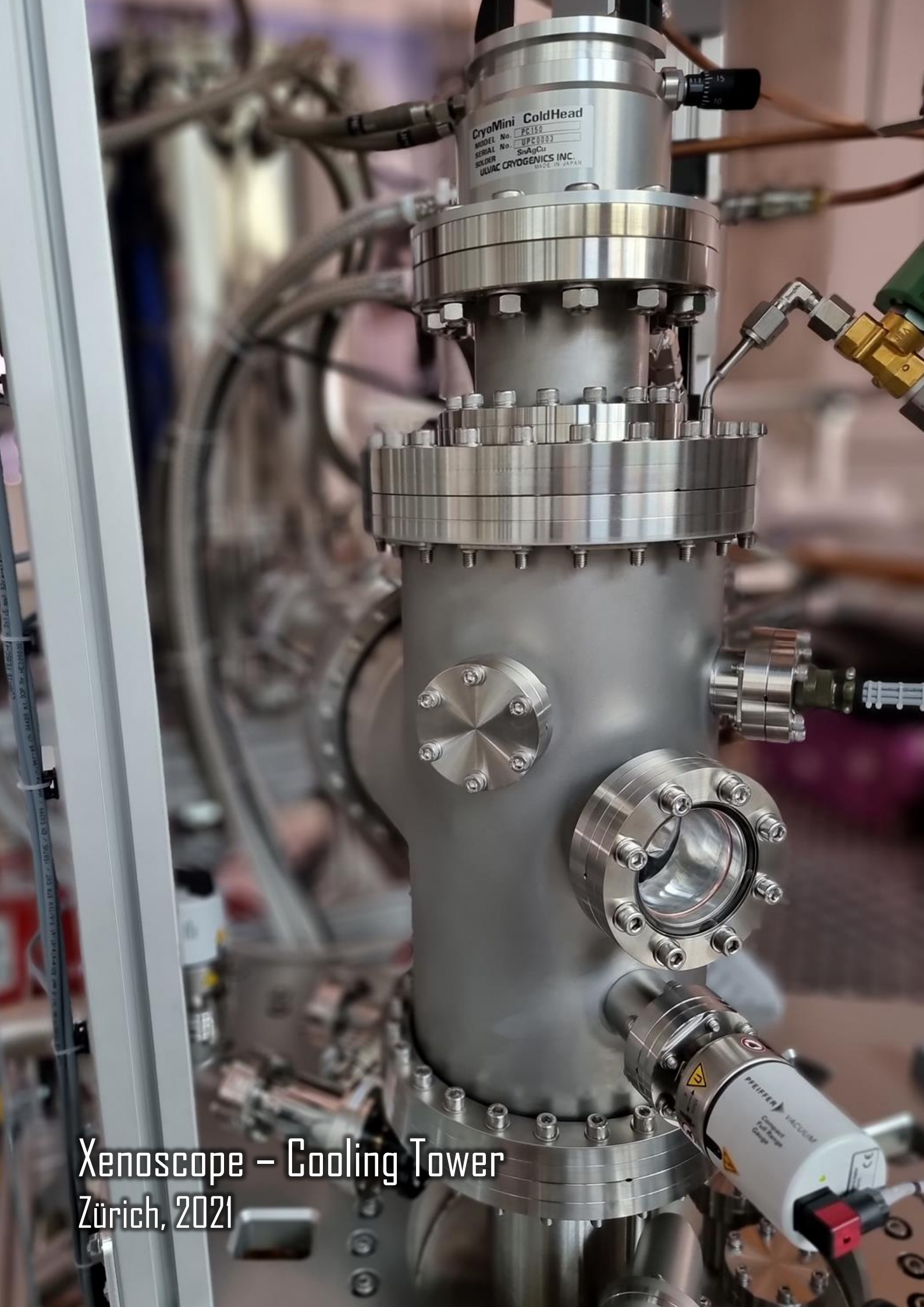

Xenoscope – Cooling Tower

Zürich, 2021

4

Operation of Xenoscope

The scientific programme of Xenoscope foresaw, from the beginning, the use of several detectors, culminating with the demonstration of the drift of electrons over 2.6 m. These detectors were designed alongside the facility and are well described in ref. [259]. The completion of the design and construction phases of the facility, described in the previous chapter, naturally led to its operation.

We summarise in this chapter the operational history of Xenoscope and the design of its different detectors, both existing and future. We first discuss the facility-wide commissioning in section 4.1. We then describe in section 4.2 the design and operational history of the 0.53 m LXe purity monitor (PM) used during Phase 1, and a calculation of the performance of the cryogenic system from recorded data in section 4.2.4. A presentation of the ongoing upgrades to the facility, and the design of the 2.6 m TPC, follows in section 4.3. We conclude with a future exploitation proposal for the Xenoscope facility in section 4.4.

4.1 Facility-Wide Commissioning

In this section, we describe the commissioning phase of the Xenoscope facility, which began in early 2021. This first operational run with LXe followed the completion of the construction phase, which culminated with the installation of the cooling tower and the completion of the SC framework. The built facility is shown in figure 4.1. The goal of this test phase was to verify the functionality, reliability, and safety of all subsystems in order to qualify the facility for Phase 1 of the experiment. In particular, the maximum achievable recirculation flow, which is mostly limited by the pressure rating of the GXe compressor, and the heat exchange efficiency have been evaluated. The results of this testing phase were reported in ref. [1]. A complete and detailed analysis of the heat exchanger system can also be found in ref. [2].

The commissioning run debuted with thorough leak and pressure tests. The entire gas system and inner vessel assembly (only 1/3 of the full inner vessel height, as seen in figure 4.2) were first leak-checked, achieving a maximum leak rate of 10^{-9} mbar$\cdot$l/s per connection. The high- and low-pressure sides of the gas handling system were pressure-tested with gaseous nitrogen at 55 bar and 4.2 bar, respectively. No pressure drops were observed, which qualified the facility for its first xenon

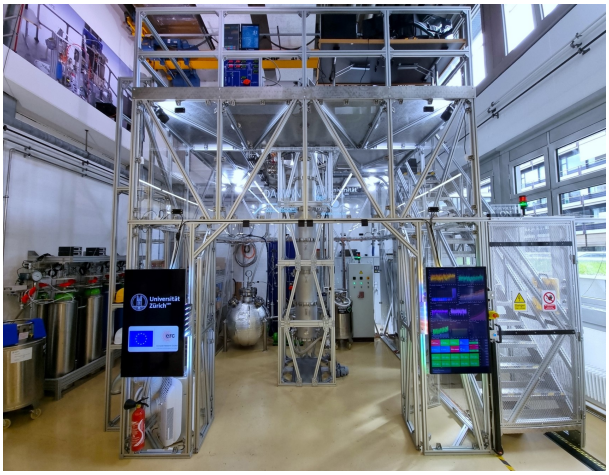

(a)

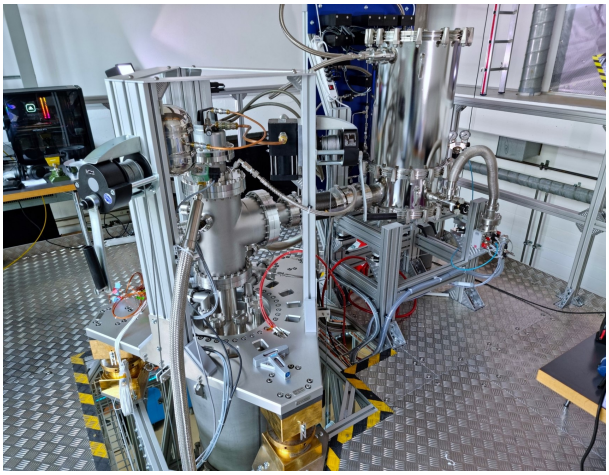

(b)

Figure 4.1: Fully constructed Xenoscope facility. **(a)** Front view of Xenoscope. The GCSA can be seen on the far-left. The cryostat is inside the inner support structure in the center of the picture, with BoX to its left. **(b)** Picture of the top platform, showing the cooling tower on the levelling system on the left, next to the heat exchanger assembly on the right.

fill.

The system was evacuated to a pressure of $\mathcal{O}(10^{-5}\,\mathrm{mbar})$ for several days to outgas both cryostat vessels. Both were isolated prior to filling. Xenon from the storage system was introduced in the purification loop through the pressure reducer located after the GXe compressor, allowing for the fine-tuning of the pressure in the system during the filling procedure. The inner vessel and gas system were at first filled with a total of 1.37 kg of GXe, resulting in a pressure of $\sim$ 2.1 bar. This first preliminary xenon fill was performed to test the filling procedure and confirm the nominal operation of the GXe compressor and getter unit. The GXe was purified for $\sim$ 44 h with the cryostat at room temperature and was then recuperated into the GCSA as a proof of concept. Note that BoX, described in section 3.3.4, was not yet available during the commissioning of the facility. The whole facility was again pumped down following the GXe recuperation to further outgas the gas handling system.

The first LXe fill was started on 25.02.2021, almost 28 months after the start of the design phase. The inner vessel was filled to 2.0 bar, and the PTR was then brought online to start the cooldown period in vacuum, just after the test recuperation. With the reduced size of the inner vessel, the cooldown was completed in only two hours, after which LXe started accumulating at the bottom of the inner vessel.

The LXe filling was performed for approximately four hours at an average of 8.6 slpm (3.0 kg/h), during which we experimented with the cooling system. At some point, the addition of LXe became impossible in this configuration, and the pressure in the inner vessel started to slowly increase uncontrollably. The emergency LN_2 cooling was triggered, demonstrating for the first time the "Chernobyl Effect" previously described in section 3.4. In an attempt to lower the pressure in the inner vessel, we incrementally lowered the temperature setpoint of the cold head down to 155 K, with limited success in reducing the gas pressure. As we slowly continued with the fill, the pressure increase accelerated, and we observed the formation of frozen xenon on the cold head, which was gradually reducing the usable cooling power from the PTR. An image of the frozen cold head can be seen in figure 3.14c. The cold head was progressively warmed back up to 170 K, which increased the heat exchange between the cold head and the xenon without solving the initial issue. This

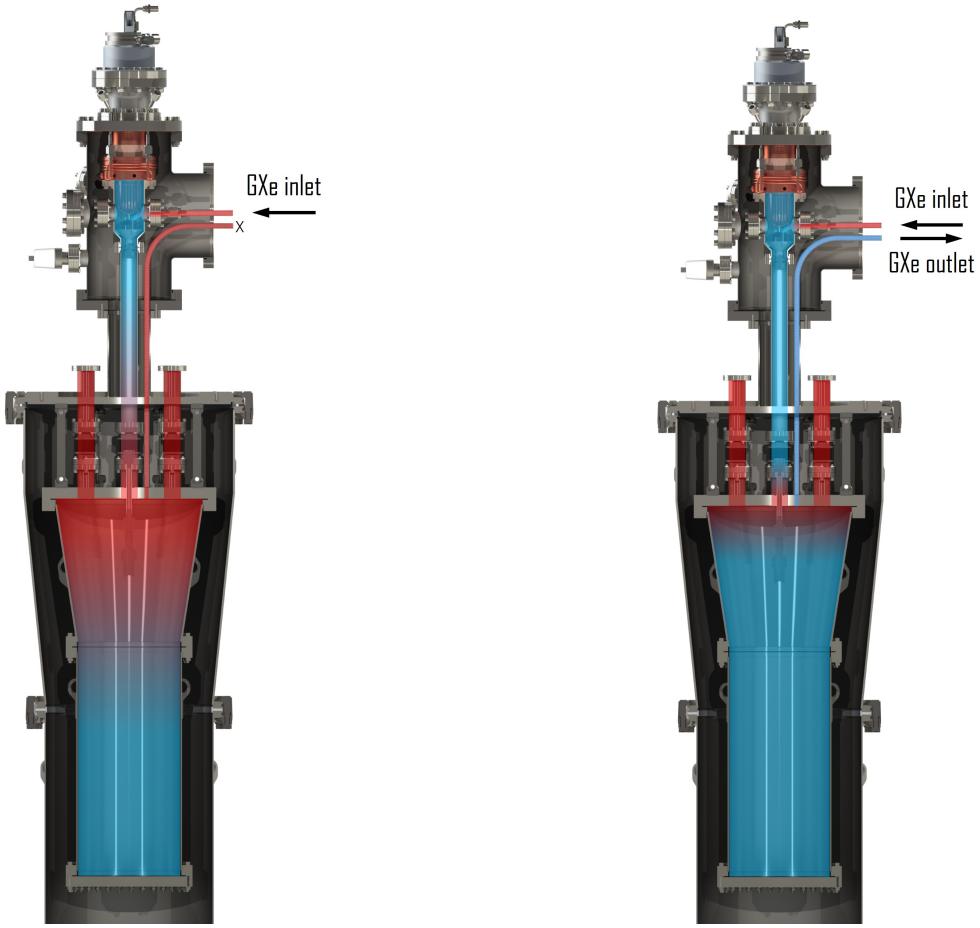

(a) (b)

Figure 4.2: Cryostat assembly during the commissioning run. The inner vessel was only composed of the conical section and one DN250CF straight section. The colors overlain over the rendering represent the thermal gradient installed during the filling of xenon. **(a)** The cold head liquefies GXe, which accumulates at the bottom of the inner vessel. The lack of convection prevents the cooldown of the whole vessel and a thermal gradient prevents the lowering of the pressure. **(b)** With the recirculation enabled, forced convection pushes cold GXe down from the cooling tower, cooling down the inner vessel more evenly.

initial inability to further add xenon to the inner vessel was finally attributed to the formation of an important thermal gradient in the absence of convection in the system, as shown schematically in figure 4.2a. This seemed to keep the pressure in the system at a higher value than expected, preventing filling as the cooling power from the cold head only offset the boiling of LXe in the inner vessel. Since the cryocooler is located high above the cryostat, inside the cold cooling tower, and the cold condensed xenon accumulates at the bottom of the inner vessel, this left the middle sections of the cryostat too warm, driving up the xenon pressure. To remedy this, the GXe recirculation was enabled, producing forced convection from the cooling tower down into the inner vessel. The enabling of the recirculation quickly reduced the xenon pressure as forced convection pushed cold GXe down from the cooling tower to the inner vessel, as shown in figure 4.2b. During the rest of the fill, GXe was continuously recirculated between 15 and 25 slpm with the GXe compressor, and the filling procedure depicted in figure 3.22 was used from this moment on. The fill was performed discontinuously over a period of 5 days, with an average filling speed of 10.95 slpm (3.6 kg/h), culminating in the transfer of 80.66 kg of xenon. At high pressure differences between the high- and low-pressure sides, fast filling speeds can lead to the freezing of the pressure reducer. Following

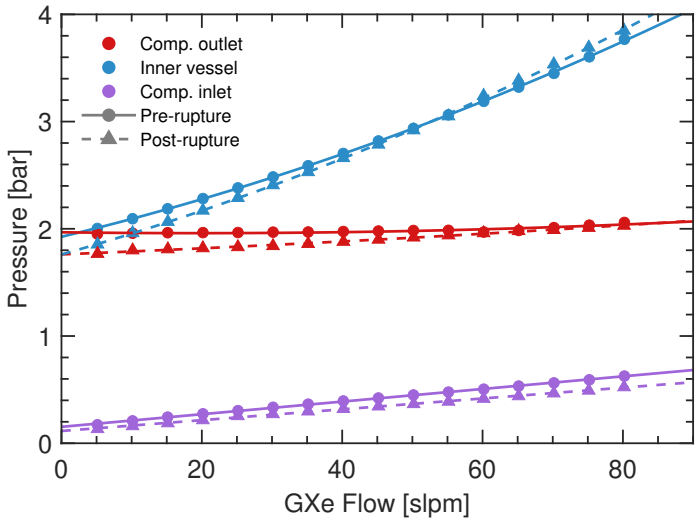

Figure 4.3: Pressure measurements vs. GXe flow. Data taken at 174.25 K cold head temperature setpoint (error bars are smaller than the markers). The solid-lines + points (dashed-line + triangle) are the data points acquired before (after) the rupture of the diaphragm. The fit function used for the post-pump pressure is a second order polynomial. Figure adapted from ref. [1].

the commissioning run, a PID-controlled heater unit was installed on the back side of the pressure reducer to prevent excessive drops in temperature from occurring.

The purification system was tested at flows ranging from 5 to 80 slpm, with a constant cold head temperature of 174.25 K. The average liquid (gas) xenon temperature was (177.1 ± 1.5) K ((184.2 ± 1.5) K). Figure 4.3 shows flow-dependent pressures before and after the GXe compressor, as well as in the inner vessel. We deduced from the data that the flow at the 4 bar abs. maximum pressure rating of the GXe compressor was 83 slpm. A subsequent flow-dependent pressure check at the GXe compressor revealed, however, a reduction in GXe flow in the same pressure conditions, with no apparent reason at that moment for this behaviour. No other changes to the facility were observed.

At the end of the commissioning run, which lasted $\sim$ 5 weeks, the xenon was transferred back to the GCSA by cryopumping, as previously described in section 3.6.2. The recuperation was performed continuously over a 40-hour period, at an average recuperation speed of 6 slpm. The system was stable at all times during this process. Within the absolute accuracy of the mass scale system of $\pm$100 g, no loss of xenon could be observed from the commissioning run.

A careful review of the GXe flow data after the recuperation revealed an anomaly, shown in figure 4.4, that did not trigger a SC alarm at the time. The SC data, however, allowed us to diagnose a potential failure of the GXe compressor, which was confirmed after an inspection of both compressor heads, as seen in figure 4.5a. The KNF N1400 series compressors are designed to be operated at an inlet pressure higher than 1.0 bar abs. Since the inlet pressure throughout the commissioning was below the minimum pressure requirement, the buildup of heat in both heads allegedly melted the diaphragm membranes, even with the use of the integrated water cooling of the compressor. Only one of the two diaphragms completely ruptured, opening a gash of 2 – 3 mm. The GXe compressor could however still be operated, thanks to the double diaphragm configuration shown in figure 4.5b, which prevents any loss of xenon in the case of a diaphragm failure. Following this discovery, the GXe compressor was outfitted with new working diaphragms with no other alterations.

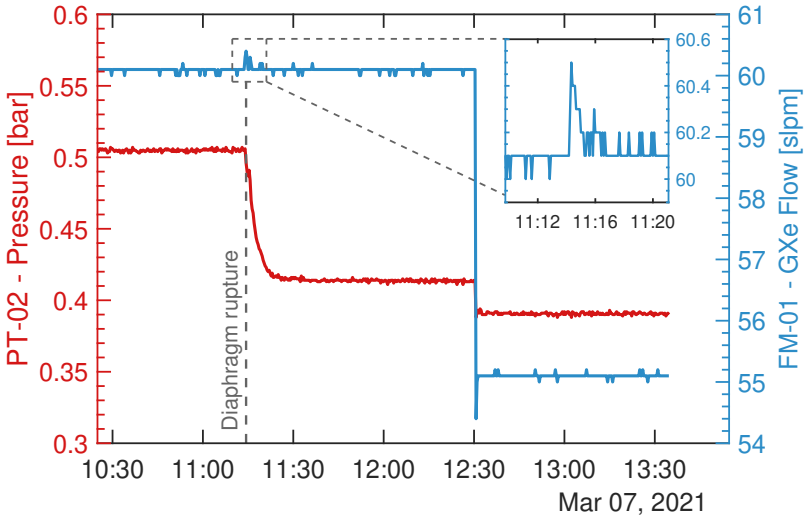

Figure 4.4: GXe diaphragm rupture. At 11:14:20, the pressure at the inlet of the compressor (purple data set) suddenly dropped. A small surplus flow can be observed in the flow meter data (blue data set). This can be attributed to the failure of at least one of the working diaphragm of the GXe compressor. The flow was changed by an operator from 60 to 55 slpm at 12:30.

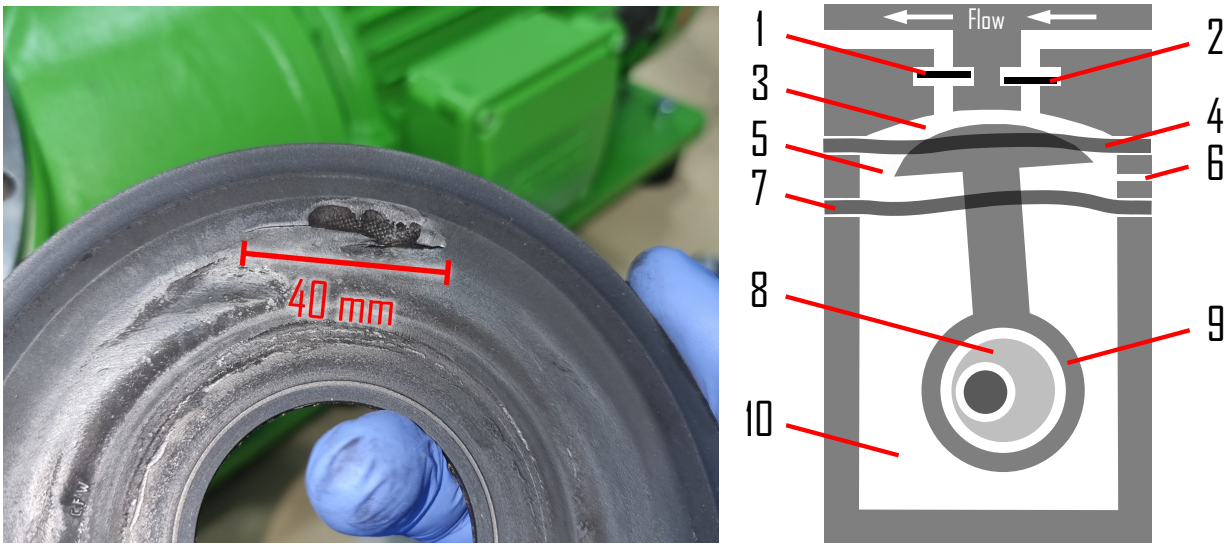

(a) (b)

Figure 4.5: Pump diaphragm damage. **(a)** Underside of a working diaphragm. The rubber membrane suffered damage with only 250 hours of operation. This is possibly due to overheating caused by the operation of the compressor in underpressure conditions at the inlet. **(b)** Schematic of the xenon compressor configuration. Legend: (1) Outlet valve; (2) Inlet valve; (3) Transfer chamber; (4) Working diaphragm; (5) Innerspace; (6) Pressure monitoring access port; (7) Safety diaphragm; (8) Eccentric; (9) Connecting rod; (10) Pump drive.

4.2 Phase 1: The Liquid Xenon Purity Monitor

As previously mentioned, the demonstration of electron drift in Xenoscope is planned in two phases. In the first phase, a 0.53 m LXe PM was deployed to easily benchmark the purification system, and confirm that sufficient xenon purity could be achieved to reach the primary goal of the

experiment. Here, we describe the concept and design of the PM in section 4.2.1 and its operational history in section 4.2.3. We also present and discuss an electron lifetime model we used to predict the achievable electron lifetime in Xenoscope in section 4.2.2. Finally, we present the results of the PM run and the application of the electron lifetime model to the data in section 4.2.5.

4.2.1 The Design of the Purity Monitor

In the traditional dual-phase TPC design described in chapter 2, ionised electrons released in particle interactions are drifted towards the anode at the top of the TPC by a vertical electric field. As they drift, these electrons can be absorbed by electronegative impurities [304]. This usually has the net effect of reducing the strength of the current-proportional scintillation signal (S2). Assuming an electric field of 200 V/cm in Xenoscope, the drift of electrons over 2.6 m requires an electron lifetime of approximately 1.75 ms, which translates to an O_2-like impurity concentration of $\sim$ 0.5 ppb [210, 305]. This is accomplished by continuously purifying the xenon by passing it through the hot metal getter, as described in section 3.3.1.

As the ultimate detector length in Xenoscope will reach a height of 2.6 m, the field cage was conceived in modules to allow the reuse of sections from the PM phase and to provide extra flexibility for future studies if needed. The detector used during the first phase of Xenoscope, the charge-sensing LXe PM, is composed of only one module with a total drift distance of 52.8 cm. Figure 4.6 shows a rendering of the PM as deployed in the first measurement campaign, which is discussed later in section 4.2.3.

The field cage is built from 34 OFHC copper rings connected by a dual-resistor chain. In the event of the failure of one of the printed circuit board (PCB)-mounted (5 ± 1) GΩ resistors, the second one allows for the slow discharge of the field cage, preventing unwanted sparking that could damage electronic components. As in a TPC, the role of the field cage is to ensure the homogeneity and constant strength of the electric field by producing equipotential planes. The rings are mounted on six insulating PAI pillars and held in place by PTFE clamping blocks attached on the inside faces of the pillars. PAI ensures the structural rigidity of the detector with its good mechanical properties. It also has excellent dielectric properties and a low outgassing rate. At LXe temperatures, the linear thermal expansion coefficient of PAI provided by the manufacturer of the tested sample in ref. [306] is $3.06 \cdot 10^{-5}\,\mathrm{K}^{-1}$. This translates to a thermal contraction of 0.4 % assuming a cooldown from 300 K to 178 K. For the PM, this then implies a 2.0 mm thermal contraction over the whole length of the drift region, while it is 10.4 mm for the drift region of the 2.6 m TPC. As the PM

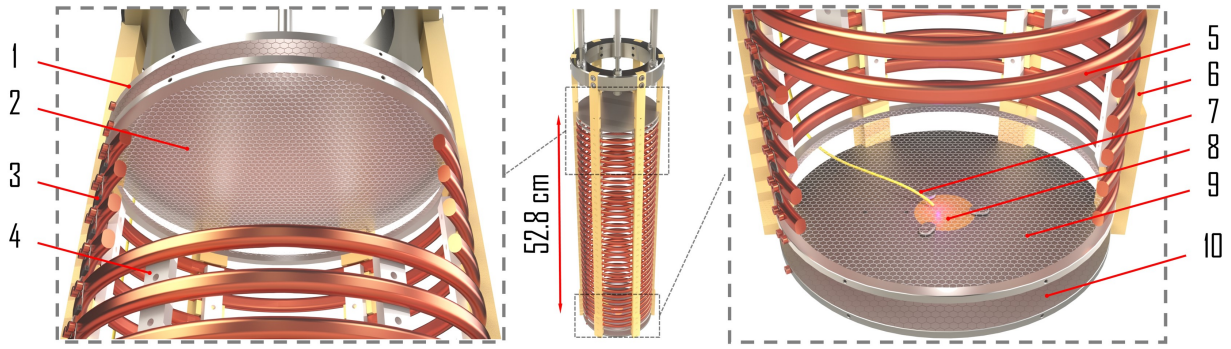

Figure 4.6: CAD rendering of the purity monitor. Legend: (1) Anode; (2) Anode grid; (3) Resistor chain; (4) PTFE locking block; (5) Field-shaping ring; (6) PAI pillar; (7) Optical fibre; (8) Photocathode; (9) Cathode grid; (10) Cathode. Figure adapted from ref. [1].

is quite small, the elongation due to gravitational forces is negligible. However, in the case of the TPC, simplified FEA simulations showed that the height-dependent elongation of the pillars could translate to a total of $\sim 6\,\text{mm}$ in added length. While these elongation and contraction parameters seem to cancel each other out, they must be treated individually as the elongation is present in air, vacuum, and in LXe, although the buoyancy of the TPC in liquid reduces the total elongation. This results in the bottom of the TPC, where the HV connection is located, sitting lower than its nominal position. The thermal contraction then lifts the bottom of the TPC, as the top is fixed to the top flange. The net effect is the upward movement of the HV connection after the cooldown of the TPC, which is compensated by a cup and spring mechanism described in section 4.3.3.

The PM is divided into three drift regions that are delimited by four electrodes. The bottom and top regions (regions 1 and 3) are used to measure the two currents induced by the drifting electrons, with the two gate electrodes shielding the readout from electrons drifting in the middle section (regions 2). This intermediate section is much longer than the other two, allowing for the depletion of the electron population due to absorption by electronegative impurities. Figure 4.7 shows a conceptual schematic of the purity monitor and a schematic graph of its expected current-proportional signals read-out at the cathode and at the anode. Pulsed ultraviolet (UV) light is channelled through an optical fibre to the bottom of the detector. The radiation produces $\mathcal{O}(10^6\ \text{e}^-)$ via the photoelectric effect, which immediately drift upward in the first region of length d_1. The drift field E_2 in the second region of length d_2 is greater than the extraction field E_1, ensuring the survival of nearly 100 % of the electrons transiting past the cathode grid. The same principle applies to the cathode grid at the beginning of the third region of length d_3, where the collection field E_3 is greater than the field E_2. The drift times t_1, t_2, and t_3 correspond to the drift of the electrons over the distances d_1, d_2, and d_3, respectively.

The drift velocity of electrons in LXe is dependent on the strength of the electric field. It is

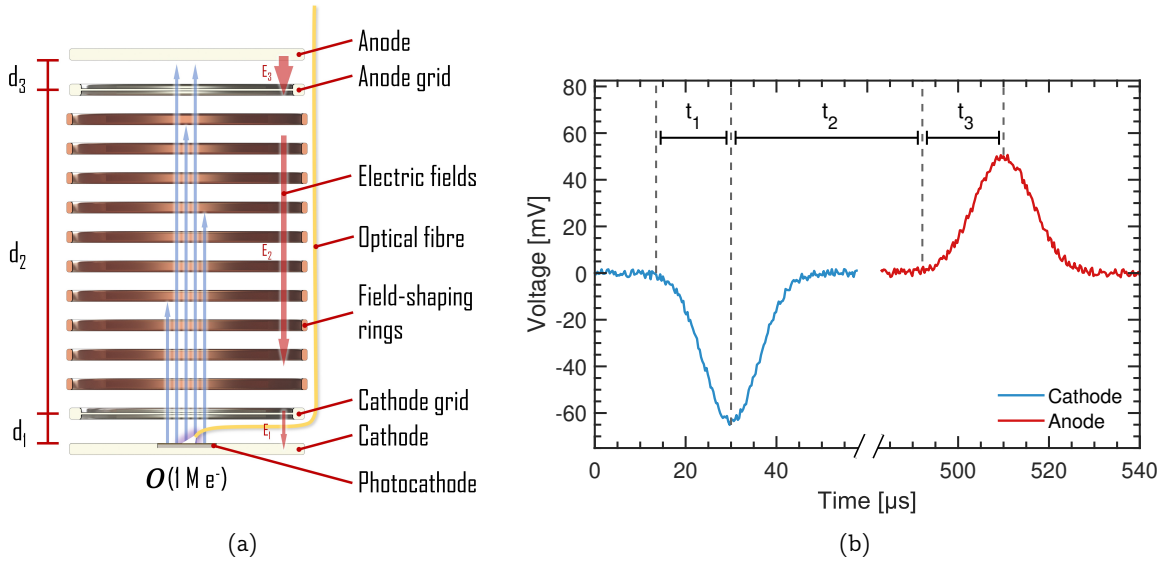

(a) (b)

Figure 4.7: **(a)** Schematic of the PM. Three drift regions (d_1, d_2, and d_3) are delimited by four electrodes. A $\sim 1\,\text{J}$ UV light pulse is transmitted through an optical fibre, producing $\mathcal{O}(10^6\ \text{e}^-)$. The first electric field is the weakest, extracting electrons from the photocathode before they can recombine in the metal. The loss of electrons as they drift passed the cathode grid is negligible due to the stronger electric field in the second region. The same principle applies at the anode grid, as the field in the third region is the strongest. **(b)** Definition of the drift times. t_1, t_2, and t_3 are respectively the times required for the electrons to drift the distances d_1, d_2, and d_3.

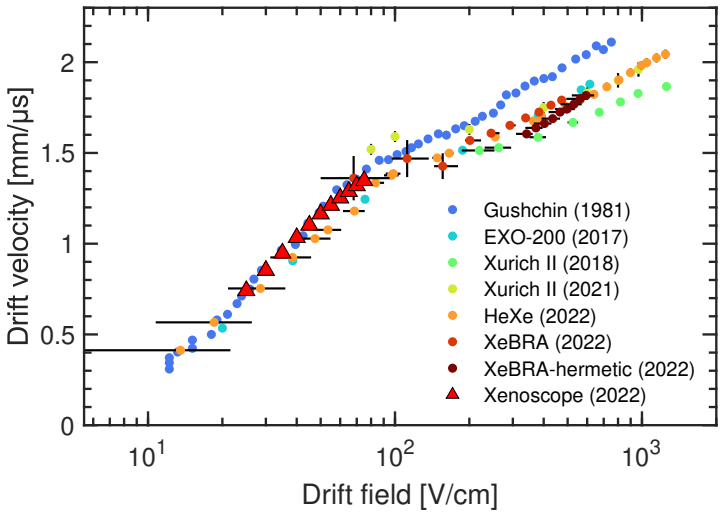

Figure 4.8: Drift velocity of electrons in LXe vs. drift field. Measurements in Xenoscope were made at 178 K. For the target electric field in Xenoscope of 192 V/cm, the electron velocity is $\sim$ 1.5 mm/µs. Literature values: Gushchin (165 K) [307], EXO-200 (167 K) [308], Xurich II (2018, 184 K) [5], Xurich II (2021, 177 K) [2], HeXe (174 K) [223], XeBRA (173 K) [309].

measured as:

$$v_{\mathrm{d}} = \frac{d}{t_{\mathrm{d}}}, \tag{4.1}$$

where d is the distance travelled, and t_{d} is the drift time. This has been measured numerous times, as shown in figure 4.8, where the electric field-dependent velocity measurement in the Xenoscope PM for the drift region 2 is compared to selected literature values. For the purity measurement in Xenoscope, this translates to drift velocities of 0.88 mm/µs, 1.18 mm/µs, and 1.76 mm/µs in regions 1, 2, and 3, respectively, while for the 2.6 m TPC, the target 192 V/cm drift field translates to a drift velocity of $\sim$ 1.5 mm/µs.

The electron lifetime, τ_{e}, defined as the time in which the number of electrons is reduced by a factor e, can be measured in a TPC with calibration data by comparing the size of the S2 signal as a function of the interaction depth [6, 310]. These calibrations can, however, last several hours, and require the use of internal or external radioactive sources. Alternatively, the use of a PM, such as those deployed in ICARUS [311], ProtoDUNE [312], and XENONnT [313], allows for the direct measurement of the ratio of the number of surviving electrons to the initial number of electrons produced. This is done with the use of charge or transimpedance readouts at the top and bottom of the drift cage, respectively. This ratio is directly related to the electron lifetime:

$$\frac{N_{\mathrm{e}}(t_{\mathrm{d}})}{N_{\mathrm{e}}(0)} = G \cdot \frac{Q_{\mathrm{e}}(t_{\mathrm{d}})}{Q_{\mathrm{e}}(0)} = \mathrm{e}^{-t_{\mathrm{d}}/\tau_{\mathrm{e}}}, \tag{4.2}$$

where t_{d} is the drift time of the electrons, and $N_{\mathrm{e}}(t)$ and $N_{\mathrm{e}}(0)$ are respectively the number of electrons produced at the top and bottom of the PM. $Q_{\mathrm{e}}(t)$ and $Q_{\mathrm{e}}(0)$ are the charges read out at the top and bottom. $G = G_b/G_t$ is the ratio of the gains of the amplifiers used at the bottom and at the top, used as a normalisation between both charge readouts. The ratio of the gains was measured *in-situ* in vacuum, where there is no loss of electrons, with a value of $G = 1.01$. Rearranging the equation 4.2, the electron lifetime can be expressed as:

Zone	Electrode	Bias voltage [kV]	Distance [mm]	Electric field [V/cm]
	Anode	(0.500 ± 0.002)		
3			$d_3 = (10.0 \pm 0.1)$	$E_3 = (500 \pm 6)$
	Anode Grid	(0.000 ± 0.002)		
2			$d_2 = (503 \pm 5)$	$E_2 = (52.7 \pm 0.6)$
	Cathode Grid	(-2.650 ± 0.003)		
1			$d_1 = (18.0 \pm 0.2)$	$E_1 = (33 \pm 3)$
	Cathode	(-2.710 ± 0.003)		

Table 4.1: Bias voltages of the electrodes, travel distances of the drift regions, and values of the electric fields in the PM. The relative uncertainty for the electric field in region 1 is large since the potential difference and the drift distance are both small.

$$\tau_e = \frac{-t_d}{\ln\left(G \cdot \frac{Q_e(t_d)}{Q_e(0)}\right)} \tag{4.3}$$

The detection of charge signals at both ends, combined with the measurement of the total drift time, is therefore a very efficient method to quickly measure the electron lifetime in a noble gas, even at low xenon purity.

The electrodes are electrically biassed by a Nuclear Instrumentation Module (NIM) HV power supply (CAEN NDT1470 [314]), which feeds the HV through a CeramTec safe high-voltage (SHV) feedthrough [315] installed on the top flange. The precision of the HV power supply is $\pm$ 2 % of the displayed voltage value, $\pm$ 2 V. The bias voltages at each electrode, the drift distance of each region, and the resulting strength of the electric field per region are shown in table 4.1. The distances are attributed a 1 % conservative systematic error to account for the thermal contraction of the PM and the cumulative tolerances of the machining of the assembly.

A photocathode is mounted on the bottom-most electrode. The photocathodes were produced in-house in the laboratory of Prof. Marta Gibert at the University of Zurich [316]. Tested materials include aluminium, silver, and gold. The latter was selected for its high work function (5.10 – 5.47 eV [317, 318]). 50 µm thick gold films were deposited on a 2 mm thick fused-silica substrate discs, pre-coated with 5 nm titanium. The deposition was done via argon sputtering in a Quorum Q150T Plus turbomolecular coater [319]. Fused-silica substrate discs were chosen as this material has a low absorption efficiency in the VUV-range, and the reflection of VUV-photons back into the gold film enhances the release of photoelectrons [320]. A complete description of the photocathode-making process can be found in ref. [259].

An externally mounted xenon flash lamp (Hamamatsu model L7685 [321]) produces up to 1 J UV-light pulses, carried to the photocathode by a LewVac solarization-resistant fused-silica optical fibre with a polyimide buffer [322]. The charges moving away from the photocathode in the extraction field vary the electromagnetic field near the electrode and produce mirror charges in the cathode in accordance with the Shockley-Ramo theorem [323, 324]. A transimpedance amplifier converts the current produced in the electrode to a voltage pulse. The integral of the pulses is then proportional to the total instantaneous charge drifting in the region, and hence to the number of drifting electrons. The same measurement method is used for the anode at the top of the PM.

4.2.2 Predictive Electron Lifetime Model for Xenoscope

Prior to the operation of the PM, we developed an electron lifetime model inspired by one developed for XENON1T, and described in ref. [325]. The electron lifetime can be measured as described in equation 4.3, but is also related to the number of impurities in the xenon. It can then be modelled with:

$$\tau_{\mathrm{e}} = \frac{1}{I_S K_S}\,, \tag{4.4}$$

where I_{S} is the concentration of impurities in ppb, and K_{S} is the attachment rate constant with units of $\mathrm{ppb}^{-1}\cdot\mu\mathrm{s}^{-1}$, a parameter related to the electric field as shown in figure 4.9. The subscript S denotes the different species of impurity. For simplicity, we consider all impurities to be O_2-like, as they are typically dominant [263].

Producing a strong and homogeneous drift field in large detectors is one of the main technical challenges. To facilitate the production of a custom electric feedthrough, the target electric field for Xenoscope was therefore chosen to be 50 kV / 260 cm = 192.3 V/cm. Such a drift field in LXe translates to an electron drift velocity of 1.5 mm/µs. Therefore, electrons drifting from the bottom-most parts of the field cage will drift on average $\sim$ 1.73 ms before they can be extracted in the gas phase to be detected as an S2. To ensure the viability of a 2.6 m tall dual-phase xenon TPC, we thus require an electron lifetime $>$ 1.75 ms to achieve a suitable sensitivity to low charge-yield events at any height in the detector.

As already mentioned, in Xenoscope, LXe is purified by extracting it directly from the LXe phase and carrying it to the heat exchangers, where it is vaporised before continuing towards the purification system. The gas is purified, as shown by the red path in figure 3.22, in the hot metal

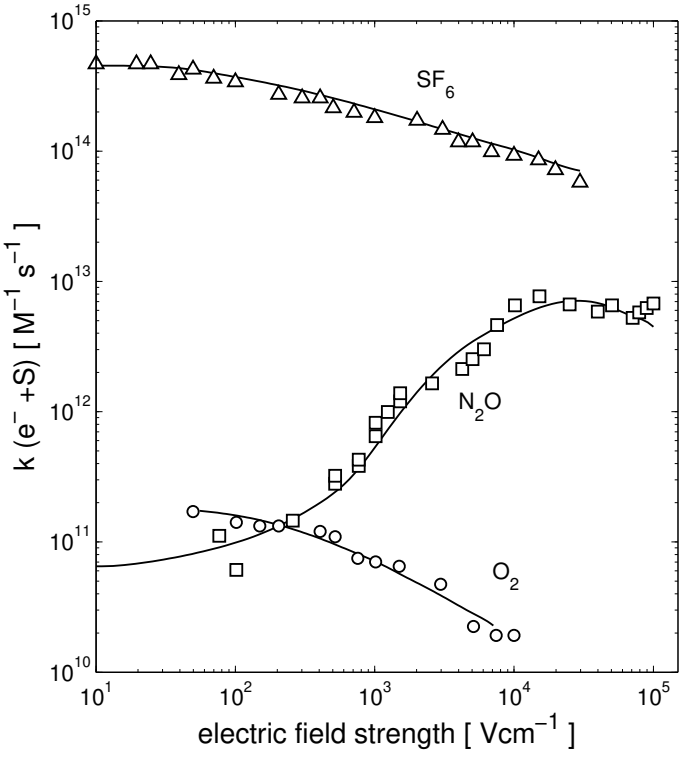

Figure 4.9: Field-dependent attachment rate vs. of electric field for O_2, N_2O and SF_6. The electron lifetime considers all impurities to be O_2-like. Figure from ref. [305].

getter heated to 420 °C. The GXe is then condensed back in the heat exchangers and in the cryogenic tower. The nominal recirculation flow, at which the getter is still guaranteed the sub-ppb removal of impurities, is 70 slpm. In this model, we assume an impurity removal efficiency of 100%. Other experiments have shown that flows of up to 100 slpm can be reached with these getter units, but noted that the purification efficiency is variable [262].

A simple electron lifetime model describing the instantaneous variation in impurity concentration $\frac{\mathrm{d}I}{\mathrm{d}t}$ for both the gas phase and the liquid phase is:

$$M_{\mathrm{g}}\frac{dI_{\mathrm{g}}}{dt} = -F_{\mathrm{g}}\rho\, I_{\mathrm{g}} + \Lambda_{\mathrm{g}} + \frac{\varepsilon_{\mathrm{vap}} P_{\mathrm{C}} I_{\mathrm{l}}}{h} - \frac{\varepsilon_{\mathrm{cond}} P I_{\mathrm{g}}}{h} \tag{4.5}$$

$$M_{\mathrm{l}}\frac{dI_{\mathrm{l}}}{dt} = -F_{\mathrm{l}}\rho\, I_{\mathrm{l}} + \Lambda_{\mathrm{l}} - \frac{\varepsilon_{\mathrm{vap}} P_{\mathrm{C}} I_{\mathrm{l}}}{h} + \frac{\varepsilon_{\mathrm{cond}} P I_{\mathrm{g}}}{h}\,, \tag{4.6}$$

where I_{g} and I_{l} are the impurity concentration of the gas and liquid phases respectively, in units of ppb. Only the liquid phase impurity concentration is used to calculate the electron lifetime described by equation 4.4. The terms of the differential equations are identified in table 4.2, and the parameters are described in table 4.3. The first term describes the effective removal of impurities from the purification loop, while the second term describes the outgassing rate from surfaces in the system, which adds impurities to the xenon. The third term describes the transfer of impurities from the liquid phase to the gas phase due to the vaporisation of the xenon at the liquid-gas interface. The fourth term accounts for impurity exchange from the gas phase to the liquid phase due to condensation of the xenon gas on the cold head.

As Xenoscope was a new facility, detector-dependent parameters, such as the purification efficiency and the outgassing rates, were not known and should be determined from electron lifetime measurements. The values are therefore adapted from the ones measured with XENON1T. The outgassing parameters have been scaled down by a factor of ~ 10, determined from:

$$R = A_{Xenoscope}/A_{XENON1T}\,, \tag{4.7}$$

the ratio of the surface areas of the detectors and cryostats of Xenoscope and XENON1T. The detector materials used in Xenoscope have not been selected to limit outgassing. The cryostat surfaces were electropolished, and the vessel can be mildly baked out before the introduction of xenon, but the cleaning and assembly are not performed under strict clean room conditions. We therefore used a conservative approach by estimating the outgassing levels to be $5\times$ that of XENON1T for the gas phase and $1.5\times$ for the liquid phase. The outgassing parameters must be determined with a data-driven approach. For this model, the number of impurities is iteratively calculated at each time interval i using the two differential equations:

#	Term	Description
1	$F_{\mathrm{g}}\rho\, I_{\mathrm{g}}/F_{\mathrm{l}}\rho\, I_{\mathrm{l}}$	Gas / Liquid flow in purification loop
2	$\Lambda_{\mathrm{g}}/\Lambda_{\mathrm{l}}$	Gas / Liquid outgassing rate of impurities
3	$\frac{\varepsilon_{\mathrm{vap}} P_{\mathrm{C}} I_{\mathrm{l}}}{h}$	Liquid to gas exchange of impurities
4	$\frac{\varepsilon_{\mathrm{cond}} P I_{\mathrm{g}}}{h}$	Gas to liquid exchange of impurities

Table 4.2: Definition of the terms in the differential equations 4.5 and 4.5.

Parameter	Description	Value
M_g	GXe mass	2 kg
M_l	LXe mass	350 kg
F_g	Recirculation flow of the gas phase	0 or 3 slpm
F_l	Recirculation flow of the liquid phase	1 to 100 slpm
ρ	GXe density at 1 bar, 0 °C	$5.823\,6 \cdot 10^{-3}$ kg/l [193]
ε_{vap}	Attachment efficiency LXe vaporisation	0.4
ε_{cond}	Attachment efficiency GXe condensation	0.41
P_C	Cooling power when there is no circulation	140 W
P	Cooling power of the cryogenics	150 W
h	Latent heat of vaporisation	95.587 kJ/kg [196]
Λ_g	Outgassing rate in the gas phase	101.4 kg · ppb/day (Xe1T: 190)
Λ_l	Outgassing rate in the liquid phase	31.2 kg · ppb/day (Xe1T: 195)
$I_{0,g}$	Initial gas impurity concentration	7 200 ppb
$I_{0,l}$	Initial liquid impurity concentration	100 ppb
K	Attachment rate	$0.002\,7\,\mu s^{-1}\,ppb^{-1}$

Table 4.3: Definition and values of the parameters used in the predictive electron lifetime model. Since Xenoscope is a new facility, most parameters are extrapolated from XENON1T models. The outgassing is assumed to be flat and conservatively higher than that of XENON1T, as no information on its time-dependence was yet available.

$$\begin{aligned} I_g(i) &= I_g(i-1) + \frac{dI_g(i)}{dt} \\ I_l(i) &= I_l(i-1) + \frac{dI_l(i)}{dt} \end{aligned} \tag{4.8}$$

$$\tau_e(i) = \frac{1}{I_l(i) \cdot K}. \tag{4.9}$$

Figure 4.10a shows the electron lifetime with assumptions taken from the electron lifetime model of XENON1T. The red contour line delimits our 1.75 ms electron lifetime target. Given our target recirculation flow of 100 slpm, this model shows the reach of a plateau after $\sim$ 7 days of continuous purification, while operations at a more modest 30 slpm show the reach of an equilibrium point after $\sim$ 14 days. With the chosen parameter values, the minimum flow rate allowing us to reach our target 1.75 ms of electron lifetime is 82 slpm.

Figure 4.10b shows the same model, with, in addition, the purification of the gas phase at a flow of 3 slpm. At 100 slpm in the liquid phase, we get an increase in electron lifetime from 2.13 ms to 2.80 ms. Depending on the outgassing level, recirculation of the gas phase could have a noticeable impact on the electron lifetime.

The time-evolution of the electron lifetime is first described by an exponential rise following the removal of most of the initial impurities, followed by an asymptotic approach to an equilibrium value where the outgassing rate is equal to the purification rate. In reality, the outgassing rate is time-dependent. Following the initial exponential rise, the electron lifetime approaches the equilibrium point as an inverted exponential with a long time constant. The time-evolution of the outgassing rate is both detector- and even run-dependent, as initial conditions, such as initial impurity concentrations, and the types and amounts of materials in the cryostat will have an impact on the global outgassing profile.

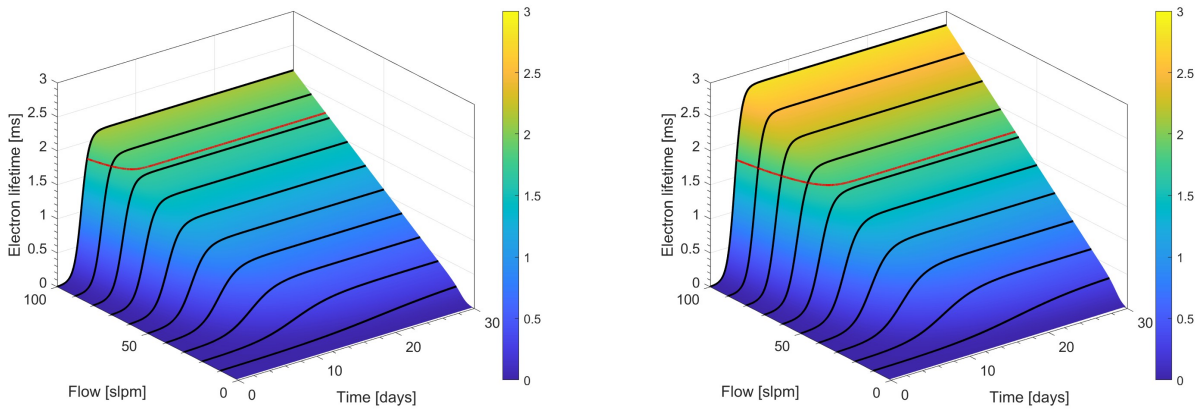

(a) (b)

Figure 4.10: Electron lifetime vs recirculation time and flow **(a)** No gas recirculation. **(b)** With gas recirculation at 3.0 slpm. The maximum electron lifetime predicted at 100 slpm without (with) gas recirculation is 2.3 ms (2.8 ms).

This model does not account for the trapping of impurities at the collar of the gas/liquid interface, where the surface tension is greater. The raising and lowering of the liquid level in the XENON1T demonstrator allowed for a noticeable increase in the electron lifetime past the plateau region [263]. This effect could be tested in Xenoscope as well, as described later in this section.

As will be shown hereafter, the operation of the PM in Xenoscope allowed for the tuning of the electron lifetime model by fitting it to the electron lifetime data to determine the interesting parameters of the system. Insights from the model can then be used to optimise Xenoscope in order to improve the electron lifetime reach, whether by introducing gas-phase purification, developing or using different cleaning techniques to reduce the effects of outgassing, or using completely different purification schemes.

4.2.3 Operation of the Purity Monitor in Xenoscope

This section describes the full operational history of the purity monitor in Xenoscope, consisting of three runs (hereafter referred to as Runs 1, 2, and 3). A complete description of the development and testing phases of the purity monitor and its electronic components, can be found in ref. [259].

Run 1

Building upon lessons learned during the full-facility commissioning, some upgrades to the facility were made prior to the start of Run 1. The inner space of the GXe compressor was instrumented with a Swagelok S Model Industrial Pressure Transducer [270]. This upgrade allowed for more stringent monitoring of the inner space pressure, which could indicate the rupture of a diaphragm. The GXe compressor was also outfitted with new working diaphragms.

Prior to its installation in Xenoscope, all the components of the PM were thoroughly cleaned, first with Elma EC 10 acidic soap [289] in an ultrasonic bath, followed by a deep cleaning in isopropyl alcohol. Stainless steel parts were cleaned with acetone, while PTFE components were treated with nitric acid. Additionally, the copper rings were electropolished to remove tool marks left from their

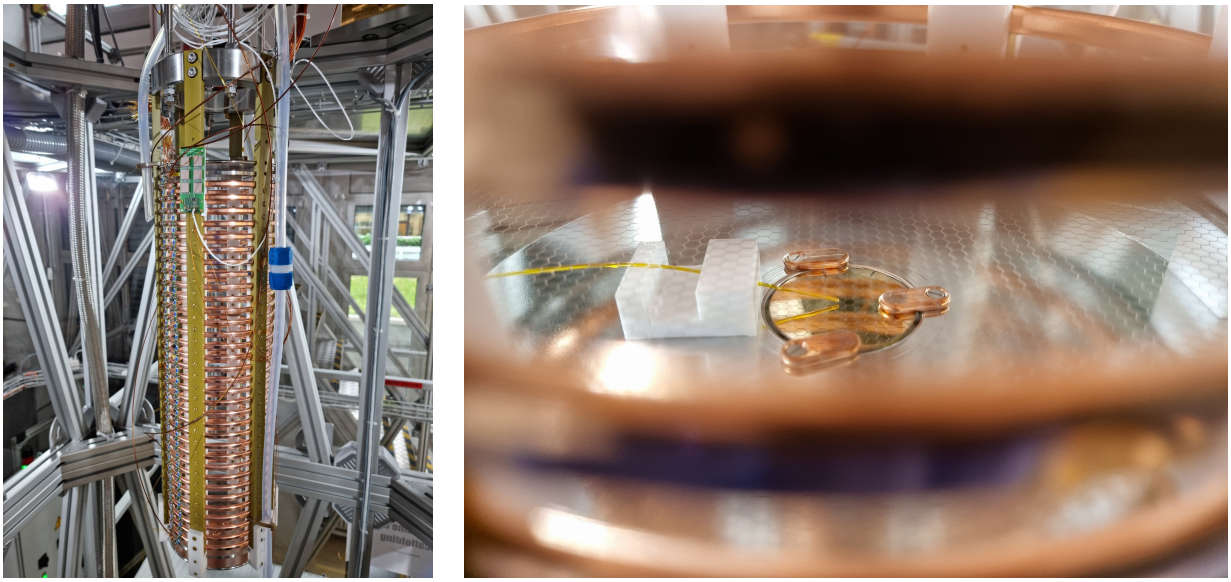

(a) (b)

Figure 4.11: Purity monitor installed under the top flange. **(a)** Overview of the PM. The drift region delimited by the photocathode at the bottom and the anode at the top is 52.7 cm tall. The top charge readout board (green PCB) and the LXe outlet tube attached to the right of the picture are shown. **(b)** Photocathode of the PM seen through the field cage. The yellow optical fibre, held by a PTFE support block, transports the UV light pulses from the xenon flash lamp at the top of the detector, to the gold-plated photocathode.

machining, as even surfaces produce a more uniform electric field. Shortly prior to the assembly of the PM, the rings were cleaned with soap, passivated in a 2 percent weight-per-weight (wt/wt %) citric acid solution, and finally rinsed with isopropyl alcohol. All components were dried with dry nitrogen gas.

The PM was first assembled in July 2021. The detector was cleaned and then installed in Xenoscope, as shown in figure 4.11. The cryostat was assembled, leak tested, and the setup was outgassed in vacuum for 9 days. Run 1 was started on July 26 2021 with a first successful demonstration of the operational capabilities of the PM in vacuum at a pressure of $5 \cdot 10^{-5}$ mbar. Electrons could be detected at both ends of the field cage, as shown in figure 4.12. The pre-cooler was used to pre-cool the cryostat but was not employed during filling. The cryostat was filled discontinuously from 27 July 2021 to 30 July 2021 with 183.76 kg of LXe at an average filling speed of 21.58 slpm (7.1 kg/h). During filling, a routine test of the charge readout while the PM was still in the GXe phase revealed that the cathode readout was not responding. Shortly after, the decision to recuperate was made. An estimated 52.96 kg was recuperated to BoX in liquid form, while the rest was evaporated and cryopumped to the GCSA, ending Run 1 on 8 August 2021. The remaining charge readout was further tested in vacuum and in GXe prior to the disassembly of the cryostat, during which it also failed. The inspection of the charge readout PCBs revealed that failed operational amplifiers (Op-Amps) were the culprits. The PCBs were therefore outfitted with new Op-Amps, and they received a thin parylene coating ($\mathcal{O}(\mu m)$ thickness) from Specialty Coating Systems [326] to increase their dielectric strength. This polymer is low-outgassing, chemically resistant, and can be chemically deposited in thin-films [327].

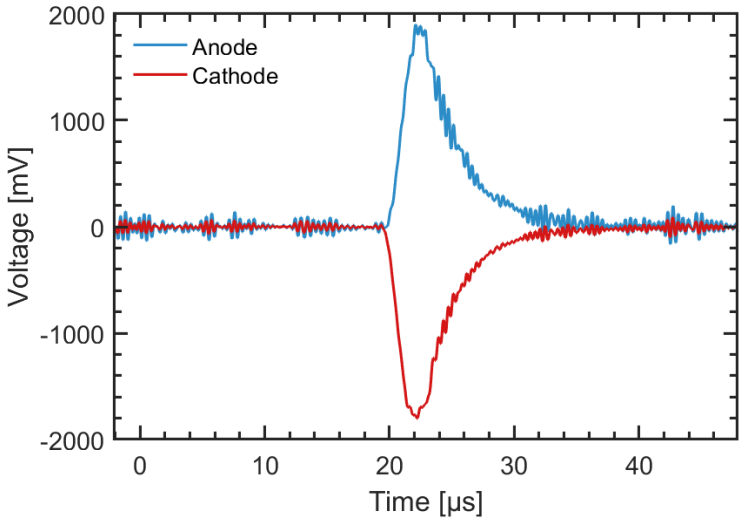

Figure 4.12: Charge waveform acquired with the PM in vacuum. The signals have inverse polarities as the electrons drift away from the cathode, and towards the anode.

Run 2

The second operational run of the PM was started at the end of October 2021. The cryostat was evacuated for 6 days prior to filling, after which 2 bar of GXe were introduced. The xenon was recirculated and purified for a period of 15 days in an attempt to scrub out electronegative impurities from surfaces prior to the cooldown of the inner vessel.

The LXe fill debuted on 17 November 2021, and was performed discontinuously until 19 November 2021, culminating in the transfer of an estimated 223.35 kg of LXe. The pre-cooler was used to effectively double the filling speed compared to Run 1, with an estimated average filling speed of 42.5 slpm (14.0 kg/h). On 20 November 2021, the pressure in the inner space of the GXe compressor suddenly dropped, indicating another failure of at least one of the compressor diaphragms. The compressor was manually stopped 15 minutes after the alarm was first triggered, and preparations for an emergency recuperation of the xenon were immediately initiated. The recuperation to BoX was started one hour later. An estimated 163.8 kg of LXe was recuperated to BoX, while the rest was cryopumped to the GCSA. In total, the recuperation lasted $\sim$ 24.5 hours.

The inspection of the GXe compressor revealed once again the degradation of both working diaphragms, similar to that observed after the commissioning run. The compressor was sent back to the manufacturer to be retrofitted with a smaller eccentric, which would then allow for the operation of the compressor with a smaller pressure gradient.

Run 3

The cryostat and most of the gas system were actively pumped down to a vacuum level of $4.3 \cdot 10^{-3}$ mbar during the downtime between Runs 2 and 3. On 25 February 2022, the cryostat was filled with 2 bar of GXe to confirm the good operation of the refurbished GXe compressor. The gas was then purified for three days to scrub impurities from the active volume.

The cooldown of the inner vessel was initiated using both the pre-cooler and the PTR on 28 February 2022. The third xenon fill was started on 1 March 2021, achieving an average filling speed

Purification flow [slpm]	Purification flow [kg/h]	Purification time [days]
30	251.6	46.6
35	293.5	20.0
40	353.4	22.8

Table 4.4: Summary table of Phase 1 - Run 3. At 40 slpm, all of the xenon can be recirculated if just over 1 h.

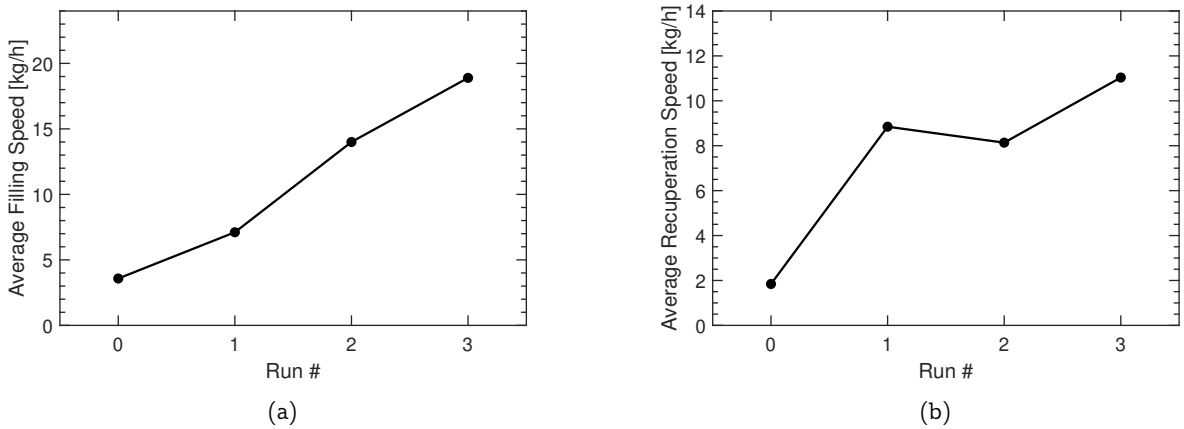

Figure 4.13: Average filling and recuperation speeds per run, where run 0 is the full facility commissioning. (a) Average filling speed. The use of the pre-cooler incrementally increased the filling speed of the facility, proportionally to the extent of its use. (b) Average recuperation speed. The addition of BoX and liquid recuperation to the recuperation scheme increased the recuperation speed by a factor of ~ 4.5.

of 57.4 slpm (18.9 kg/h). The total amount of xenon transferred from both the GCSA and BoX is estimated at 343 kg. Immediately after the completion of the filling, the purification of the xenon was enabled. Table 4.4 shows the three purification phases of the run.

The main objective of the run – the measurement of the electron lifetime – is discussed in the next section. Xenoscope was operated continuously, from initial cooldown to the completion of the recuperation, for a total of 99.5 days without significant issues. The recuperation was completed successfully in less than 48 hours of operation over three days, with the majority of the xenon transferred to BoX. After having warmed up, BoX reached a pressure of 61.78 bar at a temperature of 271.3 K. This translates to a mass of 271.3 kg.

Figure 4.13 shows the compilation of the average filling and recuperation speeds for every operational run. The addition of the pre-cooler and of BoX after the commissioning run proved beneficial for the filling and recuperation of the cryostat, respectively. The pre-cooler had different roles during each run, which can explain the progressive improvement in filling speed. It was only used to pre-cool the inner vessel in Run 1, saw moderate utilisation for filling in Run 2, and was used at full capacity during all of the filling in Run 3. On the other hand, BoX was used throughout all three PM runs. The variation in average recuperation speed can be attributed to the time spent on the gravity-assisted recuperation, as the lack of a liquid level meter made it difficult to predict when to stop the liquid recuperation. This will be remedied for Phase 2 of the experiment with the addition of two long level meters alongside the TPC, capable of measuring the height of the liquid

level with mm-level precision over the full height of the TPC. With the successful completion of the PM operation, we concluded the first operational phase of Xenoscope on 7 June 2022, and started the transition to the full-height TPC, which is discussed in section 4.3.

4.2.4 Performance of the Cryogenic System of Xenoscope

The operation of Xenoscope, both during the commissioning and PM phases, allowed us to continuously acquire a large amount of valuable data from all the systems through our slow control system. In addition, several months after the PM runs, the PTR was activated to help lower the vacuum pressure in the cryostat during the HV test discussed in section 4.3.3. This last piece of data allowed us to quantify the cooling power of the PTR, of which we present here a calculation. We also present a calculation of the heat load of the LXe-filled cryostat during the commissioning run and Run 3. The results of both of these calculations are used to calculate the evaporation and condensation rates of xenon, used in the data-driven electron lifetime model.

Calculation of the Cooling Power of the PTR

The cooling power of the PTR can be calculated with a few assumptions. The heat transfer rate of the system, at equilibrium, can generally be written as:

$$\dot{Q} = \dot{Q}_{\mathrm{PTR}} + \dot{Q}_{\mathrm{H}} + \dot{Q}_{\mathrm{cryostat}} = 0\,, \tag{4.10}$$

where $\dot{Q}_{\mathrm{PTR}} < 0$ is the cooling power of the PTR, and $\dot{Q}_{\mathrm{H}}$ is the power output of the heater module. The heat load of the cryostat, $\dot{Q}_{\mathrm{cryostat}}$, can be further written as:

$$\dot{Q}_{\mathrm{cryostat}} = \dot{Q}_{\mathrm{pur}}\left(\dot{m}\right) + \dot{Q}_{\mathrm{cond}} + \dot{Q}_{\mathrm{rad}}\,, \tag{4.11}$$

where $\dot{Q}_{\mathrm{pur}}$ is the mass flow ($\dot{m}$)-dependent heat transfer rate due to the purification of LXe, and $\dot{Q}_{\mathrm{cond}}$ and $\dot{Q}_{\mathrm{rad}}$ are respectively the heat loads from thermal conduction and radiation. Therefore:

$$\dot{Q} = \dot{Q}_{\mathrm{PTR}} + \dot{Q}_{\mathrm{H}} + \dot{Q}_{\mathrm{pur}}(\dot{m}) + \dot{Q}_{\mathrm{cond}} + \dot{Q}_{\mathrm{rad}} = 0. \tag{4.12}$$

In the absence of xenon in a warm cryostat and assuming perfect vacuum in both cryostat vessels, $\dot{Q}_{\mathrm{pur}}(\dot{m})$ in equation 4.12 goes to zero, the conductive and radiative components only apply to the cold head, and the equation can be rewritten as:

$$-\dot{Q}_{\mathrm{PTR}} = \dot{Q}_{\mathrm{H}} + \dot{Q}_{\mathrm{cond}} + \dot{Q}_{\mathrm{rad}}\,. \tag{4.13}$$

The cooling power of the PTR was therefore calculated by measuring the heater output power with the cooling tower set to a temperature of 170 K, with the rest of the cryostat at room temperature. Figure 4.14a shows the heater power and the vacuum level of the cryostat as a function of time during the HV cable feedthrough test, as described in section 4.3.3. Taking the average of the heater output over three days, we determined that $\dot{Q}_{\mathrm{H}} = (155.6 \pm 0.3)\,\mathrm{W}$ at 170 K.

We can easily demonstrate with a simplified calculation that the other two parameters had very little impact on the measurement. First, the thermal conduction can be approximated by calculating the thermal exchange power through the stainless steel pipe linking the cooling tower to the inner vessel and by assuming that both the cold head and the cooling tower are at $T_1 = 170\,\mathrm{K}$ and the inner vessel is at $T_2 = 298\,\mathrm{K}$. The pipe has a length of $d = 0.43\,\mathrm{m}$ and is 42 mm in outer diameter, with a 2 mm wall thickness. Hence, the cross-sectional area of the conductive material is

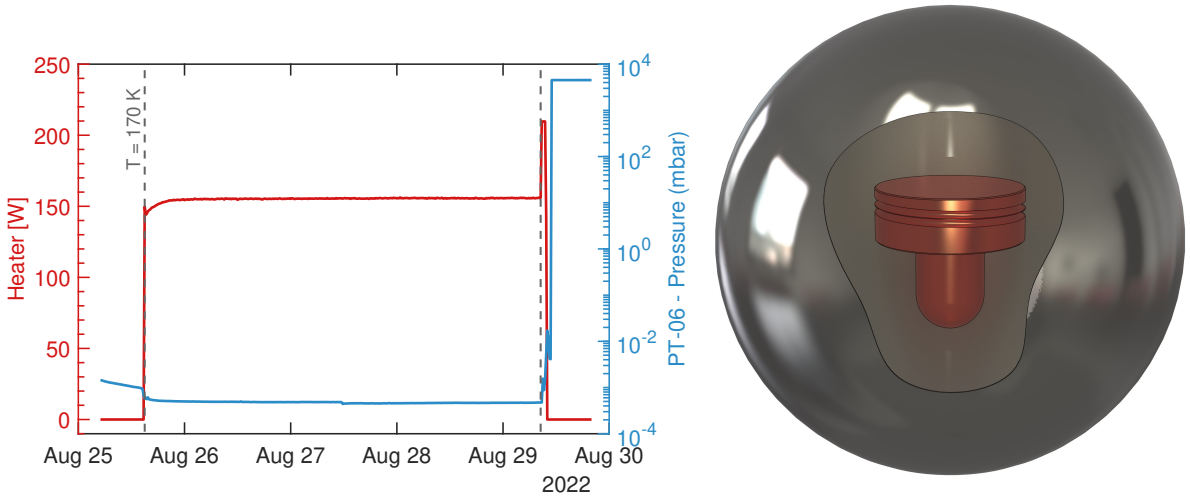

(a) (b)

Figure 4.14: Calculation of the PTR cooling power. **(a)** Heater output and vacuum level in the cryostat during the HV feedthrough test (section 4.3.3). The cold head was controlled at a temperature of $(170.000 \pm 0.001)\,\mathrm{K}$ between the two dashed lines. At equilibrium, the average heating power of the resistive heater was $(163.2 \pm 0.3)\,\mathrm{W}$. **(b)** Approximation of the radiative power, $\dot{Q}_{\mathrm{rad}}$, described in equation 4.15. A simplified model of the cold head at 170 K is installed inside a spherical stainless steel shell ($r_{\mathrm{Sph}} \gg r_{\mathrm{CH}}$), at room temperature.

$A = 2.5 \cdot 10^{-4}\,\mathrm{m}^2$. The thermal conduction power is then calculated with:

$$\dot{Q}_{\mathrm{cond}} = \frac{\kappa A\,(T_2 - T_1)}{d}\,, \tag{4.14}$$

where $\kappa = 15.256\,\mathrm{W/(m \cdot K)}$ is the thermal conductivity of 304 stainless steel [328]. The conductive heat transfer rate is therefore estimated at $(1.20 \pm 0.12)\,\mathrm{W}$, attributing a 10 % conservative error.

Secondly, the radiative heating power can be approximated by surrounding a simplified model of the cold head (subscript: CH) with a stainless steel sphere (subscript: sph) at room temperature, as shown in figure 4.14b. In reality, the cold head in Xenoscope is completely surrounded by the cooling chamber and the vacuum vessel. The surface area of the copper cold head is estimated at $0.060\,\mathrm{m}^2$. For simplicity, we can use a few assumptions: the two objects are considered "grey bodies" (i.e. bodies whose emissivities are independent of the radiated wavelength); the dimensions of the sphere are such that $r_{\mathrm{Sph}} \gg r_{\mathrm{CH}}$; the space between the objects is at perfect vacuum level such that there is no heat exchange with gases; and the temperatures of both surfaces are constant over time. As an approximation, we can use the formula for the radiative heat transfer between two concentric spheres, from the inner sphere to the outer sphere [329]:

$$\dot{Q}_{\mathrm{rad}_{\mathrm{CH}\to\mathrm{sph}}} = \frac{\sigma \cdot A_{\mathrm{CH}} \left(T_{\mathrm{CH}}^4 - T_{\mathrm{sph}}^4\right)}{\frac{1}{\varepsilon_{\mathrm{CH}}} + \frac{1-\varepsilon_{\mathrm{sph}}}{\varepsilon_{\mathrm{sph}}} \left(\frac{r_{\mathrm{CH}}}{r_{\mathrm{sph}}}\right)^2}\,, \tag{4.15}$$

where σ is the Stefan-Boltzmann constant $(5.670\,374\,419 \cdot 10^{-8}\,\mathrm{W \cdot m^{-2} \cdot K^{-4}})$ [330], A_i are the areas of the two objects, T_i are the temperatures of the objects (sphere: 298 K, cold head: 170 K), and ε_i are the emissivity coefficients (stainless steel: 0.075, copper: 0.052 [331]). Inputting these values in equation 4.15, we can estimate that the radiative heating power from the sphere to the cold head is $\sim (1.30 \pm 0.13)\,\mathrm{W}$, attributing a 10 % conservative error. Note that we assume no shielding

from the MLI, and this heating power is taken as an upper limit, assuming the MLI is also at room temperature. Inputting the three heat transfer rates into equation 4.13 yields, at a cold head temperature of 170 K:

$$\begin{aligned} -\dot{Q}_{\mathrm{PTR}} &= (155.6 \pm 0.3)\,\mathrm{W} + (1.20 \pm 0.12)\,\mathrm{W} + (1.30 \pm 0.13)\,\mathrm{W} \\ &= (158.1 \pm 0.4)\,\mathrm{W}. \end{aligned} \tag{4.16}$$

Calculation of the Heat Load of the Full Cryostat

$\dot{Q}_{\mathrm{cryostat}}$ is the heat load on the system due to the recondensation of the xenon in the cryostat, and due to thermal conduction and radiation losses. Naturally, the operation of the cooling tower alongside the xenon purification system increases the heat load on the system, as part of the LXe is extracted from the cryostat and is then evaporated in the umbilical section and in the heat exchanger. This process is energetically efficient, with a heat loss of only 2 – 3 % [2]. Using equation 4.13, we can write:

$$\begin{aligned} -(\dot{Q}_{\mathrm{PTR}} + \dot{Q}_{\mathrm{H}}) &= \dot{Q}_{\mathrm{pur}}(\dot{m}) + \dot{Q}_{\mathrm{cond}} + \dot{Q}_{\mathrm{rad}} \\ -(\dot{Q}_{\mathrm{PTR}} + \dot{Q}_{\mathrm{H}}) &= \Omega_{\mathrm{pur}} \cdot \dot{m} + \dot{Q}_{\mathrm{cond}} + \dot{Q}_{\mathrm{rad}}\,, \end{aligned} \tag{4.17}$$

where Ω_{pur} is the xenon flow heat transfer coefficient, in units of [W/slpm], $\dot{m}$ is the xenon mass flow, in units of [slpm], and $\dot{Q}_{\mathrm{cond}} + \dot{Q}_{\mathrm{rad}}$ can be expressed as one constant as we cannot measure them separately. Figure 4.15 shows $-\dot{Q}_{\mathrm{PTR}} - \dot{Q}_{\mathrm{H}}$ as a function of the xenon mass flow at thermal equilibrium, during the commissioning phase and the 0.53 m PM run. We assume that $-\dot{Q}_{\mathrm{PTR}}$ is constant in time, with the value calculated above. We can determine that the zero-flow heat input was (25.9 ± 0.3) W for the commissioning, and (20.9 ± 2.5) W for Run 3. The purification heat gain, which includes the inefficiencies of the heat exchanger as described in ref. [2], were (0.269 ± 0.008) W/slpm and (0.53 ± 0.08) W/slpm for the commissioning and the PM run respectively. The significant difference between the two operations, apart from the total mass of LXe

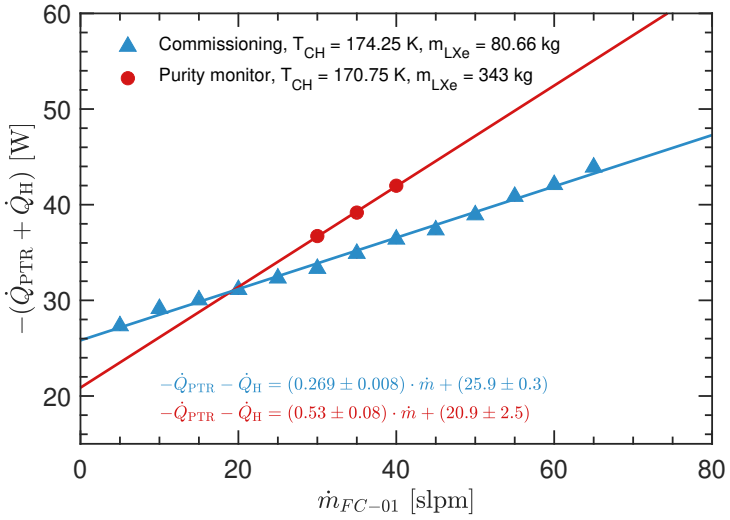

Figure 4.15: Measured heat load of the cryostat. The two measurements were performed in different thermodynamic conditions and with different amounts of LXe, which can explain the different behaviours of the facility.

deployed, is the temperature at which the cryostats were cooled. During the commissioning, the liquid temperature, and therefore the pressure in the cryostat, was allowed to vary with different flows, keeping the temperature of the cold head constant at 174.25 K. During the PM run, the temperature was adjusted to obtain a pressure of (2.00 ± 0.05) bar. We can solve for $\dot{m}$ in the two equations to determine the maximum operating mass flow for Xenoscope, attained when $\dot{Q}_{\mathrm{H}} = 0$. Hence, the maximum theoretical recirculation flow for the commissioning was 491.5 slpm and the one for the PM run was 258.9 slpm. In both cases, this theoretical limit far exceeds the performance limits of the GXe compressor.

4.2.5 Electron Lifetime Measurement and Data-Driven Model

In this section, we describe the modifications made to the electron lifetime model compared to the one presented in section 4.2.2, followed by the results of the electron lifetime measurement.

Modification of the Electron Lifetime Model

The modifications made to the definition of the electron lifetime model were supported by lessons learned from the operation of the PM in Xenoscope, and by the electron lifetime data. The first main change in the electron lifetime model is the modification of the outgassing terms Λ from equation 4.6 to a time-dependent form. As stated in ref. [263], the outgassing rate can be well described by:

$$\begin{aligned} \Lambda_{\mathrm{g}}(t) &= \frac{\Lambda_{\mathrm{g},0}}{1+\frac{t}{T_{1/2,g}}} + C_{\mathrm{g}} \\ \Lambda_{\mathrm{l}}(t) &= \frac{\Lambda_{\mathrm{l},0}}{1+\frac{t}{T_{1/2,l}}} + C_{\mathrm{l}}, \end{aligned} \tag{4.18}$$

where Λ_0 is the outgassing rate at the initial point in the model, $T_{1/2}$ are the half-lives of the exponential desorption rates, and C is a constant outgassing term, such that as oxygen adsorbed in the materials of the pressure vessel and detector parts is desorbed, $\Lambda\left(t \gg T_{1/2}\right) = C$. After a long purification time, the outgassing and purification rates equalise, yielding a constant electron lifetime.

Secondly, as will be seen further in this section, the electron lifetime trend is not ideal as in the predictive model of section 4.2.2, but instead is characterised by sudden drops in purity. We must therefore model instantaneous dynamic changes in the concentration of impurities at these "discontinuities". These should, however, be motivated by observations of thermodynamical changes in the operational conditions of the system. We mathematically model these sudden changes in impurity levels with:

$$\begin{aligned} M_{\mathrm{g}} \frac{dI_{\mathrm{G}}}{dt}^{(j)} &= M_{\mathrm{g}} \Delta I_{\mathrm{g}}^{(j)} \int \delta\left(t - t^{(j)}\right) \mathrm{d}t \\ M_{\mathrm{l}} \frac{dI_{\mathrm{l}}}{dt}^{(j)} &= M_{\mathrm{l}} \Delta I_{\mathrm{l}}^{(j)} \int \delta\left(t - t^{(j)}\right) \mathrm{d}t, \end{aligned} \tag{4.19}$$

where, for the j^{th} discontinuity, the $\Delta I^{(j)}$ are the magnitudes of the rises in impurity levels, and $\delta\left(t - t^{(j)}\right)$ are delta functions used to determine the time at which the impurity release happens [325]. Additionally, some of the impurities released at these discontinuities are expected to be adsorbed

by detector material, increasing the outgassing rate [263]. This can be seen as an instantaneous revert of the time evolution of the outgassing. We model this by substituting the time parameter t in equation 4.18 by $t-\Delta t^{(j)}$, where $\Delta t^{(j)} = \sum_1^j \Delta t^{(i)}$. The time offsets are cumulative since the dataset is fitted as a whole. The time offset in the first modelled region is, by definition, $\Delta t^{(0)} = 0$.

These dynamic rises in impurity levels can be hard to model as the precise mechanisms involved are not entirely known. We can assume, for example, that impurities in high concentration get trapped in the liquid surface collar (the region at the triple interface of the GXe, LXe, and stainless steel wall, where the surface tension is high) and are liberated following a change in liquid level. This effect is also observed in bubble chambers, where the collar trigger rate is high [332, 333]. A change in the height of the liquid level can be caused by a change in recirculation flow, by a change in pressure, or by the addition or removal of xenon. They can also be caused by the release of trapped air (from virtual leaks), or from other small leaks. The expected effect is then a rapid drop in electron lifetime. The electron lifetime trend should then return to the exponential rise as the impurities are quickly removed by purification. With time, the electron lifetime should return to the same outgassing-dominated trend as before the discontinuity.

Therefore, taking these two modifications into consideration, the full electron lifetime model can now be expressed as:

$$M_\mathrm{g}\frac{\mathrm{d}I_\mathrm{g}}{\mathrm{d}t}^{(j)} = -F_\mathrm{g}\,\rho\,I_\mathrm{g} + \left(\frac{\Lambda_{\mathrm{g},0}}{1+\frac{t-\Delta t_g^{(j)}}{T_{1/2,g}}} + C_\mathrm{g}\right) + \frac{\varepsilon_\mathrm{vap}P_\mathrm{C}I_\mathrm{l}}{h} - \frac{\varepsilon_\mathrm{cond}PI_\mathrm{g}}{h} + M_\mathrm{g}\,\Delta I_\mathrm{g}^{(j)}\int\delta\left(t-t^{(j)}\right)\mathrm{d}t \quad (4.20)$$

$$M_\mathrm{l}\frac{\mathrm{d}I_\mathrm{l}}{\mathrm{d}t}^{(j)} = -F_\mathrm{l}\,\rho\,I_\mathrm{l} + \left(\frac{\Lambda_{\mathrm{l},0}}{1+\frac{t-\Delta t_l^{(j)}}{T_{1/2,l}}} + C_\mathrm{l}\right) - \frac{\varepsilon_\mathrm{vap}P_\mathrm{C}I_\mathrm{l}}{h} + \frac{\varepsilon_\mathrm{cond}PI_\mathrm{g}}{h} + M_\mathrm{l}\,\Delta I_\mathrm{l}^{(j)}\int\delta\left(t-t^{(j)}\right)\mathrm{d}t. \quad (4.21)$$

As stated before, the superscript j identifies the regions between discontinuities. Each differential equation consists of five terms. The first equation is normalised with the masses of GXe M_g, and the second with the mass of LXe M_l. In each equation, the first term accounts for the purification rate, with F the purification flow, ρ the density of xenon at 1 bar, 0 °C, and I the concentration in O_2-like impurities. The second term accounts for the time-dependent average outgassing rate, as described above. The third and fourth terms describe the exchange of impurities between the gas and liquid phases through evaporation and condensation respectively. These processes are equivalent but opposite among the two equations. Hence, the signs are inverted. The ε parameters are the attachment probabilities for both exchange processes. P_C is the cooling power of the system in the absence of purification, which is proportional to the evaporation rate of the xenon, and P is the cooling power deployed by the cryogenics, which proportional to the condensation rate. Finally, h is the latent heat of xenon. The fifth term describes the sudden injections of impurities.

Electron Lifetime Measurement and Results

The measurement of the electron lifetime in Xenoscope was performed continuously throughout Run 3 to study the effect of the recirculation flow on the electron survival probability. This, in turn, can inform us on some facility-specific properties, such as the outgassing rate and the overall performance of the purification system.

The measurement principle discussed in section 4.2.1 was used, with the current-proportional signals measured in regions 1 and 3. As these regions are much smaller than region 2, the loss of

electrons in these regions is negligible, and the drift time used in equation 4.3 is t_2, calculated for every waveform acquired, as displayed in figure 4.7b.

A Teledyne LeCroy model Waverunner 6200 oscilloscope [334] was used to acquire both charge signals. The charge readouts at the cathode and the anode are in-house made transimpedence amplifiers. In comparison to charge amplifiers, transimpedance amplifiers are current-to-voltage converters that allow for more precise timing and signal spread analyses due to their smaller RC constant and shorter rise time. However, they are prone to electronic noise pickup, and a 800 kHz low-pass filter had to be applied to the recorded signals to filter out electronic noise caused by nearby instruments, such as the pulse generator used to trigger the xenon flash lamp, RTDs, and the UPS. Nevertheless, a 40 kHz electronic noise coming from the UPS, with a similar time characteristic to our acquisitions, remained.

Early on in the measurement campaign, it became apparent that the signal-to-noise ratio of the apparatus was not sufficient to obtain one electron lifetime measurement per flash lamp pulse. The recorded waveforms were therefore the waveform-averages over 1 000 acquisitions, acquired at a rate of 1 Hz. Each data point was therefore acquired over 16.7 minutes. This significantly reduced the effects of random noise components. While the electron lifetime is a continuously varying parameter, the outgassing and purification are continuous and monotonously decreasing with increasing electron lifetime in the absence of external factors, such as the instantaneous introduction of electronegative impurities from a leak. The electron lifetime should, therefore also be smooth and continuous. The waveform-averaging should be representative of the electron lifetime over this time-scale. Figure 4.16 shows an example of an averaged waveform at the anode. The raw waveform is displayed in blue, and the signal processed with the low-pass filter is in orange. Each waveform is processed with a three-component fit:

$$V(t) = \left[\frac{1}{\sigma\sqrt{2\pi}} \cdot e^{-\frac{(t-t_0)^2}{2\sigma^2}}\right] + [A \cdot \sin(\omega \cdot t + \phi)] + H_0\,. \tag{4.22}$$

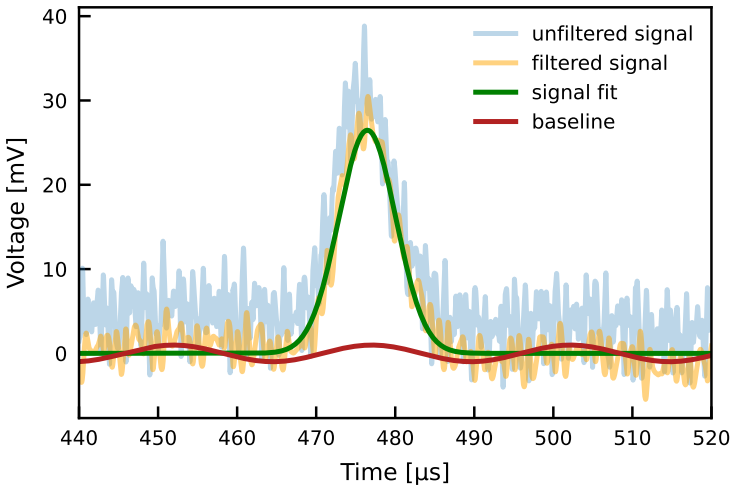

Figure 4.16: Example of a 1 000 waveform average. The raw-waveform (blue) is filtered with a 800 kHz filter (orange). The filtered waveform is then fitted with the sum of a Gaussian, a sinus and a constant. The contributions of the Gaussian (green) and the sinus + constant (red) are displayed separately. In this example, the baseline adds to the signal. In cases where the baseline is shifted by $\phi = \pi$, the baseline subtracts to the charge signal.

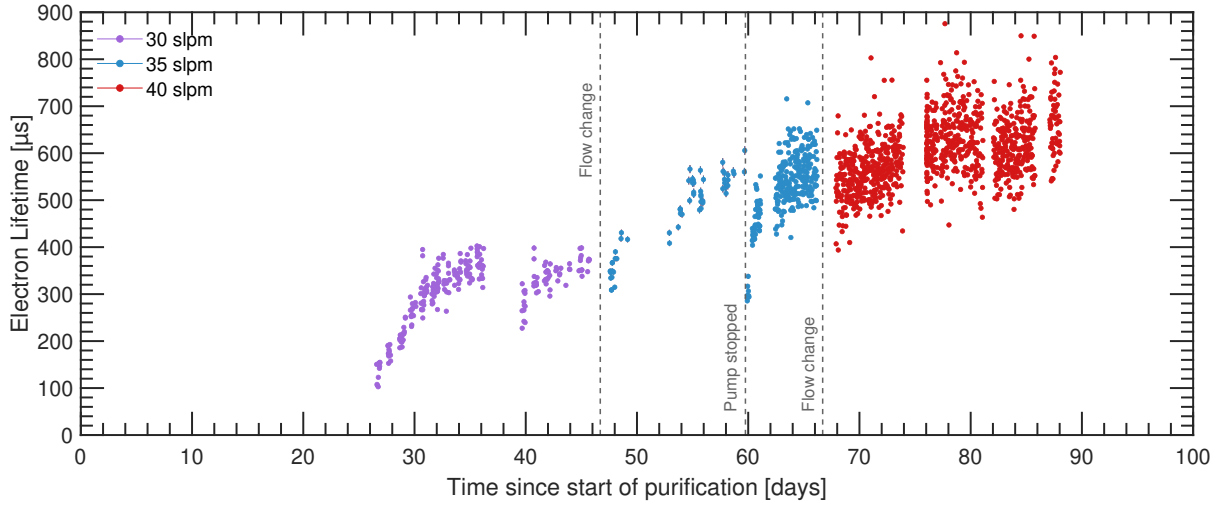

Figure 4.17: Unbinned electron lifetime measurement with the LXe purity monitor in Xenoscope. Each point is the waveform-average of 1 000 acquisitions taken over 16.7 min. The dashed vertical lines identify the moments where the electron lifetime is expected to have suffered a drop due to changes in the operating conditions of the facility.

This sum of a Gaussian function (charge signal, green), and a sine wave function and a constant (noise, red), allows us to more accurately estimate the separate contributions of the signal, and of the baseline. The latter cannot be filtered out because the wavelength of the noise is of the same time-order as that of the charge signals. The current-proportional signal is then calculated as the full integral of the Gaussian, with the statistical uncertainty obtained from the fit parameters. Additionally, the difference between fitting the signal with and without the sinus contribution is up to $\pm$ 5 %. Therefore, in waveforms where the baseline cannot be properly fitted, a conservative $\pm$ 5 % systematic error is applied. The actual charge, and hence the number of electrons, could be calculated if the absolute gain of the amplifier was known. This is however not needed, as the electron lifetime measurement relies on the ratio of the two charge signals.

Figure 4.17 shows the time-unbinned electron lifetime calculated from equation 4.3. The time $t = 0$ is the time when the purification loop was turned on at a recirculation flow of 30 slpm. The dashed vertical lines identify the two purification flow changes and the time at which the GXe compressor was stopped for a period of approximately 15 min. These three events certainly changed the thermodynamic conditions in the cryostat, slightly varying the height of the liquid level. As mentioned before, this can liberate impurities trapped in the high-surface tension region of the collar, where the LXe, the GXe, and the wall of the inner vessel interface. At least a few extra discontinuities can be discerned by eyes, although there were no prior indications that this should be the case. Due to the significant variance between the measurements, the data were weighted-averaged into 6 h time bins. The weights were chosen as $w_i = 1/\Delta\tau_{e,i}^2$, where $\Delta\tau_{e,i}$ is the uncertainty of the i^{th} point. The uncertainty on the binned data is then the standard error $\sigma/\sqrt{N-1}$, where σ is the standard deviation, and N is the number of data-points in each bin. The binned electron lifetime is shown in figure 4.18.

With the binned data, the discontinuities at both purification flow changes, respectively at 46.70 and 66.69 days after the start of the purification, are made even more evident. Additionally, the 15-minute long GXe compressor stoppage experienced at 59.75 days shows the largest drop in electron lifetime over the whole run. As this happened during a period of continuous data acquisition, data points before and after the pump stoppage were put in two different bins to avoid

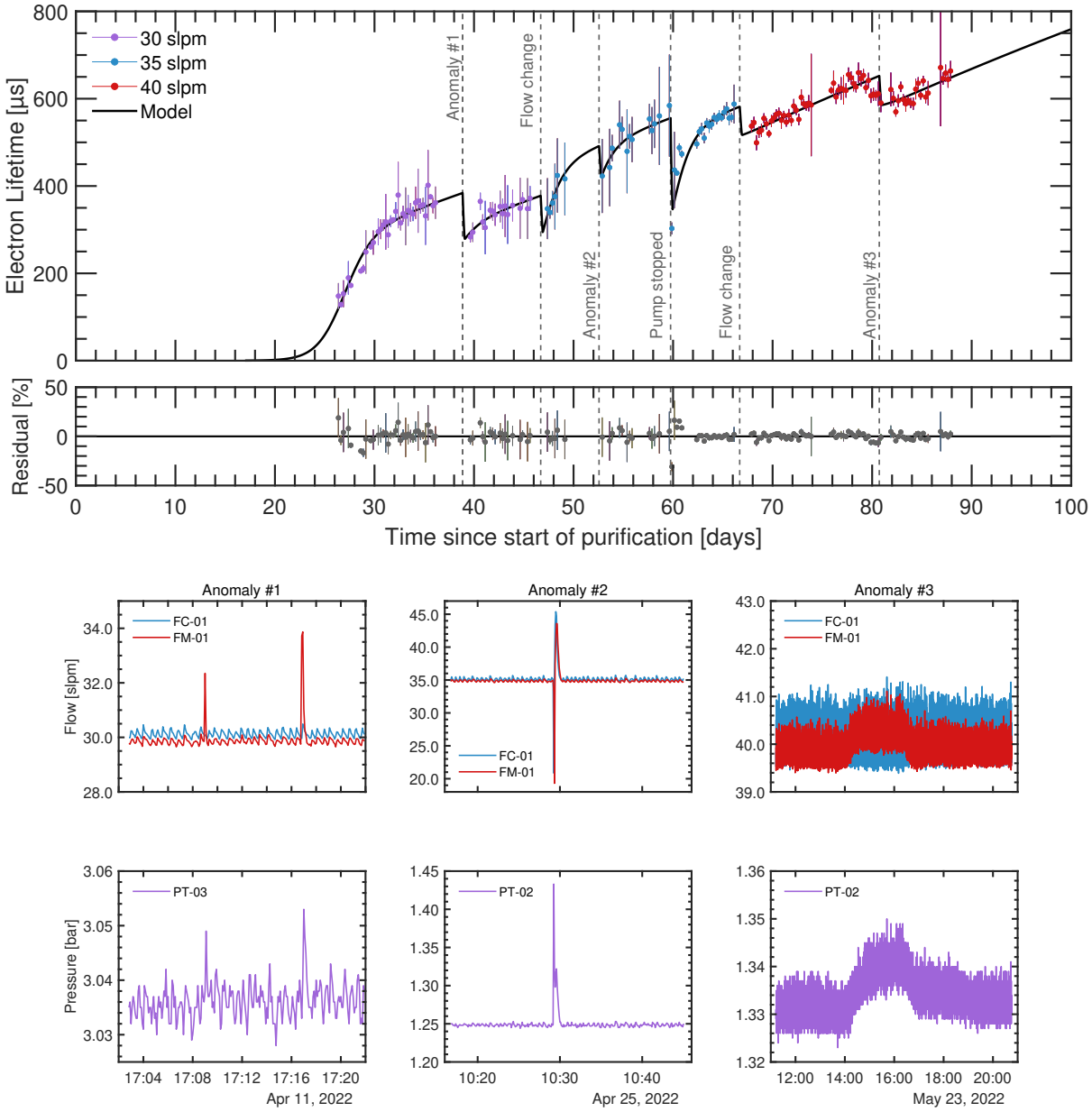

Figure 4.18: Binned electron lifetime measurement in Xenoscope. The data was weighted-averaged in 6 h time bins. The six sub-figures show the GXe flow (top row), and the GXe compressor pressures (bottom row) for the three anomalies.

mixing the two types of data (high vs. low electron lifetime), which would artificially lead to a large variance. The system promptly returned to its previous purity level within one week and the model seems to then well describe the data again. A visual analysis of the dataset permitted the identification of three unexpected regions of sharp decrease in electron lifetime. A search in the slow control data revealed three anomalies compatible with these losses of purity. These are identified in figure 4.18 by additional dashed vertical lines.

The first anomaly is characterised by two sharp flow increases that lasted less than 10 s each. Since the time resolution of the SC data is 5 s, the two events were most likely instantaneous. As no flow increase is observed in the flow controller FC-01, we can suppose that the excess flow was

caused by a microscopic leak or the release of trapped gas. Concurrently with the increase in flow, a small pressure increase downstream of the GXe compressor can be observed. No significant pressure increase in the inner vessel could be detected.

The second anomaly is a significant rise in pressure upstream of the GXe compressor. In this instance, no difference in the xenon mass flows was observed. Instead, both flow measurements, upstream and downstream of the GXe compressor, experienced a short and sharp drop, followed by a sharp rise. The pressure downstream mimicked the flow, while the pressure upstream, shown in the anomaly #2 pressure plot, shows only a rise. The net result on the inner vessel was a slight drop in pressure. The whole event spanned approximately one minute.

The third anomaly is fundamentally different than the first two, lasting more than 2.5 h. A marginal but constant flow increase can be observed in the SC data of the flow meter downstream of the GXe compressor, while the upstream flow controller kept a constant flow output. Pressures upstream and downstream of the compressor, and in the inner vessel, were slightly elevated during this time period.

Ultimately, after over 88 days of purification, we reached in Xenoscope an electron lifetime of $(681 \pm 17)\,\mu s$. While this is still considerably short of the target of 1.75 ms, the reach in the electron lifetime was limited by the maximal recirculation flow of the GXe compressor. This effect can be demonstrated with the fit of the electron lifetime model to the data of Run 3.

The electron lifetime model was calculated by solving the system of differential equations (equations 4.20 and 4.21) with a differential equations integrator (Python – spicy.integrate.odeint [335]), calculating the electron lifetime from the impurity concentration in the liquid phase with equation 4.3, and minimising with the iMinuit package (Python) [336]. This is done simultaneously in all j-regions, using a χ^2 minimisation. However, due to the nature of the differential equation integrator, instantaneous changes in impurity levels can easily make the minimiser diverge. Therefore, the injection of impurities in the system must be done over a time dt, chosen to be 0.2 days. In addition, the electron lifetime model seems not well suited for describing the conditions of Xenoscope at the moment where the purification was switched on. Indeed, the concentration in impurities and the outgassing were possibly elevated at the start of the run, and the lack of electron lifetime data prevents us to adapt the model correctly. Therefore, the model was fitted from time $t = 17$ days. The best fit of the model is displayed as a solid black curve in figure 4.18. The reduced chi-square value of the fit to the data is:

$$\chi^2_\nu = \frac{\chi^2}{\nu} = 1.47 \tag{4.23}$$

where $\chi^2 = 186$ is the chi-square value, and $\nu = n - m = 129$, the number of degrees of freedom, is the difference between the number of data points ($n = 159$) and the number of free parameters ($m = 32$). From the residuals in figure 4.18, we can see that the fit to the model is not good at the time where the pump stopped. The release of trapped impurities is most probably not well described by our current model, which assumes a homogeneous distribution of the impurities in the gas and liquid phases. Another discrepancy is found at anomaly #3. The electron lifetime seems to start decreasing before the observed anomaly. As there is no indication in the SC data as to why this is, we chose to model the electron lifetime drop according to the anomaly observed in the SC data. The best-fit parameter values are compiled in tables 4.5 and 4.6.

The masses of xenon used in the fit are, for the GXe phase $M_g = 0.652\,kg$, estimated from the CAD drawings, and for the LXe ($M_l = 343\,kg$, estimated from the filling and recuperation. While the model minimisation behaved well overall, the vaporisation and condensation parameters were troublesome. If the efficiencies are allowed to be free in the model, the minimiser tends to find

Parameter	Value	Uncertainty	Unit	Free
ρ	$5.897 \cdot 10^{-3}$	–	$\mathrm{kg/m^3}$	N
K	$1.52 \cdot 10^{-3}$	–	$\mu\mathrm{s}^{-1}\cdot\mathrm{ppb}^{-1}$	N
h	95 587	–	kJ/kg	N
M_g	0.652	–	kg	N
M_l	343	–	kg	N
F_g	0	–	slpm	N
F_l	30, 35, 40	–	slpm	N
P_C	32.37	–	W	N
$P(F_\mathrm{l}=30,35,40)$	38.18, 41.45, 44.69	–	W	N
$I_\mathrm{g}(t=17)$	$2.0 \cdot 10^4$	$8.9 \cdot 10^4$	ppb	Y
$I_\mathrm{l}(t=17)$	$3.3 \cdot 10^3$	$0.34 \cdot 10^3$	ppb	Y
ε_vap	0.326	0.650	–	C
$\varepsilon_\mathrm{cond}$	0.994	0.135	–	C
$\Lambda_{\mathrm{g},0}$	1.99e3	0.02e3	kg · ppb/d	Y
$\Lambda_{\mathrm{l},0}$	3.25e3	0.02e3	kg · ppb/d	Y
$T_{1/2,\mathrm{g}}$	2.95	0.06	d	Y
$T_{1/2,\mathrm{l}}$	2.67	0.03	d	Y
C_g	43.0	1.6	kg · ppb/d	Y
C_l	29.5	4.3	kg · ppb/d	Y

Table 4.5: Best-fit values of the parameters from the fit of the electron lifetime model to the purity monitor data. The last column indicates if a parameter was free (Y), fixed (N), or constrained (C).

Parameters	Value	Uncertainty	Unit	$t^{(i)}$ [d]	Free
$\Delta t_g^{(1)}$, $\Delta t_l^{(1)}$	6.6, 9.8	1.2, 0.3	d	38.85	Y
$\Delta t_g^{(2)}$, $\Delta t_l^{(2)}$	0.7, $5.7 \cdot 10^{-2}$	0.8, 1.3	d	46.70	Y
$\Delta t_g^{(3)}$, $\Delta t_l^{(3)}$	$7.2 \cdot 10^{-5}$, $8.9 \cdot 10^{-5}$	59, 19	d	52.56	Y
$\Delta t_g^{(4)}$, $\Delta t_l^{(4)}$	4.3, 3.3	1.3, 0.7	d	59.75	Y
$\Delta t_g^{(5)}$, $\Delta t_l^{(5)}$	15.5, 15.9	1.9, 1.0	d	66.69	Y
$\Delta t_g^{(6)}$, $\Delta t_l^{(6)}$	$1.9 \cdot 10^{-3}$, 11.5	36, 0.9	d	80.72	Y
$\Delta I_g^{(1)}$, $\Delta I_l^{(1)}$	474, 2.4			38.85	Y
$\Delta I_g^{(2)}$, $\Delta I_l^{(2)}$	350, 2.3			46.70	Y
$\Delta I_g^{(3)}$, $\Delta I_l^{(3)}$	620, 0.09			52.56	Y
$\Delta I_g^{(4)}$, $\Delta I_l^{(4)}$	$6.1 \cdot 10^{-4}$, 3.8			59.75	Y
$\Delta I_g^{(5)}$, $\Delta I_l^{(5)}$	197, 0.3			66.69	Y
$\Delta I_g^{(6)}$, $\Delta I_l^{(6)}$	$5.1 \cdot 10^{-5}$, $1.9 \cdot 10^{-3}$			80.72	Y

Table 4.6: Best-fit values of the time-dependent parameters from the fit of the electron lifetime model.

values for the best fit that seem nonphysical and counter intuitive, attributing values of $\varepsilon_\mathrm{cond} \approx 0$ and $\varepsilon_\mathrm{vap} \approx 1$. Given that Run 3 was performed with no gas phase purification ($F_\mathrm{g} = 0$), the resulting effect for this model is the accumulation of impurities in the gas phase, with no possibility for their removal. Trying to predict the electron lifetime with the addition of a small purification flow in the gas phase then lead to extreme improvements ($\tau_\mathrm{e} > 20\,\mathrm{ms}$) To remedy this, the parameters were

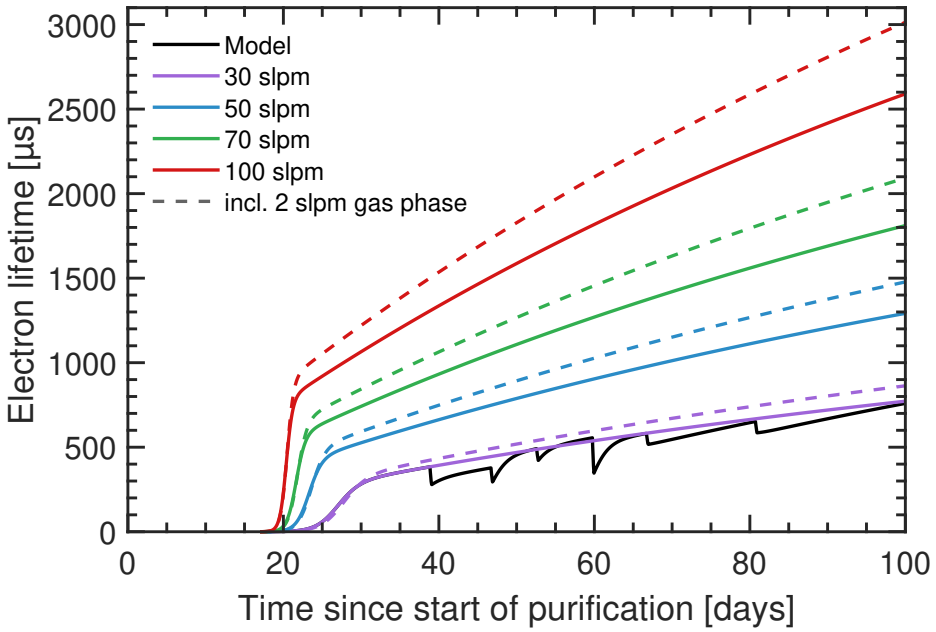

Figure 4.19: Purification flow dependent electron lifetime predictions. Assuming all things equal and idealised run conditions, an increased flow significantly reduces the purification time before the electron lifetime begins its exponential rise. Furthermore, the addition of a low-flow gas phase extraction to the purification loop can significantly improve the electron lifetime by removing impurities isolated in the gas phase, reducing the transfer of impurities through condensation.

constrained to the values obtained from the fit of the electron lifetime model of XENON1T reported in ref. [325].

Assuming the same initial conditions obtained from the fit of the model to the electron lifetime data, starting at $t = 17$ days after the start of the purification, we can produce prediction curves for the electron lifetime as a function of the purification flow. Some examples are shown in figure 4.19, where the solid lines are curves assuming the purification of the liquid phase only, and the dashed curves include a 2 slpm recirculation of the gas phase. The cooling power P is also adapted by extrapolating the heating power of the heater unit of the PTR, and assuming the PTR cooling power is constant as previously discussed. As expected, an increased purification speed would yield longer electron lifetimes, reached in a shorter purification time. Interestingly, the addition of a purification flow in the gas phase ($F_g = 2$ slpm) suggests an increase in electron lifetime of up to 15 % at the 100 day mark. To exploit this effect in the future, we have installed a parallel gas extraction line prior to the start of the TPC phase of Xenoscope. This is further discussed in section 4.3.4.

These prediction curves assume a 100 % purification efficiency. However, it is known that hot metal getters tend to lose in efficiency as they age, with the manufacturer recommending the replacement of the active material every 365 days of operations in the case of the PS4-MT50-R-535. Furthermore, at high recirculation flows, the purification efficiency tends to drop as the xenon does not spend enough time in the getter cartridge [325].

4.3 Phase 2: The 2.6 m Time Projection Chamber

Following an efficient and successful R&D campaign for the additional subsystems discussed in this section, the scientific schedule of Xenoscope was moved up in September 2022, skipping the originally planned 1.0 m TPC phase reported in ref. [1] and upgrading directly the detector to a full- DARWIN-height TPC.

In this second phase of the experiment, the PM is converted to a dual-phase xenon TPC, as shown in a CAD rendering of the top section of the detector in figure 4.20, where most of the modifications are made. A display of the aspect-ratio of the TPC can be seen on the right. Figure 4.21 shows the TPC in its assembly stage. The modular design of the field cage makes its extension straight forward. The bottom section of the PM is also reused in the TPC configuration, still providing a triggered source of electrons at a known distance from the top section. The cathode grid is, however, not needed and was therefore removed. The conversion to a dual-phase TPC requires the addition of several new subsystems.

In this section, we describe some of the significant upgrades performed before the start of Phase 2. A description of three important subsystems is first given: the liquid level monitor and control system in section 4.3.1, the SiPM array in section 4.3.2, and the HV distribution system in section 4.3.3. We also present in section 4.3.4 an upgrade of the purification system that allows for the purification of the GXe phase inside the cryostat. We finally describe a protocol for the removal of copper oxide from the field-shaping rings in section 4.3.5.

4.3.1 Liquid Level Monitor and Control System

The successful upgrade to a dual-phase TPC requires good control of the liquid level, which ensures a uniform amplification of the charge-proportional signal. As explained in section 3.2.2, the x-y levelling is achieved by adjusting the height of the levelling legs at the top of the cryostat.

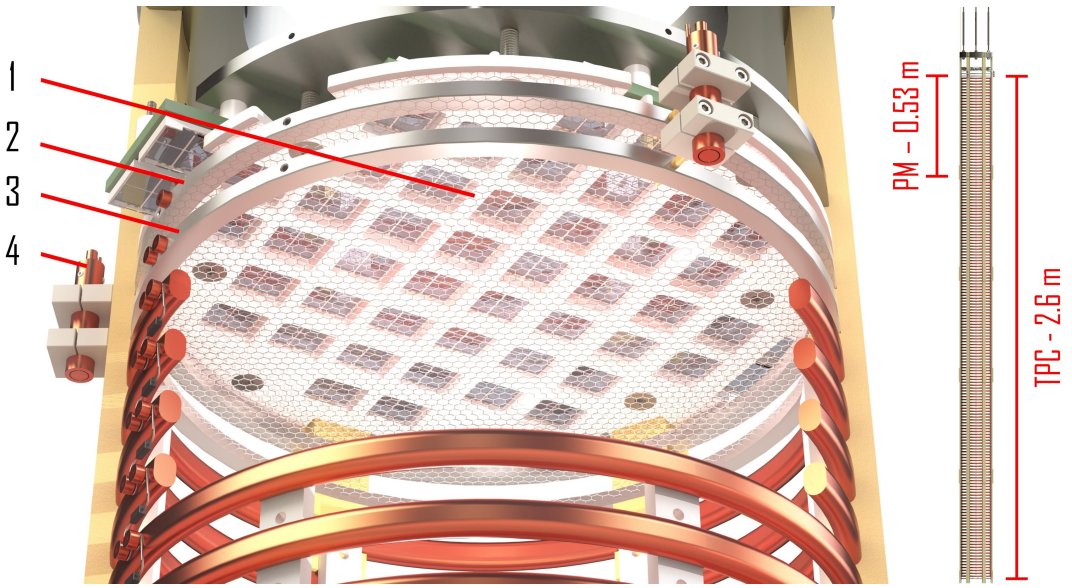

Figure 4.20: The 2.6 m TPC of Xenoscope. The upper section hosts the SiPM array and the short level meters. The aspect-ratio of the TPC is shown on the right. Legend: (1) SiPM Array; (2) Anode mesh; (3) Gate mesh; (4) Short level meter. Figure adapted from ref. [1].

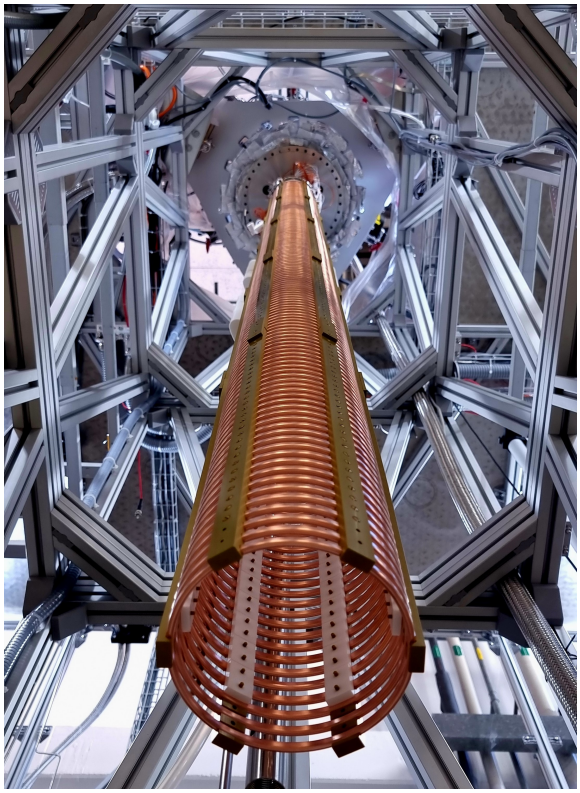

Figure 4.21: The installation of the 2.6 m TPC. In this up-looking view, the TPC is seen hanging below the top flange assembly. The photocathode is missing at the bottom, as it is the last component to be installed, concurrently with the closing of the inner vessel.

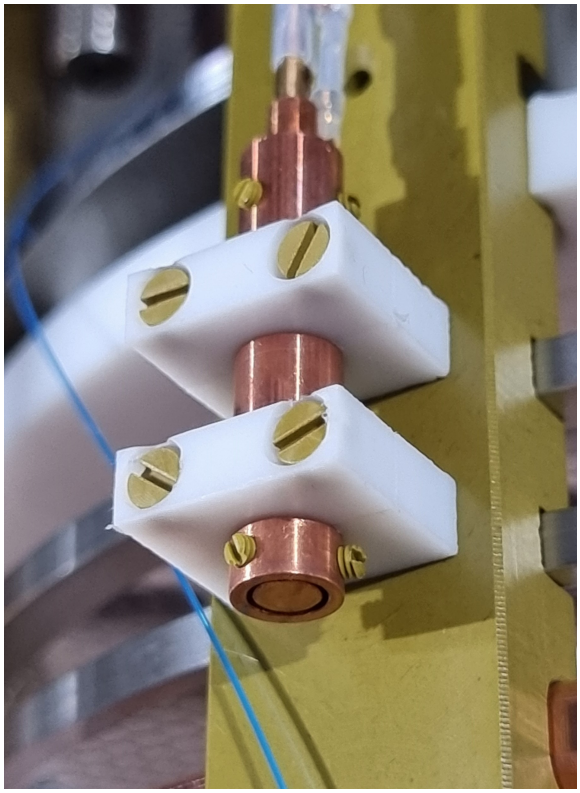

Figure 4.22: Short liquid level meter. The two capacitive cylinders are mounted concentrically, held in place with dielectric PAI screws. In this configuration, the level meters allow for a measurement range of 30 mm.

To monitor the tilt as well as the height of the liquid-gas interface relative to the TPC, three short, capacitive level meters as seen in figure 4.22 are installed at the height of the top electrodes, attached to three of the six pillars at 120° to one another [1]. The capacitance of the level meters changes as LXe enters the space between the two copper cylinders, due to the difference in relative permittivity of LXe and GXe [337]. This indicates the liquid level inside each level meter over a height of 30 mm.

The height of the liquid level is also monitored with a coarser, long level meter during filling and recuperating. Two 1.5-meter-long coaxial capacitive rods are monitoring the bottom and top halves of the cryostat, over its full length. PTFE insulating clamps discouple the level meters from the grounded support rod.

The liquid level height control system in Xenoscope is a weir, allowing for sub-mm control of the height of the gas-liquid interface. A UHVD [338] magnetically-coupled motion feedthrough, model MPP35-100-IS, is connected to the top of the weir assembly by a stainless steel rod. The vertical linear motion compresses or extends an edge-welded bellows section, which moves the overflow-hole in the central rod up or down with a resolution of 25 µm per half-turn of the stepper motor. Two limit switches restrain the range of motion of the actuator to protect the weir assembly in case of faulty command or misuse by operators. Figure 4.23 shows a schematic representation of the weir concept for Xenoscope. LXe from the central channel of the weir flows into the overspill cylinder. It is then extracted to the purification loop through a 1/2" PFA tubing. The position of the overflow

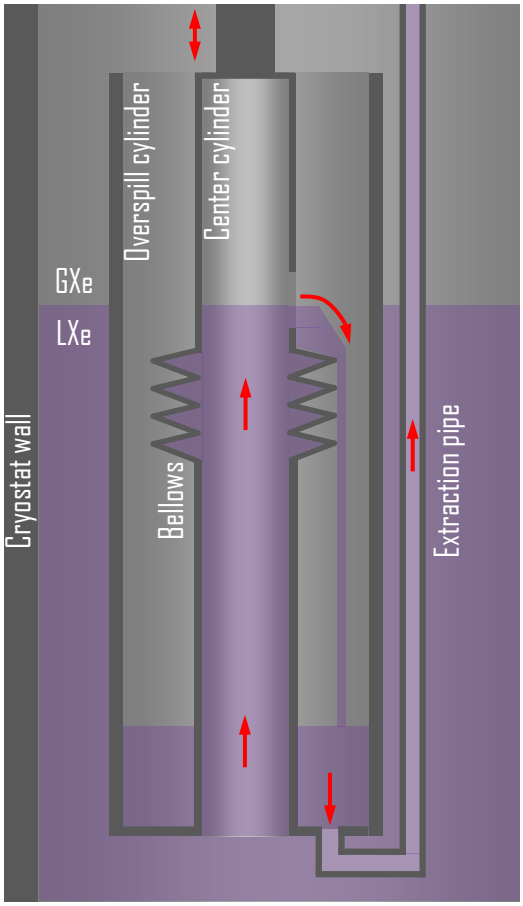

(a)

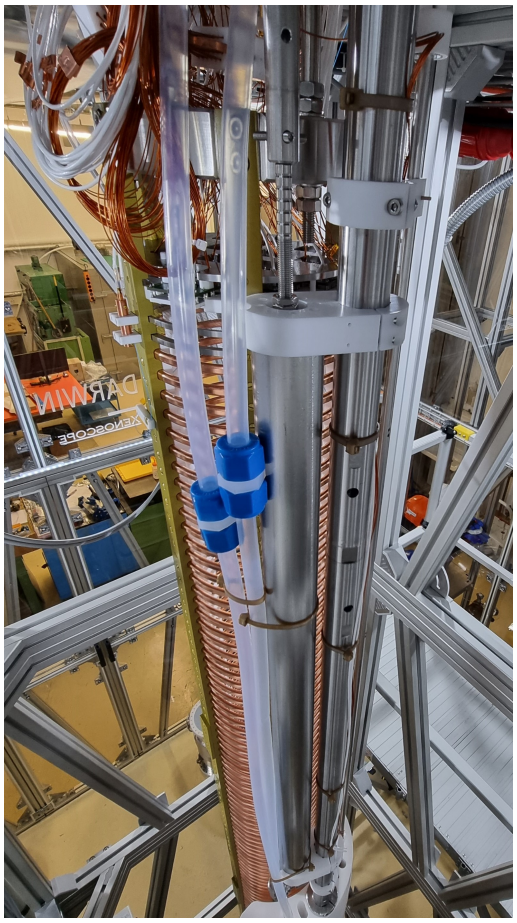

(b)

Figure 4.23: The liquid level control system. **(a)** Schematic of the liquid level control system. LXe is allowed to enter the center channel. When reaching the overflow hole, it spills into the overspill cylinder. The LXe is continuously extracted to the purification loop. **(b)** The weir installed in Xenoscope. The weir cylinder can be seen between the xenon extraction and return lines to the left, and the mounting rod to the right.

hole determines the overall height of the liquid level. Such a configuration prevents excessive variation of the liquid level due to external factors, such as pulsations from the recirculation pump, as it is a direct feedback system.

4.3.2 SiPM Array of Xenoscope

The conversion of the PM to a dual-phase TPC means the top charge readout of the PM is to be replaced by an array of photodetectors. Given the limited vertical space at the top of the cryostat, and following the successful operation of SiPMs in the Xurich II TPC [6], we decided to forgo the use of PMTs as described in the baseline design of DARWIN in chapter 2, and instead opted for SiPMs.

As is discussed in the next chapter, SiPMs have multiple advantages over PMTs, one of which is the small volume they occupy. However, this same advantage can be perceived as a major drawback, as each sensor ultimately covers a significantly smaller area. With the perspective of DARWIN, whose arrays will cover circular areas of $\mathcal{O}(2.6\,\mathrm{m})$ in diameter, we developed for Xenoscope a tiled

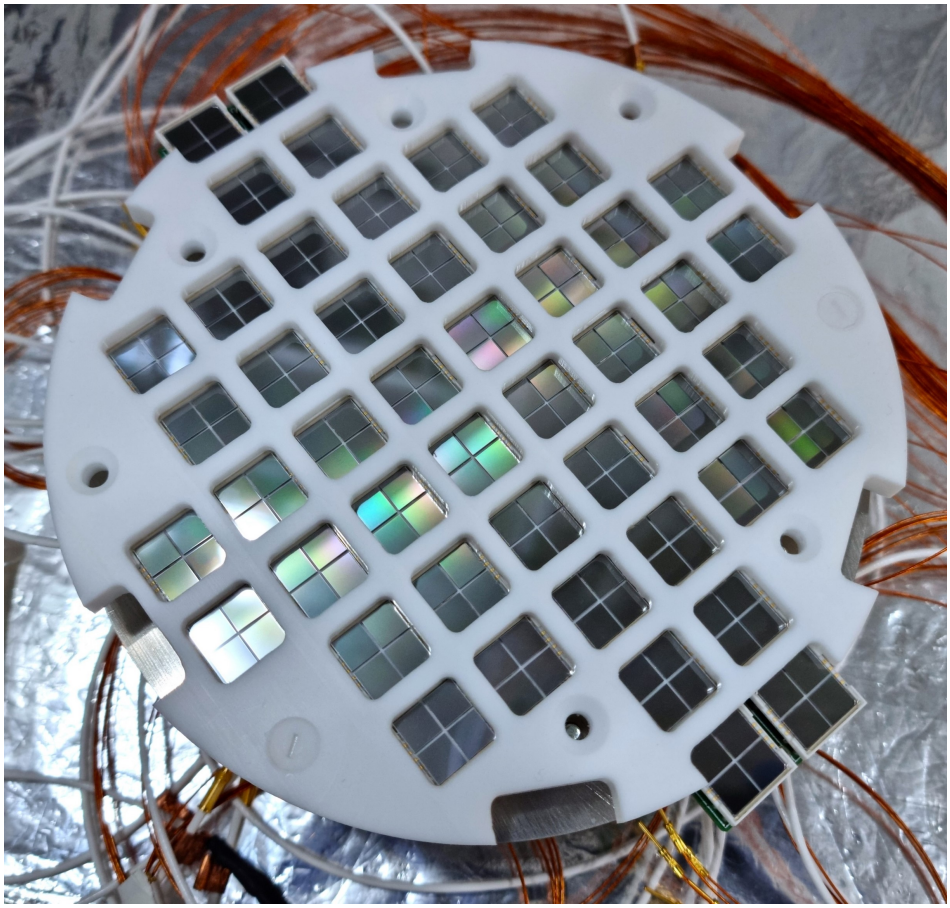

Figure 4.24: Fully assembled SiPM array of Xenoscope. Twelve tiles of 24×24 mm^2 total active area compose the array. In total, 192 individual 6×6 mm^2 SiPMs are used.

readout base, with the aim of reducing the number of readout channels by combining multiple SiPM units. This readout is inspired by a similar readout scheme published in ref. [339].

Figure 4.24 shows the fully assembled SiPM array with twelve channels, each constituted of tiles of four 12×12 mm^2 Hamamatsu VUV4 MPPCs, model S13371-6050CQ-02. Each MPPC is itself composed of four 6×6 mm^2 individual sensors. The readout scheme is shown in figure 4.25a, with a tile readout base in figure 4.25b. The readout circuit consists of the analogue sum of 16 – 6×6 mm^2 MPPC. The summed output is fed to a pre-amplifier circuit using a Texas Instruments OPA847 [340], voltage feedback Op-Amp. The 50 Ω current signals are fed to the Op-Amp, coupled to a 2 kΩ resistor, providing a gain of ×40. The signal is impedance-matched to 50 Ω, providing an amplification factor of ×20. Some tiles feature PT100 RTDs to accurately monitor the temperature as close to the SiPMs as possible.

Each quad MPPC was individually characterised for qualification purposes, and sensors were gain-matched to ensure uniform gains for all MPPCs on a given tile. The characterisation of these MPPCs is presented in refs. [234, 341]. Every MPPC passed the qualification phase, showing similar gains as a function of bias voltage. This will allow for the biasing of the full array from one common power supply, as the gain of every tile will be similar, at $\mathcal{O}\left(3 \cdot 10^6\right)$.

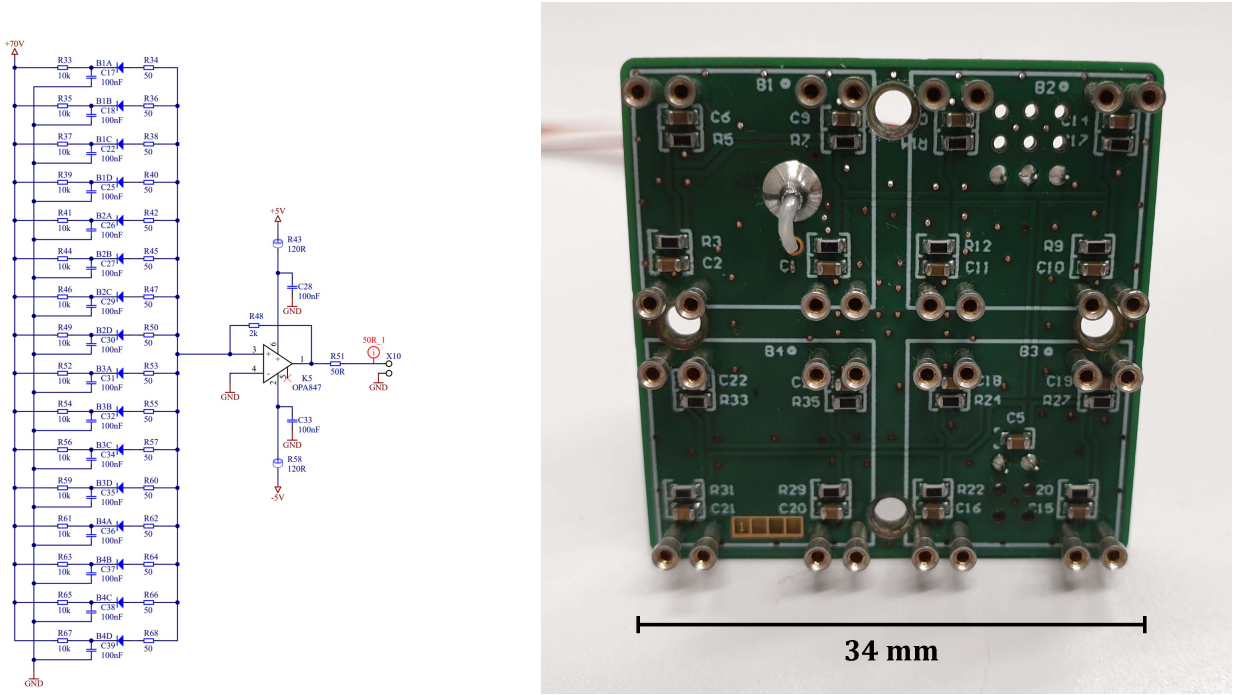

(a) (b)

Figure 4.25: Pre-amplified SiPM tile. **(a)** Schematic of the pre-amplifier circuit. A bias voltage is applied to the 16 MPPC units, and the outputs are summed. The output signal is passed through an Op-Amp, providing a gain of $\times 40$, gain matched to $50\,\Omega$ to provide an amplification factor of $\times 20$ [234]. **(b)** Pre-amplifier tile, which can host four 12×12 mm^2 quad MPPCs.

4.3.3 HV Distribution System

Air-to-vacuum HV feedthroughs are essential components in any vacuum system where HV is needed, ensuring the transmission of HV from an external power source to the vacuum chamber. Commercial HV feedthroughs are typically made of a brazed ceramic-metal junction. They have a low outgassing rate and can be used in a wide range of temperatures and pressures. They are however generally bulky, fragile, and expensive.

The LXe-to-vacuum feedthrough is a Ceramtec - Ceramaceal, 100 kV ceramic feedthrough [315]. The feedthrough was welded on a DN125CF flange, modified to reduce the risk of virtual leaks on the inner vessel side. The feedthrough assembly is rated for a pressure of 8.6 bar and a temperature range of 4 K to 723 K. To confirm the good performance of the welded flange-feedthrough configuration, the assembly was tested with 10 l of LN_2 while assembled in its final configuration in Xenoscope. The boil-off was used to produce pressures up to 4 bar, regulated with a configurable pressure relief valve.

Next, we have developed an air-to-vacuum feedthrough consisting of a commercially available 100 kV HV cable (Heinzinger HVC100 [342]) cryofitted to a custom DN40CF vacuum flange. This configuration, compared to traditional ceramic feedthroughs, is relatively simple to produce, necessitating only a small number of components. The cryofitted HV cable can then be produced in-house at a lower cost and can easily be adapted for custom applications. Figure 4.26 shows the design of the HV feedthrough. The cable has a total of six layers. From the center:

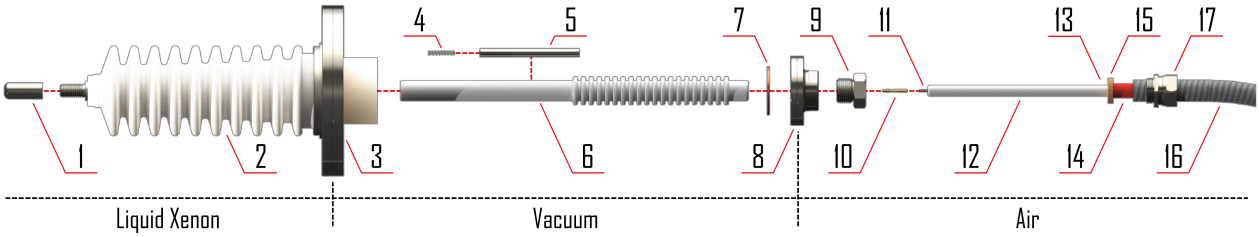

Figure 4.26: Design of the HV feedthrough. Legend: (1) Liquid-side HV terminal; (2) Ceramic HV feedthrough; (3) DN125CF flange; (4) Stainless steel spring; (5) Stainless steel connector; (6) Ultra-high molecular weight polyethylene (UHMWPE) insulator; (7) DN40CF gasket; (8) Custom DN40CF flange; (9) Grounding screw; (10) Vacuum-side HV terminal; (11) Cable core conductor; (12) UHMWPE cable insulator; (13) Cryofit region; (14) Polyvinyl chloride (PVC) cable outer layer; (15) Ground shield; (16) Plated steel outer shield; (17) Outer shield connector.

- Copper Conductor
- Black UHMWPE Core Insulator
- White UHMWPE Insulator
- Black Fabric Spacer
- Copper Shielding Braid
- Red PVC Insulator

The vacuum seal of the cable with the flange is made by stripping the cable of its three outermost layers. The white UHMWPE insulator has a nominal dimension of (10.7 ± 0.1) mm in diameter. The cable was slowly dipped in LN_2 and cooled down to 77 K. The thermal contraction of the cable is $\mathcal{O}(300-500\,\mu m)$ [343]. A hole of (10.200 ± 0.005) mm was machined on a lathe at the center of the DN40CF flange. This hole was incrementally increased by 25 µm at a time until the frozen cable easily fit in. The flange was cleaned with soap and water, acetone, and finally ethanol between each tries, to remove any residual metal particulates that could prevent the assembly to make a good vacuum seal. The HV cable was kept in LN_2 during the machining of the flange. Once inserted, the cable was positioned in the flange at the correct length, and was allowed to slowly warm up back to room temperature. The expansion of the UHMWPE effectively cryofits the cable to the flange, making a vacuum-tight seal. This procedure, including the preparation and cooldown of the cable, machining of the hole in the flange, and cryofitting of the assembly, can be performed in a few hours.

The cryofitting process is shown in figure 4.27. After cryofitting, the copper core conductor of the cable was heated with a soldering iron at both ends, melting the black UHMWPE insulator tightly around it. This ensures an airtight seal on the conductor. The DN40CF flange is grounded by pinching the copper shielding braid with an M24×1.5 screw. The HV cable is protected from accidental damage by a plated steel flexible conduit [344], attached to the grounding screw. Finally, a cable terminal was crimped and soldered to the core conductor. The vacuum feedthrough assembly was leak tested with He gas, with a leak rate better than $1.0 \cdot 10^{-9}$ mbar/(l·s). The assembly was also put under vacuum for several months, with satisfactory results.

On the vacuum side, a UHMWPE insulator assembly with a press-fitted stainless steel conductor connects the cable to the ceramic feedthrough. A small stainless steel spring is inserted in the conductor on the ceramic feedthrough side to ensure the electrical contact, adapting to possible thermal contractions.

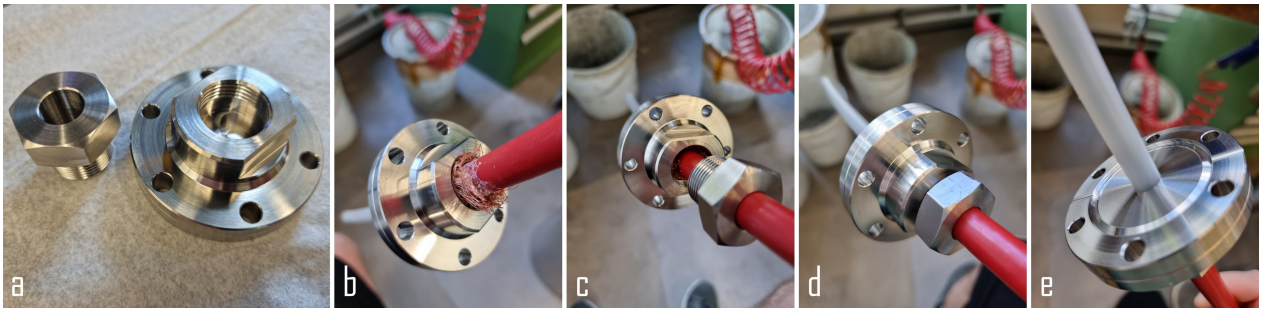

Figure 4.27: HV cable cryofitting process. From left to right: (a) Custom DN40CF flange and grounding screw. (b) Frozen cable inserted in the flange. (c-d) Grounding screw secured to the flange, pinching the copper braid. (e) Finished cryofitted air-to-vacuum HV feedthrough.

The complete HV feedthrough assembly was tested in the cryostat of Xenoscope. The ceramic feedthrough was left unconnected inside the inner vessel, while the vacuum feedthrough was fully assembled and connected to the HV power supply. We performed tests both in air and vacuum. The voltage was initially ramped up slowly, but periodic sparking occurred between 20 kV and 30 kV. Upon observation of the vacuum-side section of the feedthrough, we could identify darkening on the surface of the dielectric of the cable, as seen in figure 4.28a. Some darkening was also observed

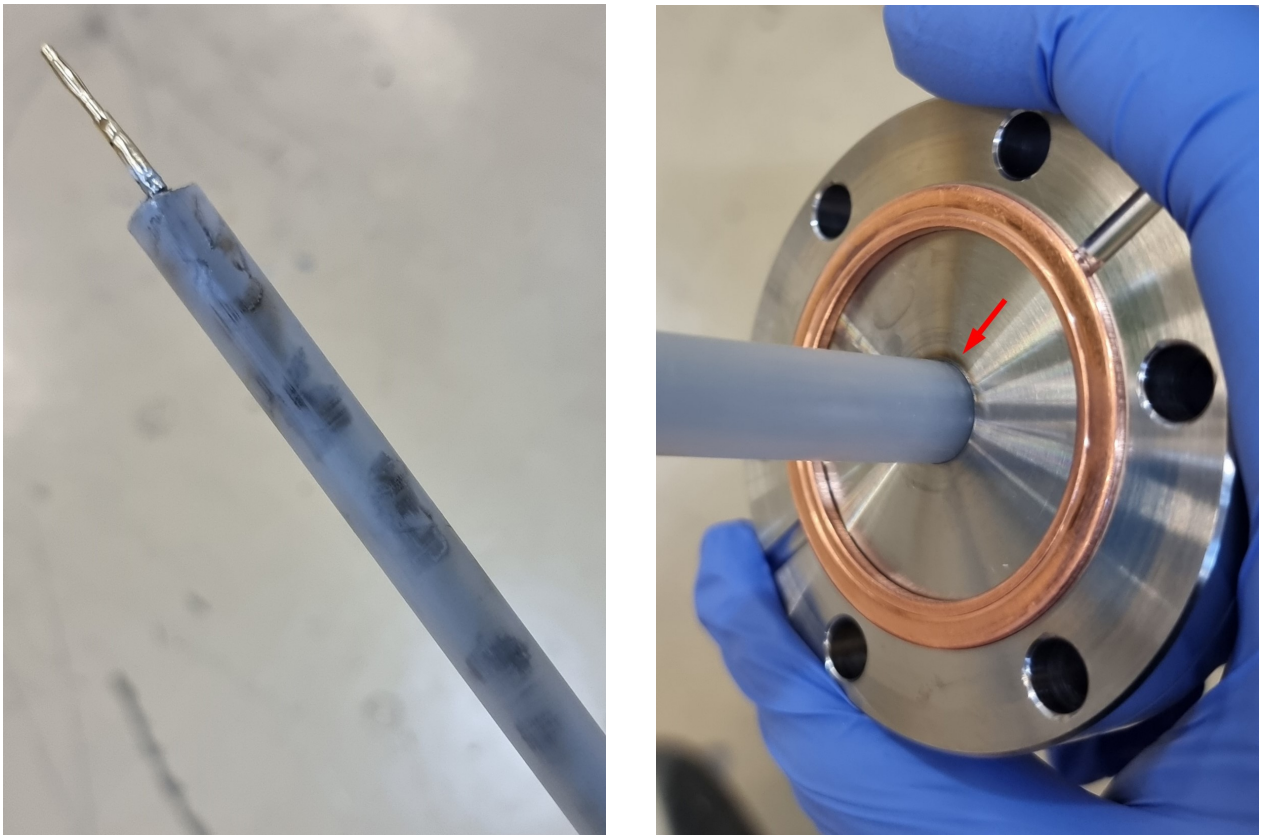

(a) (b)

Figure 4.28: HV cable after conditioning. (a) The insulator of the cable shows scorch marks following the conditioning process. Cleaning with ethanol removed the dark soot-like material. (b) DN40CF flange after the conditioning process. A darkened ring on the flange, around the cryofitted cable and indicated by the red arrow, suggests surface charges on the cable were discharged to the grounded flange.

on the DN40CF flange around the UHMWPE insulation of the HV cable as shown in figure 4.28b, which points to sparking from surface charges, discharging to the grounded flange. The observed behaviour is believed to be similar to the phenomenon described in ref. [345]. To test this theory, the vacuum-side section was doubled in length to increase the discharge path. This new configuration yielded immediate results, but sparking would still occur between 40 kV and 50 kV.

The system was then deliberately allowed to spark over several days. In this process called surface conditioning [346–351], the system is ramped up to a quasi-stable voltage where sparking occurs only periodically. Disengaging the spark protection circuit of the HV power supply allows the system to automatically be ramped back up to the set voltage after a spark. After a relatively short period ($\mathcal{O}(24\,\mathrm{h})$), the frequency of the sparking is reduced considerably, and the voltage is increased by $\mathcal{O}(1-5\,\mathrm{kV})$ at a time. With this method, we achieve a stable voltage of 50 kV over a continuous period of 4 days in vacuum. In air, we achieved considerably higher voltages, reaching up to 100 kV after conditioning.

4.3.4 Gas Phase Purification

In equation 4.20, the first term, $-F_\mathrm{g}\,\rho\,I_\mathrm{g}$, describes the rate of removal of electronegative impurities I_g from the GXe phase of the cryostat at a mass flow F_g. The GXe phase was not recirculated both during the facility commissioning and Phase 1 ($F_\mathrm{g} = 0$), relying purely on the transfer of impurities from the GXe to the LXe phase through the condensation of xenon (term 4 of equations 4.20 and 4.21. This transfer process is very slow, inefficient, and has overall a negative impact the electron lifetime, defined by the impurity level in the liquid phase.

The addition of a gas line in parallel to the liquid extraction line of the heat exchanger allows for the purification of the GXe phase with the same purification loop. Figure 4.29 shows a CAD drawing of the line added to the *Filtration and Safety Gas Panel* (section 3.3.2) and its schematic representation in the P&ID. The pressure relief line, connected to a gas feedthrough on the top flange, is connected on the other end to the return line, bypassing the heat exchanger. A flow controller (FC-02 - 0 to 20 slpm) controls the recirculated GXe mass flow ($\dot{m}_\mathrm{GXe}$). The total mass flow ($\dot{m}_\mathrm{tot}$) is still controlled by the flow controller FC-01, and can then be expressed as $\dot{m}_\mathrm{tot} = \dot{m}_\mathrm{LXe} + \dot{m}_\mathrm{GXe}$. This system will operate at the cost of an extra heat load on the cryostat, as all the xenon is brought back from the purification loop through the supply line. The extra heat load will be compensated by the cooling tower. The valve MV-16 can be used as a shut-off valve as needed.

The gas-phase purification line was installed and tested right after the PM run was completed. The whole gas system was evacuated, and the gas purification line was successfully leak-checked to a level better than $5\cdot10^{-9}\,\mathrm{mbar}\cdot\mathrm{l/s}$. The whole system was then filled to 2.0 bar GXe and recirculated for $\sim$ 12 h with the mass flow controller FC-01 set to 50.0 slpm. The mass flow controller FC-02 was cycled from 0.0 slpm to 3.0 slpm to confirm its normal behaviour. The flow in FC-01 stayed nominal throughout the test, validating the concept of the gas purification line. The line will be first used in Phase 2 - Run 1. The extra heat load on the system has yet to be measured.

4.3.5 Copper Oxide Removal

The operation of Xenoscope is an endeavour that can span over several months. As such, the proper storage of sensitive components while not in use is of high importance. Although proper

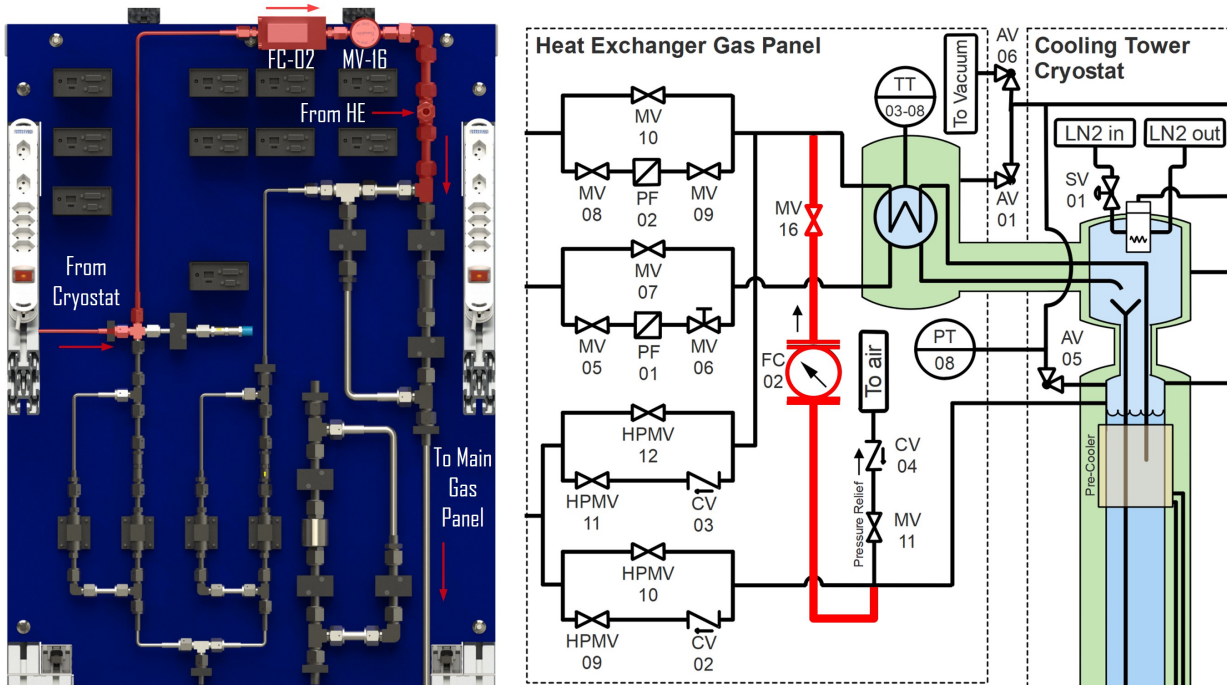

Figure 4.29: Gas-phase purification line. The addition of the gas purification line, highlighted in red, allows for the purification of the gas-phase of the cryostat. The line bridges the existing pressure relief line, directly connected to the top of the inner vessel, and the outlet of the heat exchanger return line. A mass flow controller (FC-02) controls the flow out of the gas-phase, while the main flow controller (FC-01) controls the total flow in the purification line. Valve MV-16 can be used as a shut-off valve.

care was given to storage methods, the damage or degradation of materials is sometimes hard to avoid.

A total of 185 field-shaping rings were produced for the different phases of Xenoscope: 34 rings were used in the PM, while the rest were stored on protective acrylic racks. After machining, the rings were cleaned in an ultrasonic bath with acidic soap and distilled water, followed by an ethanol rinse. The rings were air dried and stacked in racks, which were then wrapped in protective cellophane. Figure 4.30a shows the state of the rings after more than one year of storage wrapped in cellophane. For almost all the rings, copper oxide had formed inside and outside of the screw holes used to attach the resistor chain. It is unknown if the culprit is the presence of residual moisture left from the cleaning procedure or simply a green-house effect from the cellophane wrap, where moisture could have been accumulated over time with changes in room temperature and humidity levels. There exist three different oxides of copper, activated by the presence of water [352]:

$$\begin{aligned} \text{Cupric oxide: } & \mathrm{Cu} + \mathrm{H_2O} \rightarrow \mathrm{CuO} + \mathrm{H_2} \\ \text{Cuprous oxide: } & 2\,\mathrm{Cu} + \mathrm{H_2O} \rightarrow \mathrm{Cu_2O} + \mathrm{H_2} \\ \text{Cupric hydroxide: } & \mathrm{Cu} + 2\,\mathrm{H_2O} \rightarrow \mathrm{Cu(OH)_2} + \mathrm{H_2}\,. \end{aligned} \tag{4.24}$$

Normal ultrasonic cleaning, either with soap and distilled water, acetone, ethanol or nitric acid, was mostly ineffective to remove the oxide layer. Pickling with sulfuric acid (1 wt/wt% H_2SO_4) and hydrogen peroxide (3 wt/wt% H_2O_2), used for surface radioactivity removal of copper components [219], was not attempted to avoid pitting of the copper surface.

The copper oxide was successfully removed with acetic acid (5 wt/wt% CH_3COOH), diluted from

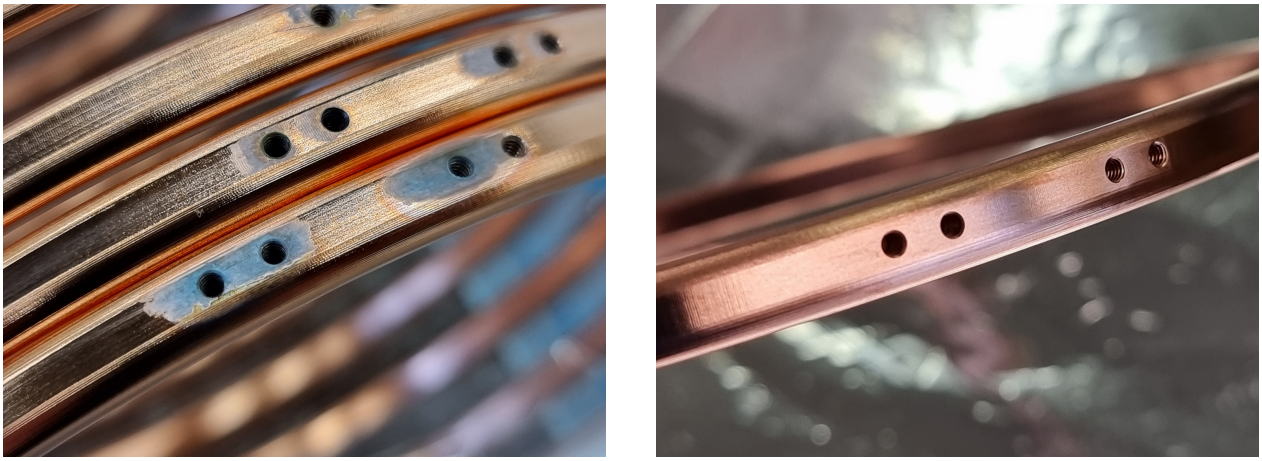

(a) (b)

Figure 4.30: Field-shaping rings before and after cleaning. **(a)** The corrosion seems to have originated from the screw holes of the resistor chain, possibly due to residual moisture from the cleaning process, or from condensed moisture over time. **(b)** Field-shaping ring after cleaning and electropolishing. The corrosion marks were sanded before the electropolishing process. The rings were cleaned a final time before their installation in the TPC.

a 100 % concentration. Acetic acid up to 100 % concentration was used on parts with persistent oxidation. The different copper oxides, when in contact with acetic acid, form cupric acetate:

$$\begin{aligned} \mathrm{CuO} + 2\,\mathrm{CH_3COOH} &\rightarrow \mathrm{Cu(CH_3COO)_2} + \mathrm{H_2O} \\ \mathrm{CuO} + 4\,\mathrm{CH_3COOH} &\rightarrow 2\,\mathrm{Cu(CH_3COO)_2} + \mathrm{H_2O} + \mathrm{H_2}\,, \end{aligned} \tag{4.25}$$

while metallic copper has excellent resistance to corrosion when in contact with acetic acid [353]. The rings were submerged in the acetic acid solution for several hours to remove the copper oxide, followed by a thorough rinse in ethanol absolute.

The process was repeated as needed until all the visible oxide was removed from the surface of the rings and inside the screw holes. Surfaces attacked by the formation of an oxide layer sometimes showed some discoloration and surface roughness. As the rings were to be electropolished before being installed in Xenoscope, they were lightly sanded with three abrasive sponge blocks of successively finer grits. Finally, the rings were again bathed in the acetic acid solution for several hours and rinsed, before being passivated in a 2 wt/wt% citric acid solution. After they were completely dried, the rings were individually packed in sealable plastic bags, each with a silica-gel desiccator to prevent further oxidation of the rings. As is the standard procedure for Xenoscope, the field-shaping rings were sent for electropolishing as close as possible in time to their assembly in the TPC.

4.4 Large Scale Photosensor Testing in Xenoscope

The baseline design of DARWIN foresees the deployment of $\sim$ 1800 3" PMTs, such as the Hamamatsu R11410-21 or other similarly sized photosensors [354]. Every photosensor must be individually tested to measure its performance and ensure its good working condition prior to its deployment in a low-background detector. Such tests are typically performed both in GXe and LXe in dedicated testing cryostats. A total of 368 additional PMTs were tested for XENONnT in three

facilities at MPIK in Germany, in Stockholm, and in Zurich [355].

We will use as an example the case of the MarmotX testing facility in Zurich. The facility could host up to ten Hamamatsu R114010-21 PMTs in a PTFE holder. A testing round, from assembly and LXe filling to xenon recuperation, lasted about 30 days, for an average testing rate of 0.33 PMT/day.

The inner vessel of Xenoscope has the same diameter as that of MarmotX but is about 10 times longer. As shown in figure 4.31, Xenoscope could potentially host 90 Hamamatsu R11410-21, 3" PMTs, or up to 386 Hamamatsu R12699-406-M4, 2" PMTs. To optimise the duration of the testing cycle, one would need to manufacture double the amount of holders needed such that a next batch of PMTs can be prepared whilst a current batch is being tested. Hence, let us assume that the opening of the cryostat, the unmounting and mounting of the PMTs, and the closing of the cryostat should last one week. From experience, pumpdown and filling should also last approximately one week. The PMT testing round should last $\sim$ two weeks. Finally, with the use of gravity-assisted recuperation, the recuperation and warm-up phases should have a duration of less than one week. We can therefore estimate that one measurement cycle could last, in total, approximately 5 weeks. This would bring the testing yield to 2.57 PMT/day, just shy of 8$\times$ greater than that achieved with the MarmotX PMT testing scheme.

At this pace, a full testing campaign for DARWIN would last two to three years, accounting for various possible delays and the testing of additional units as backup photosensors. Depending on the photosensor rejection rate, the campaign could also possibly take longer to be completed. During the XENONnT testing campaign, 26 out of the 368 PMTs tested were rejected, for a rejection rate of 7 %. This is an improvement over the XENON1T testing campaign, which saw a rejection rate

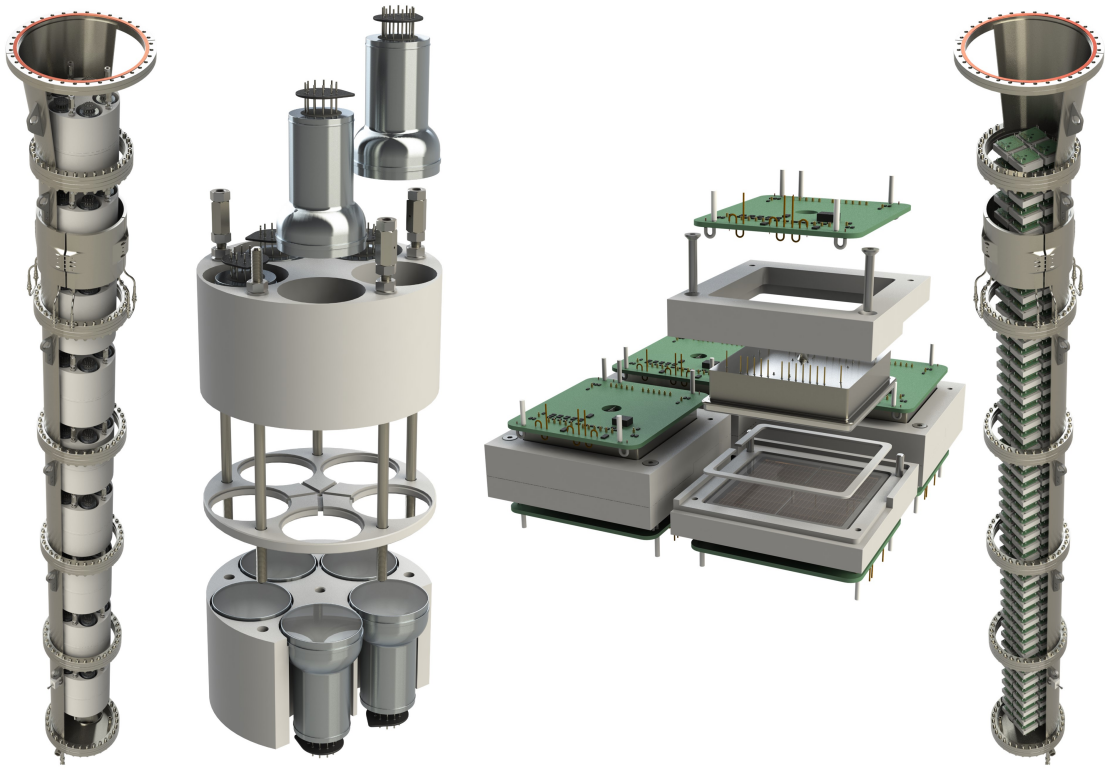

Figure 4.31: Conceptual PMT testing scheme in Xenoscope. On the left, 90 Hamamatsu R11410-21 are held in pairs in ten calibration modules. On the right, 386 Hamamatsu R12699-406-M4 are attached in pairs and arranged 2$\times$2 in the inner vessel.

of 22 % [354]. Finally, the lead time for photosensor procurement could also play a role in the time frame needed to complete the campaign.

As seen during the testing of SiPMs, which are discussed in the next chapter and in refs. [356, 357], these solid-state photosensors are much more robust than PMTs, which could lower their rejection rate considerably. However, their small size would complicate the testing of a large number of individual units, given the high number of data acquisition (DAQ) channels this would require. In this optic, SiPMs could be tested on tiles similarly to those described in section 4.3.2 and in refs. [234, 341], where the bad behaviour of a given photosensor would be first identified from the overall tile inhomogeneity in the single photoelectron (SPE) spectrum. Sensors from a tagged bad tile could then be individually tested to identify the culprit.

Even though Xenoscope could play a major role in the qualification testing of photosensors for the next generation dark matter experiment, it should not be the only testing facility involved in these tests. Unforeseen delays endured by Xenoscope would then have a major impact on the realisation of DARWIN, and thus, contributions from other testing facilities throughout the collaboration will be integral to the success of the PMT testing campaign.

4.5 Summary and Outlook

We have designed and built Xenoscope at the University of Zurich over a span of three years. The facility was successfully commissioned in early 2021 with 80.66 kg of LXe, certifying the numerous systems for continuous operation.

Phase 1 of Xenoscope was completed in May 2022 after a three-month long operation of a 0.53 m tall LXe PM, with which we assessed the purity of the LXe by measuring the electron drift. The data acquired throughout the run was used to develop a data-driven model of the electron lifetime, providing information on various attributes of the facility. The model was used to provide predictions regarding the attainable electron lifetime for higher purification flows, and demonstrated the favourable impact the purification of the gas phase would have on the ultimate achievable electron lifetime in the ideal operation of the facility.

In the final phase of Xenoscope, a dual-phase TPC was designed and is being deployed to demonstrate the drift of electrons over 2.6 m. The field cage of the PM has been reused and supplemented by four additional modules. The top charge readout has been replaced by a 12-channel SiPM array composed of SiPM tiles. A LXe level monitoring and control system has been designed and will be used to control the liquid level with sub-mm precision. Finally, a HV distribution scheme centred around a novel air-to-vacuum HV feedthrough design, was conceptualised and successfully tested at HV up to 50 kV. Alongside the achievement of the main objective, the Xenoscope facility will also be used to investigate fundamental properties of LXe, such as light absorption, and electron cloud diffusion.

The multiple operational runs have demonstrated the versatility, safety, and stability of Xenoscope. In the future, the facility will become accessible to other DARWIN collaborators. It is a unique research platform with which various technologies can be tested in conditions resembling those of large-scale LXe detectors. After the DARWIN R&D phase is completed and the collaboration advances towards the realisation of the next-generation dark matter experiment, our LXe column can ultimately be used to rapidly qualify a large number of photodetectors for use in LXe, like many other testing facilities before it.

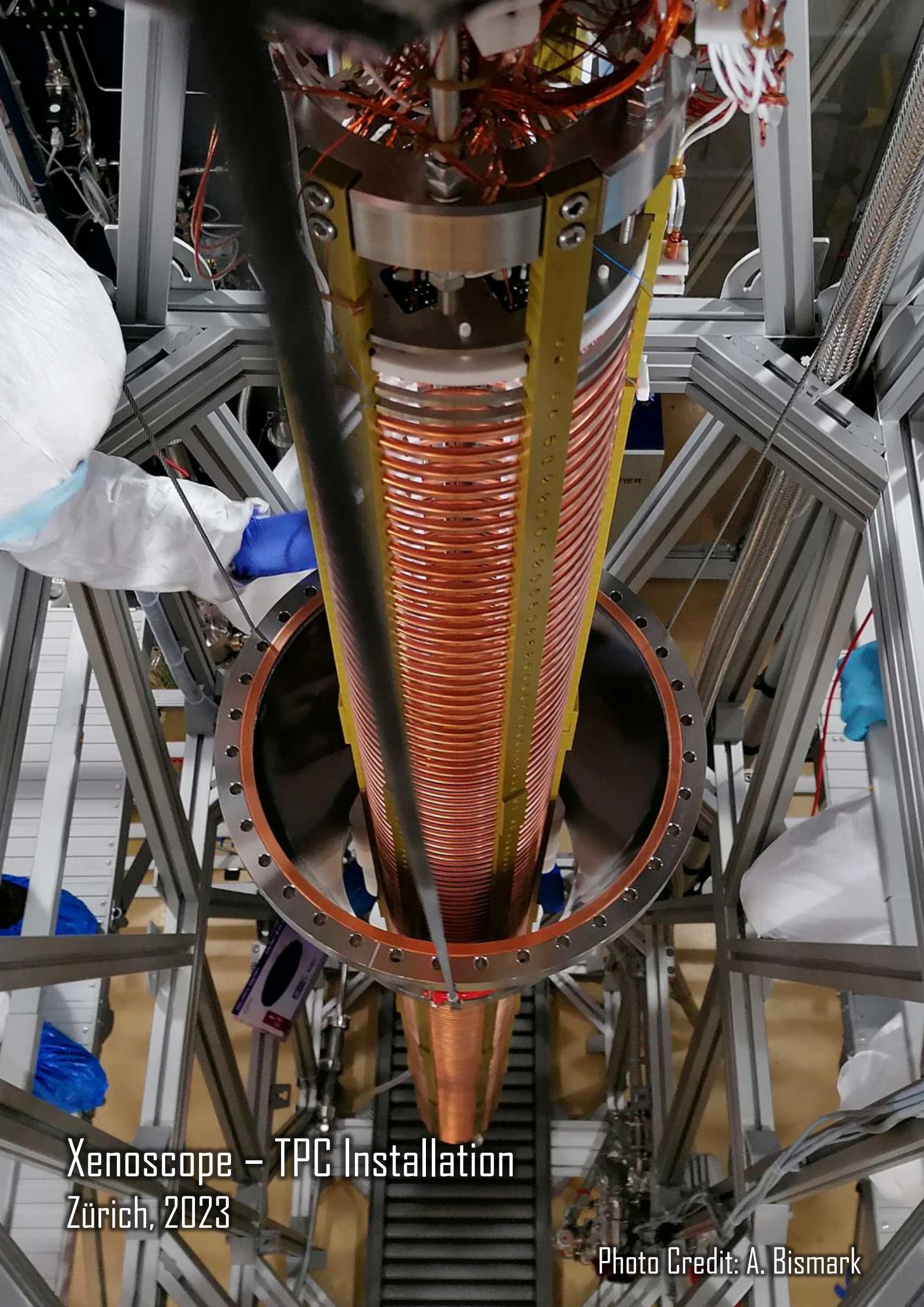

Xenoscope – TPC Installation

Zürich, 2023

Photo Credit: A. Bismark

Xenoscope
Zürich, 2021

5

Studies of Silicon Photomultiplers for DARWIN

For decades, the photosensor arrays in xenon TPCs have been composed of PMTs. These analogue light sensors are well known for their high gain, SPE resolution, and low intrinsic noise level [354]. On the negative side, they are generally bulky, fragile, and expensive. Finally, despite their good radiopurity, they are one of the major contributors to the material radioactivity of the detector [358]. As detectors get bigger and more sensitive, reducing the cost and increasing the radiopurity of photosensor arrays is becoming of paramount importance [260]. For this reason, we are looking at alternative photodetectors, SiPMs, in the search for suitable candidates as replacements for the current generation of PMTs used in dark matter detectors.

SiPMs, also known as Multi-Pixel Photon Counter (MPPC) and solid state photomultipliers (SSPMs), are solid-state light detectors that have seen a rapid rise in popularity in the last few decades for a multitude of applications. Their small form-factor, good reliability, and ease of used makes then well suited for applications such as light detection in astronomy [359], applications in medicine [360], use in high-resolution microscopy [361], and Light Detection And Ranging (LIDAR) systems [362, 363]. They are also becoming common in the fields of particle physics, γ-ray detection [364], and high-energy physics [365].

This chapter first elaborates on the concept of light detection with silicon photomultipliers in section 5.1, and requirements for photosensors in DARWIN in section 5.2. Will follow a discussion on the non-linear behaviour of SiPMs in section 5.3. In section 5.4, we present the characterisation of two SiPM models from Fondazione Bruno Kessler. Finally, we discuss the upgrade of some of the subsystems of Xurich II, the first dual-phase xenon TPC operated with a SiPM array, in section 5.5.

5.1 Light Detection Using Silicon Photomultipliers

In this section, we describe the concept of electron multiplication in silicon, and the key parameters associated with SiPMs.

5.1.1 Electron Multiplication in Silicon

The establishment of an electric field between the anode and cathode of the semiconductor allows for the displacement of charges between the p and n regions. Impinging photons can produce electron-hole pairs in the depletion region, a region of a doped semi-conductor where mobile charge carriers have been diffused away by an electric field, leaving behind ionised donors or acceptors. The electric field separate the electron and hole before they can recombine. Following the production of the electron-hole pair, three voltage-dependent behaviours of the p-n junction, shown schematically in figure 5.1, can be identified:

- **Photodiode range:** At low voltages, the produced electron-hole pair does not produce other free charges. The current produced in the semiconductor is proportional to the intensity of the light.

- **Avalanche photodiode (APD) range:** When the electric field is sufficiently high, the electron from the initial electron-hole pair can produce secondary electron-hole pairs via impact ionization. The current is proportional to the number of detected photons, or the number of initially produced electron-hole pairs. Only electrons have enough kinetic energy to produce electron-hole pairs, meaning that the current is flowing in only one direction and is self quenched.

- **SPAD range:** When the p-n junction is operated beyond a certain voltage, i.e. above the breakdown voltage (V_{bd}), holes gain sufficient kinetic energy to create secondary electron-hole pairs. In this regime, often compared to that of a Geiger-Muller counter, impinging photons absorbed in the silicon can produce self-sustaining avalanches. The current rapidly increases in the crystal and must be quenched. The quenching circuit typically consists of a series quenching resistor, although active, transistor-based quenching circuits exist. As the current increases, the electric field in the micro-cell is diminished as the bias voltage drops below the breakdown voltage, stopping the avalanche. The current falls exponentially, with a time constant characteristic of the RC circuit formed by the silicon cell and the series resistor. These parameters can be tuned to optimise the gain and timing characteristics of photosensors. Following the quenching, the voltage is restored at the p-n junction, and the sensor is reactivated. This arrangement, known as the SPAD, outputs a pulse of fixed amplitude and duration, characterised by its resistance and capacitance.

Figure 5.2 shows a schematic representation of a p-on-n SPADs. This type of arrangement is well suited for the detection of blue-to-UV light as photons are absorbed near the surface of the SPADs. Electrons that are released drift towards the positively-biassed n^- region, causing an avalanche in the p-n junction. Red-to-infrared (IR) photons penetrate the sensor deeper, reducing their detection efficiency in this configuration. In this use case, n-on-p configurations are preferred.

As seen in figure 5.3, showing a microscope image of an Hamamatsu VUV4 MPPC [321], SiPMs consist of an arrangement of thousands of SPADs, read out in parallel. The Geiger-mode operation of SPADs gives the SiPM excellent single photon resolution. The pitch of a SiPM refers to the size of one of its SPADs, which are typically square.

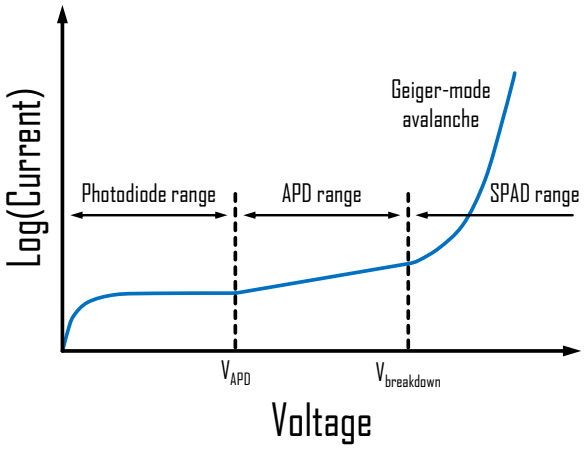

Figure 5.1: Voltage-dependent behaviour of a p-n junction. Three distinct behaviours can be observed. At lower voltages, the current output is constant. As the bias voltage is increased, the current starts to increase linearly. Finally, as the bias voltage exceeds the breakdown voltage, the current increases exponentially and diverges. Figure adapted from ref. [366].

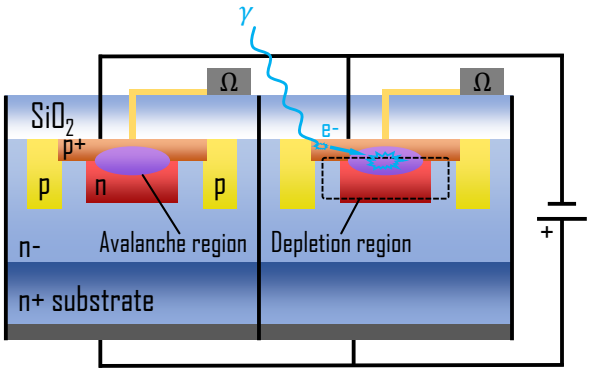

Figure 5.2: Geometry of p-on-n type single photon avalanche diodes (SPADs). Higher-energy photons (UV to blue) are absorbed closer to the surface, and electrons drift towards the depleted region, producing an avalanche in the avalanche region. Red-to-infrared photons are absorbed deeper in the crystal. Electrons are then absorbed quickly as holes produce the avalanche, resulting in a lower photon detection efficiency (PDE).

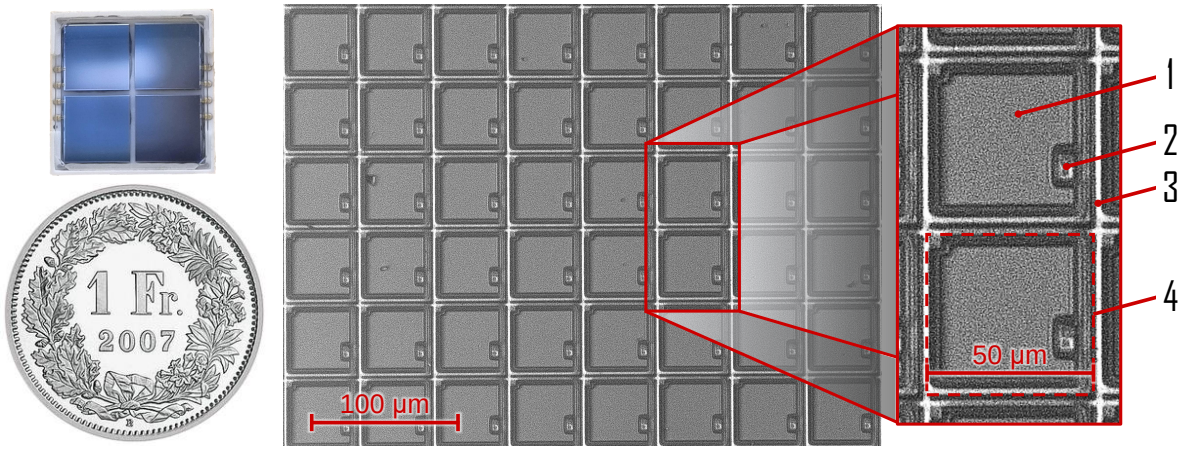

Figure 5.3: Microscope image of a Hamamatsu VUV4 MPPC. Magnification 20×. The micro-cells are all connected in parallel. The quenching resistors can be seen on the die. Legend: (1) APD; (2) Resistor; (3) Trench; (4) SPAD.

5.1.2 Characteristic Parameters of SiPMs

Gain

The gain refers to the electron multiplication factor of the SPAD. A constant number of electron-hole pairs are produced during the photoavalanche in Geiger-mode. A charge pulse is produced as the current is quenched by the integrated resistor. The pulses are typically converted to a voltage pulse by readout electronics (i.e. the base), and are digitised by an Analog-to-Digital Converter

(ADC). The gain can then be calculated as:

$$G = q/e, \tag{5.1}$$

where q is the charge of a one photoelectron (p.e.) SiPM pulse and e is the elementary charge of the electron, $1.602\,176\,634 \cdot 10^{-19}$ C [367].

The charge q can be determined from the recorded pulses by integrating the pulses and converting the recorded voltages to current:

$$q = \frac{1}{F_{amp}} \int I \, \mathrm{d}t = \frac{1}{F_{amp}} \cdot \frac{1}{R} \int V \, \mathrm{d}t, \tag{5.2}$$

where F_{amp} is the cumulative external amplification factor (from pre-amplifiers of amplifier modules), I is the current, R is the impedance of the ADC, V is the voltage, and $\mathrm{d}t$ is the time resolution of the ADC.

Since the ADC is discretely recording voltages at constant intervals, we can rearrange equation 5.2:

$$q = \frac{1}{F_{amp}} \sum I \cdot \Delta t = \frac{1}{F_{amp}} \cdot \frac{\Delta t}{R} \sum V. \tag{5.3}$$

Finally, the voltage can be expressed as the ADC level reached, normalised to the full ADC range. Therefore:

$$q = \frac{1}{F_{amp}} \cdot \frac{\Delta t}{R} \cdot \frac{ADC_{range}}{ADC_{res}} \sum ADC_{level}, \tag{5.4}$$

where ADC_{range} is the full range of the ADC in volts, and ADC_{res} is the dynamic range of the ADC in bits (e.g. 14-bit $= 2^{14}$), and $\sum ADC_{level}$ is the sum of all ADC samples of the recorded signal, in bits.

Breakdown Voltage

When reverse-biassed, the cells of a SiPM only produce electron amplification in Geiger-mode when the applied voltage (bias voltage, V_b) exceeds a critical value, the breakdown voltage (V_bd). It is normally defined as the highest value of V_b where the gain is still zero. It is difficult to measure this value precisely, with several measurement methods generally accepted [368–370]. In this work, we measure the breakdown voltage with an alternative method. As will be shown in section 5.4, the breakdown voltage can be found experimentally by illuminating the photosensor with a constant amount of light, and calculating the amount of charge produced at different, arbitrary bias voltages above the breakdown voltage. At $V_\mathrm{b} = V_\mathrm{bd} + \varepsilon$, where $\varepsilon \ll V_\mathrm{bd}$, the gain does not increase linearly with increasing overvoltage (OV), $V_\mathrm{OV} = V_\mathrm{b} - V_\mathrm{bd}$. The value at which the charge, and hence the gain, first reaches zero is, by definition, the breakdown voltage. Empirically, and as we will see in section 5.4.2, the charge output vs. the bias voltage using this method can be expressed as:

$$q = m \cdot (V_\mathrm{b} - V_\mathrm{bd})^2 \tag{5.5}$$

$$= m \cdot V_\mathrm{ov}^2, \tag{5.6}$$

where m is a scaling factor. Due to their characteristic single-photo signature, dark events (see *Dark Count Rate* below) can be used to determine the gain of a SiPM as a function of V_b, well

above V_{bd}, by calculating the charge produced by the 1 p.e. distribution. A linear regression can be made to determine the breakdown voltage, by definition, at the zero-gain mark [371]. The difference between the two methods is typically of the order of a few percent of the value of V_{bd}.

Photodetection Efficiency

The PDE of a SiPM is a measure of the ability of a single-photon detector to detect photons [366]. The PDE can be expressed as:

$$PDE(V_{\mathrm{OV}}, \lambda) = QE(\lambda) \cdot P_T(V_{\mathrm{OV}}, \lambda) \cdot FF_{\mathrm{eff}}(V_{\mathrm{OV}}, \lambda)\,, \tag{5.7}$$

where QE is the quantum efficiency (QE) (the ratio of p.e. to the number of incident photons). Special surface coatings are often used to optimise the collection of UV photons. P_T, the avalanche triggering probability, is dependent on the OV and on the wavelength of the photon, as longer wavelength radiation typically penetrates deeper (e.g. UV: $\mathcal{O}(10\,\mathrm{nm})$, visible: $\mathcal{O}(100\,\mathrm{nm})$). Finally, FF_{eff} is the effective geometrical fill factor. The chosen geometry of the SPAD arrangement (e.g. pitch of the SPADs, resistor location and type, use of trenches, etc.) can significantly impact the total exposed sensitive area.

Dark Count Rate

Since photon detection in SiPMs is made possible by the generation of electron-hole pairs in the depleted region, which ultimately produce a detectable current from an avalanche of electrons, any phenomena leading to the generation of free electrons in the crystal also produce events that are indistinguishable from those produced by photons.

The DCR is then defined as the incidence of uncorrelated events (i.e. dark counts), which are produced in SiPMs via two processes. At higher temperatures, the thermal generation of charge carriers from impurities in the crystal in the bandgap dominates the production of the dark noise [372]. The rate of this process is temperature-dependent as 1/T, decreasing by a factor of 2 with every 5 to 10 °C [373]. At cryogenic temperatures, the high electric field in the SiPM produces temperature independent, trap-assisted tunnelling of charges, which saturates the dark count reduction. This phenomenon is dependent on the strength of the electric field in the crystal. DCR reduction in analogue SiPMs can only be achieved by improving the purity of the silicon. However, it is known that only a small fraction of the micro-cells on a SiPM produce the majority of thermally-generated dark events. Therefore, DCR can be significantly reduced in digital SiPMs (but not in analogue SiPMs), where noisy cells can be turned off [374].

As dark counts are characterised by single photon events, a typical method for measuring the DCR is to install a SiPM in a dark environment, and measure a SPE spectrum, also known colloquially as the finger plot. An example is shown in figure 5.4. The 1 p.e. peak is identified, and the DCR is calculated as the the sum of all the bins from the 0.5 p e threshold, divided by the acquisition time:

$$\mathrm{DCR}_{0.5\ p.e.} = \frac{\sum_{0.5\ p.e.}^{\infty} samples}{t} \tag{5.8}$$

In order to compare different photosensors, the DCR is normally expressed area normalised, by dividing the DCR by the active area.

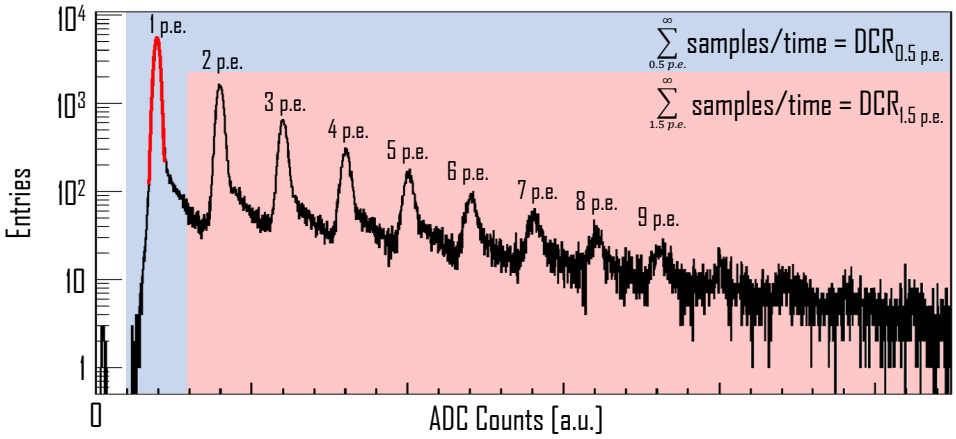

Figure 5.4: Example of a single photoelectron binned spectrum and DCR calculation. The dark count rate (DCR) is calculated by summing the spectrum from the 0.5 p e threshold, and dividing by the acquisition time (blue region). The sum from the 1.5 p e threshold (red region) is used to calculate the crosstalk probability.

Afterpulse Probability

Afterpulses (APs) are a type of correlated event that occurs as a result of a primary event, such as a detected photon or a dark count, and are caused by the trapping and release of charge carriers in the high-field regions of the crystal. AP signals are usually of lower gain than the primary events. The AP probability is affected by the purity of the silicon, the release time constant from traps, and the recharge time of the micro-cells. Manufacturers can reduce the after-pulse rate by tuning the recharge time constant of the SiPM. Allowing for a longer recharge time ensures the release of trapped electrons before the cell has fully recharged.

Furthermore, photons emitted during the avalanche process can be absorbed in the neutral region of the same SPAD. Generated charge carriers can then diffuse to the avalanche region within $\mathcal{O}(100\,\mathrm{ns})$. The selection of a low-lifetime substrate material, which releases trapped electrons before the avalanche is fully quenched, can help mitigate this process.

Crosstalk Probability

Crosstalk events are a second type of correlated event. It is well known that optical photons are produced during an avalanche, by hot-intraband luminescence in a SPAD [375]. If these photons are absorbed in the same SPAD, the charge production is unaffected. They can, however, propagate to neighbouring cells, where they can be detected. Three types of crosstalk events can be identified, as shown in figure 5.5.

The first type, known as prompt or direct crosstalk, occurs when a secondary photon is absorbed in the depleted region of a neighbouring cell, resulting in a second avalanche. As the distances travelled by photons are normally short ($\mathcal{O}(10-100\,\mu\mathrm{m})$), prompt crosstalk events happen in a few hundred picoseconds, producing events with multi-photon signatures. One way manufacturers can lower the crosstalk probability (CTP) is by engraving and filling trenches in the silicon with metals and oxides to reduce the direct propagation of photons between cells [376].

The second type is delayed crosstalk. Photons can be absorbed in un-depleted regions of neighbouring cells, and the resulting charge carriers can diffuse to the avalanche region. Diffusion times

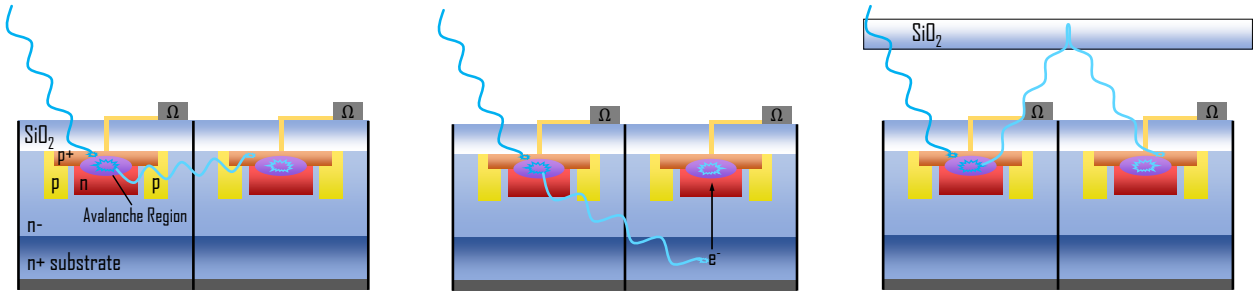

Figure 5.5: Types of crosstalk in SiPMs. **(a)** Prompt crosstalk. A photon generated during the primary photoavalanche propagates to a neighbouring cell, is absorbed in the depleted region, and produces a second avalanche. **(b)** Delayed crosstalk. A secondary photon is absorbed in the non-depleted region. An electron diffuses towards the avalanche region, where it triggers a second avalanche. **(c)** External crosstalk. A secondary photon escapes the crystal, and is reflected back towards the SiPM by an object, triggering an event in a separate SPAD.

can be longer than the recharge time of the SPADs, although some delayed crosstalks can happen very close in time to the initial event, such that both signals cannot be resolved.

The third type of crosstalk event is external crosstalk. Photons propagating outside of the crystal can be reflected back by, for example, a layer of fused silica or epoxy. These photons can then trigger other SPADs.

As dark counts are characterised by 1 p.e., and crosstalk event by event of 2 or more p.e., the CTP can be defined as:

$$\mathrm{CTP} = \frac{\mathrm{DCR}_{1.5\ p.e.}}{\mathrm{DCR}_{0.5\ p.e.}}, \tag{5.9}$$

where $\mathrm{DCR}_{0.5\ p.e.}$ and $\mathrm{DCR}_{1.5\ p.e.}$ are the dark count rate at a threshold of 0.5 and 1.5 p.e. respectively.

5.2 Requirements for Photosensors in DARWIN

In order to qualify for use in DARWIN, photosensors must meet numerous requirements. Perhaps the most important, if not obvious, is a high sensitivity to LXe scintillation light, which is emitted in the VUV range, between 175-178 nm [197, 198]. Secondly, as the DARWIN experiment is first and foremost a dark matter search experiment, it will be attempting to detect low-energy recoils from WIMPs with xenon. As discussed in chapter 2, such low-energy interactions ($\mathcal{O}(1\,\mathrm{keV})$) result in a relatively low light yield [208]. It is therefore imperative that photosensors deployed in DARWIN be sensitive to single photons, which requires a high gain, a high PDE, and a good SPE resolution.

The chosen photosensors should also allow for dense packing to maximise the geometrical coverage of the photosensor arrays. Concurrently to low-energy searches, DARWIN will also investigate high-energy physics channels, such as the $0\nu\beta\beta$ of ^{136}Xe, where the Q-value of $(2\,457.83 \pm 0.37)\,\mathrm{keV}$ [377] will lead to light yields of $\mathcal{O}(10^5\,\mathrm{photons})$. The photosensors should therefore feature a large dynamic range to enable the detection of highly luminous events.

These requirements are, for the most part, met by the current generation of PMTs [354, 355], which are part of the base design for DARWIN. Nonetheless, PMTs have several drawbacks that

can hinder the DARWIN experiment in its scientific agenda. First, the design of low-radioactivity, UV-sensitive PMTs, is based on vacuum-tube technology. This makes them bulky and inherently fragile, requiring careful handling and cautious installation. Moreover, despite significant reductions in intrinsic radioactivity by manufacturers over the last decades, PMTs still contribute significantly to the radioactive background of astroparticle dark matter detectors [248].

To improve on these drawbacks, several novel photosensors and photosensing techniques are being investigated as potential replacements for PMTs in DARWIN, such as the ABALONE photosensor [235] and Liquid-Hole Multipliers [378]. The SiPM is also a potential candidate, as their small form factor, especially in height, makes for ultra-compact array geometries, while, at the same time, featuring a dense array packing, as seen in the concept image in figure 5.6. SiPMs can be tiled to form larger-area channels, as discussed in section 4.3.2, while having the possibility to increase the granularity in key locations, for example, at the outer perimeter of the array, to increase the resolution of the position reconstruction, a key feature for maximising the xenon fiducial volume. SiPMs do not require high bias voltages, typically have a lower intrinsic radioactivity per covered area than PMTs, and feature fast pulse rise times, resulting in excellent timing resolution. SiPMs are a proportional output photon counting solution at low light levels, but generally lack linearity at higher illumination, an effect that can be corrected for, as will be discussed in section 5.3. SiPMs usually output very little heat, which makes them excellent candidates for use in the cryogenic conditions of dual-phase xenon TPCs. However, if pre-amplifiers are used directly on their readout boards, the heat output can reach several mW per active mm^2, which can lead to the boiling of LXe or excess strain on the cryogenic system. Therefore, in situations of low light sensing, the deployment of low-heat output pre-amplifier systems must be preferred.

For SiPMs to qualify for use in large-scale dark matter detectors, they should present a low DCR, and low afterpulse and crosstalk probabilities. With a proposed run time of up to 10 years,

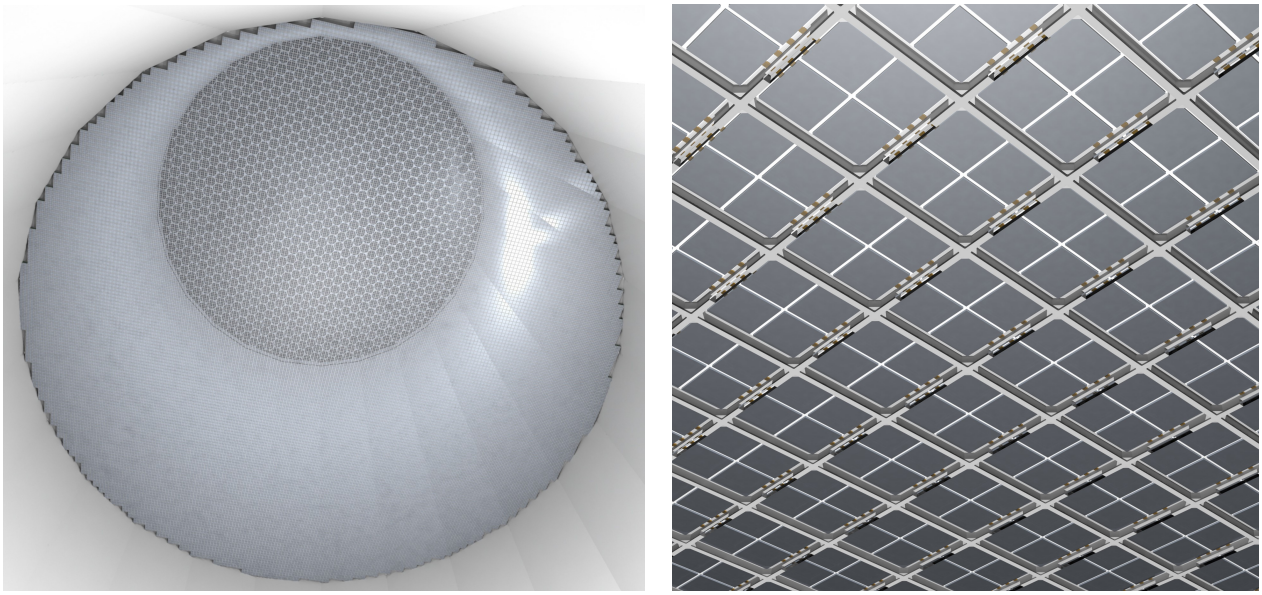

(a) (b)

Figure 5.6: Conceptual-rendering of the DARWIN TPC with a top SiPM array. **(a)** Global view of the conceptual SiPM array, composed of tiled and non-tiled SiPMs, surrounded by white reflector panels. In the reflection of the array, a bottom 3" PMT array can be seen. **(b)** Close up view of the SiPM array. In this concept, Hamamatsu Photonics K.K. VUV4 SiPMs are showcased. The ceramic packaging of the quad-channel VUV4s, seen in off-white, could be further optimised to increase the photosensor packing.

the photosensors used in DARWIN must stay reliable over extended periods of time. PMTs are known to lose QE over time, primarily due to photocathode ageing [379]. For their part, SiPMs are typically more constant over time, although multiple years operation at LXe temperatures has yet to be assessed [6, 380].

5.3 Dynamic Range Measurement - Hamamatsu VUV3 MPPC

The Geiger-mode operation of SPADs in SiPMs ensures that the SPE charge yield is uniform across the whole array. This mode of operation, however, prevents the detection of two photons simultaneously by a single SPAD, as schematically shown in figure 5.7. The linear proportionality between the number of detected p.e. and interacting photons is expected with the assumption that the number of interacting photons is low, and hence the probability of two photons interacting in the same cell is low. The expected number of firing cells as a function of the number of impinging photons can be expressed as:

$$N_f = N_c \cdot \left(1 - e^{-\frac{N_\gamma \cdot PDE}{N_c}}\right), \tag{5.10}$$

where N_c is the number of SPADs in the SiPM, N_γ is the number of photons incident on the SiPM and PDE is the photon detection efficiency.

This non-linear behaviour was studied with a Hamamatsu VUV3 MPPC. The test setup was installed in SandBox, a light-tight container, at room temperature. The SiPM and a PMT (Hamamatsu 1" - R8520) were installed in a holder side-by-side, as seen in figure 5.8a. Figure 5.8b shows a block diagram of the experimental setup. Under the downward-facing photosensors, a blue LED was installed, angled slightly towards the SiPM. A pulse generator was used to power the LED, passing a 100 ns square pulse (5 ns rising and falling edges). A TTL signal was fed from the pulse generator to a CAEN v1724 Versa Module Europa (VME) ADC [314] for signal trigger synchronisation.

The PMT, used as a reference light detector, was operated at low illumination to ensure a linear response. Its exposed sensitive area was masked-off to reduce it to the same area as that of the SiPM. Two power supplies were used to bias the photosensors at the same voltage for every

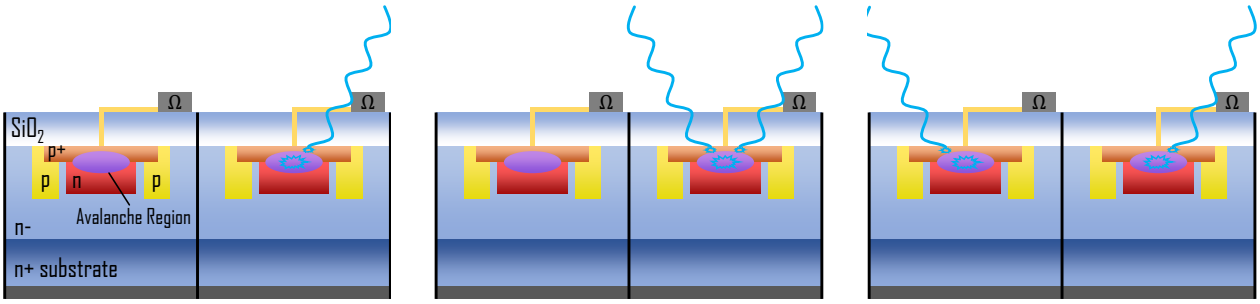

(a) (b) (c)

Figure 5.7: Scheme of photon counting in two SPADs of a SiPM. (a) One photon interacts in one SPAD, resulting in the detection of one p.e. (b) Two photons interact in the same SPAD, resulting in the detection of one p.e. (c) Two photons interact in two SPADs, resulting in the detection of one p.e.

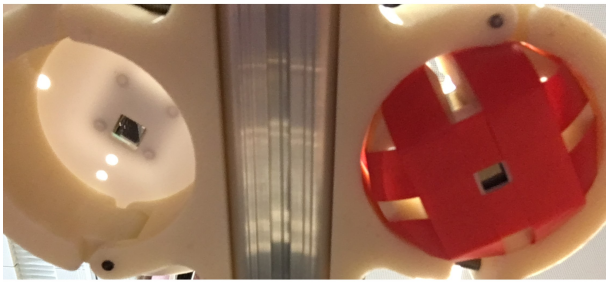

(a)

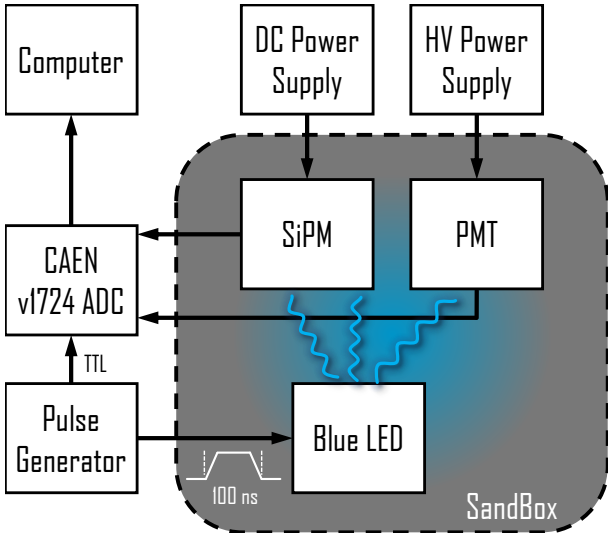

(b)

Figure 5.8: Dynamic range measurement setup. **(a)** Hamamatsu VUV3 MPPC (left) and Hamamatsu R8520 1" PMT (right). A blue Light-Emitting Diode (LED) is installed bellow, equidistant to the two sensors (not shown). **(b)** Block diagram of the linearity measurement. The two photosensors are installed in SandBoX, illuminated by an LED triggered by a pulse generator. A TTL signal is distributed to the ADC to simultaneously trigger the data acquisition.

measurement (SiPM: 56.0 V, PMT: 800 V). The number of incident photons was varied by changing the voltage applied to the LED. For each LED voltage, 500 000 waveforms from both photosensors were recorded. The data were processed with the data processor used in ref. [357].

A SPE spectrum was first acquired with low illumination of the LED to identify the 1.0 p.e. level with a Gaussian fit of the 1.0 p.e peak. Photon distributions with high LED illumination were also fitted with a Gaussian, and the means of the fits were taken as the average number of ADC counts measured. This number was then normalised with the area of the 1.0 p.e value to provide the number of measured p.e.:

$$N_{\text{p.e.}} = \frac{Area}{Area_{SPE}}. \tag{5.11}$$

Figure 5.9 shows the number of detected p.e. in the SiPM vs. the number of p.e. detected in the PMT.

The red curve is a linear fit using the first three data points and passing through (0,0). The black curve represents a fit to equation 5.10, with $N_\gamma = \alpha \cdot N_{PMT}$, where α is a free parameter ($\alpha_{fit} = 110.3$), and N_{PMT} is the number of p.e. detected in the PMT. N_c was set to 14 400 and PDE at 0.10 [381]. The two subplots in figure 5.7 show the residuals of the data for the two fits.

This measurement shows that it is possible to correct for the non-linear behaviour of SiPMs. Basic knowledge of the parameters of the photosensor, such as the PDE and number of SPADs per channel, is sufficient to apply a correction from the number of detected p.e. to the expected number of incident photons using:

$$N_{\gamma_{SiPM}} = -\frac{N_c}{PDE} \cdot \ln\left(1 + \frac{N_f}{N_c}\right), \tag{5.12}$$

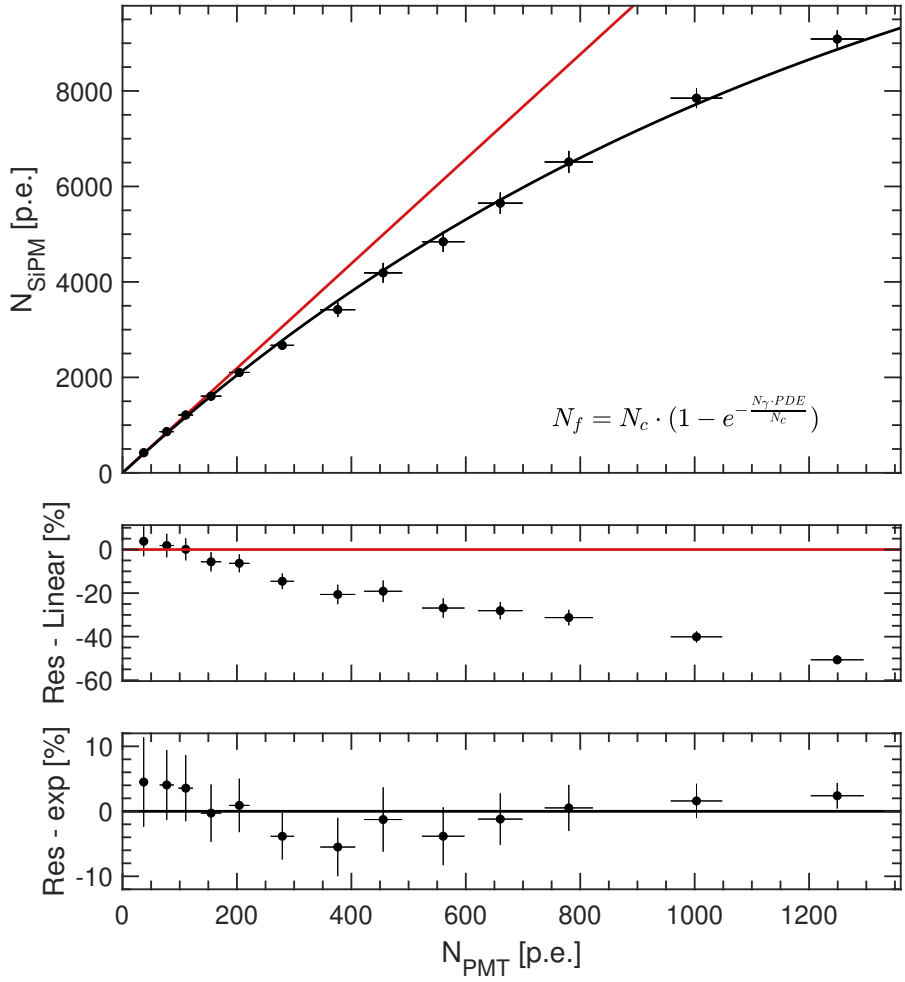

Figure 5.9: Detected photoelectrons, SiPM vs. PMT. The red curve is a linear fit performed over the first three points, passing through (0,0), corresponding to the expected behaviour from a perfectly linear photosensor affected by a constant PDE. The black curve is an exponential fit from equation 5.10 where $N_\gamma = \alpha \cdot N_{PMT}$.

as opposed to the typical PDE correction applied for linear photosensors such as PMTs:

$$N_{\gamma_{PMT}} = \frac{N_f}{PDE}. \tag{5.13}$$

Figure 5.10 shows the discrepancy between the two corrections for the Hamamatsu VUV3 MPPC, calculated as:

$$D = \left(\frac{N_{\gamma_{SiPM}}}{N_{\gamma_{PMT}}} - 1 \right) \cdot 100\% \,. \tag{5.14}$$

For this particular sensor, applying the same PDE correction as a PMT for a 285 p.e. signal would result in a 1% discrepancy with the proposed SiPM correction. As a result, in this SiPM, signals below 100 p.e. can be considered linear, as the probability of two photons interacting in the same cell is low.

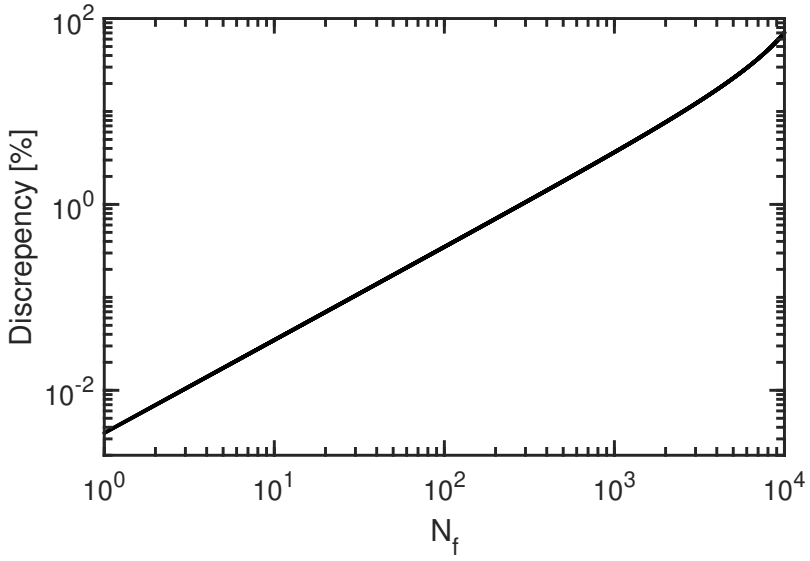

Figure 5.10: Discrepancy between the two light collection corrections applied to the Hamamatsu VUV3 MPPC as a function of the number of fired cells. At 300 detected p.e., the discrepancy is $\sim 1\,\%$.

5.4 Characterisation of Fondazione Bruno Kessler SiPMs

As stated in chapter 2, the DARWIN TPC, in its base design, features about 1 800 3" PMTs distributed between the top and bottom arrays. These photosensors contribute significantly to the radioactive background budget of the experiment [205]. They are delicate [233], but have been shown to withstand much higher pressures than those used in LXe experiments, typically between 2 and 3 bar [382]. With the push to develop solid-state photosensing technologies, SiPMs have become a viable alternative to PMTs for low-background physics experiments. Although they are far superior in many scenarios, they still have one major drawback when compared to PMTs in low-energy searches, namely their high DCR.

Our research group has now been testing SiPMs for over eight years [357]. We first describe the SiPM testing facility – the Liquid Argon Setup (LArS) – in section 5.4.1. The results of the characterisation campaign of two SiPMs from FBK are presented side by side in section 5.4.2, presented side-by-side. A discussion and comparison with other photosensors is presented in section 5.4.3.

5.4.1 Experimental Setup

The SiPMs were tested in the LArS, at the University of Zurich. Previously used to test photosensors in liquid argon for the GERDA experiment [383], LArS has been re-purposed as a general photosensor testing facility. Figure 5.11 shows a CAD rendering of the inner and outer components of the setup.

The main chamber consists of a double-walled, vacuum-insulated pressure vessel that can be filled with inert gases (Ar, N_2, He). A pressure relief valve is used to reliably set the pressure of the main chamber to 1.9 bar, while preventing pressure buildup, which naturally happens during the warm-up phases of the temperature cycle of the setup. The gas is cooled by the boil-off of flowing LN_2 from a self-pressurised Dewar in a coiled copper pipe.

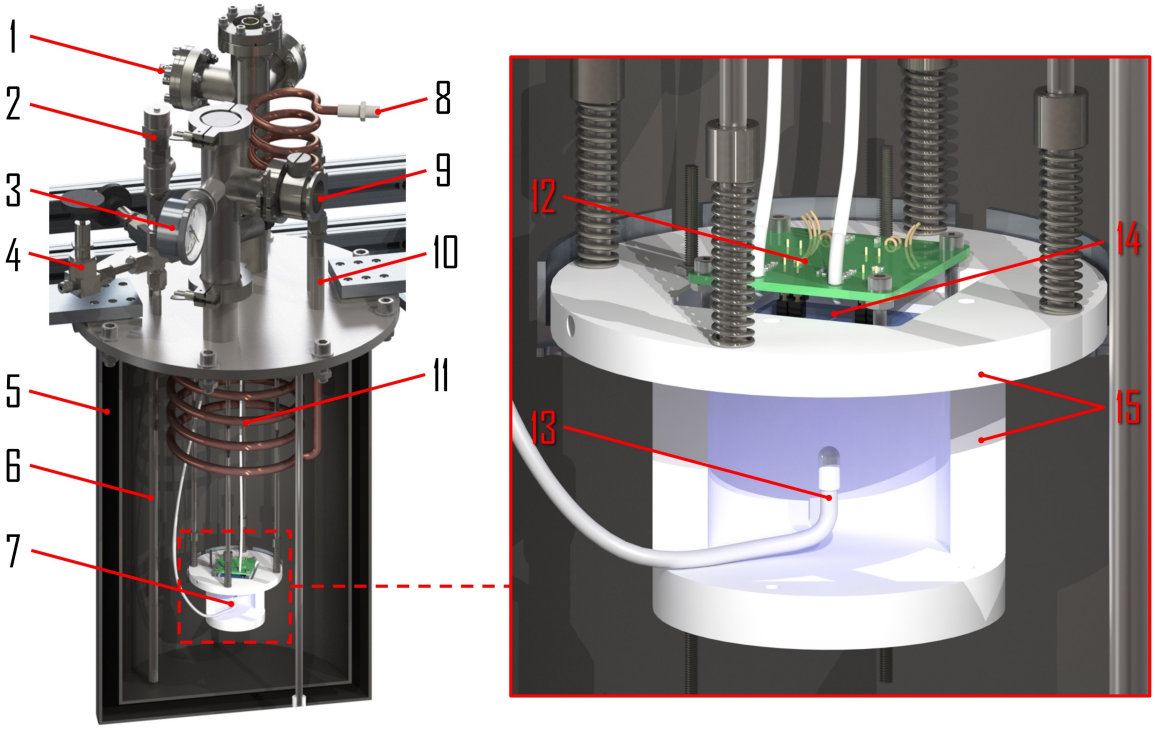

Figure 5.11: Left: Components view of LArS. The testing facility is made of an instrumented double-walled cryostat filled with GN_2. The temperature is controlled by adjusting the flow of LN_2 flowing in the cooling coil. Legend: (1) Electrical and instrumentation feedthrough; (2) Pressure relief valve; (3) Manometer; (4) GN_2 inlet; (5) Cryostat; (6) GN_2 outlet; (7) SiPM cell; (8) LN_2 outlet (solenoid valve not shown); (9) Vacuum port; (10) LN_2 inlet; (11) Cooling coil; (12) $\times 10$ pre-amplifier board; (13) SiPMs; (14) Blue LED; (15) PTFE reflectors.

A block diagram of the instrumentation used in LArS is shown in figure 5.12. A PID controller (Cryo-con, model 32b [286]) controls the flow of LN_2 by opening and closing a servo-controlled valve at the output of the LN_2 line, using inputs from one of two PT100 RTDs inside the pressure vessel. The temperature stability achieved using dry nitrogen gas as the inert gas is within $\pm$ 0.5 K. One of the RTDs is usually placed in close proximity to the tested sensors, while the second one is placed close to the cooling coil. Since our SiPM bases feature a powered pre-amplifier [357], it is believed that the temperatures measured by the RTDs might have been lower than the actual temperature of the photosensor. One RTD was therefore soldered on the SiPM readout base during the testing of the FBK VUV-HD Cryo quad-channel 6×6 mm^2 (2019), ensuring a direct thermal contact for increased temperature determination. Surface-mounted RTDs located directly under the photosensors have become a standard instrument for characterising SiPMs in our research unit, but these have not been used for the measurements described in section 5.4.

Inside the pressure vessel, a PTFE sensor cell hosts two SiPMs. If the two sensors showed similar behaviours, only one channel was used when acquiring dark count data to reduce the size of the data files. The readout board with an on-board $\times 10$ pre-amplifier was designed by the electronic workshop of the physics department at the University of Zurich. A in-house made $\times 10$ external amplifier, developed for XENONnT, brings the total amplification to $\times 100$. A blue LED is located beneath the sensors and is used for calibration purposes. It is pulsed with a waveform generator. The SiPM signals are recorded with a CAEN v1724 ADC. A computer reads and stores the data through a CAEN a2818 Peripheral Component Interconnect (PCI) CONET Controller

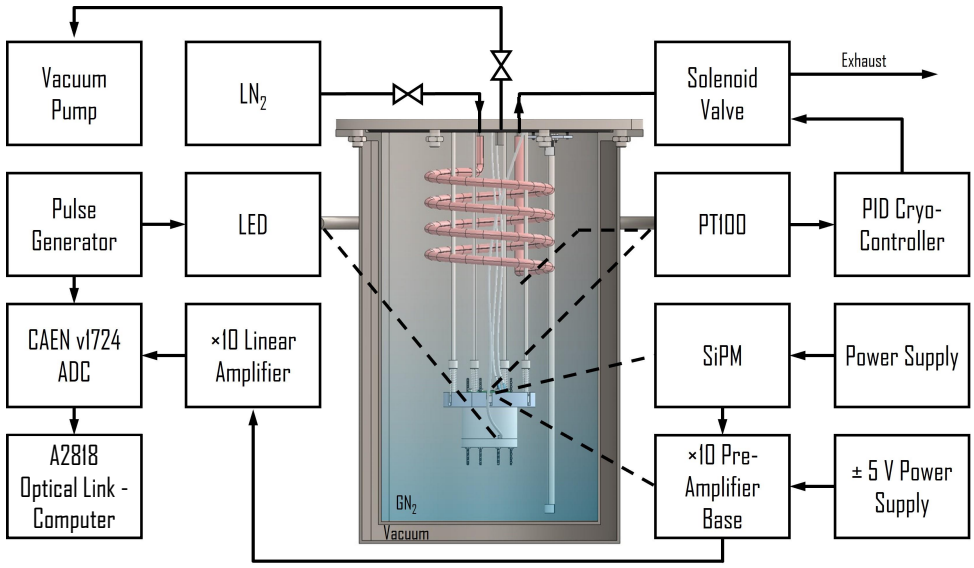

Figure 5.12: Block diagram of the instrumentation of LArS. The SiPM cell is connected to the DAQ, which is composed of an analogue $\times 10$ external amplifier and a CAEN v1724 ADC, read by a computer through an optical link.

optical link [314].

The raw data was processed with our in-house written processor, described in ref. [2]. The pulse-finding algorithm identifies pulses and extracts useful information, such as the peak height, width, area, and position in the waveform. Figure 5.13 shows three different types of pulses. The first is

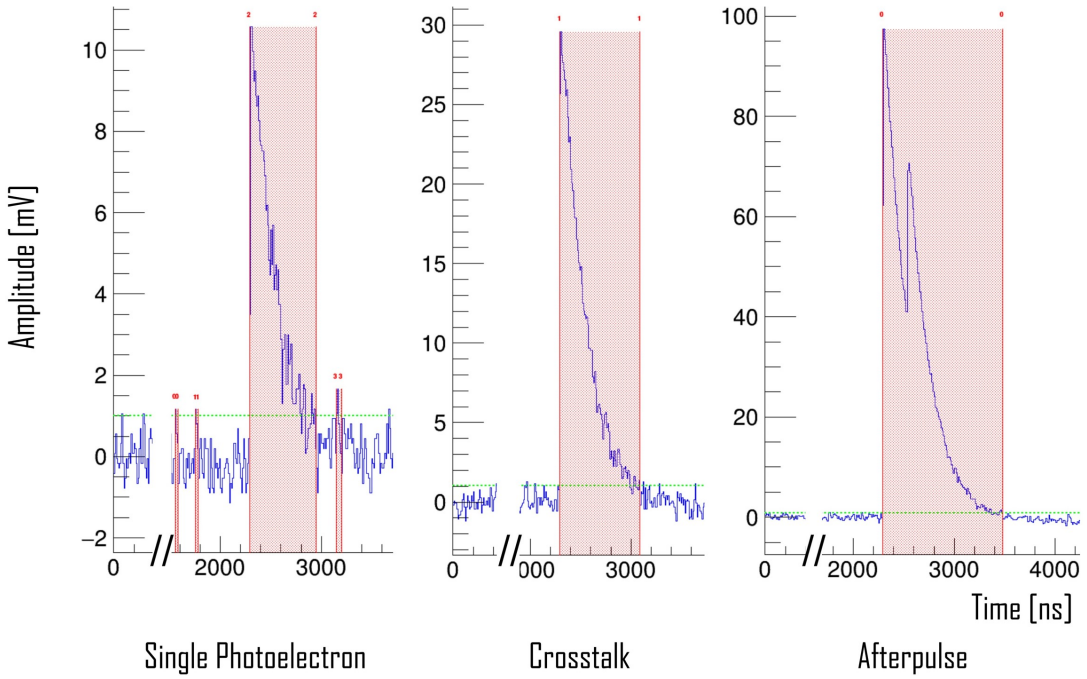

Figure 5.13: Three types of waveforms. On the left is a SPE. In the center, a crosstalk event, indistinguishable from a 2.0 p.e. event. On the right, an AP event with a delayed secondary peak.

a SPE, a pulse characteristic of dark counts, with a typical amplitude between 7 and 10 mV. The pulse in the middle is a crosstalk event, which is the indistinguishable summed signals of two or more SPADs. Finally, the last image shows an AP event, where two peaks can be visually identified. The processor does not differentiate merged AP events from crosstalk events.

5.4.2 The characterisation of the FBK VUV-HD SiPMs

The first sensor we have characterised is the FBK VUV-HD 10×10 mm^2 SiPM (2018)[7]. These photosensors are advertised as a UV-sensitive photosensor with a 40 µm pitch. Figure 5.14a shows a picture of the tested photosensor, and a microscope image under a magnification of $20\times$. At this magnification, individual cells can be observed, separated by trenches, which help in reducing prompt crosstalk. From the image, the estimated fill-factor is 77 %. As per the recommendations of the manufacturer, the VUV-HD photosensor can be operated up to 5.0 V OV, at LXe temperatures.

The second photosensor we have characterised from FBK is the VUV-HD Cryo (2019)[8], a quad-channel, 6×6 mm^2 (nominal), 35 µm pitch, VUV-sensitive SiPM. Results from the characterisation of a 3×3 mm^2 sensor of the same type can be found in ref. [384]. This photosensor is optimised for operations at cryogenic (LN_2) temperatures, showing a lower saturation current. As such, they can be operated up to 9.0 V OV, at a similar gain to that of the previous generation. Figure 5.14b shows the VUV-HD Cryo under a magnification of $20\times$. The fill-factor estimated from the image is 82 %, in good agreement with the reported value of 80 %.

Both sensors were characterised separately in two different characterisation campaigns.

Breakdown Voltage Determination

The first step in the characterisation of SiPMs is the determination of the temperature dependence on the breakdown voltage. As a standard procedure, the blue of the LED SiPM testing cell was pulsed at 500 Hz with 60 ns square pulses to illuminate the SiPMs with $\mathcal{O}(100)$ p.e. The intensity of the LED was kept constant throughout the measurement at a fixed temperature in order to ensure a constant level of illumination. Six bias voltages were arbitrarily chosen at 0.5 V increments just above the breakdown voltage. For each voltage, 500 000 pulses were recorded. The waveforms were processed with the Xurich II processor, described in [2, 6]. Baselines were calculated for every waveform using the first 50 samples. For the VUV-HD, peaks were identified using a 3 root mean square (rms) threshold above the baseline value to ensure the identification of every 1.0 p.e. peak. A threshold of 5 rms was used for the VUV-HD Cryo to account for its slightly higher noise level. At this low threshold, noise fluctuations are often misidentified as peaks, as seen in the left plot in figure 5.13. The misidentified peaks compose the pedestal (i.e. 0 p.e. peak). Most can be excluded from the datasets with width and/or height cuts, as SiPM pulses are usually very uniform in pulse width and height. The pulse area distribution for every dataset was fitted with a Gaussian, as in the example shown in figure 5.15. The mean values of the fits were normalised with the 1.0 p.e. value, obtained from dark counts acquired separately, and were used to calculate the mean charge using equation 5.2. Table 5.1 compiles the values of the parameters used in the charge calculation.

Figure 5.16 shows an example of the charge produced as a function of bias voltage for the VUV-HD at 170 K. The breakdown voltage can be calculated directly by fitting the bias voltage

[7] Hereafter referred to as *VUV-HD*.
[8] Hereafter referred to as *VUV-HD Cryo*.

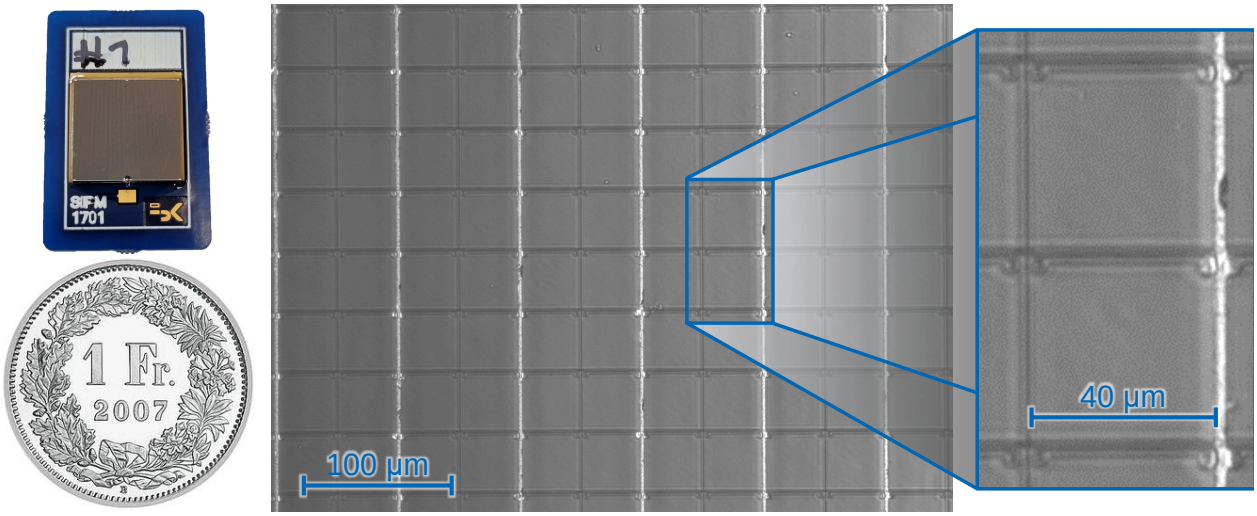

(a) FBK VUV-HD (2018)

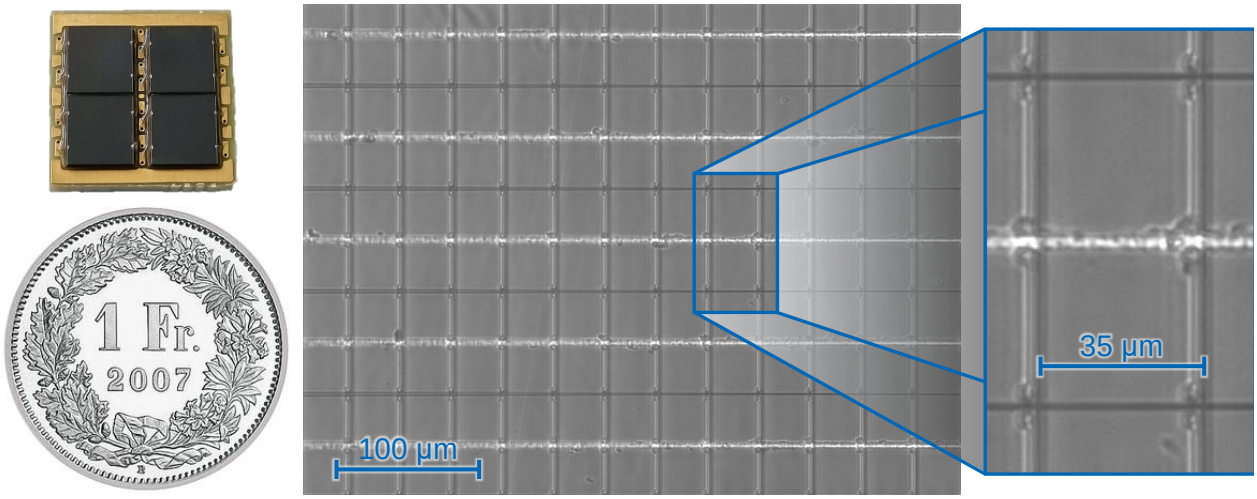

(b) FBK VUV-HD Cryo (2019)

Figure 5.14: Photographs and microscope images of the FBK VUV-HD SiPMs. Magnification 20×. The readout traces can be seen as white vertical (horizontal) lines. The individual cells can be seen, separated by trenches. The nominal pitch of the SPADs is 40 µm and 35 µm respectively.

Parameter	Value
F_{amp}	×100
Δt	10 ns
R	50 Ω
ADC_{range}	2.25 V
ADC_{res}	14 bit

Table 5.1: Parameters used for charge calculation (equation 5.2).

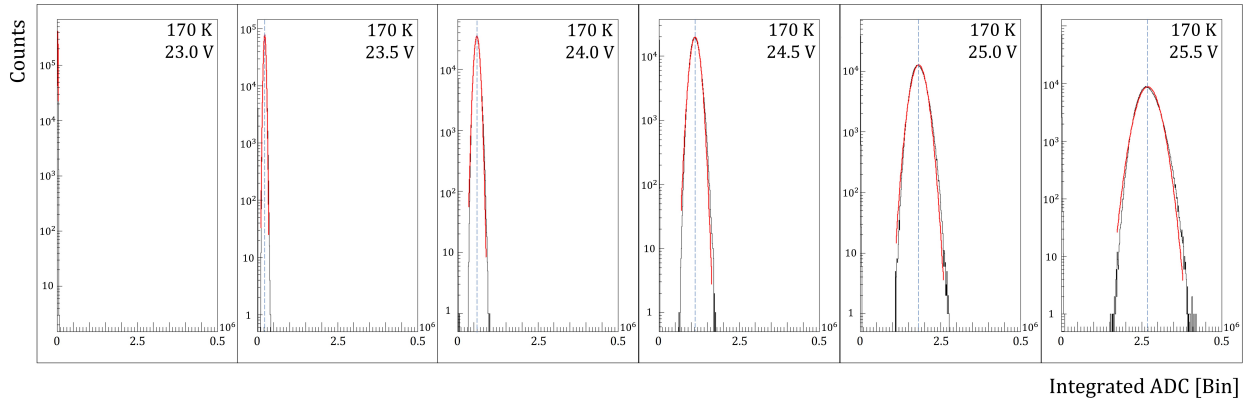

Figure 5.15: FBK VUV-HD - Example of breakdown voltage measurement. The LED illuminates the SiPM with $\mathcal{O}(100)$ photons. The bias voltage is set such that the SiPM signal is barely perceptible by eye, and 500 000 events are acquired. The peak area distribution is fitted with a Gaussian function, the mean of the fit representing the average number of p.e. detected. With a constant LED light output, the procedure is repeated for 5 more bias voltages.

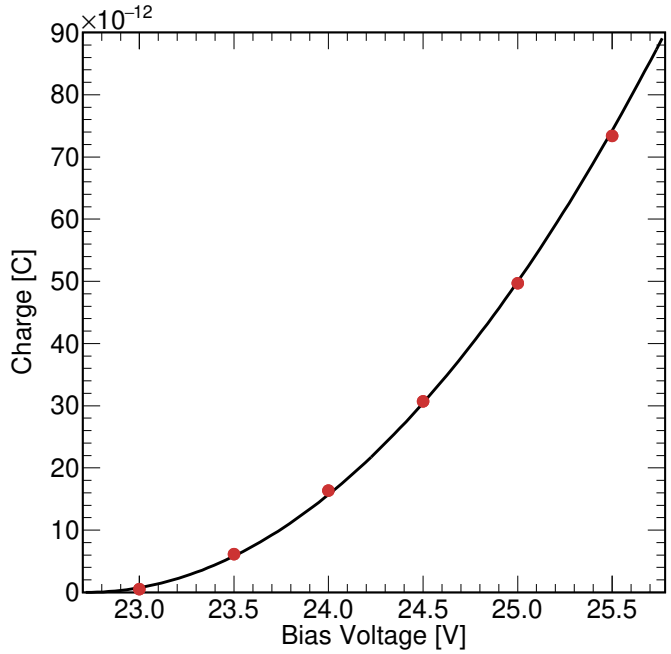

Figure 5.16: FBK VUV-HD - Example of breakdown voltage determination. Charge vs. bias voltage at 170 K. The black curve is a fit to the data with the formula from equation 5.5. The x-intercept value is defined as the breakdown voltage (i.e. charge = 0). The error on the bias voltage is $\pm$ 0.01 V, while the error on the charge is obtained from the Gaussian fit of the charge distribution: both are small enough to be covered by the data points.

V_b vs charge with equation 5.5. Again, the breakdown voltage V_{bd} is the value of the x-axis intercept. Finally, figure 5.17 shows the breakdown voltage as a function of temperature for both photosensors, where the black line is a linear regression. From this measurement, we can characterise the breakdown voltage with the equation:

$$V_\mathrm{bd}(T) = T \cdot V_{\mathrm{bd}_0} + \alpha\,, \tag{5.15}$$

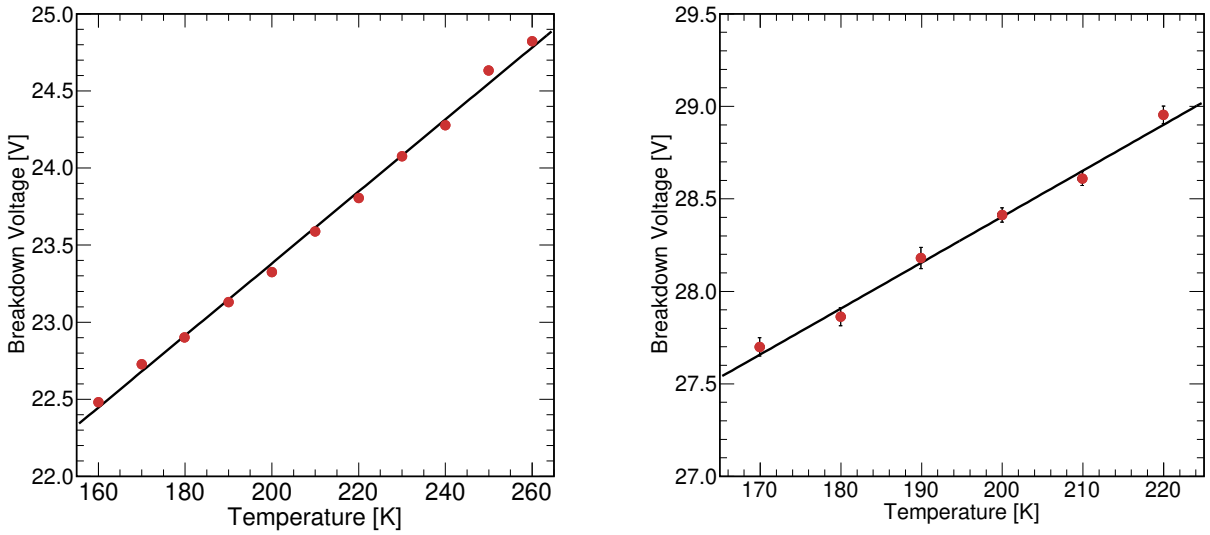

(a) FBK VUV-HD (2018)

(b) FBK VUV-HD Cryo (2019)

Figure 5.17: Breakdown voltage measurement. The temperature stability was better than 0.3 K. **(a)** Breakdown voltage vs temperature. The breakdown voltage can be calculated with the equation $V_{\mathrm{bd}}(T) = (18.71 \pm 0.02)\,\mathrm{V} + T \cdot (2.34 \pm 0.01) \cdot 10^{-2}\,\mathrm{V/K}$. **(b)** Breakdown voltage vs temperature. The breakdown voltage can be calculated with the equation $V_{\mathrm{bd}}(T) = (23.5 \pm 0.3)\,\mathrm{V} + T \cdot (2.484 \pm 0.011) \cdot 10^{-2}\,\mathrm{V/K}$.

where V_{bd_0} is the projected breakdown voltage at $T = 0\,\mathrm{K}$, and the slope of the fit is α. The two breakdown voltage characteristic equations are therefore:

$$\mathrm{VUV-HD}: V_{\mathrm{bd}}(T) = (18.71 \pm 0.02)\,\mathrm{V} + T \cdot (2.34 \pm 0.01) \cdot 10^{-2}\,\mathrm{V/K}$$
$$\mathrm{VUV-HD\ Cryo}: V_{\mathrm{bd}}(T) = (23.5 \pm 0.3)\,\mathrm{V} + T \cdot (2.484 \pm 0.011) \cdot 10^{-2}\,\mathrm{V/K}\,.$$

Gain, Dark Count Rate and Crosstalk Probability

Dark count data was acquired without LED pulses between 160 K and 210 K, as the DCR at higher temperatures would exceed the bandwidth of the ADC, which would put the acquisition board in busy mode. Figure 5.18 shows an example of the peak area SPE distribution at 190 K, with 5.0 V OV for the VUV-HD, and 7.0 V OV for the VUV-HD Cryo. For the first, a few p.e. peaks are identifiable, due to crosstalk events and/or APs. The second shows a significantly different behavior, with multiple ($\mathcal{O}(10)$ p.e. peaks easily identifiable. This points to a high crosstalk and/or AP probabilities.

We used the dark count data to perform the gain calibration. The characteristic 0 p.e. noise pedestal is partially removed from this data set with a width cut, as shown in figures 5.19 and 5.20. We fit the 1.0 p.e. peak of the area SPE spectrum with a Gaussian function to determine the mean pulse area of the 1.0 p.e. peak. The SPE resolutions of both sensors are shown in figure 5.21, obtained from the Gaussian fit and defined as the ratio of the expected value over the standard deviation of the 1.0 p.e. peak, $r_{\mathrm{SPE}} = \mu/\sigma$. The resolution of the VUV-HD is good enough to resolve multiple p.e. peaks, measured to be between 16.3 % (5.0 V OV) and 34.8 % (2.5 V OV). The resolution of the VUV-HD Cryo is however far superior, ranging between 4.4 % (9.0 V OV) and

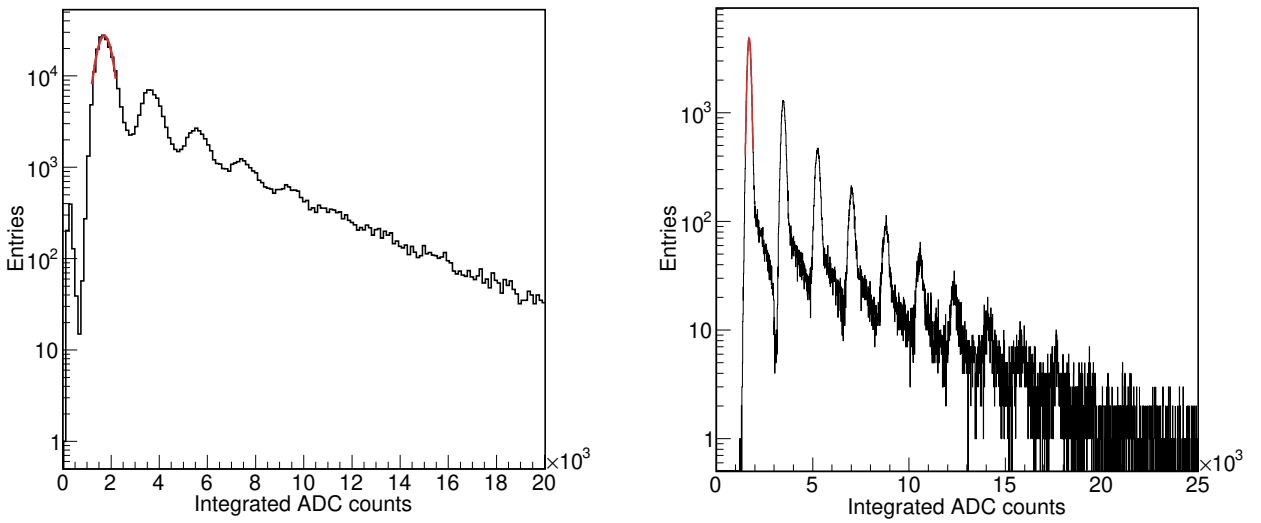

(a) FBK VUV-HD (2018)

(b) FBK VUV-HD Cryo (2019)

Figure 5.18: Area SPE spectra **(a)** Area SPE distribution at 190 K, 5.0 V OV. The 1.0 p.e. peak is fitted with a Gaussian function (in red). The SPE resolution is measured at 19.0 %. The mean value of the fit is used to calculate the 1.0 p.e. value. Photoelectron peaks can be identified up to 5.0 p.e. **(b)** Area SPE spectrum at 190 K, 7.0 V OV. The 1.0 p.e. peak is fitted with a Gaussian function (in red). The SPE resolution is measured at 4.75 %. The mean value of the fit is used to calculate the 1.0 p.e. value. This "finger" plot is characterised by multiple higher p.e. peaks, with up to 10 p.e. being easily identifiable.

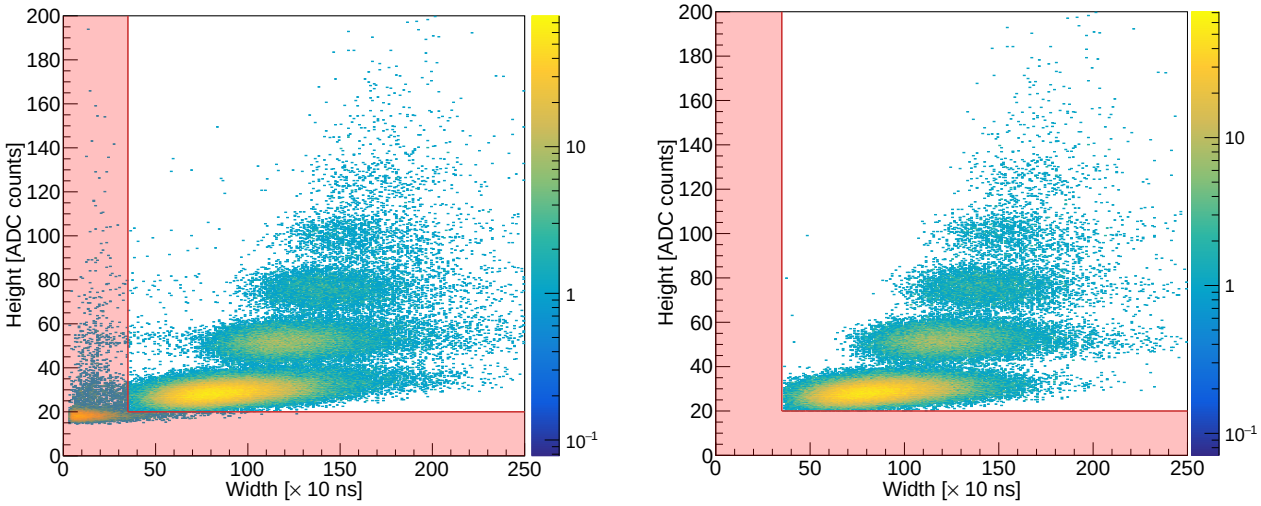

(a)

(b)

Figure 5.19: FBK VUV-HD - Example of a height and width distribution, and cuts, at 200 K and 4.5 V OV. **(a)** With no cuts applied. **(b)** With cuts applied. Most of the pedestal (on the left) is removed with the height and width cuts. A position cut is also applied to only select the triggering peak, which removes some of the events around the main p.e. populations, which can be attributed to AP events.

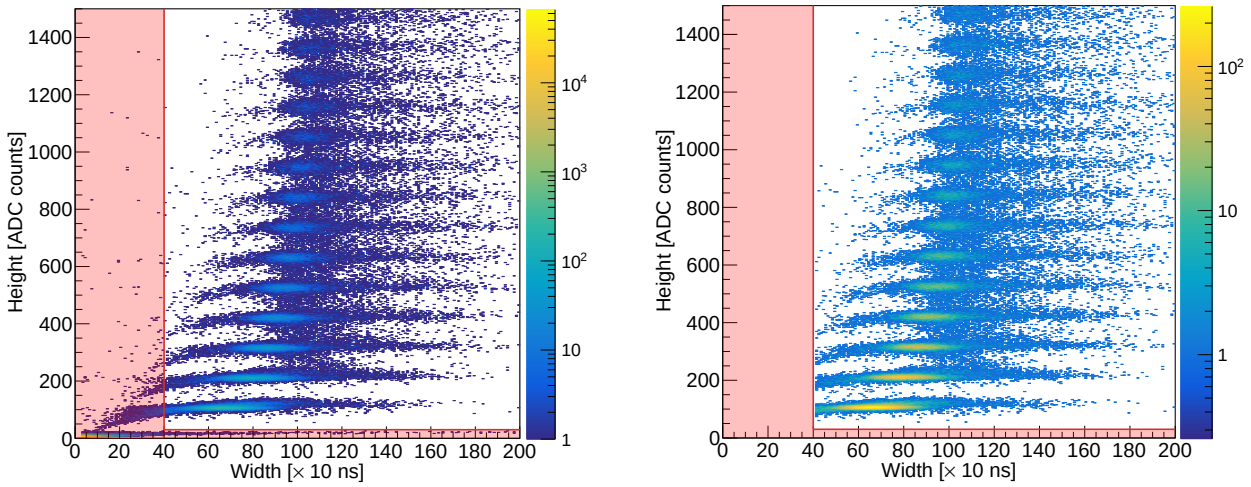

(a) (b)

Figure 5.20: FBK VUV-HD Cryo - Example of a height and width distribution, and cuts. Note the different scales of the color maps. **(a)** With no cuts applied. **(b)** With cuts applied. Most of the pedestal is removed with the height and width cuts. A position cut is also applied to only select the triggering peak.

6.5 % (5.0 V OV).

Figure 5.22 shows the gain (equation 5.1) as a function of the bias voltage for multiple temperatures, using the charge of the 1.0 p.e. peak calculated with equation 5.4. For both sensors, the measured gain is $\mathcal{O}\left(10^6\right)$, slightly lower than that of a typical VUV-sensitive PMT [354]. The gain is slightly higher for the VUV-HD Cryo. Our on-board $\times 10$ pre-amplifier allows us to easily detect

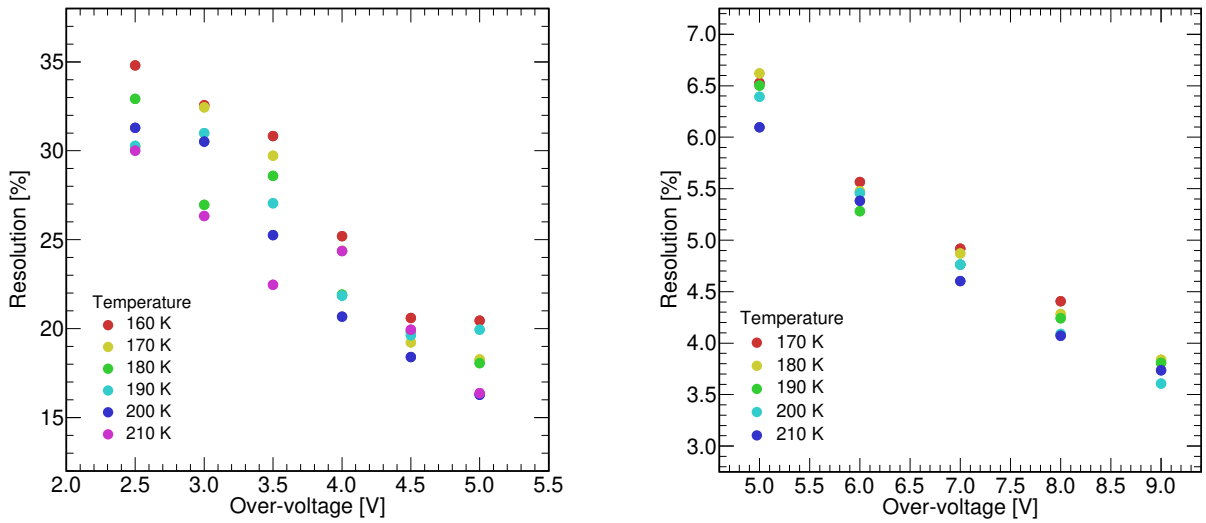

(a) FBK VUV-HD (2018) (b) FBK VUV-HD Cryo (2019)

Figure 5.21: SPE resolution vs. overvoltage. The resolution is improving with increasing OV. **(a)** The resolution is good overall, ranging between 16.3 % and 34.8 %. **(b)** The resolution is excellent, ranging between 4.4 % and 6.5 %.

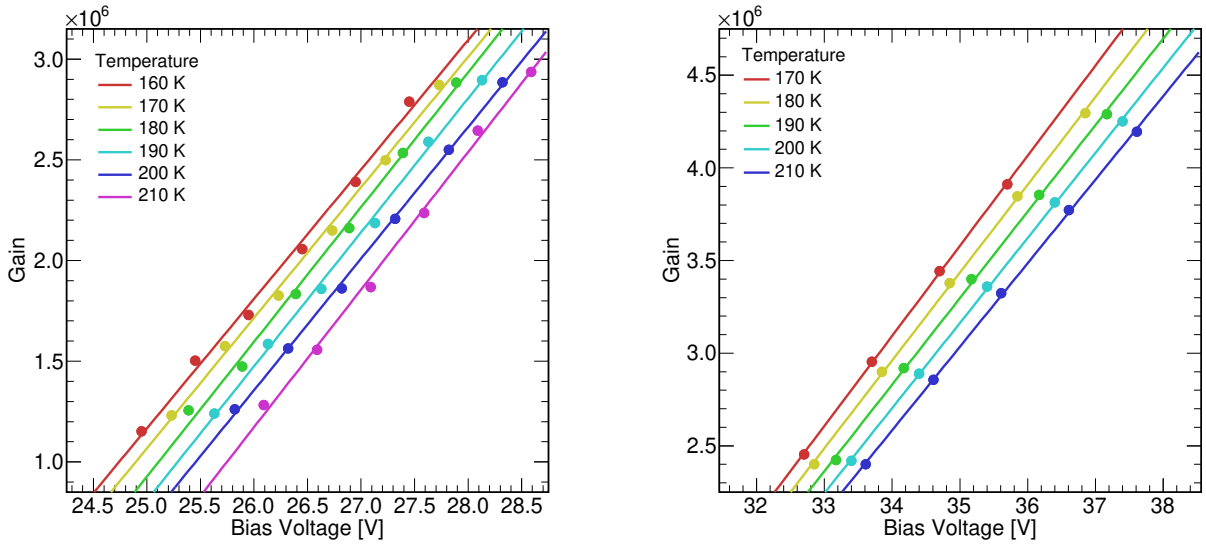

(a) FBK VUV-HD (2018)

(b) FBK VUV-HD Cryo (2019)

Figure 5.22: Gain vs. bias voltage. The gain linearly increases with increasing bias voltage.

1.0 p.e. pulses nonetheless.

The pedestal, composed of noise events not removed by the width and/or height cuts, is removed from the DCR calculation by defining the DCR as the sum of uncorrelated pulses above a threshold of 0.5 p.e., divided by the total run time. The trigger rate was low enough to ensure 100 % live time, which we require to get an accurate time measurement. In the event that the rate is high enough to bring the ADC into a busy state, randomly triggered events with much longer exposures ($t_{\text{event}} = \mathcal{O}(1\,\text{ms})$) could be acquired, with the timing calculated from the number of recorded events (i.e. $t_{\text{run}} = n \cdot t_{\text{event}}$) [234]. In this analysis, the time stamp resolution of the DAQ is 1.0 s. Figure 5.23a shows the measured area-normalised DCR as a function of temperature for OV from 2.5 V to 5.0 V for the VUV-HD, and from 5.0 V to 9.0 V for the VUV-HD Cryo. Close to the operating temperature of LXe in a dual-phase TPC, 170 K, we observed a DCR of $(1.08 \pm 0.02)\,\text{Hz/mm}^2$ at 2.5 V OV for the former, and $(0.117\,8 \pm 0.000\,5)\,\text{Hz/mm}^2$ at 5.0 V OV for the latter. These are therefore 10 to 100 times higher than those of the Hamamatsu 3" PMTs (R11410-21 [354]). However, temperatures in gas regions, where top arrays are located, are typically closer to 190 K, where the DCR is much higher [6]. As previously mentioned, heat generated from preamplifiers could increase the temperature of the sensors themselves, and hence the DCR, even more. Note that the VUV-HD Cryo was unstable (full breakdown resulting in a very high trigger rate) at 170 K, 9.0 V OV. The data point was therefore removed from the measurement.

At low enough count rates (i.e. when pileup is unlikely), pure dark counts are characterised by a SPE population. However, multi-p.e. populations are clearly visible. We can identify two contributing phenomena. First, as discussed in section 5.1, prompt crosstalk events are observed as multi-p.e. peaks in the peak area SPE distribution. In crosstalk events, a photoavalanche in a SPAD produces secondary photons, which can be detected in neighbouring cells. The second phenomenon, APs, is the result of a secondary photoavalanche triggered by electrons trapped in impurities during the primary photoavalanche and released a few hundred nanoseconds to a few microseconds later, sometimes resulting in two overlapping peaks in the waveform. Overlapping pulses are not distinguished by our processor, while fully separated, but correlated events (i.e. recorded in the 10^4 ns time window) are removed with a peak position cut to minimise the calculation

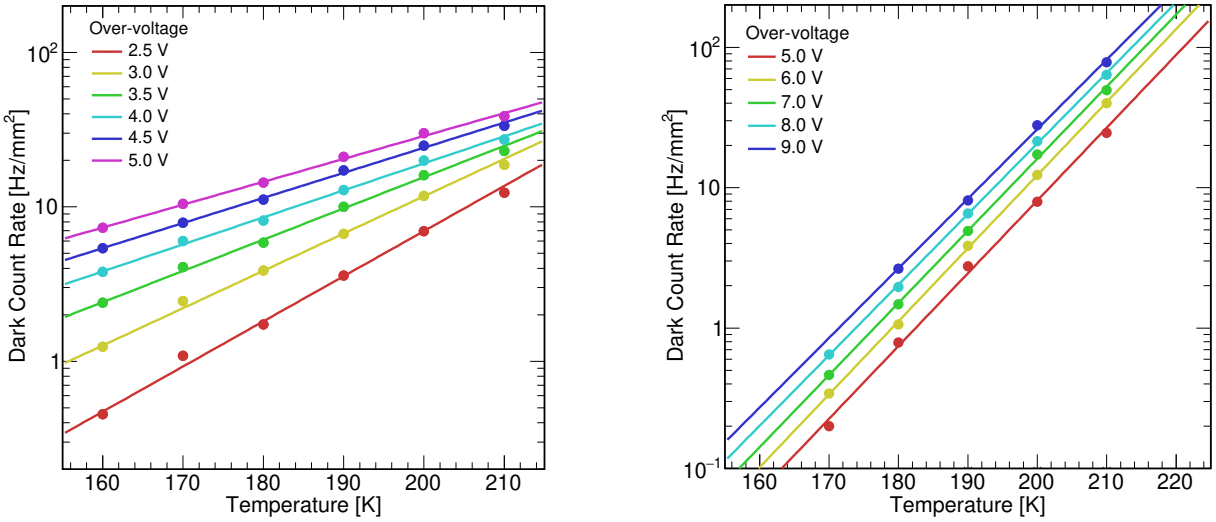

(a) FBK VUV-HD (2018) (b) FBK VUV-HD Cryo (2019)

Figure 5.23: Area-normalised dark count rate vs. temperature. The DCR exhibits an exponential behaviour for both sensors, consistent with the prediction of thermally generated charge carriers in the silicon. At 170 K: **(a)** $(1.08 \pm 0.02)\,\mathrm{Hz/mm^2}$ at 2.5 V OV. **(b)** $(0.1178 \pm 0.0005)\,\mathrm{Hz/mm^2}$ at 5.0 V OV.

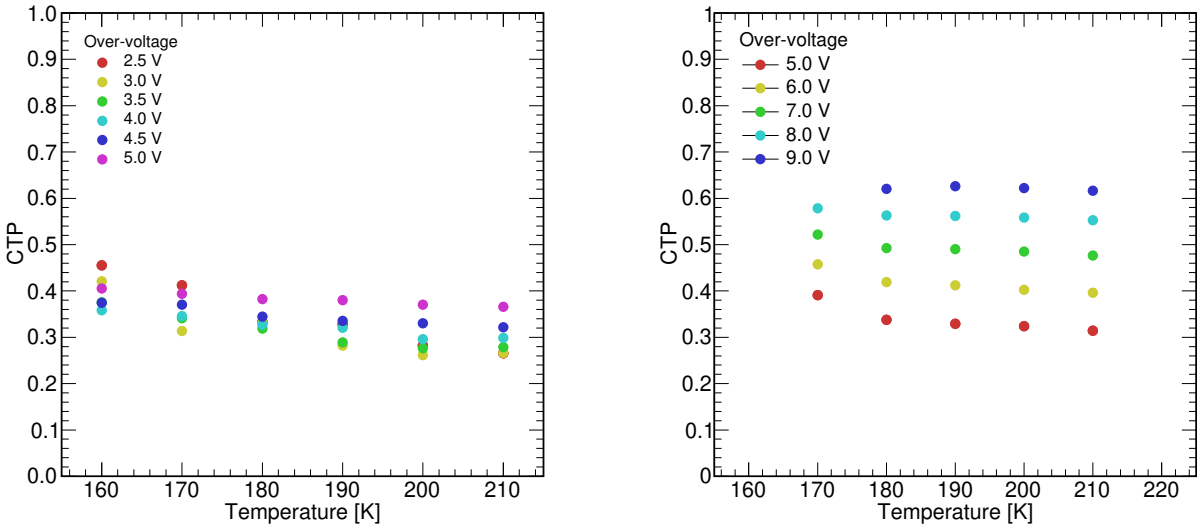

(a) FBK VUV-HD (2018) (b) FBK VUV-HD Cryo (2019)

Figure 5.24: Crosstalk probability vs. temperature. The CTP is OV-dependent. **(a)** This sensor yielded between 26.5 % and 41.2 % CTP, between 2.5 V and 5.0 V OV. A slight temperature dependence can be observed, possibly due to APs partially piling-up with the main pulse. **(b)** The sensor yielding 35 % and 65 % between 5.0 V and 9.0 V OV. We observe a small temperature dependence, again possibly coming from the AP contribution to the correlated noise.

of afterpulse events in the crosstalk analysis.

The CTP is then defined as in equation 5.9, as the ratio of the DCR at the 1.5 p.e. level to the DCR at the 0.5 p.e. level. Figure 5.24 shows the CTP as a function of temperature for

both sensors. This probability should be temperature invariant, but both sensors show a slight temperature dependence, possibly due to the calculation of fast afterpulses. For the VUV-HD, the CTP is measured to be between 31.3 % and 41.3 %, The CTP for the VUV-HD Cryo is estimated to be between 24.5 % and 62.1 %. Both sensors show significantly higher CTP than, for example, the Hamamatsu VUV-4 MPPC, with a measured CTP of 4.1 % at 5.6 V OV.

5.4.3 Discussion

The results of the characterisation of the two FBK SiPMs are collected in table 5.2, along with results from two other studies performed at the University of Zurich, and published in [357] and [354] for the Hamamatsu VUV4, 6×6 mm^2 MPPC and the Hamamatsu R11410-21, 3" PMT, respectively. A direct comparison shows that the Hamamatsu VUV4 MPPC is performing similarly to the FBK VUV-HD in gain and DCR, while the VUV-HD Cryo features a higher gain than both sensors with

[9] at 5.6 V OV [357].

	FBK VUV-HD (2018)	FBK VUV-HD Cryo (2019)	Hamamatsu VUV4 MPPC [357]	Hamamatsu R11410-21 PMT [354, 355]
Form factor	10×10 mm^2	quad 6×6 mm^2	quad 6×6 mm^2	3" circular
Nominal area [mm^2]	100	36	36	4 388
Cell pitch [µm]	40	35	50	N/A
Pre-amplified	On base	On base	On base	No
PDE (QE*) at 175 nm [%]	15 - 20 [385]	20 - 27 [385]	15 - 20	28 - 34
Breakdown voltage [V]	22.75	27.70	45.5	N/A
Operational voltage [V]	25.5 - 27.5	32.7 - 36.7	48.5 - 52.5	∼ 1 500
Gain [×10^6]	1.32 - 2.88	2.45 - 3.91	∼ 1.5 [9]	∼ 5
SPE resolution [%]	18.3 - 30.2	4.4 - 6.5	∼ 9 [9]	∼ 30
DCR [Hz/mm^2]	1.09 - 10.45	0.12 - 0.65	0.82 [9]	0.01
DCR [Count/cell/day]	151 - 1 445	12.7 - 68.8	177 [9]	N/A
CTP [%]	31.3 - 41.3	39.1 - 57.8	∼ 4.1 [9]	N/A

Table 5.2: Photosensor comparison at 170 K. The DCR of the FBK VUV-HD is approximately 110 to 1 000 times higher than that of the Hamamatsu Photonics K.K R11410-21 3" PMT, while the quad-channel VUV-HD Cryo 6×6 mm^2 SiPM exhibits between 12 and 65 times more dark events. While the Hamamatsu Photonics K.K VUV4 MPPC performs similarly to the FBK VUV-HD, it is outperformed by the VUV-HD Cryo in terms of area-normalised DCR. The latter, however, exhibits over 10 times higher CTP.

a significant reduction in DCR. However, all these SiPMs have lower gains, and a much higher DCR, than the Hamamatsu R11410-21 3" PMT. The CTP of both FBK SiPMs is much higher than that of the VUV4 MPPC, a factor that could severely impact its proportionality in photon counting.

The performance of SiPMs is constantly improved by manufacturers, as demonstrated by FBK with their VUV-HD line of photosensors. The FBK quad-channel VUV-HD Cryo $6\times6\,mm^2$ SiPM shows almost a ten-fold reduction in DCR over the previous VUV-HD generation, improving even on the Hamamatsu VUV4 MPPC. Both VUV-HD sensors do, however, demonstrate very high CTPs, which can significantly affect their linearity. This cannot, in principle, be corrected on an event-by-event basis. This non-linear effect adds to the intrinsic non-linearity of SiPMs as discussed in section 5.3.

5.5 Xurich II with SiPMs

As previously discussed, the SiPM technology has evolved to the point where solid-state photosensors are being considered for use in cryogenic environments where single photon sensitivity is required. The DCR is still the major drawback for large photosensor arrays, but not so much at small scales. In this context, we outfitted Xurich II, with a 16-channel array of SiPMs as a first demonstration of the use of SiPMs in a dual-phase xenon TPC.

5.5.1 Experimental Setup

The Xurich II TPC with SiPMs, shown schematically in figure 5.25a, is an upgrade from the TPC described in ref. [5]. Figure 5.25b shows the 16-channel SiPM array, which is comprised of a 2×2 arrangement of four VUV4 MPPCs (Hamamatsu, model S13371), replacing the previously used 2" PMT at the top. Each channel has a nominal active area of $6\times6\,mm^2$ and is pre-amplified with a pre-amplifier circuit based around the Texas Instruments OPA847 [340] voltage feedback operational amplifier. The pre-amplifiers are integrated with the readout circuit on the PCB [357], hosting all 16 channels. The SiPMs are connected on their cathode side to the bias voltage through a $10\,k\Omega$ series resistor, protecting the sensors from excessive currents that could damage the photosensors. On the anode side, the sensors are coupled to ground through a $50\,\Omega$ resistor, the same as the impedance of the ADCs. The 16 operational amplifiers output a total of $\sim 3\,W$ of dissipated heat, which is compensated by the xenon cooling system.

A 2" PMT (Hamamatsu, R6041-06 MOD) is used as the single-channel bottom sensor to detect both the S1 and S2 signals. The cylindrical active volume of $31\,mm\times31\,mm$ (diameter$\times$height) is defined by a PTFE reflector, a cathode mesh at the bottom, and gate and anode meshes at the top. The gate is electrically grounded, and the anode, placed 4 mm above it, is biassed to 4.0 kV, producing an extraction field at the liquid-gas interface of 10 kV/cm. The cathode is biassed at 0.25-3.0 kV, producing drift fields in the active region in the range of $80-968\,V/cm$. Seven copper field shaping rings are separated by PTFE spacers and coupled together with a resistor chain, ensuring the homogeneity and verticality of the electric field.

Three parallel plate capacitors are positioned concentrically 120° apart around the TPC, and are used to measure the liquid level, allowing for both the measurement of the tilt of the TPC in the x-y plane, and the height of the liquid level. A weir system similar to the one described in section 4.3.1 is used to adjust the height of the liquid with a height-resolution of $\pm\,5\,\mu m$.

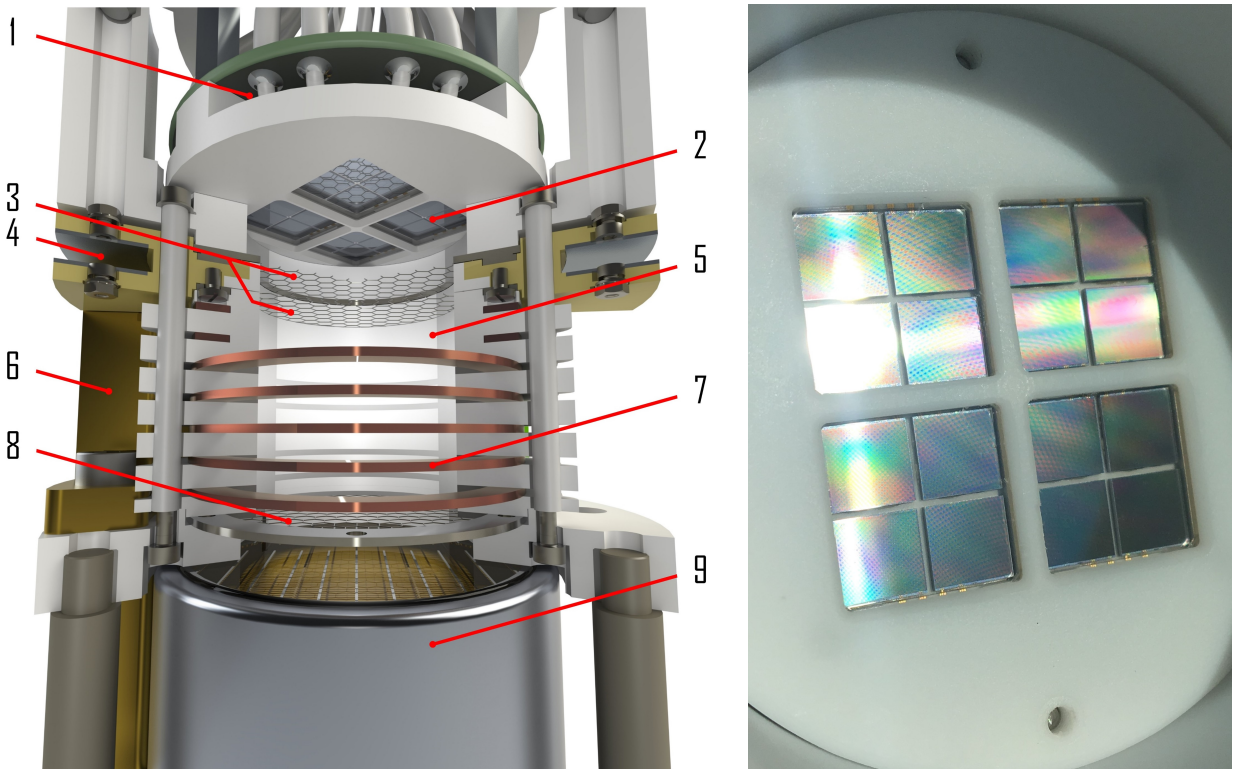

(a) (b)

Figure 5.25: Xurich II with SiPMs. **(a)** Rendering of the upgraded Xurich II TPC. The active LXe is contained within a PTFE cylinder and surrounded by copper field-shaping rings. A 2" PMT is placed in the liquid, and an array of 16 SiPMs is placed in the gaseous phase at the top. For the sake of visualisation, two field-shaping rings have been cut. Legend: (1) PCB with $\times 10$ preamplifier; (2) SiPM array; (3) Anode and gate mesh; (4) LXe level meters; (5) PTFE reflector wall; (6) Weir for liquid level control; (7) Copper field-shaping rings; (8) Cathode; (9) PMT. Figure adapted from ref. [6]. **(b)** SiPMs in the PTFE holder.

The TPC is mounted inside a vacuum-insulated, double-walled cryostat. The inner vessel is mechanically coupled to a cold finger dipped in LN_2, with thermal conduction providing the cooling power needed to liquefy xenon on the top flange of the inner vessel. An automatic filling system similar to the one described in section 3.3.3 continuously supplies LN_2 from a self-pressurised Dewar to a Dewar flask located under the cryostat. A 5 W heater strip installed on the outside of the inner top flange and controlled by a Cryo-con model 32B is used to control the temperature of the LXe, with a temperature stability better than $\pm$ 0.001 K.

LXe is extracted from the weir using a double diaphragm compressor, and is passed through the gas handling system, as shown in the P&ID in figure 5.26. The xenon is purified with an SEAS Pure Gas Monotorr getter, model PS3MT3-R, up to a maximum of 5 slpm. In the absence of a heat exchanger, the recirculation speed is limited by the total cooling power of the cryostat. The gas system features two radioactive source insertion chambers. The first is a small chamber that houses ^{83}Rb, allowing ^{83m}Kr to be introduced into the TPC. The second is an ^{37}Ar insertion chamber, described in detail in refs. [2, 6].

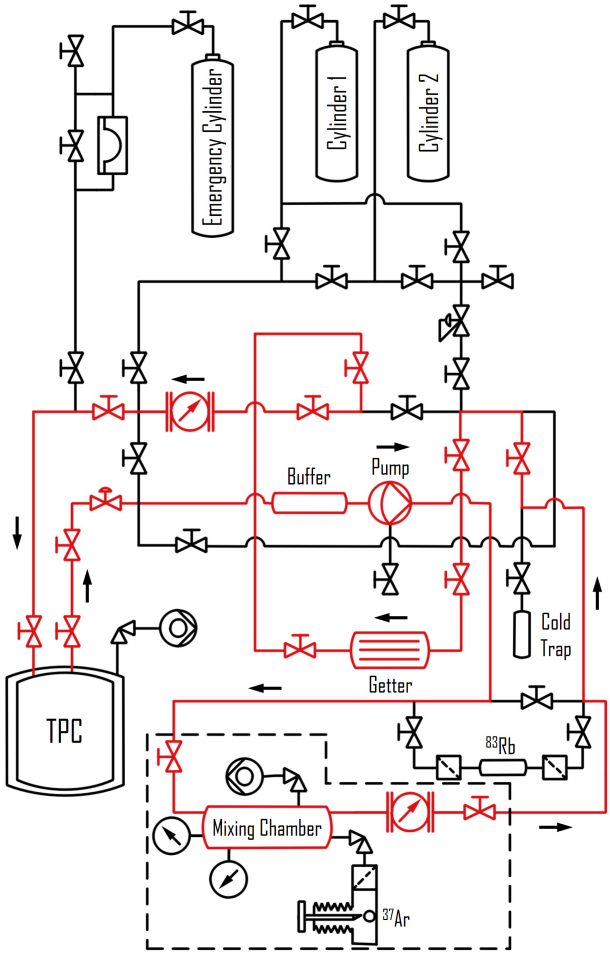

Figure 5.26: P&ID of the gas handling system of Xurich II. The path highlighted in red shows the recirculation path used for the introduction of ^{37}Ar in the TPC. Figure adapted from ref. [6].

5.5.2 DAQ and Zero Length Encoding

The DAQ system used in Xurich II with SiPMs was adapted from the one presented in ref. [5]. However, both the DAQ hardware scheme and the DAQ software were upgraded to accommodate the 8.5-fold increase in the number of readout channels.

DAQ Hardware Configuration

Figure 5.27 shows a block diagram of the DAQ hardware. As it fully covers the bottom array, and hence is exposed to more light, PMT signals were used to generate NIM logic trigger signals. Analog PMT signals were therefore first duplicated with a CAEN 625 Fan In/Fan Out unit: one copy was sent to a CAEN N840 leading-edge discriminator to generate NIM logic trigger signals, which a triplicated by a CAEN 625 Fan In/Fan Out unit, and sent to the three 8-channel CAEN V1724 ADCs; the second was sent to ADC0. This triggering scheme circumvents the high DCR of

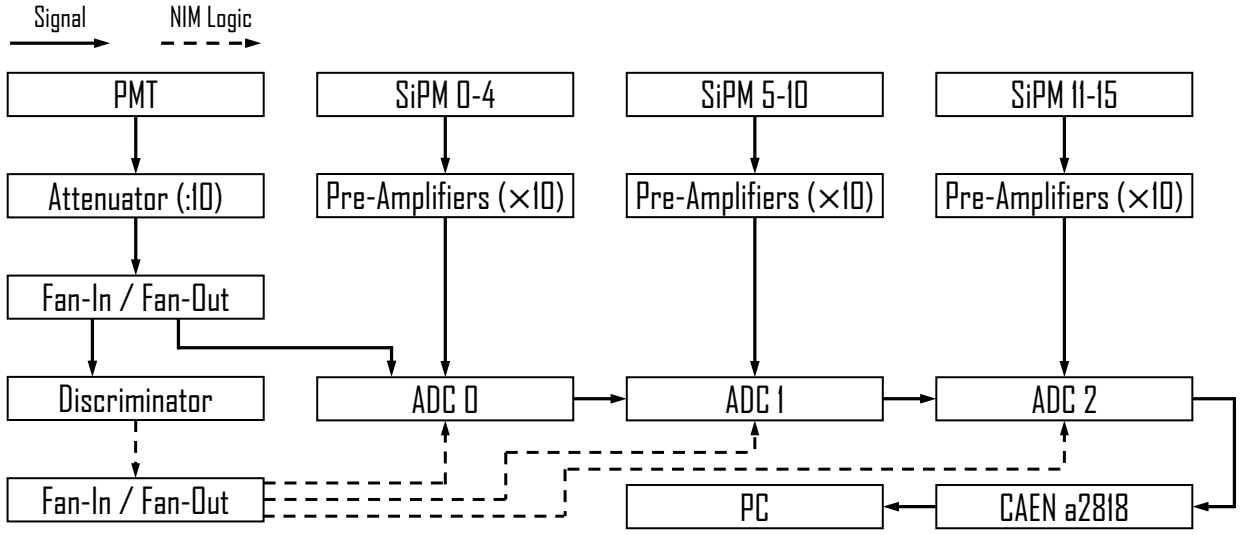

Figure 5.27: Block diagram of the DAQ of Xurich II. SiPM signals are fed to three daisy chained ADCs. The PMT signal is fed to a Fan In/Fan Out unit, after which one of the duplicated signals is directed to a discriminator to produce a NIM logic trigger. The trigger is then propagated to all three ADCs. The complete set of raw data is read by a personal computer (PC) using a CAEN a2818 PCI optical link. Figure adapted from ref. [2].

the SiPMs. Three daisy-chained CAEN v1724 ADCs were used to digitise the waveforms from the 17 channels (16 SiPMs + 1 PMT). Each ADC operates with a bandwidth of 100 MHz, with 14-bit resolution, and a 2.25 V dynamic range. During the recommissioning of the DAQ, the firmwares of CAEN hardware components (the a2818 optical link and the three v1724 ADCs) were upgraded to CONET2, a CAEN proprietary serial protocol used for optical link communication, increasing the data-communication speed by 50 % compared to CONET1.

Busy State Propagation

At high event rates, such as during radioactive source calibrations, the limited memory volume per ADC can get completely full in between raw data pull requests from the PC, sending the ADC into a "busy" state (Busy $FALSE \rightarrow TRUE$). This state change also automatically switches the veto state of this (and only this) ADC (Veto $FALSE \rightarrow TRUE$). These states must be propagated to stop the data acquisition in the rest of the ADC chain, ensuring event alignment between all the ADCs. This is achieved using LVDS, as shown by the block diagram in figure 5.28. The LVDS signals can be interpreted as $FALSE$ (i.e. no voltage difference), or $TRUE$ (i.e. voltage difference).

Table 5.3 details the functions of each cable pair, forming 4×4 groups on the LVDS connector. The Trigger and Run LVDS functions were not used with Xurich II, as trigger propagation was ensured by the PMT signal discriminator, and the *run start* signal was transmitted through the optical link. The busy state propagation was transmitted in a cascade through the ADC chain. A busy ADC transmits a busy $TRUE$ signal from its "Busy IN" to the "Busy OUT" of the next ADC, switching its Busy state to $TRUE$ as well. The last ADC in the chain then sends a busy $TRUE$ signal to the "veto IN" of the first ADC. The veto $TRUE$ is sequentially transmitted to all the ADCs, stopping the data acquisition of the whole chain. The signals are all switched to $FALSE$ as soon as the memories of all the ADCs have been liberated.

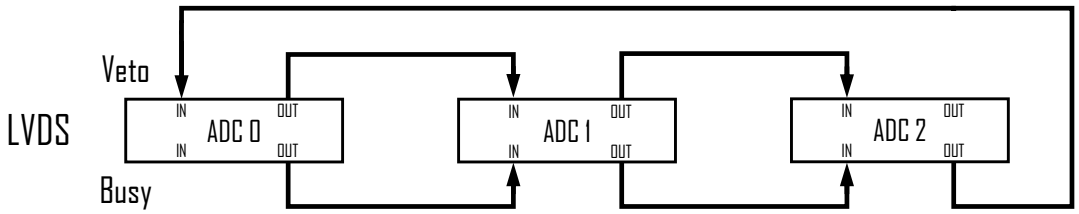

Figure 5.28: Block diagram of the busy state propagation. If the memory of an ADC gets full, its busy state is switched to *TRUE*, and a busy signal is sent through LVDS to the next ADC down the chain, also switching its busy state to *TRUE*. The signal is transmitted until the last ADC in the chain. This ADC then sends a signal from its "busy OUT" to the "Veto IN" of the first ADC in the chain, switching the veto state to *TRUE*. The veto signal is then propagated through the chain, stopping the acquisition of all the boards. When the memory of the first busy ADC in the chain is liberated, the busy signal propagation stops, resuming acquisition.

LVDS pair	Function
n+0	Busy
n+1	Veto
n+2	Trigger
n+3	Run

Table 5.3: Low-Voltage Differential Signalling (LVDS) connector grouping. $n = 0, 1, 2, 3$. represents the four LVDS groups. The Trigger and Run (start) LVDS pairs were not used with Xurich II.

Zero Length Encoding

The software used to operate the DAQ was upgraded to include Zero Length Encoding (ZLE), an active pre-processing tool used to significantly reduce the size of the raw data files. This option can be enabled by end-users by modifying the Extensible Markup Language (XML) file declared at the launch of a data acquisition.

ZLE employs a user-defined threshold scheme to only retain data above (below) threshold for positive (negative) pulses. For simplicity, we will assume that the ZLE polarity is positive throughout this section. It is important to distinguish the ZLE threshold from the trigger threshold used in "self trigger" mode (i.e. trigger logic based on the amplitude of selected channels).

In Xurich II, following a trigger obtained from the PMT and propagated to every board, all 17 waveforms are stored in the internal memory of the ADC. Upon their acquisition, the raw data are immediately processed by the FPGAs of the ADCs. Figure 5.29 is a schematic representation of the ZLE processing. The stored waveforms are converted into two smaller data vectors: the CW vector and the "good-samples" vector. Samples below threshold (in Xurich II, chosen between 6 and 20 ADC bins – 0.82 and 2.75 mV – depending on the sensor and type of acquisition [2]) are tagged as "skipped"; only the number of skipped samples is stored in the CW vector as a negative integer. These samples are immediately discarded, freeing some ADC memory. Samples over the threshold are tagged as "good". The number of good samples is stored in the CW vector as a positive integer, while the "good" raw data is copied to the good-samples vector. The ZLE algorithm also enables the end user to specify a number of samples to be saved before and after the "good samples" selection. This ensures the complete recording of peaks in the waveform, down to the signal baseline. In the event of overlapping "good samples", the pulses are considered one good region and are saved as a single event.

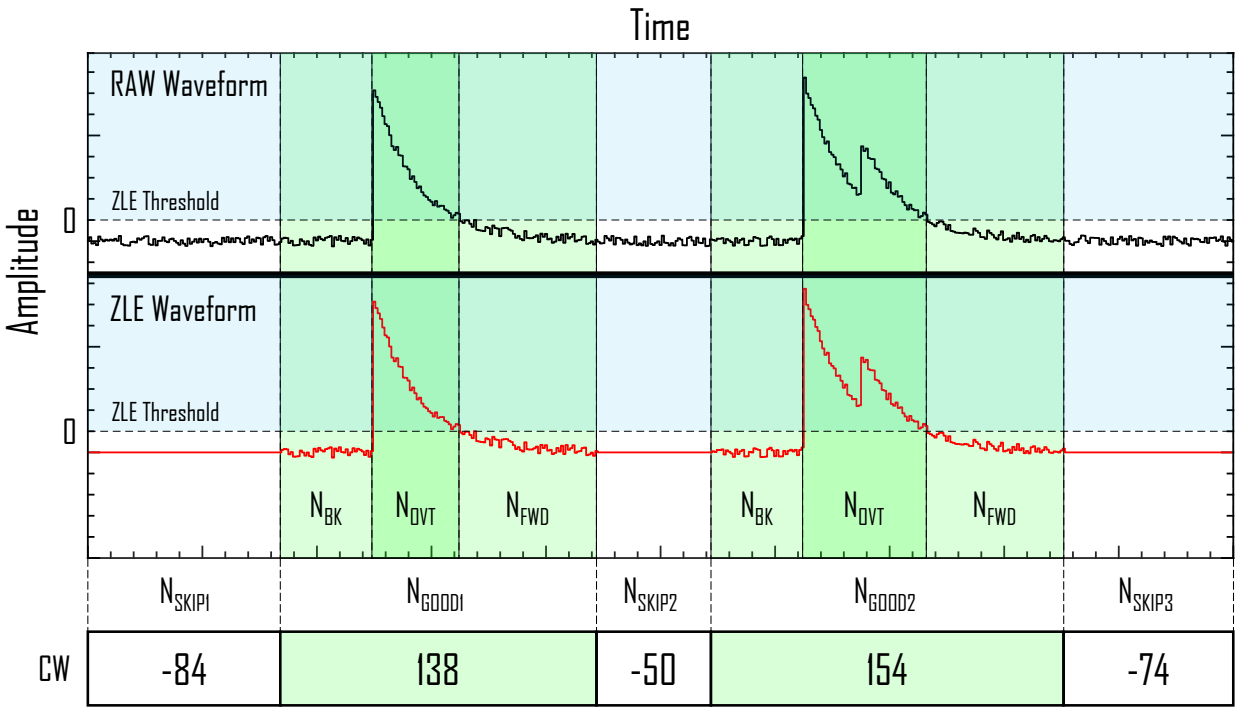

Figure 5.29: Schematic of the Zero Length Encoding (ZLE) data processing. Following a board trigger, the ADC stores the raw data (black) in its flash memory. The Field Programmable Gate Array (FPGA) processes the data by identifying over-threshold samples (N_{OVT}). The processor also saves N_{BK} samples before the threshold crossing, and N_{FWD} samples after the last sample over-threshold. These samples form the first set of good samples (N_{GOOD1}), and the number of samples saved is stored in the control word (CW) data vector as a positive integer. The same applies to N_{GOOD2}, and the data of both peaks are saved into a vector of integers. Any additional data (N_{SKIP}) are discarded and lost. The number of discarded samples is saved in the CW vector as a negative integer. The two vectors are then pulled from the flash memory by the DAQ computer and saved to disk. The number of samples (in this example, 500) can be higher than the event size defined by the user if a peak, including its N_{FWD} and N_{BK} samples, exceeds the limits. The event can be reconstructed (red) with the two vectors.

The size reduction factor of the raw data files with ZLE depends on multiple factors, such as the event rate, the length of events, and the sizes of the N_{BK} and N_{FWD}. A direct comparison with Xurich II revealed a $\sim 40\times$ reduction in data file size. In Xurich II with ZLE enabled, raw data files for 500 000 events can typically take up to $\sim$ 6 GB of disk space [2].

5.5.3 Performance of the SiPMs in Xurich II

Xurich II with SiPMs was commissioned in January 2019, and was operated in stable conditions for over one year. As they are out of the scope for this chapter on photosensors, the main results of the measurement campaign will not be discussed here. The results of the detector calibration with ^{83m}Kr and ^{37}Ar were published in ref. [6], while the calculation of the *W*-value of xenon can be found in ref. [228]. Both of these measurement are also presented in more details in ref. [2].

Following the acquisition of raw data, the waveforms go through a three-stage processing. The first stage ensures event alignment and merges the data files from the three ADCs into a single file. The second stage identifies and retrieves peak information event-per-event, such as their height, width, and area. Peak coincidence amongst the channels is then determined and pulses are cate-

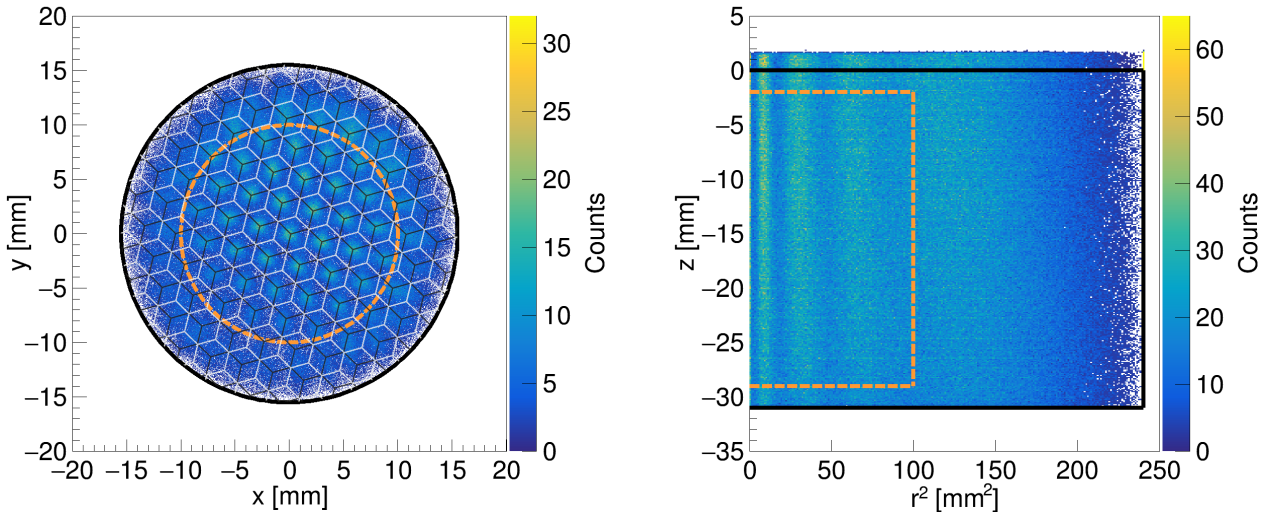

(a) (b)

Figure 5.30: Volume fiducialisation for the ^{37}Ar K-shell capture data. The detector limits are drawn in black, and the fiducial volume in orange. **(a)** x-y event distribution. The two electrodes [gate (black), anode (white)] are overlaid with the event distribution, highlighting the focusing effect of the meshes. **(b)** r^2-z event distribution. The z-fiducial cut was placed at 2 mm from the electrodes. Figures from ref. [6].

gorised (S1, S2, noise). The third step is the associations of S1 and S2 signals to form complete events.

The new implementation of the top array provided, for the first time in Xurich II, position reconstruction. The x-y event positions were calculated with a geometry and gain-weighted sum of the integrated S2 charge of each sensor [10]:

$$x = \frac{1}{Q_{\mathrm{S2}}^{\mathrm{tot}}} \sum_{i=1}^{16} X_i \cdot \frac{Q_{\mathrm{S2}}^{i}}{g_i}, \tag{5.16}$$

where $Q_{\mathrm{S2}}^{\mathrm{tot}} = \sum_{i=1}^{16} \frac{Q_{\mathrm{S2}}^{i}}{g_i}$ is the total charge of the S2, while g_i is the gain of the i^{th} SiPM. The square arrangement of the array lead to a biased, non-circular position reconstruction. The x-y map was therefore normalised to a unit square, and was then re-mapped onto a unit circle. The map was then scaled using the node-pattern produced by the focusing effect of the two top electrodes. At a radius $r > 10$, the position reconstruction is no longer linear, but can instead be described as the projection of the reconstructed position on a sphere. This condition determined the radial limit of the fiducial volume. The z-position reconstruction was obtained for each event from the time difference between the S1 and S2 signal. The z-fiducial cut was place at 2 mm above (below) the cathode (anode) to avoid high and/or non-uniform electric field regions. The final x-y and r^2-z event distribution for the ^{37}Ar K-shell capture data can be seen in figure 5.30. The position resolution of the SiPM array was determined to be $\sim$1.5 mm, due to the strong focusing effect of the electrode meshes. In reality, the position resolution of the SiPM array itself is most certainly much higher.

The DCR of the array was measured in a similar manner to that presented in section 5.4. The error-weighted mean value measured was $(8.05 \pm 0.03)\,\mathrm{Hz/mm^2}$ at a bias voltage of 51.5 V at 190 K, which is consistent to the extrapolated value obtained from ref. [357]. Two channels demonstrated a DCR twice that of the average.

[10] The reconstruction is performed analogously for the y-position.

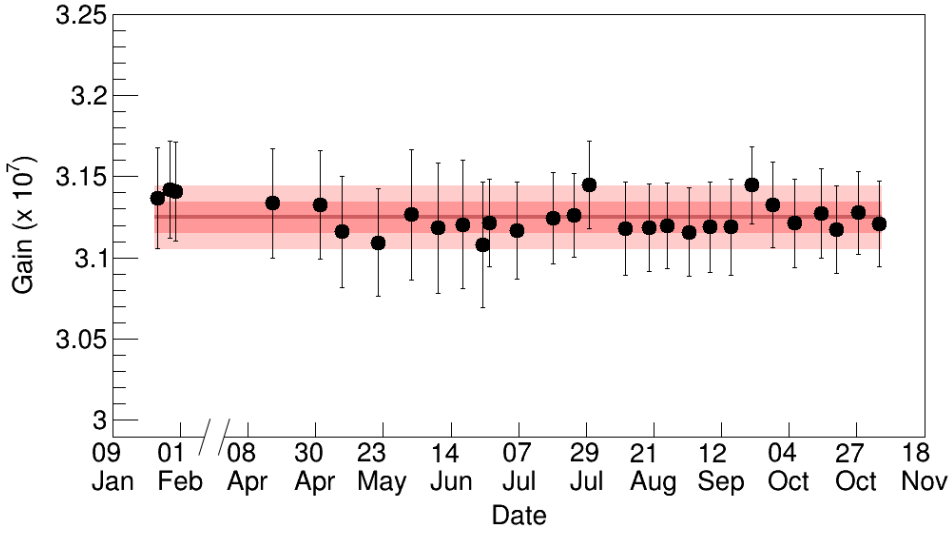

Figure 5.31: Error-weighted mean gain (tenfold amplified) of the 16 SiPM channels over the entire data taking period in 2019. We measured a gain of $(3.12 \pm 0.01) \cdot 10^7$. The $\pm 1\,\sigma$ and $\pm 1\,\sigma$ uncertainty bands around the mean are shown in red. Data with ^{83m}Kr (^{37}Ar) was acquired before (after) the time-axis break. Figure from ref. [6].

Finally, the long-term performance of the SiPMs was assessed. Figure 5.31 shows the evolution of the average gain of the array. The gain stayed constant over more than one year.

5.6 Summary and Outlook

The SiPM technology is in constant evolution. As manufacturers perfect their production methods, the quality of the silicon increases, leading to the production of ever more sensitive photosensors. SiPMs are nowadays competitive photodetectors, due to their compact geometries, ease of use, resilience, and high gain.

We have characterised two SiPMs from FBK in the search for a substitute for the PMTs that have typically been used in dark matter experiments. First, the FBK VUV-HD (2018) offers an attractive package, with a 10×10 mm^2 active area, a cell pitch of 40 µm and a fill factor of $\sim$ 77 %. This sensor offers a good gain and a decent SPE resolution. It performed similarly to the Hamamatsu VUV4 MPPC in terms of DCR, but we measured a much higher CTP.

We have also characterised the FBK VUV-HD Cryo (2019), an upgraded version of the VUV-HD designed for cryogenic operations. The lower pitch, at 35 µm, gives this sensor a slightly higher dynamic range while featuring a similar fill factor of 82 %. Its improved geometry confers higher gain than its competitor, while significantly reducing its DCR. The incredible SPE resolution, between 4.4 and 6.5 %, is only overshadowed by the very CTP of this photosensor.

Finally, we have demonstrated the use, for the first time, of SiPMs in a dual-phase xenon TPC. The high sensitivity and small form factor of the Hamamatsu VUV4 MPPCs played an instrumental role in the upgrade of Xurich II, providing position reconstruction for the first time in this small-scale setup. We have upgraded the DAQ software of Xurich II, enabling multi-ADC operations, and we reduced the amount of raw data retained during the operation of the TPC by including the ZLE strategy in our DAQ software.

Despite the technological advances made in recent years in the context of SiPMs for low-energy searches, PMTs still seem to offer, in general, better performances at LXe temperatures, mainly in terms of gain and uncorrelated noise. In the near future, however, SiPMs could match the performance of PMTs, in addition to their lower cost, intrinsic radioactive background, and low-voltage operation. It is also interesting to note the deployment of SiPMs in near-future noble-liquid experiments, such as DarkSide-20k, a liquid argon TPC for dark matter searches [157], and nEXO, a single phase xenon TPC enriched in ^{136}Xe, for $0\nu\beta\beta$ search [207].

In summary, SiPMs are a promising technology, well suited for several applications: at low temperatures, where DCR is not the dominant source of noise, or in high illumination scenarios, such as in $0\nu\beta\beta$ searches, where single photon sensitivity is not needed.

FBK – VUV-HD Cryo SiPM (2019)
Zürich, 2020

Concluding Remarks

The existence of dark matter is well established, but its nature remains one of the greatest mysteries in modern physics. Astrophysical and cosmological observations strongly suggest that some form of non-luminous, non-relativistic, chargeless, and, at the very least, weakly interacting beyond-the-SM matter is present throughout the Universe. Its gravitational effects are thought to be key to the formation of extra-galactic large-scale structures, and even galaxies themselves. Given the resounding success of the SM, it is suggested that dark matter might be composed of particles. One of the favourite candidate type is the WIMP, naturally predicted by many beyond-the-SM theories. Many experiments, past, present, and future, were designed to search for dark matter, either through its production in large particle colliders, by detecting the annihilation products of dark matter particles, or by detecting the low-energy elastic scattering of dark matter with baryonic matter. The field of direct detection is currently led by experiments using tonne-scale targets of liquefied noble gases. The most sensitive detectors, dual-phase xenon TPCs, have set the most stringent upper limits on the WIMP mass-dependent interaction cross-sections with baryonic matter, with yet no evidence for a direct detection.

DARWIN, with its proposed 50 t (40 t instrumented) LXe target in a dual-phase TPC will, amongst other goals, explore the entire accessible parameter space for dark matter search, down to the neutrino-fog, where neutrinos will become an irreducible background. This sensitivity to neutrino interactions will enable DARWIN to study neutrinos, either solar or cosmic. Additionally, DARWIN will be aiming to detect the $0\nu\beta\beta$ of ^{136}Xe, which can inform on the nature neutrinos, and on the neutrino mass ordering. As with any new generation of detectors, the realisation of DARWIN requires technological improvements on key aspects compared to the current generation of dark matter detectors.

With a cylindrical instrumented volume of 2.6 m in diameter and 2.6 m in height, DARWIN will require improved structural integrity and reliability of large detector components, such as the electrodes used to produce the inner electric field, which are subject to deformation under the influence of gravity, buoyancy, and electrical attraction. It will also need the capability to drift electrons in LXe over its full height, which requires excellent purity. We therefore built, at the University of Zurich, Xenoscope, a vertical DARWIN demonstrator, to demonstrate for the first time the feasibility of drifting electrons in LXe over 2.6 m. In the context of this thesis, we have therefore designed and constructed key systems of the facility, including the support infrastructure,

the gas handling and purification system, the cooling tower and related cryogenic systems, and the cryostat. We have participated in the realisation of an x-y levelling system of the cryostat assembly and coordinated the global assembly of the whole facility, leading to its commissioning. We have performed a successful commissioning run over 5 weeks with 80.66 kg of LXe, demonstrating the operational capabilities of the facility, and benchmarking the purification and cryogenic systems. We then participated in the first scientific phase of the Xenoscope project, with the operation of a 0.53 m tall LXe PM used to measure the electron lifetime, a parameter related to the concentration of electronegative impurities. We then used a data-driven approach to model the time-evolution of the electron lifetime in Xenoscope, which can then inform on the effects of purification flows and outgassing on the survival of electrons during their drift. We finally described the second phase of Xenoscope, the 2.6 m TPC, for which we have developed a 50 kV HV distribution system. As the DARWIN observatory is being designed and requirements for its realisation become more concrete, Xenoscope will be made accessible to other groups in the DARWIN collaboration as a unique platform to test detector components in a LXe environment similar to that of DARWIN.

We have also investigated SiPMs, a type of solid-state photosensor, as a potential replacement for the PMTs currently in the baseline design of DARWIN. Two VUV-sensitive SiPMs from FBK were characterised. Although both photosensors show characteristics that are desirable for use in DARWIN, such as a suitable gain, a very good single photon resolution, and a lower intrinsic radioactive background per active area compared to PMTs, they still present high levels of crosstalk probability and dark count rate, forms of correlated and uncorrelated noise components respectively. This makes them, at least for the moment, unsuitable for use in large-scale detectors. We also reported on some upgrades to the DAQ system of Xurich II, the first small-scale dual-phase xenon TPC instrumented with a SiPM array, which was successfully operated at the University of Zurich.

The realisation of the DARWIN observatory is well underway, with a solid physics agenda and a strong, international workforce composed of over 38 research groups. Sensitivity studies have already shown the immense potential of the future observatory as a multi-physics platform. Therefore, even in the event of no dark matter signal, DARWIN will still be a valuable asset for the particle physics community on multiple fronts. There is no doubt that, as it has been in the recent past, the future of particle physics holds many more surprises.

"It could be worse..."

Frédéric Girard, 2019

Commissioning of Xenoscope

Zürich, 2021

Bibliography

[1] L. Baudis *et al.*, *Design and construction of Xenoscope — a full-scale vertical demonstrator for the DARWIN observatory*, *Journal of Instrumentation* **16** (2021) P08052 [2105.13829].

[2] K. Thieme, *The Low-Energy and Large-Scale Frontier of Dual-Phase Xenon Time Projection Chambers for Dark Matter Search*, Ph.D. thesis, University of Zurich, Switzerland, 2022.

[3] Deutsches Patent- und Markenamt - Registerauskunft Gebrauchsmuster. [Online] Available: `https://register.dpma.de/DPMAregister/pat/register?AKZ=2020211014121` (accessed Nov. 2022).

[4] F. Girard and K. Thieme, *Mehrteilige Lagervorrichtung und Stützsegment*, Patent No. CH718439A2, Sept. 2022.

[5] L. Baudis *et al.*, *A dual-phase xenon TPC for scintillation and ionisation yield measurements in liquid xenon*, *The European Physical Journal C* **78** (2018) 351 [1712.08607].

[6] L. Baudis *et al.*, *The first dual-phase xenon TPC equipped with silicon photomultipliers and characterisation with* ^{37}Ar, *The European Physical Journal C* **80** (2020) 477 [2003.01731].

[7] W. Kapferer, *The Mystery of Dark Matter: In Search of the Invisible*, Astronomers' Universe, Springer, Berlin, Heidelberg (2021), 10.1007/978-3-662-62202-5.

[8] The Standard Model. [Online] Available: `https://www.iop.org/explore-physics/big-ideas-physics/standard-model` (accessed Feb. 2023).

[9] J. J. Thomson, *XL. Cathode Rays*, *The London, Edinburgh, and Dublin Philosophical Magazine and Journal of Science* **44** (1897) 293–316.

[10] Particle Data Group, *Review of Particle Physics*, *Progress of Theoretical and Experimental Physics* **2022** (2022) 083C01.

[11] The Standard Model. [Online] Available: `https://home.cern/science/physics/standard-model`

[12] The Nobel Prize in Physics 2015. [Online] Available: `https://www.nobelprize.org/prizes/physics/2015/press-release/` (accessed Feb. 2023).

[13] G. 't Hooft, *The making of the standard model*, *Nature* **448** (2007) 271–273.

[14] The CDF Collaboration, *Observation of top quark production in $\overline{p}p$ collisions with the collider detector at fermilab*, *Physical Review Letters* **74** (1995) 2626–2631 [hep-ex/9503002].

[15] The DONUT Collaboration, *Observation of tau neutrino interactions*, *Physics Letters B* **504** (2001) 218–224 [hep-ex/0012035].

[16] The ATLAS Collaboration, *Observation of a new particle in the search for the Standard Model Higgs boson with the ATLAS detector at the LHC*, *Physics Letters B* **716** (2012) 1–29 [1207.7214].

[17] The CMS Collaboration, *Observation of a new boson at a mass of 125 GeV with the CMS experiment at the LHC*, *Physics Letters B* **716** (2012) 30–61 [1207.7235].

[18] J. L. Feng, *Dark Matter Candidates from Particle Physics and Methods of Detection*, *Annual Review of Astronomy and Astrophysics* **48** (2010) 495–545 [1003.0904].

[19] F. Zwicky, *Die Rotverschiebung von extragalaktischen Nebeln*, *Helvetica Physica Acta* **6** (1933) 110–127.

[20] E. Öpik, *Selective absorption of light in space, and the dynamics of the Universe.*, *Bulletin de la Société Astronomique de Russie* **21** (1915) 150–158 [2203.14871].

[21] J. C. Kapteyn, *First Attempt at a Theory of the Arrangement and Motion of the Sidereal System*, *Astrophysical Journal* **55** (1922) 302.

[22] J. H. Jeans, *The Motions of Stars in a Kapteyn-Universe*, *Monthly Notices of the Royal Astronomical Society* **82** (1922) 122–132.

[23] J. H. Oort, *The force exerted by the stellar system in the direction perpendicular to the galactic plane and some related problems*, *Bulletin of the Astronomical Institutes of the Netherlands* **6** (1932) 249.

[24] V. C. Rubin and W. K. Ford, Jr., *Rotation of the Andromeda Nebula from a Spectroscopic Survey of Emission Regions*, *The Astrophysical Journal* **159** (1970) 379.

[25] D. Lynden-Bell, *Statistical mechanics of violent relaxation in stellar systems*, *Monthly Notices of the Royal Astronomical Society* **136** (1967) 101 [astro-ph/0212205].

[26] A. M. Green, *Astrophysical uncertainties on the local dark matter distribution and direct detection experiments*, *Journal of Physics G: Nuclear and Particle Physics* **44** (2017) 084001 [1703.10102].

[27] K. G. Begeman, A. H. Broeils, and R. H. Sanders, *Extended rotation curves of spiral galaxies: Dark haloes and modified dynamics*, *Monthly Notices of the Royal Astronomical Society* **249** (1991) 523–537.

[28] Y. Sofue and V. Rubin, *Rotation Curves of Spiral Galaxies*, *Annual Review of Astronomy and Astrophysics* **39** (2001) 137–174 [astro-ph/0010594].

[29] Nick Priore, Gravitational Lensing Demonstration M31. [Online] Available: `https://www.youtube.com/watch?v=y30bsSuTAIo` (accessed Apr. 2012).

[30] J. Renn, T. Sauer, and J. Stachel, *The Origin of Gravitational Lensing: A Postscript to Einstein's 1936 Science Paper*, *Science* **275** (1997) 184–186 [2891896].

[31] A. Einstein, *Lens-Like Action of a Star by the Deviation of Light in the Gravitational Field*, *Science* **84** (1936) 506–507.

[32] O. J. Lodge, *Gravitation and Light*, *Nature* **104** (1919) 354.

[33] A. S. Eddington, *Space, Time and Gravitation: An Outline of the General Relativity Theory*, Cambridge University Press (1920).

[34] M. Markevitch, *Chandra observation of the most interesting cluster in the Universe* (2005) [astro-ph/0511345].

[35] D. Clowe, A. Gonzalez, and M. Markevitch, *Weak-Lensing Mass Reconstruction of the Interacting Cluster 1E 0657–558: Direct Evidence for the Existence of Dark Matter**, *The Astrophysical Journal* **604** (2004) 596 [astro-ph/0312273].

[36] D. Clowe *et al.*, *A Direct Empirical Proof of the Existence of Dark Matter**, *The Astrophysical Journal* **648** (2006) L109 [astro-ph/0608407].

[37] The Chandra X-ray Observatory - Photo Album - 1E 0657-56. [Online] Available: `https://chandra.harvard.edu/photo/2006/1e0657/`

[38] The Chandra X-ray Observatory - Photo Album - Abell 2744. [Online] Available: `https://chandra.harvard.edu/photo/2011/a2744/`

[39] Planck Collaboration, *Planck 2018 results. I. Overview and the cosmological legacy of Planck*, *Astronomy and Astrophysics* **641** (2020) A1 [1807.06205].

[40] K. A. Olive, *Review of Particle Physics*, *Chinese Physics C* **38** (2014) 090001.

[41] D. J. Fixsen, *The Temperature of the Cosmic Microwave Background*, *The Astrophysical Journal* **707** (2009) 916 [0911.1955].

[42] A. A. Penzias and R. W. Wilson, *A Measurement of Excess Antenna Temperature at 4080 Mc/s.*, *The Astrophysical Journal* **142** (1965) 419–421.

[43] The Nobel Prize in Physics 1978. [Online] Available: `https://www.nobelprize.org/prizes/physics/1978/press-release/` (accessed Feb. 2023).

[44] C. L. Bennett *et al.*, *Four-Year COBE* DMR Cosmic Microwave Background Observations: Maps and Basic Results*, *The Astrophysical Journal* **464** (1996) L1 [astro-ph/9601067].

[45] C. L. Bennett *et al.*, *Nine-year Wilkinson Microwave Anisotropy Probe (WMPA) observations: Final maps and results*, *The Astrophysical Journal Supplement Series* **208** (2013) 20 [1212.5225].

[46] J.-L. Starck, M. J. Fadili, and A. Rassat, *Low-l CMB analysis and inpainting*, *Astronomy and Astrophysics* **550** (2013) A15 [1210.6587].

[47] Planck Collaboration, *Planck 2018 results. VI. Cosmological parameters*, *Astronomy and Astrophysics* **641** (2020) A6 [1807.06209].

[48] R. Myrzakulov, D. Sáez-Gómez, and A. Tureanu, *On the ΛCDM Universe in f(G) gravity*, *General Relativity and Gravitation* **43** (2011) 1671–1684 [1009.0902].

[49] J. Feng *et al.*, *Planning the Future of U.S. Particle Physics (Snowmass 2013): Chapter 4: Cosmic Frontier*, (2014) [1401.6085].

[50] X. Calmet and F. Kuipers, *Theoretical bounds on dark matter masses*, *Physics Letters B* **814** (2021) 136068 [2009.11575].

[51] L. Roszkowski, E. M. Sessolo, and S. Trojanowski, *WIMP dark matter candidates and searches—current status and future prospects*, *Reports on Progress in Physics* **81** (2018) 066201 [1707.06277].

[52] C. Frenk and S. White, *Dark matter and cosmic structure*, *Annalen der Physik* **524** (2012) 507–534 [1210.0544].

[53] S. W. Randall *et al.*, *Constraints on the Self-Interaction Cross Section of Dark Matter from Numerical Simulations of the Merging Galaxy Cluster 1E 0657–56*, *The Astrophysical Journal* **679** (2008) 1173 [0704.0261].

[54] G. Jungman, M. Kamionkowski, and K. Griest, *Supersymmetric dark matter*, *Physics Reports* **267** (1996) 195–373 [9506380].

[55] E. W. Kolb and M. S. Turner, *The Early Universe*, vol. 69, CRC Press (1990), 10.1201/9780429492860.

[56] H. Goldberg, *Constraint on the Photino Mass from Cosmology*, *Physical Review Letters* **50** (1983) 1419–1422.

[57] J. Ellis *et al.*, *Supersymmetric relics from the big bang*, *Nuclear Physics B* **238** (1984) 453–476.

[58] S. P. Martin, *A supersymmetry primer*, in *Perspectives on Supersymmetry*, vol. 18, *Advanced Series on Directions in High Energy Physics*, 1–98, WORLD SCIENTIFIC (1998), DOI: 10.1142/9789812839657_0001 [hep-ph/9709356].

[59] Th. Kaluza, *Zum Unitätsproblem der Physik*, *Sitzungsber. Preuss. Akad. Wiss. Berlin (Math. Phys.)* **1921** (1921) 966–972.

[60] H.-C. Cheng, J. L. Feng, and K. T. Matchev, *Kaluza-Klein Dark Matter*, *Physical Review Letters* **89** (2002) 211301 [hep-ph/0207125].

[61] G. Servant and T. M. P. Tait, *Is the lightest Kaluza–Klein particle a viable dark matter candidate?*, *Nuclear Physics B* **650** (2003) 391–419 [hep-ph/0206071].

[62] G. Servant, *Status report on universal extra dimensions after LHC8*, *Modern Physics Letters A* **30** (2015) 1540011 [1401.4176].

[63] B. Carr, *Baryonic Dark Matter*, *Annual Review of Astronomy and Astrophysics* **32** (1994) 531–590.

[64] C. Alcock *et al.*, *EROS and MACHO Combined Limits on Planetary-Mass Dark Matter in the Galactic Halo*, *The Astrophysical Journal* **499** (1998) L9 [astro-ph/9803082].

[65] G. Bertone, D. Hooper, and J. Silk, *Particle dark matter: Evidence, candidates and constraints*, *Physics Reports* **405** (2005) 279–390 [hep-ph/0404175].

[66] M. Milgrom, *A modification of the Newtonian dynamics as a possible alternative to the hidden mass hypothesis.*, *The Astrophysical Journal* **270** (1983) 365–370.

[67] J. D. Bekenstein, *Relativistic gravitation theory for the modified Newtonian dynamics paradigm*, *Physical Review D* **70** (2004) 083509 [astro-ph/0403694].

[68] R. D. Peccei and H. R. Quinn, CP *conservation in the presence of pseudoparticles*, *Physical Review Letters* **38** (1977) 1440–1443.

[69] S. Weinberg, *A New Light Boson?*, *Physical Review Letters* **40** (1978) 223–226.

[70] F. Wilczek, *Problem of strong p and t invariance in the presence of instantons*, *Physical Review Letters* **40** (1978) 279–282.

[71] J. Preskill, M. B. Wise, and F. Wilczek, *Cosmology of the invisible axion*, *Physics Letters B* **120** (1983) 127–132.

[72] L. Visinelli and P. Gondolo, *Dark matter axions revisited*, *Physical Review D* **80** (2009) 035024 [0903.4377].

[73] N. Du, *Recent Results with the ADMX Experiment*, *Springer Proc. Phys.* **245** (2020) 17–22.

[74] N. Crisosto *et al.*, *ADMX SLIC: Results from a Superconducting LC Circuit Investigating Cold Axions*, *Physical Review Letters* **124** (2020) 241101 [1911.05772].

[75] The CAST Collaboration, *An improved limit on the axion–photon coupling from the CAST experiment*, *Journal of Cosmology and Astroparticle Physics* **2007** (2007) 010 [hep-ex/0702006].

[76] Particle Data Group, *Review of Particle Physics*, *Progress of Theoretical and Experimental Physics* **2020** (2020) 083C01.

[77] L. Rinchiuso, *Latest results on dark matter searches with H.E.S.S*, *EPJ Web of Conferences* **209** (2019) 01023 [1901.05299].

[78] B. Zitzer, *The VERITAS Dark Matter Program*, *PoS* **ICRC2017** (2018) 904 [1708.07447].

[79] M. Doro, *A review of the past and present MAGIC dark matter search program and a glimpse at the future*, in *25th European Cosmic Ray Symposium* (2017) [1701.05702].

[80] T. Yapici and A. J. Smith, *Dark Matter Searches with HAWC*, *PoS* **ICRC2017** (2018) 891 [1708.07461].

[81] The Fermi-LAT Collaboration, *Searching for Dark Matter Annihilation from Milky Way Dwarf Spheroidal Galaxies with Six Years of Fermi Large Area Telescope Data*, *Physical Review Letters* **115** (2015) 231301 [1503.02641].

[82] E. Charles *et al.*, *Sensitivity projections for dark matter searches with the Fermi large area telescope*, *Physics Reports* **636** (2016) 1–46 [1605.02016].

[83] M. G. Aartsen *et al.*, *Improved limits on dark matter annihilation in the Sun with the 79-string IceCube detector and implications for supersymmetry*, *Journal of Cosmology and Astroparticle Physics* **2016** (2016) 022 [1601.00653].

[84] N. Iovine, on behalf of IceCube collaboration, *Indirect search for dark matter in the Galactic Centre with IceCube*, *Journal of Instrumentation* **16** (2021) C09009 [2107.11224].

[85] S. Adrián-Martínez *et al.*, *Limits on dark matter annihilation in the sun using the ANTARES neutrino telescope*, *Physics Letters B* **759** (2016) 69–74 [1603.02228].

[86] A. Albert *et al.*, *Search for dark matter towards the Galactic Centre with 11 years of ANTARES data*, *Physics Letters B* **805** (2020) 135439 [1912.05296].

[87] M. G. Aartsen *et al.*, *PINGU: A vision for neutrino and particle physics at the South Pole*, *Journal of Physics G: Nuclear and Particle Physics* **44** (2017) 054006 [1607.02671].

[88] A. Bäckström, R. Catena, and C. P. de los Heros, *Assessing the sensitivity of PINGU to effective dark matter-nucleon interactions*, *Journal of Cosmology and Astroparticle Physics* **2019** (2019) 023 [1812.08270].

[89] C. R. Das, O. Mena, S. Palomares-Ruiz, and S. Pascoli, *Determining the dark matter mass with DeepCore*, *Physics Letters B* **725** (2013) 297–301 [1110.5095].

[90] The AMS Collaboration, *Antiproton Flux, Antiproton-to-Proton Flux Ratio, and Properties of Elementary Particle Fluxes in Primary Cosmic Rays Measured with the Alpha Magnetic Spectrometer on the International Space Station*, *Physical Review Letters* **117** (2016) 091103.

[91] O. Adriani *et al.*, *Cosmic-Ray Positron Energy Spectrum Measured by PAMELA*, *Physical Review Letters* **111** (2013) 081102 [1308.0133].

[92] N. Trevisani, *Collider Searches for Dark Matter (ATLAS + CMS)*, *Universe* **4** (2018) 131.

[93] E. Tolley and on behalf of the ATLAS Collaboration, *Dark Matter searches with the ATLAS Detector*, in *Proceedings of The 39th International Conference on High Energy Physics — PoS(ICHEP2018)*, vol. 340, 171, SISSA Medialab (2019).

[94] D. Vannerom, on behalf of the CMS Collaboration, *Dark Matter searches with CMS*, in *Proceedings of XXVII International Workshop on Deep-Inelastic Scattering and Related Subjects — PoS(DIS2019)*, vol. 352, 111, SISSA Medialab (2019).

[95] Y. Andreev *et al.*, *Improved exclusion limit for light dark matter from e^+e^- annihilation in NA64*, *Physical Review D* **104** (2021) L091701 [2108.04195].

[96] The MiniBooNE-DM Collaboration, *Dark matter search in nucleon, pion, and electron channels from a proton beam dump with MiniBooNE*, *Physical Review D* **98** (2018) 112004 [1807.06137].

[97] R. Essig, P. Schuster, N. Toro, and B. Wojtsekhowski, *An electron fixed target experiment to search for a new vector boson A' decaying to e^+e^-*, *Journal of High Energy Physics* **2011** (2011) 9 [1001.2557].

[98] S. J. Paul, *Searching for A Dark Photon in the HPS Experiment*, Ph.D. thesis, William-Mary Coll., 2018. DOI: 10.21220/s2-8bz0-kd50.

[99] D. H. Dongwi, on behalf of the TREK/E36 Collaboration, *Search for Light Neutral Bosons in The TREK/E36 Experiment at J-PARC*, *Journal of Physics: Conference Series* **2391** (2022) 012012 [2212.10813].

[100] N. Anand, A. L. Fitzpatrick, and W. C. Haxton, *Weakly interacting massive particle-nucleus elastic scattering response*, *Physical Review C* **89** (2014) 065501.

[101] The XENON Collaboration, *Search for inelastic scattering of WIMP dark matter in XENON1T*, *Physical Review D* **103** (2021) 063028 [2011.10431].

[102] G. H. Vineyard, *Multiple Scattering of Neutrons*, *Physical Review* **96** (1954) 93–98.

[103] G. Takeda and K. M. Watson, *Scattering of Fast Neutrons and Protons by Atomic Nuclei*, *Physical Review* **97** (1955) 1336–1343.

[104] M. Schumann, *Direct detection of WIMP dark matter: Concepts and status*, *Journal of Physics G: Nuclear and Particle Physics* **46** (2019) 103003 [1903.03026].

[105] J. I. Read, *The local dark matter density*, *Journal of Physics G: Nuclear and Particle Physics* **41** (2014) 063101 [1404.1938].

[106] K. Freese, M. Lisanti, and C. Savage, *Colloquium: Annual modulation of dark matter*, *Reviews of Modern Physics* **85** (2013) 1561–1581 [1209.3339].

[107] H. H. Koppelman and A. Helmi, *Determination of the escape velocity of the Milky Way using a halo sample selected based on proper motion*, *Astronomy & Astrophysics* **649** (2021) A136.

[108] A. F. Pacheco and D. Strottman, *Nuclear-structure corrections to estimates of the spin-dependent WIMP-nucleus cross section*, *Physical Review D* **40** (1989) 2131–2133.

[109] M. T. Ressell and D. J. Dean, *Spin-dependent neutralino-nucleus scattering for $A \sim 127$ nuclei*, *Physical Review C* **56** (1997) 535–546 [hep-ph/9702290].

[110] B. Feldstein, A. L. Fitzpatrick, and E. Katz, *Form factor dark matter*, *Journal of Cosmology and Astroparticle Physics* **2010** (2010) 020 [0908.2991].

[111] T. Marrodán Undagoitia and L. Rauch, *Dark matter direct-detection experiments*, *J. Phys. G* **43** (2016) 013001 [1509.08767].

[112] A. L. Fitzpatrick *et al.*, *The effective field theory of dark matter direct detection*, *Journal of Cosmology and Astroparticle Physics* **2013** (2013) 004 [1203.3542].

[113] The XENON Collaboration, *Effective field theory search for high-energy nuclear recoils using the XENON100 dark matter detector*, *Physical Review D* **96** (2017) 042004 [1705.02614].

[114] H. Kraus *et al.*, *EURECA — the European Future of Dark Matter Searches with Cryogenic Detectors*, *Nuclear Physics B - Proceedings Supplements* **173** (2007) 168–171.

[115] C. Levy *et al.*, *Xenon bubble chambers for direct dark matter detection*, *Journal of Instrumentation* **11** (2016) C03003 [1601.05131].

[116] D. Baxter *et al.*, *First Demonstration of a Scintillating Xenon Bubble Chamber for Detecting Dark Matter and Coherent Elastic Neutrino-Nucleus Scattering*, *Physical Review Letters* **118** (2017) 231301 [1702.08861].

[117] CEνNS Theory Group at IF-UNAM, *Physics reach of a low threshold scintillating argon bubble chamber in coherent elastic neutrino-nucleus scattering reactor experiments*, *Physical Review D* **103** (2021) L091301 [2101.08785].

[118] The SIMPLE Collaboration, *First Results of the Phase II SIMPLE Dark Matter Search*, *Physical Review Letters* **105** (2010) 211301 [1003.2987].

[119] E. Behnke *et al.*, *Final results of the PICASSO dark matter search experiment*, *Astroparticle Physics* **90** (2017) 85–92 [1611.01499].

[120] SNOLAB. [Online] Available: `https://www.snolab.ca/` (accessed Feb. 2023).

[121] E. Behnke *et al.*, *Spin-Dependent WIMP Limits from a Bubble Chamber*, *Science* **319** (2008) 933–936 [0804.2886].

[122] The PICO Collaboration, *PICASSO, COUPP and PICO - search for dark matter with bubble chambers*, *EPJ Web of Conferences* **95** (2015) 04020.

[123] The PICO Collaboration, *Improved dark matter search results from PICO-2L Run 2*, *Physical Review D* **93** (2016) 061101 [1601.03729].

[124] The PICO Collaboration, *Dark matter search results from the PICO-60 CF_3I bubble chamber*, *Physical Review D* **93** (2016) 052014 [1510.07754].

[125] The PICO Collaboration, *Dark matter search results from the complete exposure of the PICO-60 C_3F_8 bubble chamber*, *Physical Review D* **100** (2019) 022001 [1902.04031].

[126] The PICO Collaboration, *Data-driven modeling of electron recoil nucleation in PICO C_3F_8 bubble chambers*, *Physical Review D* **100** (2019) 082006 [1905.12522].

[127] M. Bressler *et al.*, *A buffer-free concept bubble chamber for PICO dark matter searches*, *JINST* **14** (2019) P08019 [1905.07367].

[128] G. Giroux, *Search for Dark Matter with the PICO-500 Experiment*, *Journal of Physics: Conference Series* **2156** (2021) 012068.

[129] D. Chiesa, for the CUORE Collaboration, *Results from the CUORE experiment*, *Journal of Physics: Conference Series* **1137** (2019) 012052.

[130] The EDELWEISS Collaboration, *Final results of the EDELWEISS-I dark matter search with cryogenic heat-and-ionization Ge detectors*, *Physical Review D* **71** (2005) 122002 [astro-ph/0503265].

[131] The EDELWEISS Collaboration, *Final results of the EDELWEISS-II WIMP search using a 4-kg array of cryogenic germanium detectors with interleaved electrodes*, *Physics Letters B* **702** (2011) 329–335 [1103.4070].

[132] L. Hehn *et al.*, *Improved EDELWEISS-III sensitivity for low-mass WIMPs using a profile likelihood approach*, *The European Physical Journal C* **76** (2016) 548 [1607.03367].

[133] THE CDMS II COLLABORATION, *Dark Matter Search Results from the CDMS II Experiment*, *Science* **327** (2010) 1619–1621.

[134] M. C. Fritts, *Background Characterization and Discrimination in the Final Analysis of the CDMS II Phase of the Cryogenic Dark Matter Search*, Ph.D. thesis, Minnesota U., 2011. DOI: 10.2172/1128109.

[135] The SuperCDMS Collaboration, *New Results from the Search for Low-Mass Weakly Interacting Massive Particles with the CDMS Low Ionization Threshold Experiment*, *Physical Review Letters* **116** (2016) 071301.

[136] The SuperCDMS Collaboration, *Search for low-mass dark matter with CDMSlite using a profile likelihood fit*, *Physical Review D* **99** (2019) 062001 [1808.09098].

[137] The SuperCDMS Collaboration, *Projected sensitivity of the SuperCDMS SNOLAB experiment*, *Physical Review D* **95** (2017) 082002 [1610.00006].

[138] G. Angloher *et al.*, *Limits on WIMP dark matter using sapphire cryogenic detectors*, *Astroparticle Physics* **18** (2002) 43–55.

[139] The CRESST Collaboration, *First results from the CRESST-III low-mass dark matter program*, *Physical Review D* **100** (2019) 102002 [1904.00498].

[140] G. Angloher *et al.*, *Results on light dark matter particles with a low-threshold CRESST-II detector*, *The European Physical Journal C* **76** (2016) 25 [1509.01515].

[141] The COSINUS Collaboration, *Results from the first cryogenic NaI detector for the COSINUS project*, *Journal of Instrumentation* **12** (2017) P11007 [1705.11028].

[142] The DEAP Collaboration, *Search for dark matter with a 231-day exposure of liquid argon using DEAP-3600 at SNOLAB*, *Physical Review D* **100** (2019) 022004 [1902.04048].

[143] The XMASS Collaboration, *Search for sub-GeV dark matter by annual modulation using XMASS-I detector*, *Physics Letters B* **795** (2019) 308–313 [1808.06177].

[144] The XMASS Collaboration, *A direct dark matter search in XMASS-I*, *Physics Letters B* **789** (2019) 45–53 [1804.02180].

[145] The COSINE-100 Collaboration, *Search for a Dark Matter-Induced Annual Modulation Signal in NaI(Tl) with the COSINE-100 Experiment*, *Physical Review Letters* **123** (2019) 031302 [1903.10098].

[146] J. Amaré *et al.*, *Annual modulation results from three-year exposure of ANAIS-112*, *Physical Review D* **103** (2021) 102005 [2103.01175].

[147] F. J. Petriello and K. M. Zurek, *DAMA and WIMP dark matter*, *Journal of High Energy Physics* **2008** (2008) 047 [0806.3989].

[148] R. Bernabei *et al.*, *First Model Independent Results from DAMA/LIBRA–Phase2*, *Universe* **4** (2018) 116 [1805.10486].

[149] F. Froborg and A. R. Duffy, *Annual modulation in direct dark matter searches*, *Journal of Physics G: Nuclear and Particle Physics* **47** (2020) 094002 [2003.04545].

[150] The DRIFT collaboration, *Improved sensitivity of the DRIFT-IId directional dark matter experiment using machine learning*, *Journal of Cosmology and Astroparticle Physics* **2021** (2021) 014 [2103.06702].

[151] Q. Arnaud *et al.*, *First results from the NEWS-G direct dark matter search experiment at the LSM*, *Astroparticle Physics* **97** (2018) 54–62 [1706.04934].

[152] The DAMIC Collaboration, *Results on Low-Mass Weakly Interacting Massive Particles from an 11 kg d Target Exposure of DAMIC at SNOLAB*, *Physical Review Letters* **125** (2020) 241803 [2007.15622].

[153] E. Hand, *A CoGeNT result in the hunt for dark matter*, *Nature* (2010) .

[154] Dark Matter Limit Plotter | SuperCDMS | Super Cryogenic Dark Matter Search. [Online] Available: `https://supercdms.slac.stanford.edu/dark-matter-limit-plotter` (accessed Feb. 2023).

[155] J. N. Marx and D. R. Nygren, *The Time Projection Chamber*, *Physics Today* **31** (1978) 46–53.

[156] The DarkSide Collaboration, *DarkSide-50 532-day dark matter search with low-radioactivity argon*, *Physical Review D* **98** (2018) 102006 [1802.07198].

[157] C. E. Aalseth *et al.*, *DarkSide-20k: A 20 tonne two-phase LAr TPC for direct dark matter detection at LNGS*, *The European Physical Journal Plus* **133** (2018) 131 [1707.08145].

[158] M. G. Boulay *et al.*, *Direct comparison of PEN and TPB wavelength shifters in a liquid argon detector*, *The European Physical Journal C* **81** (2021) 1099 [2106.15506].

[159] P. Kryczynski, *Pulse Shape Discrimination in liquid argon and its implications for Dark Matter searches using depleted argon*, *Acta Phys. Polon. B* **43** (2012) 1509–1520 [1210.1019].

[160] The LUX Collaboration, *Results from a Search for Dark Matter in the Complete LUX Exposure*, *Physical Review Letters* **118** (2017) 021303 [1608.07648].

[161] G. J. Alner *et al.*, *First limits on WIMP nuclear recoil signals in ZEPLIN-II: A two-phase xenon detector for dark matter detection*, *Astroparticle Physics* **28** (2007) 287–302 [astro-ph/0701858].

[162] V. N. Lebedenko *et al.*, *Results from the first science run of the ZEPLIN-III dark matter search experiment*, *Physical Review D* **80** (2009) 052010 [0812.1150].

[163] The LUX-ZEPLIN Collaboration, *LUX-ZEPLIN (LZ) Conceptual Design Report* (2015) [1509.02910].

[164] The LUX-ZEPLIN Collaboration, *Projected WIMP sensitivity of the LUX-ZEPLIN dark matter experiment*, *Physical Review D* **101** (2020) 052002 [1802.06039].

[165] The XENON Collaboration, *First Results from the XENON10 Dark Matter Experiment at the Gran Sasso National Laboratory*, *Physical Review Letters* **100** (2008) 021303 [0706.0039].

[166] The XENON Collaboration, *XENON100 dark matter results from a combination of 477 live days*, *Physical Review D* **94** (2016) 122001 [1609.06154].

[167] The XENON Collaboration, *Dark Matter Search Results from a One Ton-Year Exposure of XENON1T*, *Physical Review Letters* **121** (2018) 111302 [1805.12562].

[168] The XENON Collaboration, *Projected WIMP sensitivity of the XENONnT dark matter experiment*, *Journal of Cosmology and Astroparticle Physics* **2020** (2020) 031–031 [2007.08796].

[169] Q. Wang *et al.*, *Results of dark matter search using the full PandaX-II exposure **, *Chinese Physics C* **44** (2020) 125001 [2007.15469].

[170] H. Zhang *et al.*, *Dark matter direct search sensitivity of the PandaX-4T experiment*, *Science China Physics, Mechanics & Astronomy* **62** (2018) 31011 [1806.02229].

[171] The PandaX-4T Collaboration, *Dark Matter Search Results from the PandaX-4T Commissioning Run*, *Physical Review Letters* **127** (2021) 261802 [2107.13438].

[172] The DARWIN Collaboration, *DARWIN: Towards the ultimate dark matter detector*, *Journal of Cosmology and Astroparticle Physics* **11** (2016) 17 [1606.07001].

[173] D. Z. Freedman, *Coherent effects of a weak neutral current*, *Physical Review D* **9** (1974) 1389–1392.

[174] D. Z. Freedman, D. N. Schramm, and D. L. Tubbs, *The Weak Neutral Current and its Effects in Stellar Collapse*, *Annual Review of Nuclear Science* **27** (1977) 167–207.

[175] A. Drukier and L. Stodolsky, *Principles and applications of a neutral-current detector for neutrino physics and astronomy*, *Physical Review D* **30** (1984) 2295–2309.

[176] C. A. J. O'Hare, *New Definition of the Neutrino Floor for Direct Dark Matter Searches*, *Physical Review Letters* **127** (2021) 251802 [2109.03116].

[177] B. Dutta and L. E. Strigari, *Neutrino Physics with Dark Matter Detectors*, *Annual Review of Nuclear and Particle Science* **69** (2019) 137–161 [1901.08876].

[178] R. S. Bergman, J. M. Davenport, and R. L. Hansler, *Xenon-metal halide lamp particularly suited for automotive applications*, Patent No. CA1301238C, May 1992.

[179] W. G. Myers, J. R. Dahl, and M. C. Graham, *Xenon-127m: A New Radionucide for Applications in Nuclear Medicine*, *Journal of Nuclear Medicine* **31** (1990) 489–492.

[180] J. E. Roos, H. P. McAdams, S. S. Kaushik, and B. Driehuys, *Hyperpolarized Gas MRI: Technique and Applications*, *Magnetic resonance imaging clinics of North America* **23** (2015) 217–229.

[181] M. R. Rao *et al.*, *Imaging human brain perfusion with inhaled hyperpolarized* ^{129}Xe *MR imaging*, *Radiology* **286** (2018) 659–665.

[182] R. R. Kennedy, J. W. Stokes, and P. Downing, *Anaesthesia and the 'Inert' Gases with Special Reference to Xenon*, *Anaesthesia and Intensive Care* **20** (1992) 66–70.

[183] J. R. Beattie, J. N. Matossian, and R. Robson, *Status of xenon ion propulsion technology*, *Journal of Propulsion and Power* **6** (1990) 145–150.

[184] J. R. Beattie *et al.*, *Xenon ion propulsion subsystem*, *Journal of Propulsion and Power* **5** (1989) 438–444.

[185] M. M. Stark, S. Nakajima, and R. B. Lachenbruch, *Xenon enhanced plasma etch*, Patent No. EP0296419A2, Dec. 1988.

[186] E. R. Ault, R. S. Bradford, and M. L. Bhaumik, *High-power xenon fluoride laser*, *Applied Physics Letters* **27** (1975) 413–415.

[187] S. A. Lawton *et al.*, *The high-pressure neutral infrared xenon laser*, *Journal of Applied Physics* **50** (1979) 3888–3898.

[188] The Nobel Prize in Chemistry 1904. [Online] Available: `https://www.nobelprize.org/prizes/chemistry/1904/summary/` (accessed Feb. 2023).

[189] W. Ramsay, *An attempt to estimate the relative amounts of krypton and of xenon in atmospheric air*, *Proceedings of the Royal Society of London* **71** (1903) 421–426.

[190] M. Shino, H. Takano, J. Nakata, and K. Noro, *Production process of xenon*, Patent No. US4874592A, Oct. 1989.

[191] F. G. Kerry, *Industrial Gas Handbook: Gas Separation and Purification*, CRC Press (Feb. 2007).

[192] J. R. Rumble, *CRC Handbook of Chemistry and Physics*, CRC Press (June 2022).

[193] P. J. Linstrom and W. G. Mallard, *NIST Chemistry WebBook*, vol. NIST Standard Reference Database Number 69, 20899, *Retrieved December 10, 2020*, American Chemical Society, Gaithersburg MD (Sept. 2001).

[194] R. C. Kemp, W. R. G. Kemp, and P. W. Smart, *The Triple Point of Xenon as a Possible Defining Point on an International Temperature Scale*, *Metrologia* **21** (1985) 43.

[195] I. M. A. Fonseca and L. Q. Lobo, *Thermodynamics of liquid mixtures of xenon and methyl fluoride*, *Fluid Phase Equilibria* **47** (1989) 249–263.

[196] Gas Encyclopedia Air Liquide - Xenon. [Online] Available: `https://encyclopedia.airliquide.com/xenon` (accessed Oct. 2018).

[197] K. Fujii *et al.*, *High-accuracy measurement of the emission spectrum of liquid xenon in the vacuum ultraviolet region*, *Nuclear Instruments and Methods in Physics Research Section A: Accelerators, Spectrometers, Detectors and Associated Equipment* **795** (2015) 293–297.

[198] J. Jortner, L. Meyer, S. A. Rice, and E. G. Wilson, *Localized Excitations in Condensed Ne, Ar, Kr, and Xe*, *The Journal of Chemical Physics* **42** (1965) 4250–4253.

[199] F. G. Kondev *et al.*, *The NUBASE2020 evaluation of nuclear physics properties **, *Chinese Physics C* **45** (2021) 030001.

[200] A. Minamino *et al.*, *Self-shielding effect of a single phase liquid xenon detector for direct dark matter search*, *Astroparticle Physics* **35** (2012) 609–614 [0912.2405].

[201] XCOM: Photon Cross Sections Database. [Online] Available: `https://www.nist.gov/pml/xcom-photon-cross-sections-database` (accessed Sept. 2009).

[202] National Institute of Standards and Technology, *Stopping-Power & Range Tables for Electrons, Protons, and Helium Ions*, *NIST* (2009) .

[203] The XENON Collaboration, *Observation of two-neutrino double electron capture in ^{124}Xe with XENON1T*, *Nature* **568** (2019) 532–535 [1904.11002].

[204] The XENON Collaboration, *Search for New Physics in Electronic Recoil Data from XENONnT*, *Physical Review Letters* **129** (2022) 161805 [2207.11330].

[205] The DARWIN Collaboration, *Sensitivity of the DARWIN observatory to the neutrinoless double beta decay of ^{136}Xe*, *The European Physical Journal C* **80** (2020) 808 [2003.13407].

[206] The EXO-200 Collaboration, *Search for neutrinoless double-β decay with the complete EXO-200 dataset*, *Physical Review Letters* **123** (2019) 161802 [1906.02723].

[207] The nEXO Collaboration, *nEXO: Neutrinoless double beta decay search beyond 1028 year half-life sensitivity*, *Journal of Physics G: Nuclear and Particle Physics* **49** (2021) 015104 [2106.16243].

[208] B. Lenardo *et al.*, *A Global Analysis of Light and Charge Yields in Liquid Xenon*, *IEEE Transactions on Nuclear Science* **62** (2015) 3387–3396 [1412.4417].

[209] V. N. Solovov *et al.*, *Measurement of the refractive index and attenuation length of liquid xenon for its scintillation light*, *Nuclear Instruments and Methods in Physics Research Section A: Accelerators, Spectrometers, Detectors and Associated Equipment* **516** (2004) 462–474 [physics/0307044].

[210] E. Aprile and T. Doke, *Liquid xenon detectors for particle physics and astrophysics*, *Reviews of Modern Physics* **82** (2010) 2053–2097 [0910.4956].

[211] S. Kubota, M. Hishida, and J. Raun, *Evidence for a triplet state of the self-trapped exciton states in liquid argon, krypton and xenon*, *Journal of Physics C: Solid State Physics* **11** (1978) 2645–2651.

[212] A. Hitachi *et al.*, *Effect of ionization density on the time dependence of luminescence from liquid argon and xenon*, *Physical Review B* **27** (1983) 5279–5285.

[213] S. Kubota, M. Hishida, M. Suzuki, and J.-z. Ruan(Gen), *Dynamical behavior of free electrons in the recombination process in liquid argon, krypton, and xenon*, *Physical Review B* **20** (1979) 3486–3496.

[214] W. H. Lippincott *et al.*, *Scintillation time dependence and pulse shape discrimination in liquid argon*, *Physical Review C* **78** (2008) 035801 [0801.1531].

[215] M. Ibe, W. Nakano, Y. Shoji, and K. Suzuki, *Migdal effect in dark matter direct detection experiments*, *Journal of High Energy Physics* **2018** (2018) 194 [1707.07258].

[216] The XENON Collaboration, *Search for Light Dark Matter Interactions Enhanced by the Migdal Effect or Bremsstrahlung in XENON1T*, *Physical Review Letters* **123** (2019) 241803 [1907.12771].

[217] J. Lindhard, V. Nielsen, M. Scharff, and P. V. Thomsen, *INTEGRAL EQUATIONS GOVERNING RADIATION EFFECTS. (NOTES ON ATOMIC COLLISIONS, III)*, *Kgl. Danske Videnskab., Selskab. Mat. Fys. Medd.* **Vol: 33: No. 10** (1963) .

[218] P. Sorensen and C. E. Dahl, *Nuclear recoil energy scale in liquid xenon with application to the direct detection of dark matter*, *Physical Review D* **83** (2011) 063501.

[219] The XENON Collaboration, *The XENON1T dark matter experiment*, *The European Physical Journal C* **77** (2017) 881 [1708.07051].

[220] J. Xu *et al.*, *Electron extraction efficiency study for dual-phase xenon dark matter experiments*, *Physical Review D* **99** (2019) 103024 [1904.02885].

[221] The XENON Collaboration, *Signal yields of keV electronic recoils and their discrimination from nuclear recoils in liquid xenon*, *Physical Review D* **97** (2018) 092007 [1709.10149].

[222] T. Doke *et al.*, *Absolute Scintillation Yields in Liquid Argon and Xenon for Various Particles*, *Japanese Journal of Applied Physics* **41** (2002) 1538.

[223] F. Jörg *et al.*, *Characterization of alpha and beta interactions in liquid xenon*, *The European Physical Journal C* **82** (2022) 361 [2109.13735].

[224] V. Atrazhev *et al.*, *Electron transport coefficients in liquid xenon*, in *IEEE International Conference on Dielectric Liquids, 2005. ICDL 2005.*, 329–332 (2005).

[225] The XENON Collaboration, *XENON1T dark matter data analysis: Signal reconstruction, calibration, and event selection*, *Physical Review D* **100** (2019) 052014 [1906.04717].

[226] C. E. Dahl, *The physics of background discrimination in liquid xenon, and first results from XENON10 in the hunt for WIMP dark matter*, Ph.D. thesis, Princeton U., 2009.

[227] The EXO-200 Collaboration, *Measurement of the scintillation and ionization response of liquid xenon at MeV energies in the EXO-200 experiment*, *Physical Review C* **101** (2020) 065501 [1908.04128].

[228] L. Baudis, P. Sanchez-Lucas, and K. Thieme, *A measurement of the mean electronic excitation energy of liquid xenon*, *The European Physical Journal C* **81** (2021) 1060.

[229] V. I. Barsanov *et al.*, *Artificial neutrino source based on the ^{37}Ar isotope*, *Physics of Atomic Nuclei* **70** (2007) 300–310.

[230] R. F. Lang *et al.*, *A ^{220}Rn source for the calibration of low-background experiments*, *Journal of Instrumentation* **11** (2016) P04004 [1602.01138].

[231] Laboratoire sous-terrain de Modane. [Online] Available: `http://www.lsm.in2p3.fr/` (accessed Mar. 2023).

[232] Sanford Underground Research Facility. [Online] Available: `https://sanfordlab.org/` (accessed Mar. 2023).

[233] Hamamatsu Photonics K.K., *PHOTOMULTIPLIER TUBES - Basics and Applications*, *Hamamatsu Photonics K.K.* (2007) .

[234] R. Peres, *SiPM array of Xenoscope, a full-scale DARWIN vertical demonstrator*, in *LIDINE 2022* (2022).

[235] V. D'Andrea *et al.*, *The ABALONE photosensor*, *Journal of Instrumentation* **17** (2022) C01038 [2111.02924].

[236] M. Keller and P. Fischer, *CMOS based SPAD Arrays for light detection in rare event search experiments*, in *Lidine 2021*, (Online) (2021).

[237] The XENON Collaboration, *Conceptual design and simulation of a water Cherenkov muon veto for the XENON1T experiment*, *Journal of Instrumentation* **9** (2014) P11006 [1406.2374].

[238] S. A. Malik *et al.*, *Interplay and characterization of Dark Matter searches at colliders and in direct detection experiments*, *Physics of the Dark Universe* **9–10** (2015) 51–58 [1409.4075].

[239] Linde, Xenon - Product brochure. [Online] Available: `http://hiq.linde-gas.com/en/images/Rare%20Gas%20Xenon_tcm899-92272.pdf` (accessed Feb. 2023).

[240] S. Lindemann and H. Simgen, *Krypton assay in xenon at the ppq level using a gas chromatographic system and mass spectrometer*, *The European Physical Journal C* **74** (2014) 2746 [1308.4806].

[241] The XENON Collaboration, *Application and modeling of an online distillation method to reduce krypton and argon in XENON1T*, *Progress of Theoretical and Experimental Physics* **2022** (2022) 053H01 [2112.12231].

[242] The XENON Collaboration, *XENON1T dark matter data analysis: Signal and background models and statistical inference*, *Physical Review D* **99** (2019) 112009 [1902.11297].

[243] P. Majewski *et al.*, *Performance data from the ZEPLIN-III second science run*, *Journal of Instrumentation* **7** (2012) C03044 [1112.0080].

[244] The EXO-200 Collaboration, *Cosmogenic backgrounds to $0\nu\beta\beta$ in EXO-200*, *Journal of Cosmology and Astroparticle Physics* **2016** (2016) 029 [1512.06835].

[245] Particle Data Group, *Review of Particle Physics*, *Physical Review D* **98** (2018) 030001.

[246] The EXO Collaboration, *Improved measurement of the $2\nu\beta\beta$ half-life of ^{136}Xe with the EXO-200 detector*, *Physical Review C* **89** (2014) 015502.

[247] L. Baudis *et al.*, *Neutrino physics with multi-ton scale liquid xenon detectors*, *Journal of Cosmology and Astroparticle Physics* **2014** (2014) 044 [1309.7024].

[248] The XENON Collaboration, *Material radioassay and selection for the XENON1T dark matter experiment*, *The European Physical Journal C* **77** (2017) 890 [1705.01828].

[249] The LUX-ZEPLIN Collaboration, *Identification of radiopure titanium for the LZ dark matter experiment and future rare event searches*, *Astroparticle Physics* **96** (2017) 1–10 [1702.02646].

[250] The DARWIN Collaboration, *Solar neutrino detection sensitivity in DARWIN via electron scattering*, *The European Physical Journal C* **80** (2020) 1133 [2006.03114].

[251] A. Serenelli, *Alive and well: A short review about standard solar models*, *The European Physical Journal A* **52** (2016) 78 [1601.07179].

[252] M. Asplund, N. Grevesse, A. J. Sauval, and P. Scott, *The Chemical Composition of the Sun*, *Annual Review of Astronomy and Astrophysics* **47** (2009) 481–522 [0909.0948].

[253] N. Grevesse and A. Sauval, *Standard Solar Composition*, *Space Science Reviews* **85** (1998) 161–174.

[254] K. Kumar, S. Mantry, W. Marciano, and P. Souder, *Low-Energy Measurements of the Weak Mixing Angle*, *Annual Review of Nuclear and Particle Science* **63** (2013) 237–267.

[255] The XENON Collaboration, *Removing krypton from xenon by cryogenic distillation to the ppq level*, *The European Physical Journal C* **77** (2017) 275 [1612.04284].

[256] A. de Gouvêa, E. McGinness, I. Martinez-Soler, and Y. F. Perez-Gonzalez, *pp solar neutrinos at DARWIN*, *Physical Review D* **106** (2022) 096017 [2111.02421].

[257] R. F. Lang *et al.*, *Supernova neutrino physics with xenon dark matter detectors: A timely perspective*, *Physical Review D* **94** (2016) 103009 [1606.09243].

[258] A. M. Suliga, J. F. Beacom, and I. Tamborra, *Towards probing the diffuse supernova neutrino background in all flavors*, *Physical Review D* **105** (2022) 043008 [2112.09168].

[259] Y. Biondi, *Sensitivity of DARWIN to Rare Events and the Purity Monitor for Xenoscope*, Ph.D. thesis, University of Zurich, Switzerland, 2022.

[260] J. Aalbers *et al.*, *A next-generation liquid xenon observatory for dark matter and neutrino physics*, *Journal of Physics G: Nuclear and Particle Physics* **50** (2022) 013001 [2203.02309].

[261] J. Dierle, *Background and Sensitivity Studies for the DARWIN Low-Background Observatory*, Ph.D. thesis, Albert-Ludwigs-Universität Freiburg, Germany, 2022.

[262] E. Aprile *et al.*, *Performance of a cryogenic system prototype for the XENON1T detector*, *Journal of Instrumentation* **7** (2012) P10001 [1208.2001v1].

[263] G. Plante, E. Aprile, J. Howlett, and Y. Zhang, *Liquid-phase purification for multi-tonne xenon detectors*, *The European Physical Journal C* **82** (2022) 860 [2205.07336].

[264] K. Stifter, *Recent results from the LZ System Test platform at SLAC*, *APS April meeting* (2018) 36.

[265] Dassault Systemes - SolidWorks. [Online] Available: `https://www.solidworks.com/` (accessed Jan. 2023).

[266] P. E. Connolly, *CAD Software Industry Trends and Directions*, *The Engineering Design Graphics Journal* **63** (1999) .

[267] Roffler Ingenieure GmbH. [Online] Available: `https://roing.ch/` (accessed May 2021).

[268] Bosch Rexroth. [Online] Available: `https://www.boschrexroth.com/en/dc/` (accessed Oct. 2021).

[269] FMS Technik AG. [Online] Available: `https://www.fms-technik.ch/` (accessed Sept. 2021).

[270] Swagelok Company. [Online] Available: `https://www.swagelok.com/en` (accessed Nov. 2022).

[271] KNF Neuberger GmbH. [Online] Available: `https://knf.com/en/ch` (accessed July 2021).

[272] SMC Pneumatics. [Online] Available: `https://www.smcpneumatics.com/` (accessed Jan. 2023).

[273] Teledyne Hastings. [Online] Available: `https://www.teledyne-hi.com/` (accessed July 2021).

[274] SAES Pure Gas. [Online] Available: `https://www.entegris.com/shop/en/USD/Products/Gas-Filtration-and-Purification/Gas-Purifiers/c/gaspurifiers` (accessed July 2021).

[275] Mettler-Toledo. [Online] Available: `https://www.mt.com/ch/en/home.html` (accessed July 2021).

[276] KGW-Isotherm. [Online] Available: `.https://kgw-isotherm.com/` (accessed July 2021).

[277] KASAG Swiss AG. [Online] Available: https://www.kasag.com/ (accessed Oct. 2022).

[278] Helbling Technik AG. [Online] Available: https://roing.ch/ (accessed May 2021).

[279] Pfeiffer Vacuum - HiPace 80. [Online] Available: https://www.pfeiffer-vacuum.com/en/products/vacuum-generation/turbopumps/hybrid-bearing/hipace-80/32024/hipace-80 (accessed Nov. 2022).

[280] Pfeiffer Vacuum GmbH. [Online] Available: https://www.pfeiffer-vacuum.com/en/ (accessed Oct. 2021).

[281] Pfeiffer Vacuum - HiScroll 12. [Online] Available: https://www.pfeiffer-vacuum.com/en/products/vacuum-generation/scroll-pumps/hiscroll-12/42783/hiscroll-12-scroll-pump-with-pressure-sensor (accessed Oct. 2021).

[282] D. Singh *et al.*, *Heat radiation reduction in cryostats with multilayer insulation technique*, *Journal of Instrumentation* **15** (2020) P07032 [2002.09586].

[283] RUAG Space AG. [Online] Available: https://www.ruag.com/en (accessed Oct. 2021).

[284] Cryogenic Polyester Tape COOLCAT B-R50. [Online] Available: https://www.ruag.com/system/files/media_document/2019-08/Cryogenic_Polyester_Tape_COOLCAT%20B-R50.pdf (accessed May 2021).

[285] ULVAC Technologies Inc. - Iwatani. [Online] Available: https://www.ulvac-cryo.com/products-en/refrigerator-en/cryocoolers/?lang=en (accessed Oct. 2021).

[286] Cryogenic Control Systems, Inc.. [Online] Available: https://www.cryocon.com/ (accessed Oct. 2021).

[287] Apiezon N Grease. [Online] Available: https://apiezon.com/products/vacuum-greases/apiezon-n-grease/ (accessed Nov. 2022).

[288] Hositrad Holland B.V.. [Online] Available: https://www.hositrad.com/ (accessed Oct. 2022).

[289] Elma EC 10 - Elma Schmidbauer GmbH. [Online] Available: https://www.elma-ultrasonic.com/en/products/cleaning-chemistry/elma-dent-med-clean (accessed Nov. 2022).

[290] E. W. Hoppe *et al.*, *Cleaning and passivation of copper surfaces to remove surface radioactivity and prevent oxide formation*, *Nuclear Instruments and Methods in Physics Research Section A: Accelerators, Spectrometers, Detectors and Associated Equipment* **579** (2007) 486–489.

[291] C. C. Lim, *Indium seals for low-temperature and moderate-pressure applications*, *Review of Scientific Instruments* **57** (1986) 108–114.

[292] Sigma-Aldrich - Indium wire, diam. 1.0 mm. [Online] Available: https://www.sigmaaldrich.com/CH/en/product/aldrich/357073 (accessed Nov. 2022).

[293] J. P. Gatica, Outgassing of Materials with respect to XENON. [Online] Available: https://www.nevis.columbia.edu/reu/2016/GaticaPaper.pdf (accessed Oct. 2022).

[294] K. L. Giboni *et al.*, *Xenon recirculation-purification with a heat exchanger*, *Journal of Instrumentation* **6** (2011) P03002 [1103.0986].

[295] D. S. Akerib *et al.*, *The LUX prototype detector: Heat exchanger development*, *Nuclear Instruments and Methods in Physics Research Section A: Accelerators, Spectrometers, Detectors and Associated Equipment* **709** (2013) 29–36 [1207.3665].

[296] Kelvion Holding GmbH. [Online] Available: `https://www.kelvion.com/` (accessed Dec. 2021).

[297] D. Edwards, *The influence of virtual leaks on the pressure in high and ultra-high vacuum systems*, *Vacuum* **29** (1979) 169–172.

[298] P. Jamshidi *et al.*, *Microservices: The Journey So Far and Challenges Ahead*, *IEEE Software* **35** (2018) 24–35.

[299] SIMATIC - The automation brand by Siemens. [Online] Available: `https://new.siemens.com/global/en/products/automation/topic-areas/simatic.html` (accessed Nov. 2022).

[300] Raspberry Pi. [Online] Available: `https://www.raspberrypi.org/` (accessed Nov. 2022).

[301] OPC Foundation. [Online] Available: `https://opcfoundation.org/` (accessed Nov. 2022).

[302] Prometheus. [Online] Available: `https://prometheus.io/` (accessed Nov. 2022).

[303] Grafana. [Online] Available: `https://grafana.com/` (accessed Nov. 2022).

[304] C. Hasterok, *Gas Purity Analytics, Calibration Studies, and Background Predictions towards the First Results of XENON1T*, Ph.D. thesis, University of Heidelberg, Germany, 2017.

[305] G. Bakale, U. Sowada, and W. F. Schmidt, *Effect of an electric field on electron attachment to sulfur hexafluoride, nitrous oxide, and molecular oxygen in liquid argon and xenon*, *The Journal of Physical Chemistry* **80** (1976) 2556–2559.

[306] G. Ventura *et al.*, *Thermal expansion and thermal conductivity of Torlon at low temperatures*, *Cryogenics* **39** (1999) 481–484.

[307] E. M. Gushchin, A. A. Kruglov, and I. M. Obodovskii, *Electron dynamics in condensed argon and xenon*, *JETP* **55** (1982) 650.

[308] The EXO-200 Collaboration, *Measurement of the drift velocity and transverse diffusion of electrons in liquid xenon with the EXO-200 detector*, *Physical Review C* **95** (2017) 025502 [1609.04467].

[309] D. Baur *et al.*, *The XeBRA platform for liquid xenon time projection chamber development*, *Journal of Instrumentation* **18** (2023) T02004 [2208.14815].

[310] The XENON Collaboration *et al.*, *Design and Performance of the XENON10 Dark Matter Experiment*, *Astropart. Phys.* **34** (2011) 679–698 [1001.2834].

[311] The ICARUS Collaboration, *Analysis of the liquid argon purity in the ICARUS T600 TPC*, *Nuclear Instruments and Methods in Physics Research Section A: Accelerators, Spectrometers, Detectors and Associated Equipment* **516** (2004) 68–79.

[312] R. Diurba and On behalf of the DUNE Collaboration, *Purity monitoring for ProtoDUNE*, *Proceedings of 40th International Conference on High Energy physics — PoS(ICHEP2020)* **390** (2021) 198.

[313] S. Moriyama, *Direct dark matter search with XENONnT*, *International symposium on revealing the history of the universe with underground particle and nuclear research, Sendai, Japan,* (2019) .

[314] CAEN S.p.A. [Online] Available: `https://www.caen.it/` (accessed Nov. 2022).

[315] CeramTec GmbH. [Online] Available: `https://www.ceramtec-group.com/en/` (accessed Nov. 2022).

[316] Marta Gibert Group - University of Zurich. [Online] Available: `http://www.physik.uzh.ch/en/groups/gibert.html` (accessed Jan. 2023).

[317] J. Hölzl and F. K. Schulte, *Work Function of Metals*, Springer Tracts in Modern Physics, Springer, Berlin, Heidelberg (1979), 10.1007/BFb0048919.

[318] A. Kahn, *Fermi level, work function and vacuum level*, *Materials Horizons* **3** (2015) 7–10.

[319] Q150T Plus - Turbomolecular pumped coater. [Online] Available: `https://www.quorumtech.com/q150t-turbo-pumped-sputter-coatercarbon-coater/` (accessed Feb. 2023).

[320] A. Valentini, E. Nappi, and M. A. Nitti, *Influence of the substrate reflectance on the quantum efficiency of thin CsI photocathodes*, *Nuclear Instruments and Methods in Physics Research Section A: Accelerators, Spectrometers, Detectors and Associated Equipment* **482** (2002) 238–243.

[321] Hamamatsu Photonics K.K. [Online] Available: `https://www.hamamatsu.com/eu/en.html` (accessed Nov. 2022).

[322] LewVac - Fibre Optic Cables. [Online] Available: `https://www.lewvac.co.uk/product/fibre-optic-cable-assembly-components-accessories/` (accessed Jan. 2023).

[323] W. Shockley, *Currents to Conductors Induced by a Moving Point Charge*, *Journal of Applied Physics* **9** (1938) 635–636.

[324] S. Ramo, *Currents Induced by Electron Motion*, *Proceedings of the IRE* (1939) .

[325] Z. Greene, *The XENON1T Spin-Independent WIMP Dark Matter Search Results and a Model to Characterize the Reduction of Electronegative Impurities in Its 3.2 Tonne Liquid Xenon Detector*, Ph.D. thesis, Columbia University, United States of America, 2018. DOI: 10.7916/D87M1RTN.

[326] Specialty Coating Systems - Parylene Conformal Coatings. [Online] Available: `https://scscoatings.com/` (accessed Jan. 2023).

[327] A. Dhar *et al.*, *Low-background temperature sensors fabricated on parylene substrates*, *Journal of Instrumentation* **10** (2015) P12002 [1508.05757].

[328] NIST Cryogenics - Property Calculator. [Online] Available: `https://trc.nist.gov/cryogenics/calculators/propcalc.html` (accessed Dec. 2022).

[329] S. Saedodin, M. Torabi, J. Kandelousi, and N. Maghsodloo, *Application of net radiation transfer method for optimization and calculation of reduction heat transfer, using spherical radiation shields*, *World Applied Sciences Journal* **11** (2010) 457–461.

[330] E. Tiesinga, P. J. Mohr, D. B. Newell, and B. N. Taylor, *The 2018 CODATA Recommended Values of the Fundamental Physical Constants*, Gaithersburg, MD 20899, National Institute of Standards and Technology (2019).

[331] Emissivity Coefficients common Products. [Online] Available: `https://www.engineeringtoolbox.com/emissivity-coefficients-d_447.html` (accessed Dec. 2022).

[332] Michael Crisler: "New Results from the PICO Dark Matter Search Experiment". [Online] Available: `https://indico.cern.ch/event/455636/` (accessed Oct. 2015).

[333] T. Noble, Recent Results and Future Plans for Dark Matter Searches with PICO. [Online] Available: `https://indico.cern.ch/event/472838/contributions/2202009/` (accessed Feb. 2023).

[334] Teledyne LeCroy. [Online] Available: `https://teledynelecroy.com/` (accessed Jan. 2023).

[335] Python documentation - scipy.integrate.odeint - SciPy v1.10.1. [Online] Available: `https://docs.scipy.org/doc/scipy/reference/generated/scipy.integrate.odeint.html` (accessed Mar. 2023).

[336] F. James and M. Roos, *Minuit: A System for Function Minimization and Analysis of the Parameter Errors and Correlations*, *Comput. Phys. Commun.* **10** (1975) 343–367.

[337] R. L. Amey and R. H. Cole, *Dielectric Constants of Liquefied Noble Gases and Methane*, *The Journal of Chemical Physics* **40** (1964) 146–148.

[338] UHV Design - MPP linear unguided motion. [Online] Available: `https://www.uhvdesign.com/products/push-pull-devices/magnetically-coupled-devices/mpp-linear-unguided-motion/` (accessed Nov. 2022).

[339] F. Arneodo *et al.*, *Cryogenic readout for multiple VUV4 Multi-Pixel Photon Counters in liquid xenon*, *Nuclear Instruments and Methods in Physics Research Section A: Accelerators, Spectrometers, Detectors and Associated Equipment* **893** (2018) 117–123 [1707.08004].

[340] Texas Instruments Incorporated. [Online] Available: `https://www.ti.com/` (accessed Nov. 2022).

[341] R. Peres, *Title Pending*, Ph.D. thesis, University of Zurich, Switzerland, To be published, 2023.

[342] Heinzinger electronic GmbH. [Online] Available: `https://www.heinzinger.com/` (accessed Oct. 2022).

[343] Omnexus - Coefficient of Linear Thermal Expansion. [Online] Available: `https://omnexus.specialchem.com/polymer-properties/properties/coefficient-of-linear-thermal-expansion` (accessed Nov. 2022).

[344] Flexa - Protective metal conduits. [Online] Available: `https://www.flexa.de/Produkte/EN_index_1105.html?grpid=bc066a36-2509-489c-b177-d896f327916a` (accessed Nov. 2022).

[345] L. Hatfield *et al.*, *A treatment which improves surface withstand voltage in vacuum*, *IEEE Transactions on Electrical Insulation* **23** (1988) 57–61.

[346] P. Brown, G. Geschonke, H. Henke, and I. Wilson, *Status of the LEP accelerating structure*, *Proceedings of the 1989 IEEE Particle Accelerator Conference. Accelerator Science and Technology* (1989) 1128–1130 vol.2.

[347] C. Adolphsen *et al.*, *Processing studies of X-band accelerator structures at the NLCTA*, *PACS2001. Proceedings of the 2001 Particle Accelerator Conference (Cat. No.01CH37268)* **1** (2001) 478–480 vol.1.

[348] C. Adolphsen, *Normal-conducting rf structure test facilities and results*, *Proceedings of the 2003 Particle Accelerator Conference* **1** (2003) 668–672 Vol.1.

[349] J. Rodriguez *et al.*, *30 GHz high-gradient accelerating structure test results*, *2007 IEEE Particle Accelerator Conference (PAC)* (2007) 3818–3820.

[350] N. Catalan-Lasheras *et al.*, *Experience Operating an X-band High-Power Test Stand at CERN*, *5th International Particle Accelerator Conference, Dresden, Germany* (2014) 2288–2290.

[351] A. Degiovanni, W. Wuensch, and J. Giner Navarro, *Comparison of the conditioning of high gradient accelerating structures*, *Physical Review Accelerators and Beams* **19** (2016) 032001.

[352] K. L. Chavez and D. W. Hess, *A Novel Method of Etching Copper Oxide Using Acetic Acid*, *Journal of The Electrochemical Society* **148** (2001) G640.

[353] J. R. Davis, ASM International, and Handbook Committee, *Metals Handbook, 2nd Ed., p. 554*, ASM International, Materials Park, Oh. (1998).

[354] P. Barrow *et al.*, *Qualification tests of the R11410-21 photomultiplier tubes for the XENON1T detector*, *Journal of Instrumentation* **12** (2017) P01024 [1609.01654].

[355] V. C. Antochi *et al.*, *Improved quality tests of R11410-21 photomultiplier tubes for the XENONnT experiment*, *Journal of Instrumentation* **16** (2021) P08033 [2104.15051].

[356] J. Wulf, *Direct Dark Matter Search with XENON1T and Developments for Multi-Ton Liquid Xenon Detectors*, Ph.D. thesis, University of Zürich, 2018.

[357] L. Baudis *et al.*, *Characterisation of Silicon Photomultipliers for liquid xenon detectors*, *Journal of Instrumentation* **13** (2018) P10022 [1808.06827].

[358] The XENON Collaboration, *Physics reach of the XENON1T dark matter experiment.*, *Journal of Cosmology and Astroparticle Physics* **2016** (2016) 027 [1512.07501].

[359] N. S. Nightingale, *A new silicon avalanche photodiode photon counting detector module for astronomy*, *Experimental Astronomy* **1** (1990) 407–422.

[360] M. G. Bisogni, A. Del Guerra, and N. Belcari, *Medical applications of silicon photomultipliers*, *Nuclear Instruments and Methods in Physics Research Section A: Accelerators, Spectrometers, Detectors and Associated Equipment* **926** (2019) 118–128.

[361] M. G. Giacomelli, *Evaluation of silicon photomultipliers for multiphoton and laser scanning microscopy*, *Journal of Biomedical Optics* **24** (2019) 106503.

[362] R. Agishev *et al.*, *Lidar with SiPM: Some capabilities and limitations in real environment*, *Optics & Laser Technology* **49** (2013) 86–90.

[363] F. Acerbi *et al.*, *Silicon photomultipliers and single-photon avalanche diodes with enhanced NIR detection efficiency at FBK*, *Nuclear Instruments and Methods in Physics Research Section A: Accelerators, Spectrometers, Detectors and Associated Equipment* **912** (2018) 309–314.

[364] A. Hahn *et al.*, *Development of three silicon photomultiplier detector modules for the MAGIC telescopes for a performance comparison to PMTs*, *Nuclear Instruments and Methods in Physics Research Section A: Accelerators, Spectrometers, Detectors and Associated Equipment* **912** (2018) 259–263.

[365] E. Garutti, *Silicon photomultipliers for high energy physics detectors*, *Journal of Instrumentation* **6** (2011) C10003 [1108.3166].

[366] S. Gundacker and A. Heering, *The silicon photomultiplier: fundamentals and applications of a modern solid-state photon detector*, *Physics in Medicine & Biology* **65** (2020) 17TR01.

[367] D. B. Newell and E. Tiesinga, *The international system of units (SI):: 2019 edition*, Tech. Rep. NIST SP 330-2019, National Institute of Standards and Technology, Gaithersburg, MD (Aug. 2019), DOI: 10.6028/NIST.SP.330-2019.

[368] F. Acerbi and S. Gundacker, *Understanding and simulating SiPMs*, *Nuclear Instruments and Methods in Physics Research Section A: Accelerators, Spectrometers, Detectors and Associated Equipment* **926** (2019) 16–35.

[369] R. Klanner, *Characterisation of SiPMs*, *Nuclear Instruments and Methods in Physics Research Section A: Accelerators, Spectrometers, Detectors and Associated Equipment* **926** (2019) 36–56 [1809.04346].

[370] Yu. Musienko *et al.*, *Radiation damage studies of silicon photomultipliers for the CMS HCAL phase I upgrade*, *Nuclear Instruments and Methods in Physics Research Section A: Accelerators, Spectrometers, Detectors and Associated Equipment* **787** (2015) 319–322.

[371] C. Piemonte *et al.*, *Characterization of the First Prototypes of Silicon Photomultiplier Fabricated at ITC-irst*, *IEEE Transactions on Nuclear Science* **54** (2007) 236–244.

[372] G. Vincent, A. Chantre, and D. Bois, *Electric field effect on the thermal emission of traps in semiconductor junctions*, *Journal of Applied Physics* **50** (1979) 5484–5487.

[373] A. N. Otte, D. Garcia, T. Nguyen, and D. Purushotham, *Characterization of three high efficiency and blue sensitive silicon photomultipliers*, *Nuclear Instruments and Methods in Physics Research Section A: Accelerators, Spectrometers, Detectors and Associated Equipment* **846** (2017) 106–125 [1606.05186].

[374] S. Mandai and E. Charbon, *Multi-channel digital SiPMs: Concept, analysis and implementation*, *2012 IEEE Nuclear Science Symposium and Medical Imaging Conference Record (NSS/MIC)* (2012) 1840–1844.

[375] A. Lacaita, F. Zappa, S. Bigliardi, and M. Manfredi, *On the bremsstrahlung origin of hot-carrier-induced photons in silicon devices*, *IEEE Transactions on Electron Devices* **40** (1993) 577–582.

[376] R. Pagano *et al.*, *Optimized silicon photomultipliers with optical trenches*, *2011 Proceedings of the European Solid-State Device Research Conference (ESSDERC)* (2011) 183–186.

[377] M. Redshaw, E. Wingfield, J. McDaniel, and E. G. Myers, *Mass and double-beta-decay Q value of* ^{136}Xe, *Physical Review Letters* **98** (2007) 053003.

[378] E. Erdal *et al.*, *Recent advances in bubble-assisted Liquid Hole-Multipliers in liquid xenon*, *Journal of Instrumentation* **13** (2018) P12008 [1708.06645].

[379] M. Y. Barnyakov and A. V. Mironov, *Photocathode aging in MCP PMT*, *Journal of Instrumentation* **6** (2011) C12026.

[380] B. Dolgoshein *et al.*, *Status report on silicon photomultiplier development and its applications*, *Nuclear Instruments and Methods in Physics Research Section A: Accelerators, Spectrometers, Detectors and Associated Equipment* **563** (2006) 368–376.

[381] Hamamatsu Photonics K.K., Product Flyer - VUV4 MPPC. [Online] Available: `https://hamamatsu.su/files/uploads/pdf/3_mppc/s13370_vuv4-mppc_b_(1).pdf` (accessed Feb. 2023).

[382] K. Lung *et al.*, *Characterization of the Hamamatsu R11410-10 3-in. photomultiplier tube for liquid xenon dark matter direct detection experiments*, *Nuclear Instruments and Methods in Physics Research Section A: Accelerators, Spectrometers, Detectors and Associated Equipment* **696** (2012) 32–39 [1202.2628].

[383] L. Baudis *et al.*, *Enhancement of light yield and stability of radio-pure tetraphenyl-butadiene based coatings for VUV light detection in cryogenic environments*, *Journal of Instrumentation* **10** (2015) P09009.

[384] M. Capasso *et al.*, *FBK VUV-sensitive Silicon Photomultipliers for cryogenic temperatures*, *Nuclear Instruments and Methods in Physics Research Section A: Accelerators, Spectrometers, Detectors and Associated Equipment* **982** (2020) 164478.

[385] G. Gallina, *Light detection with SiPMs for the nEXO experiment*, *TIPP2021* (2021) .

List of Abbreviations

ν_e	electron neutrino
$0\nu\beta\beta$	neutrinoless double beta
ADC	Analog-to-Digital Converter
AP	afterpulse
APD	avalanche photodiode
BoX	Ball of Xenon
CAD	computer-aided design
CCD	charge-coupled device
CDM	cold dark matter
CEνNS	coherent elastic neutrino-nucleus scattering
CMB	Cosmic Microwave Background
CTP	crosstalk probability
CW	control word
DAQ	data acquisition
DARWIN	DARk matter WImp search with liquid xenoN
DCR	dark count rate
ER	electronic recoil
FBK	Fondazione Bruno Kessler
FEA	Finite Element Analysis
FOS	factor of safety
FPGA	Field Programmable Gate Array
GCSA	gas cylinder storage array
GN_2	gas nitrogen
GXe	gaseous xenon
HAR	high aspect ratio
HPGe	high-purity germanium
HPMV	high-pressure manual valve
HV	high-voltage
IR	infrared
KK	Kaluza–Klein
LAr	liquid argon
LArS	Liquid Argon Setup
LED	Light-Emitting Diode
LET	linear energy transfer
LHC	Large Hadron Collider
LIDAR	Light Detection And Ranging
LKK	Lightest Kaluza–Klein

LN_2	liquid nitrogen
LNGS	Laboratori Nazionali del Gran Sasso
LO_2	liquid oxygen
LSP	lightest supersymmetric particle
LSR	local standard of rest
LTE	Long-Term Evolution
LVDS	Low-Voltage Differential Signalling
LXe	liquid xenon
MACHO	massive compact halo object
MLI	multi-layer insulation
MOND	modified Newtonian dynamics
MPPC	Multi-Pixel Photon Counter
MRI	magnetic resonance imaging
NIM	Nuclear Instrumentation Module
NR	nuclear recoil
NTP	Normal Temperature and Pressure
OFHC	oxygen-free high thermal conductivity
Op-Amp	operational amplifier
OPC	Open Platform Communications
OV	overvoltage
p.e.	photoelectron
P&ID	Piping and Instrumentation Diagram
PAI	polyamide-imide
PC	personal computer
PCB	printed circuit board
PCI	Peripheral Component Interconnect
PDE	photon detection efficiency
PEEK	polyether ether ketone
PFA	perfluoroalkoxy alkane
PID	Proportional–Integral–Derivative
PLC	Programmable Logic Controller
PM	purity monitor
PMT	photomultiplier tube
POM	polyoxymethylene
ppb	parts per billion
ppm	parts per million
ppt	parts per trillion
PSD	pulse shape discrimination
PTFE	polytetrafluoroethylene
PTR	pulse tube refrigerator
PVC	polyvinyl chloride
QE	quantum efficiency
R&D	research and development
rms	root mean square
RTD	resistor temperature detector
SC	slow control
SD	spin-dependent
SHV	safe high-voltage
SI	spin-independent

SiPM	silicon photomultiplier
slpm	standard litres per minute
SM	Standard Model
SPAD	single photon avalanche diode
SPE	single photoelectron
SSPM	solid state photomultiplier
TPC	time projection chamber
UED	universal extra dimension
UHMWPE	ultra-high molecular weight polyethylene
UPS	uninterruptible power supply
UV	ultraviolet
VME	Versa Module Europa
VUV	vacuum ultraviolet
WAN	Wide Area Network
WIMP	Weakly Interacting Massive Particle
XML	Extensible Markup Language
ZLE	Zero Length Encoding

Index